INVESTIGATION OF THE THERMOSTABILITY AND ACTIVITY OF BIOMOLECULES IN DEEP EUTECTIC SOLVENTS

A Dissertation

Presented to

the Faculty of the Graduate School

at the University of Missouri-Columbia

In Partial Fulfillment

of the Requirements for the Degree

Doctor of Philosophy

by

JENNIFER ANN KIST

Professor Gary A. Baker, Dissertation Supervisor

MAY 2023

The undersigned, appointed by the Dean of the Graduate School, have examined the dissertation entitled

INVESTIGATION OF THE THERMOSTABILITY AND ACTIVITY OF BIOMOLECULES IN BIO-FRIENDLY DEEP EUTECTIC SOLVENTS

Presented by

Jennifer Ann Kist,

a candidate for the degree of Doctor of Philosophy of Chemistry,

and hereby certify that, in their opinion, it is worthy of acceptance.

_____

Professor Gary A. Baker, Advisor and Committee Chair

_____

Professor Susan Lever, Departmental Member

_____

Professor Silvia S. Jurisson, Departmental Member

_____

Professor Michael T. Henzl, External Member

ACKNOWLEDGEMENTS

First and foremost, I have to thank Jesus Christ, for through Him and with Him I can do anything. Praise God! Second, I am so thankful for my mom, Mary Kist. I have been so lucky to have her with me throughout this journey. She is one of my best friends and I love her so much. Third, I want to thank my brother, Dr. Matthew Kist, and my sister-in-law, Emma Kist. They are amazing people, and I am so thankful for them. I am also so thankful for baby Holden. I cannot wait to be your Aunt Jenny! My family is my rock, my inspiration, my favorite people in the world, and there are not enough words to express how grateful I am for them. They are the most supportive and encouraging people and I know I can come to them with anything in life and they will be there. I love you all so much! I could not have done this without you. I also want to thank my dad, Joseph Kist, for his continued support and encouragement.

I also want to thank my research mates, but really, my good friends. To the previous graduate students who are now doctors, Jeremy Essner, Nate Larm, Laxmi Adhikari, Nakara (Snacky) Bhawawet, and Kanishka Sikligar; your friendships mean the world to me, and I will always cherish you in my heart. To the current Baker graduate students, Asher Siegel, Dustin Boogaart, Piyuni Ishtaweera, Angira Roy, Megan Taylor, Saamia Salik, and Ashen Samaranayake; you seriously made graduate school so much fun these last few years. I truly enjoyed getting to know all of you and I will miss all of our conversations, whether it be science-related, food-centered, or whatever. I love you all so much! I hope we can collaborate once we are all doctors thriving in our professions. Also, I have to shout out my undergraduate student I work with, Isabelle (Izzy) Davis. I have

really enjoyed working with you. Thank you for being an excellent student and for all the fun chats in between work. Good luck in graduate school. You are going to kick butt!

To my girlfriends, Alicia May and Sarah Cherry back in Savannah, GA; we have not talked as much as I want, but I truly love you and miss you so much. You ladies are the most amazing and I hope I get to see you soon! Thanks for being my friends who I know I can go to with anything.

Last, but certainly not least, I have to thank my advisor and mentor, Professor Gary Baker, for everything he has done for me over the years. You have made me a better scientist and I will forever be grateful to you for all of the knowledge you have imparted on me.

TABLE OF CONTENTS

Page

LIST OF SCHEMATICS AND FIGURES

Page

LIST OF TABLES

LIST OF COMMONLY USED ACRONYMS

ABS:	Aqueous biphasic system
BSA:	Bovine serum albumin
CAGE:	Choline bicarbonate and geranic acid
CALB:	Candida Antarctica lipase B
ChAc:	Choline acetate
ChCl:	Choline chloride
CD:	Circular dichroism
DESs:	Deep eutectic solvents
DNA:	Deoxyribonucleic acid
DSC:	Differential scanning calorimetry
EAC:	Ethylammonium chloride
HRP:	Horseradish peroxidase
HBA:	Hydrogen bond acceptor
HBD:	Hydrogen bond donor
ILs:	Ionic liquids
NADES:	Natural deep eutectic solvents
PBS:	Phosphate buffered saline
PEG:	Polyethylene glycol

RNase A:	Ribonuclease A
THEDES:	Therapeutic deep eutectic solvents
Tm:	Transition temperature

INVESTIGATION OF THE THERMOSTABILITY AND ACTIVITY OF BIOMOLECULES IN BIO-FRIENDLY DEEP EUTECTIC SOLVENTS

Jennifer A. Kist

Professor Gary A. Baker, Dissertation Supervisor

ABSTRACT

The solvent environment of a biomolecule is critical to its optimal performance in various scenarios, including biocatalysis, drug delivery, therapeutics, and biosensing. This dissertation mainly discusses the implementation of deep eutectic solvents (DESs) as an emerging and alternate solvent system for biomolecular applications, including aspects of protein thermostabilization and extraction and the role of DESs in biocatalytic systems, such as those involving lipases or whole cells. Additionally, a discussion of DESs for the modulation of nucleic acid systems, drug solubilization and delivery, and emerging biomedical applications is included. Overall, the intent of this dissertation is to elucidate some of the advantages of implementing DESs in an array of biomolecule-driven purposes and illustrate the versatility and potential of these unique, environmentally responsible solvents for next-generation biotechnological and biomedical applications.

Chapter 1: The Study and Application of Biomolecules in Deep Eutectic Solvents†

†This chapter is based on a published manuscript in Journal of Materials Chemistry B. The information contained herein is adapted with permission from **Kist, J. A.;** Zhao, H.; Mitchell-Koch, K. R.; and Baker, G. A., The study and application of biomolecules in deep eutectic solvents. J. Mater. Chem. B, **2021**, 9, 536-566.

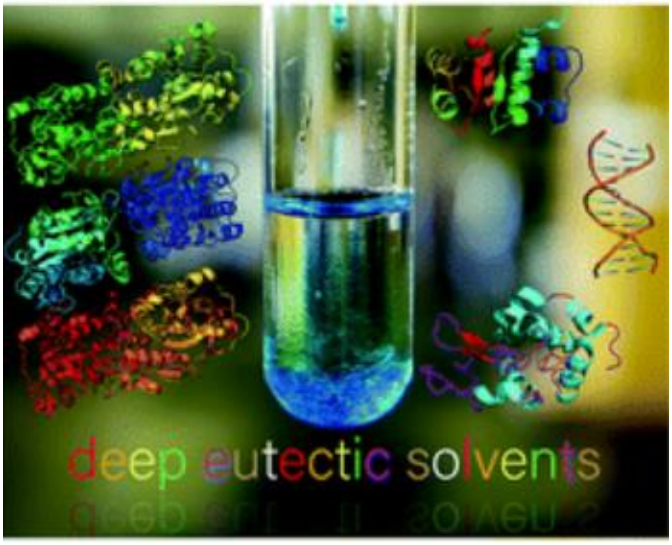

Scheme 1.1 Graphical abstract alluding that deep eutectic solvents can interact with proteins.

Abstract

Biomolecules have been thoroughly investigated in a multitude of solvents historically in order to accentuate or modulate their superlative properties in an array of applications. Ionic liquids have been extensively explored over the last two decades as potential replacements for traditional organic solvents, however, they are sometimes associated with a number of limitations primarily related to cost, convenience, accessibility, and/or sustainability. One potential solvent which is gaining considerable traction in recent years is the so-called deep eutectic solvent which holds a number of striking advantages, including biodegradability, inherently low toxicity, and a facile, low-cost, and solventless preparation from widely available natural feedstocks. In this chapter, the recent progress and insights into biomolecular behavior within deep eutectic solvent-containing systems, including discussions of their demonstrated utility and prospects for the biostabilization of proteins and nucleic acids, free enzyme and whole-cell biocatalysis, various extraction processes (*e.g.*, aqueous biphasic systems, nano-supported separations), drug solubilization, lignocellulose biomass treatment, and targeted therapeutic drug delivery has been highlighted. All indications point to the likelihood that these emerging solvents have the capacity to satisfy the requirements of environmental responsibility while unlocking biomolecular proficiency in established biomedical and biotechnological pursuits as well as a number of academic and industrial ventures not yet explored.

Introduction

Introduction of Deep Eutectic Solvents

The solvent environment of a biomolecule is critical to its optimal performance in various scenarios, including biocatalysis, drug delivery, therapeutics, and biosensing. Many

researchers have implemented ionic liquids (ILs) as alternative solvent systems for biomolecules due to a range of advantages such as low vapor pressure, stability (*e.g.*, thermal, chemical, redox), non-flammability, and tailorability. While this chapter is not directly concerned with conventional ILs, it appears sensible to briefly distinguish between an ionic liquid and its cousin, the deep eutectic solvent. Over the past two decades, ILs have become one of the most widely studied topics in science and engineering.[1-2] A commonly accepted general definition of an IL is that of a fluid solely comprising ions that remains molten at temperatures below 100°C. Besides their potential environmental impact, the cost associated with the synthesis, purification, recycling, and disposal of ILs has presented a barrier to more widespread use. Although ILs certainly display many fine qualities, it has been shown in certain settings that ILs can be prohibitively costly to synthesize and can also be toxic to cells and enzymes.[3-4] In the light of these limitations, the recent emergence of deep eutectic solvents (DESs) is both significant and timely.

Briefly, DESs are low-melting mixtures of Lewis or Brønsted acids and bases. Notably, these melts are related to ILs and exhibit many of their favorable features but are frequently based on nontoxic, inexpensive, readily available, and completely biodegradable natural compounds. Additionally, DESs can generally be prepared by simple mixing of the desired components in specific molar ratios,[5-14] usually with gentle heating in the 50-100°C range to encourage mixing (other methods of synthesis include the freeze-drying method[15-16] or solventless mortar-and-pestle grinding of components, although these are less common). The purity of the starting materials defines the final DES purity and, in contrast to ILs (which produce stoichiometric waste during metathesis), DES preparation is essentially 100% atom efficient. With these decisive benefits, DESs have

emerged as a highly promising class of green solvent, retaining many of the versatile properties displayed by ILs, while offering additional advantages in terms of cost and sustainability.

The DESs most pertinent to biomolecular studies are "type III" DESs consisting of a hydrogen bond acceptor (HBA; typically, a quaternary ammonium salt like choline chloride (ChCl), choline acetate (ChAc), or ethylammonium chloride) and a hydrogen bond donor (HBD; such as an amine, amide, carboxylic acid, sugar or other polyol). The molar ratio of the individual components is very important, and, at a particular eutectic ratio, a number of molecules of the HBD (typically 1-4) bonds per salt (ion pair) to form a liquid mixture at a temperature well below the melting points of the individual constituents. DESs can be prepared that are more hydrophilic than conventional ILs and most are water miscible. The conception of DESs was first introduced by Abbott *et al.* in 2003 where ChCl (melting point 302°C) was mixed with urea (melting point 133°C) to form a DES with a reported melting point of 12°C.[12] The charge delocalization arising from hydrogen bonding between the halide anion and the HBD moiety (in this case, urea) was assigned as being responsible for the decreased melting point observed for the mixture relative to the melting points of the individual components. In terms of nomenclature, DESs are typically classified into four groups, as summarized in Table 1.1. DESs can be described by the basic formula $Cat^{+}X_z^{-}Y$, in which Cat^{+} represents the cation of various sulfonium, ammonium, or phosphonium salts, X^{-} is the halide (typically) anion of the salt, Y is a Lewis or Brønsted acid, and z is the number of molecules of Y. Among the four types of DESs listed, type III is the most encountered in the literature because of their simple preparation, low cost,

Table 1.1 General formulas for the classification of DESs adapted with permission from ref. 17.

Type	General Formula	Terms
Type I	$Cat^{+}X_z^{-}MCl_x$	M = Zn, Sn, Fe, Al, Ga, In
Type II	$Cat^{+}X_z^{-}MCl_x \cdot yH_2O$	M= Cr, Co, Cu, Ni, Fe
Type III	$Cat^{+}X_z^{-}RZ$	Z= $CONH_2$, COOH, OH
Type IV	$MCl_x + RZ = MCl_{x-1}^{+} \cdot RZ + MCl_{x+1}^{-}$	M = Al, Zn, and Z = $CONH_2$, OH

nonreactivity with water, and biocompatibility. To date, the most widely used HBA is choline chloride (ChCl) because it is cheap, extensively available, biodegradable, and presents low toxicity (*e.g.*, it is used in animal feed; choline itself is present in foodstuffs as phosphatidylcholine). Currently, the most popularly studied DESs comprise choline chloride mixed with a two-fold molar equivalent of the HBD species urea, ethylene glycol, or glycerol to produce reline, ethaline, or glyceline, respectively, as shown in Figure 1.1A. Examples of the depressed melting points observed for representative binary mixtures between choline chloride and HBD species are provided in Figure 1.1B using reported DES melting points taken from the literature.[6]

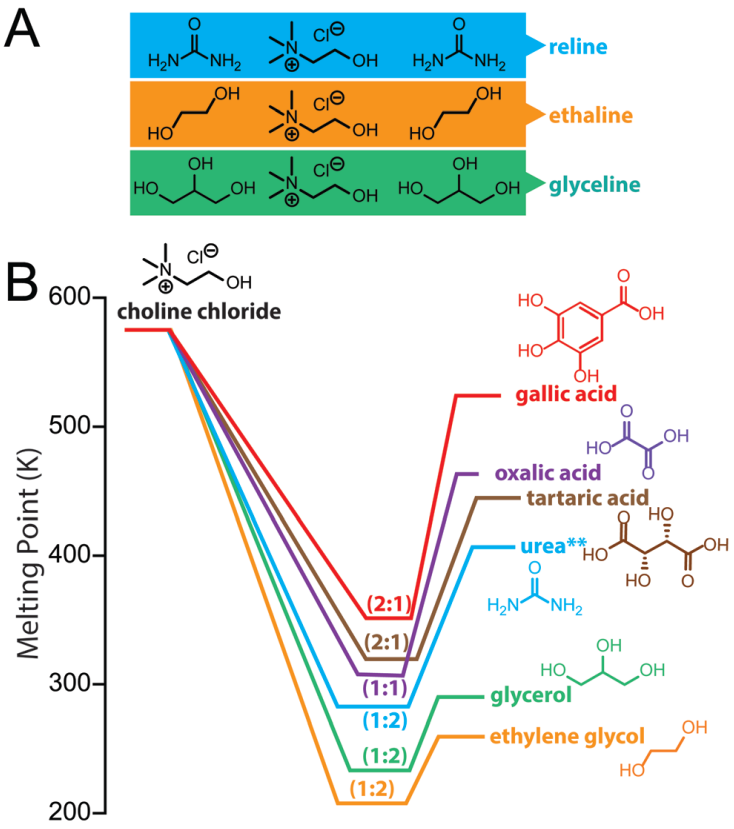

Figure 1.1 (A) The "notorious three" DESs (*i.e.*, reline, ethaline, glyceline) currently responsible for the bulk of the research activity in the area. (B) Diagram of select binary combinations of choline chloride with various hydrogen bond donor species illustrating the melting points of the constituent compared with the eutectic formed at the stoichiometry indicated. **It is noteworthy that the trend shown for 1:2 choline chloride: urea coincides nearly exactly with that of the 1:1 choline chloride: malonic acid system.

Due to their environmentally responsible qualities as well as their tailorable physicochemical properties, there is considerable interest in applying DESs in a number of important areas. Not surprisingly, the number of publications focused on DES synthesis, properties, and applications has grown exponentially since their emergence.[17-19] DESs have already been explored as media or co-solvents for organic synthesis, electrochemistry (*e.g.*, electrodeposition of metal films), polymers, chemical analysis (*e.g.*, CO_2 and SO_2 capture)

and nanotechnology, in addition to biotechnological utilization in biocatalysis, lignocellulose processing, and pharmaceutical and biomedical application examples, a number of which will be summarized herein.

Natural DESs (NADES) were distinguished for the first time by Choi *et al.* in 2011 as eutectic solvents being composed of primary plant metabolites (*e.g.,* sugars, carboxylic acids, amino acids) that appear in living tissues and play an important role in cellular processes.[20] NADES were introduced into analytical practice as an alternative type of extraction solvent. Besides the many advantages of DESs, some have argued that NADES are even more environmentally friendly due to their natural origin. The genesis of this notion is that NADES may occur in all organisms and are thought to be involved in the biosynthesis, solubilization, and storage of hydrophobic metabolites, and unstable compounds in living cells. Given the growing interest in NADES for extractive processes, biotransformations, nucleic acid manipulation, biocatalysis, pharmaceuticals and therapeutics, it is important to include them in this chapter, however, it should be noted that they fall well within the purview of conventional DESs in all respects.

This chapter is focused on the implementation of DESs as an emerging and alternate solvent system for biomolecular applications, including aspects of protein thermostabilization and extraction (*e.g.,* aqueous biphasic systems) and the role of DESs in biocatalytic systems, such as those involving lipases or whole cells. Additionally, a discussion of DESs for the modulation of nucleic acid systems, drug solubilization and delivery, and emerging biomedical applications (*e.g.,* therapeutic deep eutectic solvents). Overall, the intent of this chapter is to elucidate some of the advantages of implementing DESs in a multitude of biomolecule-driven purposes and illustrate the versatility and

potential of these unique, environmentally responsible solvents for next-generation biotechnological and biomedical applications.

Proteins in Deep Eutectic Solvents

Model protein folding studies and thermostability

Proteins behave differently depending on the solvent in which they reside, which makes solvent environment of utmost importance. For many years, the use of enzymes was restricted to dilute aqueous solutions; however, the use of organic solvents became increasingly more popular which widened the field to many more applications.[21-22] Even though organic solvents have played a major role in protein folding studies, there have been numerous disadvantages of these solvents showing toxicity, instability, degradation, and inactivation of some proteins. Therefore, considerable attention has been focused on developing novel solvents, including the use of ILs, and, although some of these ILs show great enhancement in protein thermal stability, some have been proved to be protein denaturants and expensive to synthesize. DESs have become increasingly popular in protein stability studies to further enhance their thermostability, while also providing a more biofriendly solvent environment.

Esquembre *et al.* were among the first groups to study the thermal unfolding and refolding of hen egg white lysozyme in neat DESs consisting of ChCl: urea and ChCl: glycerol, both employing a 1:2 molar ratio.[23] Thermal treatment of the protein to 80°C resulted in stabilization when ChCl: glycerol was used, while ChCl: urea effectively destabilized lysozyme as confirmed by fluorescence spectroscopy and circular dichroism (CD) measurements, as can be seen in Figure 1.2.

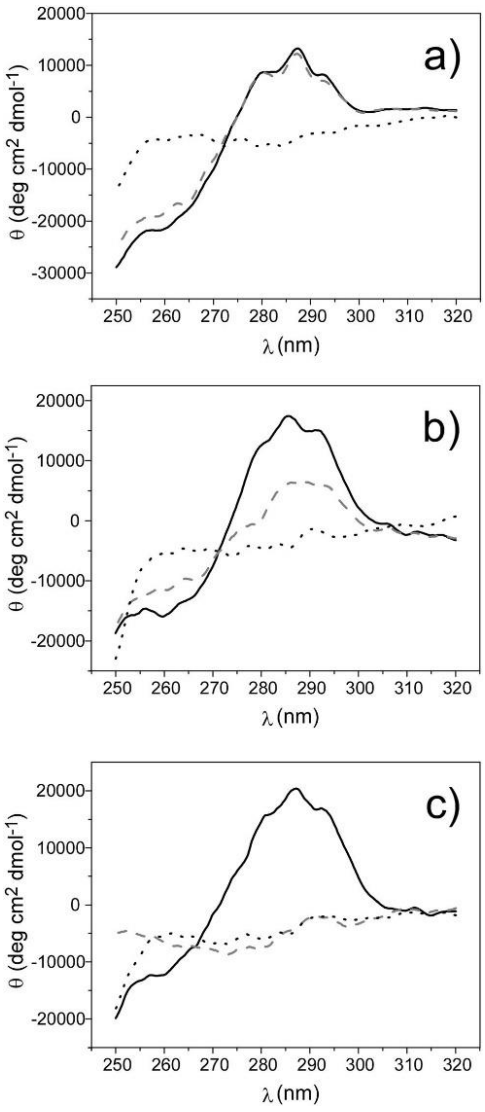

Figure 1.2 Near UV CD spectra of lysozyme dissolved in MES buffer solution (a), neat ChCl: glycerol (b), and neat ChCl: urea (c), at 20°C before thermal treatment (solid line), at 80°C (dotted line), and at 20°C after cooling (dashed grey line). Reprinted with permission from ref. 23. Copyright © 2012 Royal Society of Chemistry.

Small-angle neutron scattering (SANS) has also been implemented to investigate any conformational changes seen in lysozyme as well as bovine serum albumin (BSA) when neat and hydrated solutions of ChCl: glycerol and ChCl: urea were used as solvents.[24]

In neat ChCl: urea, the maximum dimension of the scatterer (D_{max}), an indicator of protein conformation, was similar to the protein in ChCl: glycerol, although it displayed a lower intensity. The D_{max} values for lysozyme in neat ChCl: glycerol and neat ChCl: urea were $D_{max} = 57.3 \pm 1.1$ Å and 58.0 ± 0.8 Å, respectively. This result was interesting because urea has been known to denature proteins, but according to the SANS data, lysozyme retained its structure in a solvent with high urea content. In comparison with data presented from Esquembre *et al.*,[23] a decrease in protein activity was seen with increasing DES concentration. Therefore, although the structure of the protein might remain the same in high urea concentrations, the activity could potentially be reduced. Additionally, although the protein structure remained intact, higher ionic strength and slower diffusion (due to increased DES viscosity) could lead to decreased protein activity. Furthermore, by replacing any water naturally available around the active site of the protein with DES, activity can be further reduced due to specific binding and decreasing any solvophobic effect. CD results showed that lysozyme in the DES/water mixtures (50 and 75 wt% DES) retained its conformation, indicative of protein stabilization.

It was also determined that SANS data for BSA in DES/water mixtures with 50 and 75 wt% DES ($D_{max} = 94 \pm 5$ Å, 98 ± 3 Å, respectively), agreed well with results from BSA in phosphate buffered saline (PBS) ($D_{max} = 93 \pm 3$ Å). However, for BSA in neat ChCl: glycerol, the D_{max} was larger and slightly red shifted but still shorter than the fully denatured protein ($D_{max} = 131 \pm 4$ Å in neat DES *vs.* 314 ± 12 Å for denatured BSA). As a result of this, it was concluded that the protein in neat DES showed a partially folded structure, whereas the addition of water allowed the protein to fold into a more efficient globular shape. Overall, when water was incorporated alongside a DES, it ultimately

formed a shell around the active sites of the protein, most likely due to hydrogen bonding, allowing for better protein folding.

Xin *et al.* have performed differential scanning calorimetry (DSC) measurements from 30-90°C to determine the thermostability of lysozyme in 25, 50, and 75 wt% ChCl: trehalose (3:1 molar ratio). The transition temperature, T_m, for lysozyme in water was 70.2°C, while the protein in 25 and 50 wt% DES showed increased transition temperatures of 74.4°C and 80.6°C, respectively, indicating that these DESs increased protein stability.[25] The thermal stability of lysozyme was further increased in 75 wt% ChCl: trehalose due to the disappearance of any denaturing peak in the DSC spectrum. Upon thermal treatment to 90°C, CD measurement displayed an intact tertiary structure and complete folding/unfolding reversibility in 75 wt% DES, and partial reversibility in 25 and 50 wt% DES for the protein. Additionally, the individual DES components were studied alongside lysozyme and agreed with previous literature reports that have stated that the supramolecular complexes that form DESs begin to break down when DES concentrations are less than 50 wt% resulting in DES solution that have basically become solutions of their individual components, thus losing some of their unique properties.[5, 15-16, 26] In general, when the concentration of a DES is above 50 wt%, the hydrogen bonding between the hydrogen bond acceptors and donors will remain intact. Since trehalose provides many areas for hydrogen bonding, this DES allowed for increased protein stabilization.

Fibrillar formation in hen egg white lysozyme has been successfully studied by Silva *et al.* who used ChCl: acetic acid (1:1 molar ratio) with lysozyme along with HCl and glycine at 70°C to create fibrils, which were then indirectly measured through fluorescence spectroscopy.[27] Higher temperatures and low pH (around 2) favoured the unfolding of

lysozyme; once cooled back down, it refolded into a β-sheet configuration which led to the formation of protein nanofibers. Thioflavin T is a cationic benzothiazole dye that binds to these β-sheet amyloid structures, therefore, an increase in β-sheets led to an increase in fluorescence intensity. Fluorescence spectra showed that solutions made with 5% (v/v) DES displayed the highest fluorescence intensity (out of 1, 5, and 10% v/v DES) and fibrillar formation did not occur without the aid of the DES. Additionally, the use of ChCl alone produced high fluorescence intensity, similar to aqueous 5% (v/v) DES; however, no increase in fluorescence intensity was seen when acetic acid alone was used. Therefore, it was determined that ChCl played the major role in fibril formation, although an enhanced fluorescence was seen when the DES was used. Overall, after thermal treatment, more than 90% of the native lysozyme misfolded upon cooling, rearranging into nanofibers.

DESs have also been employed as solvent environments for proteins other than lysozyme and BSA. The activity and stability of horseradish peroxidase (HRP) have been investigated with various DESs, with a consensus that, although an increase in DES concentration can negatively affect the activity, the stability of the protein will be enhanced. Wu *et al.* showed that the overall activity of HRP was higher in aqueous ChCl-based DESs over DESs that used choline acetate (ChAc) as the HBA.[28] Although the protein activity was favoured in ChCl-based DESs over ChAc-based DESs, the protein stability was increased with ChAc-based DESs. Similar activity results have been seen with Sanchez-Leija *et al.* who determined that the catalytic activity of HRP was higher in 80% ChCl: glycerol over 80% ChCl :urea (both at 1:2 molar ratio), however, the activity decreased in both systems with increasing DES concentration.[29]

Papadopoulou *et al.* later determined that ethylammonium chloride (EAC) as a HBA, along with the same HBDs of urea, glycerol, and ethylene glycol, showed enhanced HRP activity over ChCl-based DES when used for the oxidation of guaiacol.[30] It was also determined that EAC-based DESs led to higher cytochrome c peroxidase activity over ChCl-based DESs. For instance, 30% (v/v) ChCl: urea (1:2) resulted in an 8-fold peroxidase activity enhancement, while 30% (v/v) EAC: urea (1:1.5 molar ratio) displayed almost 100-fold activity enhancement. The increased peroxidase activity of cytochrome c in EAC-based DESs could be due to different interactions between the protein and salt as well as the changes in viscosities, since ChCl-based DESs tend to be more viscous, potentially increasing mass transfer limitations. Interestingly, the use of urea resulted in a relatively higher activation of cytochrome c as compared to glycerol and ethylene glycol, regardless of which salt was used. This result contradicts previous reports that claim that urea is a protein denaturant. The heme group in this protein is somewhat responsible for catalyzing peroxidation reactions and when the protein was in the urea-containing DES, this heme group potentially became exposed, which could allude to the increased activity observed.[31] The CD spectra displayed similar results, showing that the protein in 30% (v/v) EAC- or ChCl-based DES underwent an orientation in the active site, allowing the heme active center of cytochrome c to be more accessible, which led to increased peroxidase activity.

Most recently, Kist *et al.* studied the thermostability of bovine ribonuclease A (RNase A) in DESs using DSC.[32] RNase A, although widely studied with ILs, has not been rigorously investigated with DESs; therefore, ChCl: urea, ChCl: ethylene glycol, and ChCl: glycerol (all in 1:2 molar ratio) ranging from 5–35 wt% were studied alongside the protein.

Using DSC, iterative thermal cycles from 10–80°C showed that enhanced thermal stability of RNase A was achieved in all concentrations of ChCl: glycerol and ChCl: ethylene glycol as compared to the protein in water. However, RNase A showed complete denaturation in solutions above 5 wt% ChCl: urea after only one thermal cycle. The transition temperatures (T_m), as can be seen in Figure 1.3, steadily increased with increasing ChCl: glycerol (glyceline) concentration, yielding a T_m = 63.0°C at 35 wt% ChCl: glycerol, as compared to a T_m = 59.7°C for the protein in water. The transition temperature was fairly constant for ChCl: ethylene glycol (ethaline) regardless of concentration; however, the transition temperature for the protein in ChCl: urea (reline) continually decreased from T_m = 57.0°C at 5 wt% to 51.8°C in 35 wt%. The IL 1-butyl-3-methylimidazolium chloride ([bmim]Cl) was also investigated with RNase A for comparison purposes, to show the strong denaturing ability of that solvent on the protein.

DESs have also been used to increase stability of therapeutic proteins. Lee *et al.* evaluated NADES as a stabilizing medium for the therapeutic protein, human interferon-α2 (IFN-α2), which is used clinically to treat hepatitis B and C, leukemia, and AIDS-related Kaposi's sarcoma.[33] DESs composed of ChCl: fructose, ChCl: citric acid, and ChCl: malic acid all in 1:1 molar ratio, were used to evaluate their capability of thermally stabilizing IFN-α2 during short- and long-term storage. Interestingly, the DES-protein formulations were synthesized by the freeze-drying method which involved the weighed DES components mixed together along with deionized water, after which the protein was incorporated. The resulting formulation was then freeze-dried to ensure that the protein integrity remained intact. Among the DESs tested, ChCl: fructose was the only one that showed no detrimental effect on the IFN-α2 activity as compared to the other two DESs,

that drastically decreased IFN-α2 activity. Regarding the short-term storage, the activity of IFN-α2 in PBS buffer was greatly reduced after 30 minutes at 70°C and CD results showed loss of secondary structure and complete unfolding of the protein. However, when IFN-α2 was incorporated with ChCl: fructose, the activity remained consistent after 120 minutes at 70°C and no structural changes were seen after thermal treatment as confirmed by CD and fluorescence spectroscopy.

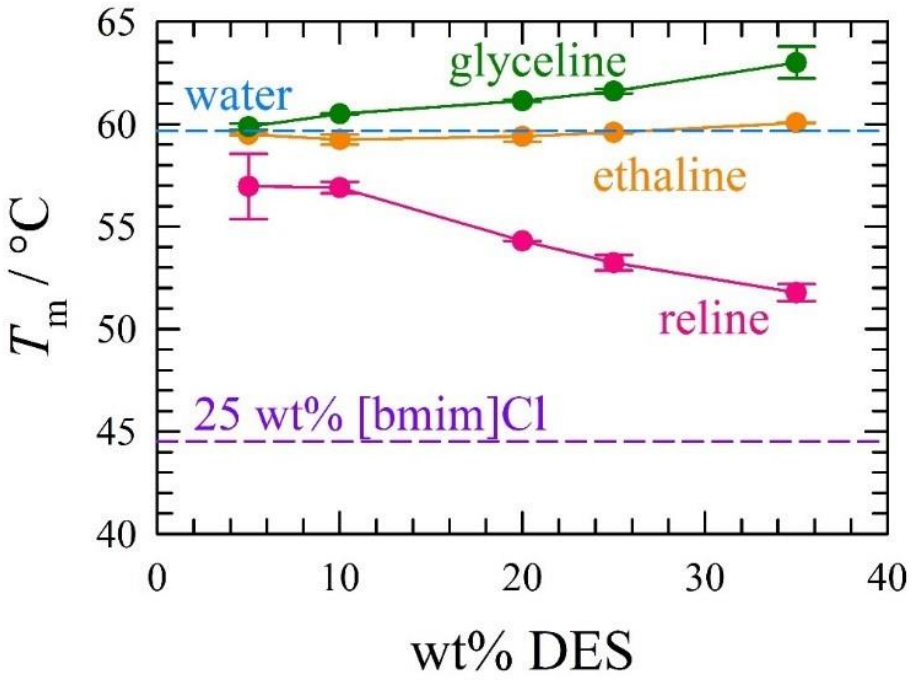

Figure 1.3 The transition temperature, T_m, versus wt% DES. The ionic liquid [bmim]Cl shows a much lower T_m, confirming its reputation as a protein denaturant. The T_m for RNase A in water is shown for reference. Reprinted with permission from ref. 32. Copyright © 2019 American Chemical Society.

When 30% or more water was added to the DES-protein system, conformational changes were seen in CD spectra as well as an increase in fluorescence, which was indicative of IFN-α2 inactivation. No conformational changes were seen in the proteins'

structure when the protein was stored for 90 days at 37°C, showing that the DES of ChCl: fructose can be a suitable solvent for the storage of a therapeutic protein.

Overall, DESs can provide excellent thermostability for proteins, depending on the hydrogen bond acceptors and donors implemented while also providing new and more environmentally friendly alternatives to aqueous or organic solvents. Additionally, these solvents may help to give more insight on protein activity and behavior in extreme environments (*e.g.* cryogenic temperatures or total absence of water) that can further advance the information gained in this field.

Protein Solubilization and Extraction

Aqueous Biphasic Systems (ABSs)

There has been great interest in isolating and extracting pure proteins, however, the main challenge is to maintain the proteins' structure and function after extraction. Traditional methods for protein extraction and purification include ammonium sulfate precipitation, electrophoresis, ion exchange, and affinity chromatography; however, they typically involve organic solvents which have proven to be inefficient due to high costs and low yields.[34-35] More recently, aqueous biphasic (or two-phase) systems (ABS) have been proposed as an alternative and environmentally friendly extraction method with the use of ILs.[36] Due to the limitations of ILs mentioned in the introduction section, researchers have turned their attention to implementing DESs into these novel and efficient protein extraction systems. Figure 1.4 shows a generalized scheme for DES-based ABSs for extracting proteins. In a typical ABS set up, once various parameters have been optimized, an appropriate amount of DES is added to a centrifuge tube. Afterwards, a salt solution (typically K_2HPO_4) is added followed immediately by the protein of interest. The ABS

system is then shaken for an appropriate amount of time, resulting in two separate distinguishable phases to form during which the protein of interest preferentially resides in the DES-rich top layer, allowing for facile extraction. Once the protein has been extracted, the concentration is determined by measuring the absorbance and then the extraction efficiency can be calculated using the following equation:

$$E = C_t V_t/(C_t V_t + C_b V_b) \quad (1)$$

where C_t and C_b are the concentrations of the proteins in the DES-rich top phase and salt-rich bottom phase, respectively, and V_t and V_b are the volumes of the top phase and bottom phase, respectively. Generally, the following parameters are investigated to yield the optimal extraction efficiency per mass of DES used, concentration of salt solution, separation/shaking time, and temperature. Zeng *et al.* were among the first groups to extract proteins using DESs in aqueous biphasic systems.[37] BSA and trypsin were easily extracted with ChCl: urea (1:2), yielding extraction efficiencies of 99.94% and 95.53%, respectively. The extraction efficiencies were also high for BSA in tetramethylammonium chloride (TMACl): urea (1:2) and trypsin in ChCl: methylurea (1:2), yielding 91.69% and 95.27%, respectively. Interestingly, when the protein ovalbumin was studied, the extraction efficiencies were ≤ 50% in all DESs investigated.

Trypsin and BSA have also shown high extraction efficiencies when ChCl: glycerol (1:2) has been implemented into an ABS, yielding 94.36% and 98.16%, respectively.[38] Additionally, Xu *et al.* have analyzed a mixed sample of BSA and bovine hemoglobin (BHb) in ChCl: glycerol resulting in extraction efficiencies of 96.19% and 62.09%, respectively. When the DES of betaine: urea: H_2O (1:2:1) was used in an aqueous biphasic system, Li *et al.* were able to successfully extract and separate BSA and BHb from a mixed

sample with extraction efficiencies of 96.28% and 91.26%, respectively, showing a 30% improvement for BHb extraction, most likely due to increased hydrogen bonding in the DES.[39]

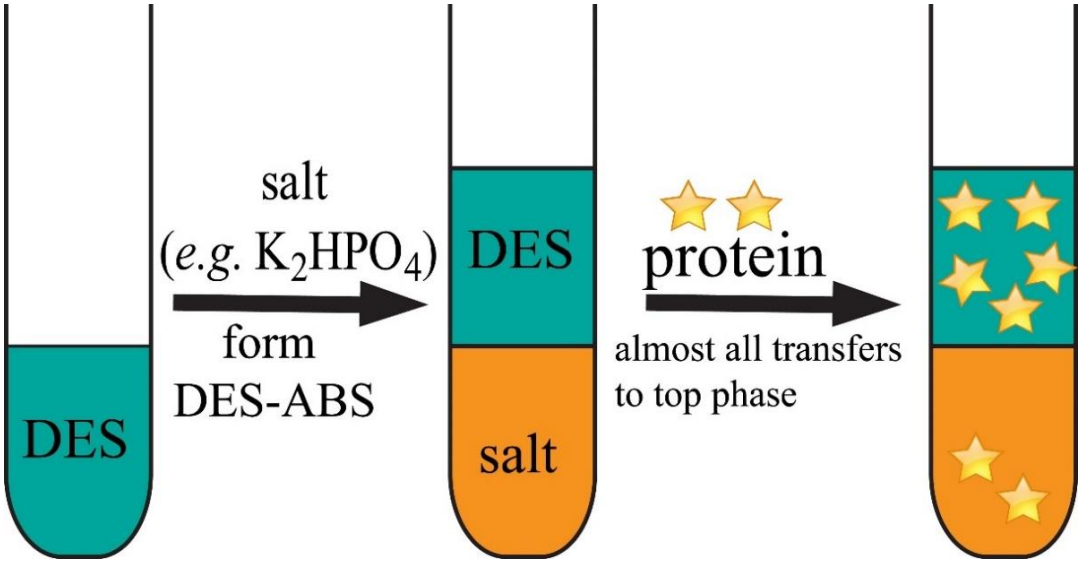

Figure 1.4 General schematic of the extraction process of process using an aqueous biphasic system implementing deep eutectic solvents. Adapted with permission from ref. 37-39. Copyright © 2014 Royal Society of Chemistry; 2015, 2016 Elsevier.

Similar results have reported that higher extraction efficiencies can be found with betaine-containing DESs as compared to ChCl containing DESs for these biphasic systems,[40] although this area of research is still in its infancy. Typically K_2HPO_4 is used as the aqueous salt-rich phase due to its high solubility and strong phase-forming ability in water, however, Pang *et al.* synthesized an ABS using Na_2CO_3 as the aqueous salt-rich phase and ChCl: polyethylene glycol 2000 (ChCl: PEG; 20:1 molar ratio) as the DES-rich phase to extract BSA and papain separately, yielding extraction efficiencies of 95.16% and 90.95%, respectively, after parameter optimization.[41]

Another interesting approach to these aqueous biphasic systems has been to implement ternary DESs. Zhang *et al.* compared binary and ternary DESs in ABSs for the extraction of BSA.[42] The ternary DES composed of tetramethylammonium chloride (TMAC): glycerol: urea (1:1:1) was able to successfully extract BSA with an efficiency of 98.95%, comparing well with the extraction efficiencies of the binary DES of TMAC: urea (1:2), which gave results of 99.31%. Interestingly, the ternary DES was able to achieve a higher back extraction of protein (71.89%) as compared to the binary DES which only yielded 21.02%. Lastly, these biphasic systems have been synthesized with two DESs, specifically, tetrabutylammonium chloride: polypropylene glycol 400 (TBAC: PPG400; 1:2 molar ratio) and L-proline: xylitol (1:1 molar ratio), the latter of which replaced the salt-rich phase, which allowed chymotrypsin to preferentially reside.[43] This DES/DES ABS gave an overall extraction efficiency of 97.30% for chymotrypsin. Overall, the results discussed herein show that DESs can provide a stable environment for proteins in these aqueous biphasic systems.

Protein Extraction Using Magnetic NPs and DESs

Magnetic composites for solid-phase extraction of proteins

Graphene oxide (GO) has been used in magnetic solid-phase extraction processes over the years due to its large number of carboxyl and hydroxyl groups. These functional groups can form hydrogen bonds or have electrostatic interactions with various adsorbates containing oxygen- and nitrogen functionalized groups. Yuzhi Wang's research group have loaded magnetic Fe_3O_4 nanoparticles (NPs), onto GO alongside DESs to increase the hydrophilicity and enhance the extraction efficiency of proteins. Three similar approaches to protein recovery using magnetic solid-phase extraction are briefly discussed with Figure

1.5 summarizing the general setup and procedure. As discussed in the ABS section, various parameters need to be optimized in order to achieve the best extraction capability, including temperature, extraction time, protein concentration, and amount of magnetic GO/DES used. In the first study, a DES consisting of ChCl: glucose (1:1) was coated onto the surface of Fe_3O_4@GO NPs to aid in extracting BSA.[44] Once the protein was extracted, the Fe_3O_4@GO-DES NPs were recovered using an external magnetic and the concentration of the protein was determined via UV-Vis. The Fe_3O_4@GO-DES NPs were able to be fully recovered and therefore could be used again for subsequent extractions. The extraction amount (Q) was calculated by the following equation:

$$Q = (C_0 - C)V/m \qquad (2)$$

where Q (mg g^{-1}) is the mass of protein adsorbed onto a unit amount of Fe_3O_4@GO-DES NPs, C_0 and C (mg mL^{-1}) are the initial and final concentrations of protein in the solution, V (mL) is the volume of the initial solution and m (g) is the mass of the magnetic DES-NP substituent. Interestingly, after the incorporation of DES onto the Fe_3O_4@GO NPs, the surface charge of the material changed from negatively charged (Fe_3O_4@GO NP zeta potential = –10.6 mV) to positively charged (Fe_3O_4@GO-DES NP zeta potential = 19.4 mV), showing that the addition of DES could selectively extract acidic proteins over neutral and basic proteins. Three consecutive extraction–desorption cycles were performed although a significant decline in the amount of protein extracted occurred after each cycle: 73.1 mg g^{-1} for the first cycle, 34.0 mg g^{-1} after the second cycle, and 20.9 mg g^{-1} after the third cycle. When Fe_3O_4@GO NPs were used without any DES, the amount of protein that could be extracted was only 27.4 mg g^{-1}. In a subsequent report, it was determined that the DES of ChCl: glycerol (1:1) could be successfully coated onto a surface of Fe_3O_4–

NH_2@GO NPs to yield an extraction capability of 44.59 mg g^{-1} for BSA.[45] Interestingly, when ChCl: glycerol was coated onto the Fe_3O_4@GO NPs, the extraction capability was only 38.0 mg g^{-1}, showing that each system is able to provide varying degrees of extraction capabilities depending on the magnetic NPs implemented.

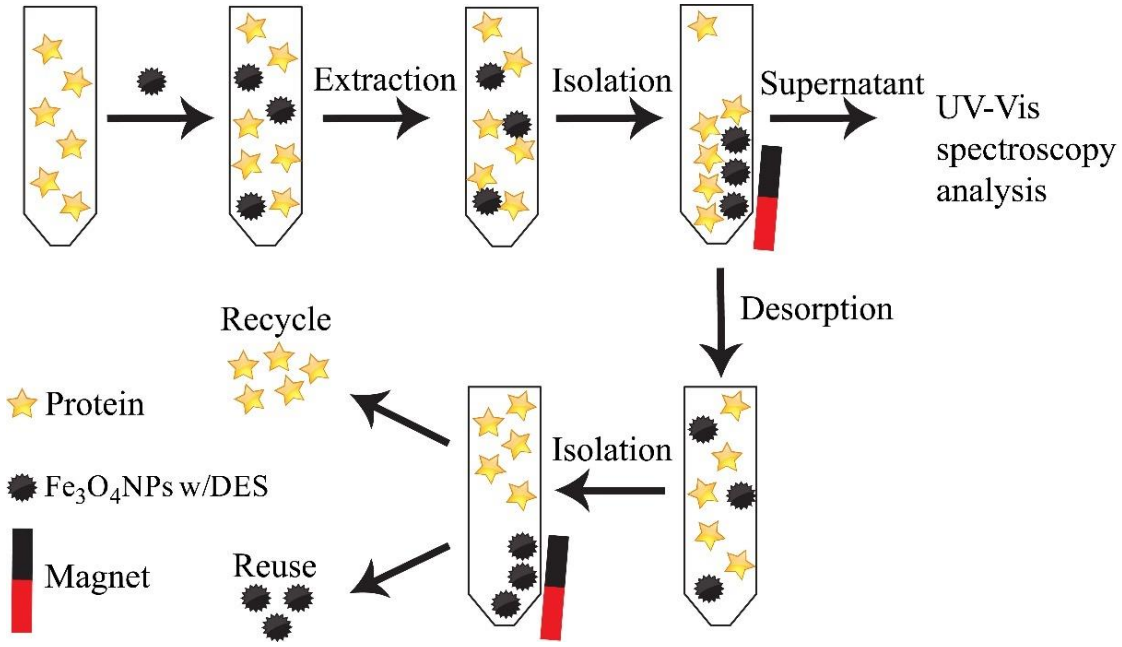

Figure 1.5 General protein extraction process using magnetic iron oxide nanoparticles with deep eutectic solvents. Adapted with permission from ref. 44-46. Copyright © 2015, 2016 Elsevier.

In a final method of extracting proteins using the magnetic solid-phase extraction technique, Fe_3O_4 NPs have been coated with tetraethyl silicate (TEOS) and further modified with 3-(trimethoxysilyl)-propyl methacrylate (γ-MPS), to make microspheres.[46] The DES ChCl: itaconic acid (1:1) was then coated onto the Fe_3O_4@SiO_2–MPS microspheres, which were then used to test the capability of extracting trypsin. Interestingly, this system could perform the extraction–desorption process with only a slight loss in the extraction capacity over six cycles, which was better than the

aforementioned systems. The extraction capability of trypsin in the magnetic microsphere-DES system was 287.5 mg g^{-1}, which was two times higher than that of typical magnetic polymers (75.9–140.65 mg g^{-1}). Overall, the magnetic solid-phase protein extraction technique has been shown to be enhanced when DESs have been coated onto magnetic nanoparticles or microspheres.

Protein extraction using Molecularly Imprinted Polymers (MIPs)

Molecular imprinting technology is very similar to the previously discussed extraction techniques although template molecules (typically the protein of interest) are incorporated into the system and once they are removed, they create cavities that can specifically adsorb the protein and successfully isolate it. Typically, for these systems, the magnetic provider has been shown to be Fe_3O_4 NPs, alongside a crosslinker and DES. The DESs have been incorporated into these systems as functional monomers that can help increase the adsorption capacity of the protein of interest. The amount of DES is critical because if not enough is added, less than optimal interactions between the DES and protein occur; however, too much DES results in a thick imprinting layer which hinders the adsorption capacity of the template molecule. The adsorption capacity, as can be seen in equation (2), is then calculated and an imprinting factor (IF) can be determined to evaluate the specific recognition ability of the magnetic DES-MIPs system, which is defined as:

$$IF = Q_{MIP}/Q_{NIP} \quad (3)$$

where Q_{MIP} and Q_{NIP} are the adsorption capacity of the protein on the magnetic DES-MIPs and the protein on the magnetic non-imprinted polymers (DES-NIPs), respectively. BHb has been successfully isolated in MIPs using various DESs. For example, Liu *et al.* used ChCl: methacrylic acid (1:2) as the functional monomer in MIPs

to yield an adsorption capacity of 175.44 mg g^{-1} and an IF of 4.77.[47] This adsorption capacity was almost four times higher than the adsorption capacity of the non-imprinted polymers, which was 39.59 mg g^{-1}. Similar results were seen when the DES (3-acrylamidopropyl) trimethylammonium chloride: urea (1:2) was used in MIPs, yielding an adsorption capacity for BHb of 164.20 mg g^{-1} and an IF of 4.93.[48] In another report, the protein transferrin was able to be isolated when ChCl: acrylic acid (1:2) was used, yielding an adsorption capacity of 37.5 mg g^{-1} and an IF of 3.50.[49] Interestingly, this MIPs system was also able to isolate BHb, with an adsorption capacity of ~14 mg g^{-1}. BHb and transferrin have similar configurations and sizes, therefore, BHb could be similar enough to successfully occupy the imprinting cavities. Overall, MIPs including DESs have shown to provide a biocompatible method for isolating and purifying proteins.

Nucleic Acids in Deep Eutectic Solvents

Known as a genetic information-carrying macromolecule, deoxyribonucleic acid (DNA) consists of repeating units called nucleotides attached to the negatively charged phosphate backbone via sugar molecules. Earlier studies have suggested that ions and ionic solvents (*e.g.* ionic liquids and DESs) have multilevel interactions with DNA molecules including electrostatic attraction between organic cations and the phosphate backbone, hydrophobic and polar interactions of ionic solvents with DNA major and minor grooves, and possible anion interactions with bases through hydrogen bonds.[50-51], Despite their structural differences, DESs have many similar properties with ionic liquids. The stability of duplex DNA in DES has been examined by several groups. The Hud group[52] visualized the secondary structures of DNA and RNA in neat ChCl: urea (1:2) by CD spectroscopy. They made several interesting findings: (a) an A-form duplex can be seen in DES for the 32 bp

mixed-sequence DNA while B-form helix was observed in aqueous salt solutions (such as 3.7 m NaCl); (b) A left-handed Z-form helix was found in DES and aqueous solutions of ChCl (3.7 m) and NaCl (3.7 m) for oligonucleotide $[d(CG)_8]_2$; (c) A similar B-form helix was formed in DES as in aqueous solutions for oligonucleotide $[d(AT)_{16}]_2$; (d) $[d(A_4T_4)_4]_2$ yielded an altered B-form helical structure (B* form). However, these DNA molecules exhibited lower duplex stability under dehydrating and high ionic strength conditions as suggested by their lower melting transition midpoints (T_M) in DES. Interestingly, certain triplex and G-quadruplex structures were observed in DES although these structures are different from those in aqueous solutions. The same group[53] further reported that neat ChCl: glycerol (1:4) enabled the folding of a two-dimensional DNA origami at 20°C in 144 h while the folding completed in 3 h in hydrated ChCl: glycerol (1:4; 90%) (see Figure 1.6). Furthermore, the hydrated ionic solvent allows for the folding of a three-dimensional DNA origami and a DNA tail system.

More interestingly, folded DNA structures are transferrable between aqueous solvent and ChCl: glycerol (1:4). The Prasad group[54] dissolved up to 5.5 wt% and 2.5 wt% salmon testes DNA in two DESs (ChCl: ethylene glycol and ChCl: glycerol, both at 1:2 molar ratios) respectively; they confirmed B-form helical structures in DES and suggested a high thermal and pH stability for the regenerated DNA. The Zhao group[55] reported that salmon testes DNA molecules preserve their characteristic B-form helical duplex structures in 1.0 M ChCl: glycerol (1:2) as confirmed by CD spectra; in addition, the use of 0.2 M ChCl: glycerol (1:2) enabled a high activity of DNA-based hybrid catalyst for the Michael addition, resulting in a high enantioselectivity (94.0%) and a high yield (88%) at room temperature for 24 h. The Kohler group[56] evaluated the excited-state deactivation in

$d(AT)_9 \cdot d(AT)_9$ duplex DNA strands dissolved in deuterated ChCl: ethylene glycol (1:2) by femtosecond time-resolved IR spectroscopy. Their data confirmed the existence of long-lived exciplex forms exclusively in the solvated duplex, but not in the denatured single strands. In addition, DES enables a longer lifetime of the exciplex state than the aqueous solution, which is attributed to reduced stabilization of the charge transfer state and slower charge recombination due to the Marcus inverted behavior. Guanine-rich nucleic acids tend to form four-stranded G-quadruplex structures by the stacking of planar quartets composed of four guanines that interact by Hoogsteen hydrogen bonding.[57-58] G-quadruplex DNA usually form polymorphic structures, *e.g.* at least five intramolecular G-quadruplexes formed from human telomeric sequences.[59]

Typically, G-quadruplex DNA structures are constructed in aqueous solutions, but recent studies reported these structures could be found in DES. G-quadruplex with the parallel-stranded structure was folded from human telomere sequence (HTS) DNA in ChCl: urea (1:2),[60] which is consistent with the observation of the parallel fold under a reduced water activity and alternative folds at a high water activity. On the other hand, after rapid cooling the thermally denatured HTS to room temperature, refolding DNA back to the parallel structure in DES took much longer time (several months) than that in aqueous solutions (< 2 min) as can be seen in Figure 1.7. Structures of ten G-quadruplexes were evaluated in neat ChCl: urea (1:2) by UV melting, CD and fluorescence spectroscopy, and various intramolecular, intermolecular, and higher-order G-quadruplex structures (particularly the parallel structure) as shown in Figure 1.8.[61] Higher thermal stability of G-quadruplexes (even at over 110°C) was found in neat DES than in aqueous media.

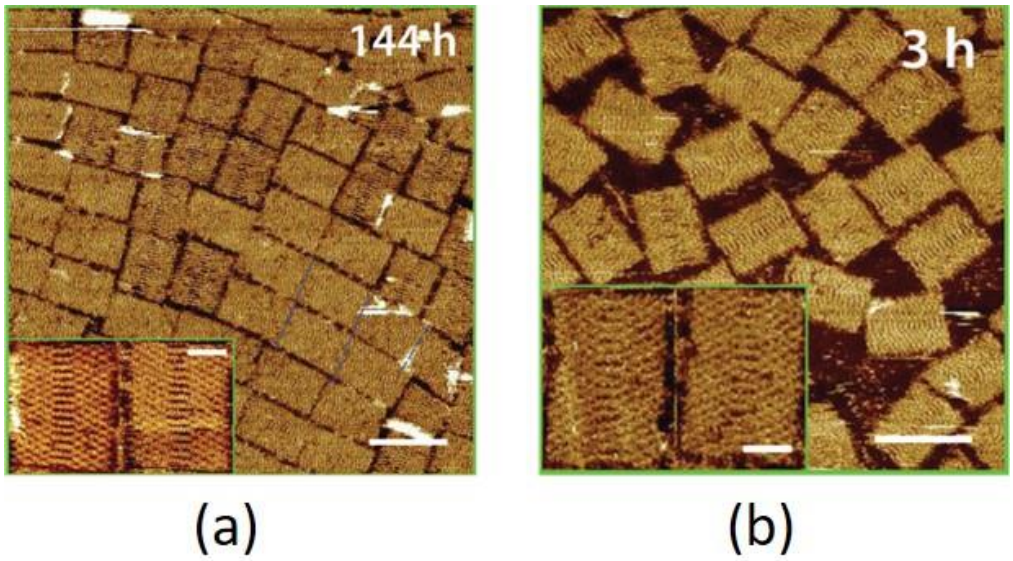

Figure 1.6 AFM illustrating the folding of DNA origami structures: (a) in anhydrous choline: glycerol (1:4) at 20°C for 144 h; (b) in (hydrated) 75% choline: glycerol (1:4) at 20°C for 3 h. Reprinted with permission from ref. 53. Copyright © 2015 Wiley.

Pal and Paul investigated the interaction between ChCl: urea (1:2) with guanine-rich quadruplex thrombin-binding aptamer (TBA) DNA at 300 K using 10 μs all-atom molecular dynamics simulations.[62] They observed that at a higher DES concentration, the higher density of DES molecules near quadruplex TBA led to more rigid DNA structure and conformation; at low DES concentrations, guanine-8 and thymine-9 nucleoside bases of loop-2 stacked to each other. Higher compatibility and stability of duplex and quadruplex DNA in DES systems allows for the preservation of these biomolecules in ionic solvents, and enables potential applications in catalysis, biosensors, and DNA-based architectures.

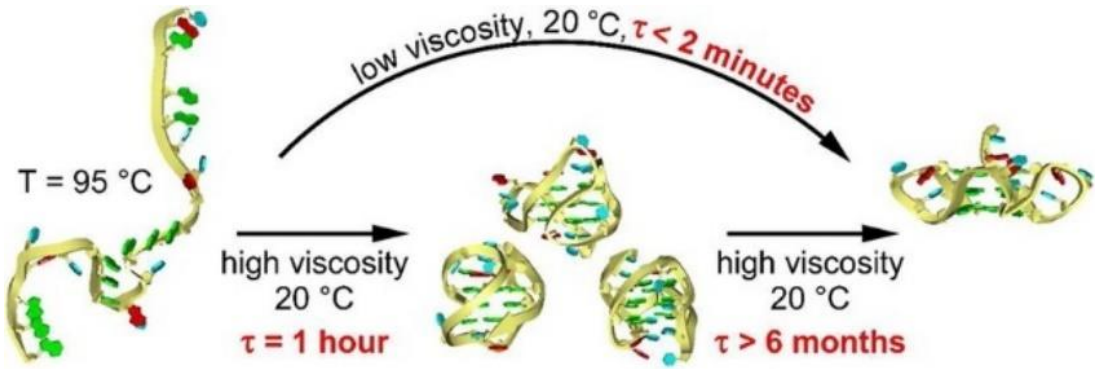

Figure 1.7 DNA refolding in viscous choline chloride: urea (1:2 molar ratio). Reprinted with permission from ref. 60. Copyright © 2012 American Chemical Society.

Biocatalysts in Deep Eutectic Solvents

Biocatalysis can be defined as a reaction catalyzed by isolated enzymes or whole cells and is considered a green and sustainable technology due to reduced synthetic steps, less energy required, decreased raw material consumption, minimized undesired side product yields, and overall, less waste generated. Solvents for biocatalysis reactions have been widely investigated in order to find an environmentally friendly replacement over the traditionally used hazardous organic solvents. Water has been considered as the greenest solvent considering its quality and quantity; however, its high polarity can hinder its application in some biocatalytic reactions due to some substrates' water immiscibility properties. Therefore, other solvents have been investigated as suitable media for both water-miscible and water immiscible enzymatic reactions. To this, Gorke *et al.* were among the first to successfully use ILs as solvent media for biocatalysis;[63] however, due to some of the aforementioned disadvantages, researchers have turned their attention to DESs as more suitable solvents for certain biocatalytic reactions.[64-65]A complete list of the discussed

works within this section including the enzyme, reaction, conditions, conversion efficiencies, *etc.* can be found in the published *J. Mater. Chem. B* article.

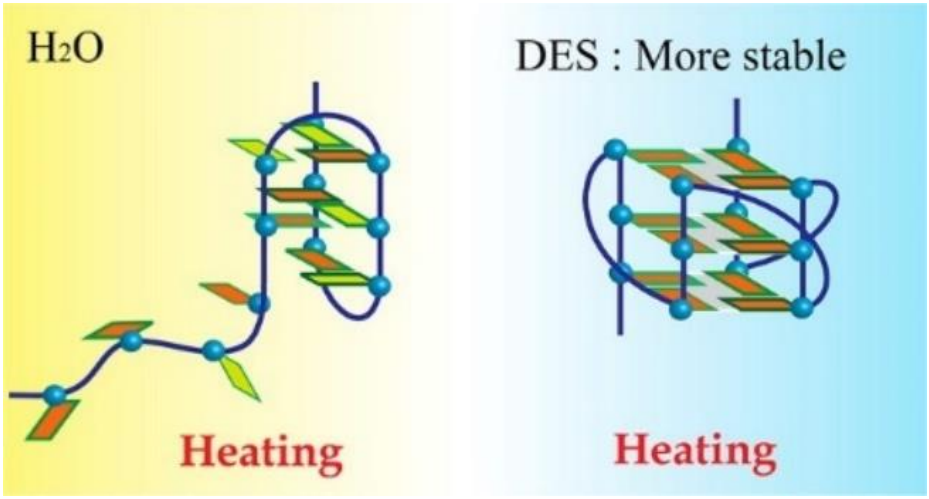

Figure 1.8 Human telomeric DNA, Tel_{22}, adopting a more stable parallel G-quadruplex structure in water-free DES (containing K^+). Reprinted with permission from ref. 61. Copyright © 2013 American Chemical Society.

Lipases

Hydrolases are the most commonly used enzymes in biocatalysis because they use water to cleave chemical bonds, dividing large molecules in multiple smaller molecules.[66] Examples of common hydrolases include epoxide hydrolases, esterases, proteases, glycosidases, nucleosidases, and lipases. Lipases, acyl hydrolases that cleave long-chain fatty acids into polar lipids, are typically more active toward transesterification reactions; however, the water by-product that results from direct esterification reactions is more desirable for greener processes. Additionally, even though most lipases maintain good activity in organic solvents and have been shown to be good catalysts in biodiesel production,[67] the toxicity and damaging properties of organics have led researchers to lean towards DESs for lipase-catalyzed biotransformations.[68] By using DESs as

transesterification media, undesired side reactions, such as hydrolysis, may be avoided, owing to limited amounts of water present in the biocatalytic systems. In some cases, DESs can even play a bifunctional role, that is, substrate and solvent, in lipase-catalyzed reactions.

Gorke *et al.* were among the first to investigate the lipase catalyzed transesterification of ethyl valerate with 1-butanol and various DESs using Candida Antarctica lipase B (CALB).[69] The use of ChCl: glycerol (1:2), ChCl: urea (1:2) and ethylammonium chloride (EAC): glycerol (1:1.5) all resulted in conversions to butyl valerate over 90% for both CALB and immobilized CALB. The immobilized CALB was also able to catalyse the aminolysis reaction of ethyl valerate with 1-butylamine in ChCl: glycerol, ChCl: urea, and ChCl: acetamide, yielding conversions of > 90%, > 90%, and 39%, respectively, after 4 h. ChCl-based DESs have also been shown to enhance the solubility of certain compounds as well as improve the activity of CALB immobilized on polyacrylate beads (Novozym® 435), which inherently results in increased conversion and product yields for other transesterification reactions.[70-71]

Papadopoulou *et al.* found that EAC-based DESs also performed well in the transesterification reaction of ethyl ferulate with 1-octanol catalysed by CALB nanoflowers to produce various esters.[72] When EAC: urea, EAC: glycerol, and EAC: ethylene glycol (molar ratios all 1:1.5) were all used as reaction media, yields were 42.5%, 14.0% and 61.4%, respectively, as compared to the ChCl-based DES, which yielded conversions of 24.6%, 13.0%, and 4.0% for ChCl: urea, ChCl: glycerol, and ChCl: ethylene glycol, respectively (molar ratios 1:2). The increased catalytic activity of CALB-nanoflowers observed in EAC-based DESs could be attributed to lower viscosity which

could decrease the mass transfer limitations of the substrates to the active site of the enzyme and/or promote conformational dynamics of the protein.[73] When seven reaction cycles were completed, the residual activity of the immobilized CALB was 50%, which was higher than that reported for immobilized lipases in organic solvents (~40%).[74]

Choline acetate (ChAc)-based DESs have also been explored as suitable solvents in the transesterification reaction of ethyl sorbate with 1-propanol catalyzed by Novozym® 435.[75] Initial lipase activity was significantly low when ChAc: ethylene glycol (1:2) and ChAc: urea (1:2) were used, yielding results of 0.07 mmol min^{-1} g^{-1} and 0.21 mmol min^{-1} g^{-1}, and selectivities of 12% and 40%, respectively. However, when ChAc: glycerol (1:1.5) was used, the initial activity was greatly enhanced to 1.02 mmol min^{-1} g^{-1}, which was twice as much as the traditional organic solvent (0.57 mmol min^{-1} g^{-1}) and compared well with ChCl-based DESs of ChCl: urea (1:2) and ChCl: glycerol (1:2) that yielded initial activities of 1.00 mmol min^{-1} g^{-1} and 1.12 mmol min^{-1} g^{-1}. Additionally, the selectivity was enhanced from 45% with ChCl: glycerol to 99% with ChAc: glycerol. Lastly, ChAc: glycerol was studied in the enzymatic synthesis of biodiesel from Miglyol® oil 812, which resulted in high conversions between 82–97% within 1–3 h using Novozym® 435. ChAc: glycerol has also been shown to increase the activity and stability of another lipase, specifically *Penicillium expansum* lipase, when the DES molar ratio was 1:2 (instead of 1:1.5), although it displayed poor performance of biodiesel production from *Millettia pinnata* seed oil, yielding a conversion of only 7.6%.[76] In similar fashion to Zhao *et al.*,[75] Novozym® 435 displayed the highest conversion of biodiesel production with *Millettia pinnata* seed oil when ChAc: glycerol (1:2) was implemented, although the yield was only 54.8%.

DESs have also been used as solvents for alcoholysis reactions. For instance, Durand *et al.* found that neat ChCl: urea (1:2) and ChCl: glycerol (1:2) were both successful in the alcoholysis reaction of vinyl laurate with varying chain length alcohols (butanol, octanol, and octadecanol), by yielding 100% conversions, regardless of what alcohol was implemented, with > 99% selectivity.[77] Additionally, ChCl: oxalic acid (1:1) and ChCl: malonic acid (1:1) showed highest conversions when 1-octanol was used, yielding 43% and 36%, respectively (> 99% selectivity for both). Interestingly, ChCl: ethylene glycol (1:2) resulted in conversions of 33% or less in all alcohols investigated while also yielding the lowest selectivities (< 30%). Ethylammonium chloride: urea (1:2) showed an excellent conversion of 94% and > 99% selectivity when butanol was the alcohol implemented; however, the conversions were ≤ 10% when octanol and octadecanol were used. Two other alcoholysis reactions, specifically the lipophilization of methyl *p*-coumarate and methyl ferulate with 1-octanol and CALB alongside DESs as solvents have also been investigated.[78]

Differing from the previous reaction, neat ChCl: urea and ChCl: glycerol both resulted in no conversions with methyl *p*-coumarate, even after four days; however, 98% conversion was seen when 10% water was added to ChCl: urea, and the hydrolysis side product remained very low. On the other hand, once 15% water was added, the hydrolysis reaction became prevalent (as well as substrate degradation) and led to an overall decrease in yield to 86%. When the alcoholysis reaction was performed with ChCl: glycerol, similar trends were seen; however, this system was much slower and resulted in lower yields (62%) even at the highest water content of 20% and hydrolysis made up 10% of the total yield. Additionally, water was found to be necessary for the alcoholysis reaction of methyl

ferulate as well. In agreement with the previous reaction, ChCl: urea resulted in faster reaction rates and higher yields (> 90%) than ChCl: glycerol (~50%) with both having 20% water, and the hydrolysis side reaction was significantly lower (< 2%) regardless of DES used and water content.

Esterification reactions have also been investigated with DESs as the solvent media in order to increase conversions and yields. Cvjetko Bubalo *et al.* investigated DESs in the Novozym® 435-catalyzed synthesis of the short chain esters of butyl acetate by the esterification of 1-butanol and acetic anhydride.[79] Similar to Durand *et al.*, when neat DESs (ChCl: glycerol, ChCl: urea, or ChCl: ethylene glycol, all in 1:2 molar ratio) were used, less than 5% conversions were seen.[78] However, when 0.5–2.5 moles of water were incorporated, the esterification yield gradually increased with the increase of water content, regardless of what DES was implemented. Interestingly, when the water content was too low, 1-butanol was strongly bound to the DES by hydrogen bonding, making it unavailable for the reaction; however, when the water content was over the optimal amount, the excess water molecules near the active site generated a hydrolysis reaction which led to lower yields. At optimal water content, the substrate was released from the hydrogen bonding network and the DES could also bind some water molecules formed during esterification in that same network, thus preventing hydrolysis altogether. The initial rate in ChCl: ethylene glycol: water at a 1:2:2 molar ratio was 1.2 μmol min^{-1} mg^{-1} which was 4-fold higher than when the ratio was 1:2:0.5 (rate = 0.3 μmol min^{-1} mg^{-1}). The highest initial rate occurred with ChCl: glycerol containing 2.5 mol of water (rate = 2.2 μmol min^{-1} mg^{-1}), however, it was still lower than the initial rate of the traditional solvent of *n*-heptane, which had a rate of 4.5 μmol min^{-1} mg^{-1}. In terms of HBD, glycerol and ethylene glycol

resulted in higher enzyme activity and esterification yield as compared to urea, which is in agreement with previously discussed results.[76, 80] Overall, the highest yield (80%) resulted from ChCl: ethylene glycol with the addition of 1.5 mol (5% w/w) water, which was strongly increased from *n*-heptane or the IL [C_5mim][Tf_2N], which resulted in yields of 50% and 41%, respectively. The addition of a small amount of water (5–20%) to DESs has also been shown to increase conversions in other esterification reactions, specifically to increase the product yield of α-monobenzoate glycerol (α-MBG),[81-82] to aid in the synthesis of menthol fatty acid esters,[83] and to assist in the synthesis of fatty acyl ethanolamines, specifically, docosahexaenoyl ethanolamide (DHEA) and eicosapentaenoyl ethanolamide (EPEA).[84] Additionally, the addition of 30% water to ChCl: glycerol and 50% water to ChCl: ethylene glycol has shown to drastically increase yields in the classic enzyme-catalyzed Henry reaction of 4-nitrobenzaldehye with nitromethane to 92.2% and 82.0%, respectively as compared to that in water, which only produced a yield of 33.4%.[85] Furthermore, the addition of 20% (v/v) water with ChCl: glycerol (molar ratios of 1:2 and 1:1.5) in a similar 4-nitrobenzaldehyde biocatalytic reaction (acetone used as a starting substituent instead of nitromethane) resulted in complete conversions with yields > 97%.[86]

It has been noticed that the lipase CALB tends to display decreased stability when tested against the harsh conditions of a chemoenzymatic epoxidation reaction as compared to esterification reactions. Therefore, Zhou *et al.* have investigated the potential benefits of incorporating DESs as the solvents with the chemoenzymatic epoxidation reaction of 1-octadecene.[87] The DESs of ChCl: urea and ChCl: acetamide (both 1:2 molar ratios) resulted in the lowest conversions, yielding only 30.2% and 13.9%, respectively. The conversion was somewhat increased to 37.7% with ChCl: ethylene glycol (1:2); however, sugar-based

DESs of ChCl: glycerol, ChCl: xylitol, and ChCl: sorbitol (all with 1:1 molar ratios) all showed even higher conversions yielding 56.7%, 65.1%, and 72.4%, respectively. When this reaction was performed in PBS buffer, the resulting conversion was 62.5%, showing that although most of the DESs do not result in increased conversions, ChCl: xylitol and ChCl: sorbitol show promise as better, more environmentally friendly solvent systems. These two DESs have also been shown to have a positive effect on the chemoenzymatic epoxidation of soybean oil, by increasing conversions 6-fold and 8-fold when 30% ChCl: xylitol (1:1) and 50% ChCl: sorbitol (1:1) were used as compared to 10% conversion in aqueous media.[88] Furthermore, Ranganathan *et al.* successfully used ChCl: xylitol (1:1), ChCl: sorbitol (1:1), and ChCl: fructose (1:2) as solvents for the CALB-catalyzed epoxidation of monoterpenes, resulting in 100% conversions after 24 h.[89]

Interestingly, ChCl: xylitol has also been shown to stabilize lipase G from *Penicillium camemberti* in the chemoenzymatic epoxidation reaction of hydrogen peroxide and glyceryl trioleate to produce epoxidized glyceryl trioleate.[90] The product formation increased more than 22-fold in ChCl: xylitol resulting in a rate of 172 μM h^{-1} as compared to the reaction in buffer, which had a rate of 7 μM h^{-1}. Additionally, 60% conversion yield was seen after 6 h, as compared to < 10% in buffer. These results were compared with Novozym® 435 as the catalyst and it was determined that lipase G gave significantly higher yields of the desired epoxide product, as confirmed by ^{1}H NMR while also resulting in no hydrolysis products.

Another interesting example of DESs being incorporated as reaction media involves the phospholipase D (PLD)-catalyzed transphosphatidylation of phosphatidylcholine (PC) with L-serine to synthesize phosphatidylserine (PS) as shown by

Yang *et al.*[91] The highest PS yield of 92.1% was achieved in ChCl: glycerol (1:2), although it required 12 h for reaction completion. A slightly decreased yet still great yield of 90.3% was obtained in only 7 h in ChCl: ethylene glycol (1:2), with the lipase displaying excellent stability, maintaining 81% of its original activity after 10 synthesis batches. ChCl-based DESs have also shown promise as cosolvents for lipase-catalyzed hydrolytic reactions by implementing two hydrogen bond donors into one DES.[92] The activity of lipase in buffer was considered to be 100%, but the activity in almost every DES investigated was > 100%, with ChCl: urea: glycerol (1:1:1 molar ratio) resulting in activity of 155%. The DESs of ChCl: urea: formamide (1:1:1), and ChCl: glycerol: formamide (1:1:1) both resulted in lipase activity between 80–90%. These results are in agreement with previous reports in which urea and glycerol are efficient HBDs for lipase-catalyzed reactions in DESs.[77-78] The DESs also greatly improved the thermal stability of lipase at 40°C from 50% activity in buffer to over 80% activity in DESs. After 12 h, the lipase activity in buffer had diminished to 0%, while the activity in 10% ChCl: ethylene glycol: formamide (1:1:1) and 10% ChCl: glycerol: ethylene glycol (1:1:1) was still 30.6% and 39.1%, respectively.

In addition to solvent media, DESs have also been used as the catalyst in some biocatalytic reactions. Singh *et al.* used ChCl: urea and ChCl: glycerol (both at 1:2) as both a catalyst and a recyclable solvent for the selective mono *N*-alkylation of aromatic primary amines.[93] The reaction was also performed with a lipase from *Pseudomonas* sp. for comparison purposes in organic solvents of ethanol, chloroform, dichloromethane, and hexane, which resulted in yields of 85%, 81%, 75%, and 50%, respectively, with reaction times anywhere from 4–12 hours. When DESs were used, the reaction times were somewhat shortened (4–8 h) and the yields for ChCl: glycerol and ChCl: urea were 65%

and 78%, respectively. The DES-catalyzed reactions were further explored in mono *N*-alkylation reactions of different aromatic amines. Overall, when the alkyl group was hexyl or butyl, the lipase-catalyzed reaction produced somewhat higher yields (74–85%); however, when benzyl alkyl groups were used, the DES-catalyzed reactions prevailed (79–89%). Even though some of the resulting yields were slightly lower in DES-catalyzed reactions, the reaction times were either the same as or faster in almost all reactions tested, as compared to lipase-catalyzed systems. DESs have also been implemented as catalysts during the synthesis of tricyanovinyl substituted aniline and indole derivatives.[94] Multiple DESs were tested, and although ChCl: malonic acid, ChCl: oxalic acid, and ChCl: urea: dichloromethane (ratios not provided) all showed high product yields of 70%, 70%, and 85%, respectively, the reaction times were relatively long (between 15–60 min). However, ChCl: urea resulted in the highest yield of 89% taking only five minutes for the reaction to proceed. It was also determined that the ChCl: urea could be recycled up to four separate runs with very little loss in activity (89–73%).

In general, water can play a crucial role in the success or failure of lipase reactions. Excess water could induce the unwanted reaction of hydrolysis, but not enough water might result in solutions with high viscosity, increasing mass transfer limitations and decreasing the overall yield. In DESs, however, even the addition of 5% water to the system has been shown to decrease the viscosity and change the activity and selectivity of the enzyme of interest. Additionally, even though urea is claimed to be a protein denaturant, when it is paired with ChCl in a DES, the hydrogen bonding that results has been shown to stabilize various lipases and increase product yields, which has been further confirmed through molecular dynamic simulations.[95]

Other hydrolases

Gorke *et al.* were among the first to investigate the effects of ChCl: glycerol (1:2) on epoxide hydrolases (EH).[69] The rate of EH-catalyzed hydrolysis of styrene oxide to styrene glycol by EH AD1 from *Agrobacterium radiobacter* resulted in a conversion of only 4.6% when buffer was used. However, upon addition of 25 vol% ChCl: glycerol to the reaction, the conversion increased 20-fold to 92%. Interestingly, when the solutions contained 50 vol% DES, the conversion of the EH AD1-catalyzed reaction drastically decreased to 2%. Lindberg *et al.* have investigated the stability and activity *Solanum tuberosum* epoxide hydrolase 1 (StEH1), using 40% (v/v) ChCl: ethanediol, ChCl: glycerol and ChCl: urea all in 1:2 molar ratios for the hydrolysis of the (1*S*,2*S*) enantiomer of *trans*-2-methylstyrene oxide (2-MeSO) substrate, and yielded enantiomeric excesses (ee) of 98%, 97%, and 96%, respectively.[80] Additionally, the regioselectivity of the (1*R*,2*R*)-2-MeSO enantiomer was improved from 15% in PBS buffer to 38% and 40% in 40% (v/v) ChCl: glycerol and 40% (v/v) ChCl: ethanediol, respectively.

The activity and stability of glucosidase in ChCl-based DESs has also been investigated. Xu *et al.* incorporated 40% (v/v) ChCl: propylene glycol, ChCl: ethylene glycol, and ChCl: glycerol (all with molar ratios of 1:2) in a β-glucosidase catalyzed hydrolysis reaction of *p*-nitrophenyl-β-glucopyranoside (*p*NPG) to produce *p*-nitrophenol (*p*NP).[96] β-glucosidase showed strongly enhanced activity of 230%, 200%, and 140% in ChCl: propylene glycol, ChCl: ethylene glycol, and ChCl: glycerol, respectively. Interestingly, the maximum reaction rates (V_{max}) were faster in the DESs containing only 6 vol% water, with V_{max} = 18.19 ± 0.46 μM min^{-1} and 15.37 ± 4.35 μM min^{-1} for the enzyme in ChCl: propylene glycol and ChCl: ethylene glycol, respectively as compared to

the neat DESs (V_{max} = 10.56 ± 3.28 μM min^{-1} and 3.79 ± 0.78 μM min^{-1}, respectively). Additionally, these results were much higher than when the enzyme was with methanol (V_{max} = 1.58 ± 0.91 μM min^{-1}), showing that DESs greatly improved β-glucosidase activity and that the addition of a little water can strongly enhance reaction rates, most likely due to decreased viscosity in the system. Similar results have been seen in the hydrolysis reaction of *p*-nitrophenyl palmitate (*p*NPP) using *Burkholderia cepacia* lipase (BCL) and DESs.[97] The DESs of 40% (v/v) ChCl: glycerol and ChCl: ethylene glycol (both 1:2 molar ratio) showed increased enzyme activity of 230% and 180%, respectively, with ChCl: ethylene glycol resulting in the fastest V_{max} regardless if it was implemented as a cosolvent (40% v/v) or main solvent (with 4% water) yielding rates of 21.78 ± 2.3 μM min^{-1} and 25.70 ± 3.1 μM min^{-1}, respectively. Additionally, the lipase activity after 20 minutes in ChCl: ethylene glycol with 4% (v/v) water was 1.5 times and 14 times faster than the IL 1-butyl-3- methylimidazolium tetrafluoroborate ([BMIM][BF_4]) and methanol, respectively. Interestingly, in the deglycosylation of hesperidin reaction using 6-*O*-α-rhamnosyl-β-glucosidase as the biocatalyst, Weiz *et al*. determined that 30% (v/v) ChCl: urea (1:2) resulted in no enzyme activity; however, the activity was greatly enhanced to 95% in 40% (v/v) ChCl: glycerol (1:2) and > 100% in 30% (v/v) ChCl: ethylene glycol (1:2).[98]

Other enzymes

There are many other enzymes that use DESs as the solvent system in biocatalysis reactions other than hydrolases. Zhao *et al.* have investigated protease activation in ChCl: glycerol and ChAc: glycerol (in various molar ratios) with catalysts subtilisin and α-chymotrypsin (both free and immobilized) in the standard transesterification reaction of *N*-acetyl-L-phenylalanine ethyl ester with 1-propanol.[99] When immobilized subtilisin was used with

ChAc: glycerol (1:2), the resulting activity was 2.0 μmol min^{-1} g^{-1} (99% selectivity), which was four times higher than the enzyme activity in *t*-butanol (with 2% (v/v) water) which was 0.50 μmol min^{-1} g^{-1} and a selectivity of only 29%. However, when the mole ratio was changed from 1:2 to 1:1.5 and water contents between 2–4% (v/v) were incorporated, the subtilisin activity decreased to 0.42–0.90 μmol min^{-1} g^{-1}, although the selectivity remained at 99%. For ChCl: glycerol (1:2) containing 3% (v/v) water, a high activity of 2.9 μmol min^{-1} g^{-1} was seen with immobilized subtilisin alongside excellent selectivity of 98%. Compared with subtilisin, α-chymotrypsin exhibited far less activity in both free and immobilized forms, resulting in 0.028 μmol min^{-1} g^{-1} and 0.031 μmol min^{-1} g^{-1}, respectively, in ChCl: glycerol (1:2) at 2% (v/v) water.

Building off of these results, Maugeri *et al.* studied α-chymotrypsin in the reaction involving *N*-acetylphenylalanine ethyl ester (APEE, **1**) and glycinamide hydrochloride (GH, **2**) to produce various peptides in ChCl-based DESs, as can be seen in Figure 1.9.[100] Typically, APEE (**1**) undergoes dissolution in hydrophobic solvents, whereas (GH, **2**) is usually more soluble in hydrophilic solvents. The resulting dipeptide, *N*-Ac-Phe-Gly-NH_2 (APG, **3**) has been shown to be useful in some therapeutic applications. One of the challenges for peptide synthesis is the solvent system, since hydrophobic and hydrophilic substrates are combined simultaneously. The use of aqueous solutions can lead to hydrolysis, therefore, DESs were used as the reaction media to help alleviate those potential issues. Additionally, it has been shown that the formation of APG **3** could be hampered if hydrolysis occurs to yield *N*-acetylphenylalanine (AP, **4**), especially if there is a significant amount of water present. Some molecules of water are crucial for the enzymatic activity, therefore, it was necessary to optimize the reaction conditions carefully to minimize the

hydrolytic side reactions (AP **4**), while still showing high production yield of APG**3**. When lower amounts of water (up to 5% v/v) were used with ChCl: glycerol (1:2), no enzyme

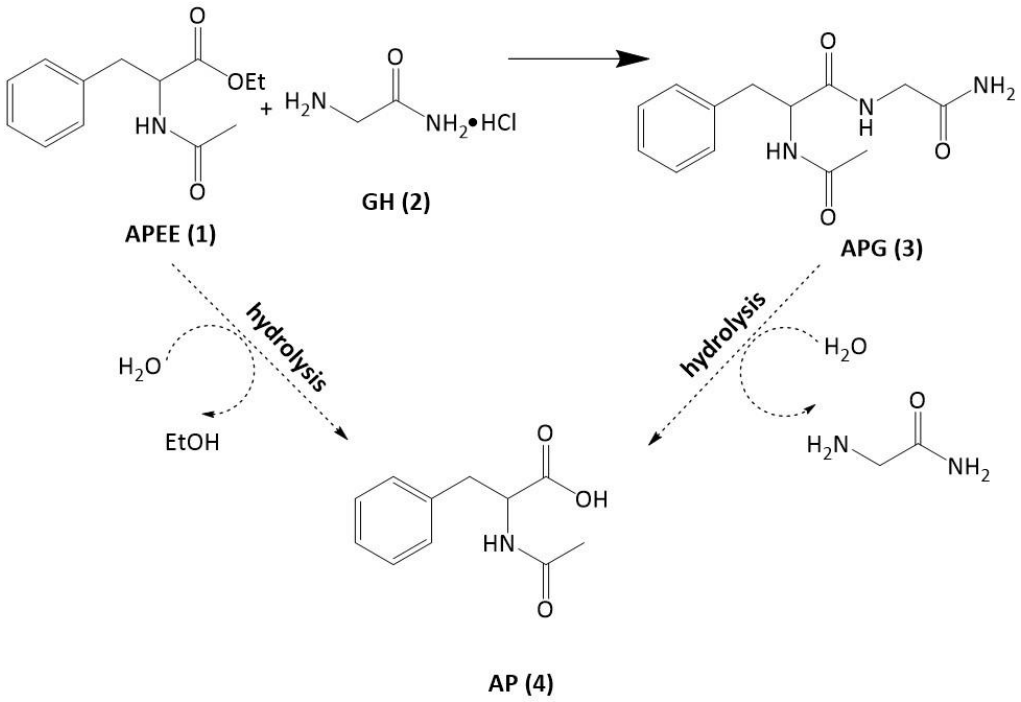

Figure 1.9 Chymotrypsin-catalyzed reaction adapted with permission from ref. 99. Copyright © 2013 Wiley.

activity was seen; however, when 10% (v/v) water was used, high enzymatic activity was seen with the production of APG **3** in 90% yield. This high yield continued to be seen in solutions containing 25% (v/v) water, which differed somewhat from the aforementioned paper, showing that the amount of water affects systems differently. Conversions between 80–90% were seen with ChCl: urea (1:2) and ChCl: isosorbide (1:2) with 10% (v/v) water; however, ChCl: xylitol (1:1) with the same amount of water only yielded conversions around 40%. Interestingly, a higher water content (40%) was necessary with ChCl: glycerol when thiamine-diphosphate dependent lyase (ThDP-lyase), specifically benzaldehyde

lyase (BAL) from *Pseudomonas fluorescens*, was used in a biocatalytic reaction to produce chiral α-hydroxy ketones.[101] The conversions and enantiomeric excesses were 96% (52% *R*), 98% (27% *R*), 95% (> 99% *R*), and 75% (63% *R*), when butyraldehyde, valeraldehyde, benzaldehye, and 2-furaldehyde, were used as the starting substrates, respectively.

Haloalkane dehalogenases (HLDs) are also enzymes that have been investigated with DESs. Specifically, ChCl: ethylene glycol (1:2) was used in the hydrolysis reaction of 1-iodohexane and its effect on the structure, stability, and enantioselectivity of three hydrophobic haloalkane dehalogenases (HLDs), including DbjA from *Bradyrhizobium japonicum* USDA1110, DhaA from *Rhodococcus rhodochrous* NCIMB13064, and LinB from *Sphingobium japonicum* UT26 was determined.[102] The most DES-tolerant enzyme was determined to be DhaA, followed by DbjA and then LinB as can be seen in Figure 1.10. Even at a very high concentration of ChCl: ethylene glycol (90% v/v), activities in all three enzymes were still observed, which was much improved from the lack of activity seen when traditional solvents of methanol or acetone were used with concentrations of 50% or above. When the individual DES components were studied alongside the enzymes, the activity of DhaA was decreased, which is consistent with previous literature which stated that lipases are more stable in the DES as compared to its individual components.[69]

DESs have also been used as solvents in reactions involving both ketoreductases (KREDS) and oxidoreductases. Cicco *et al.* investigated multiple DESs in the bioreduction of propiophenone to 1-phenyl-1-propanol catalyzed by ten different KREDs.[103]

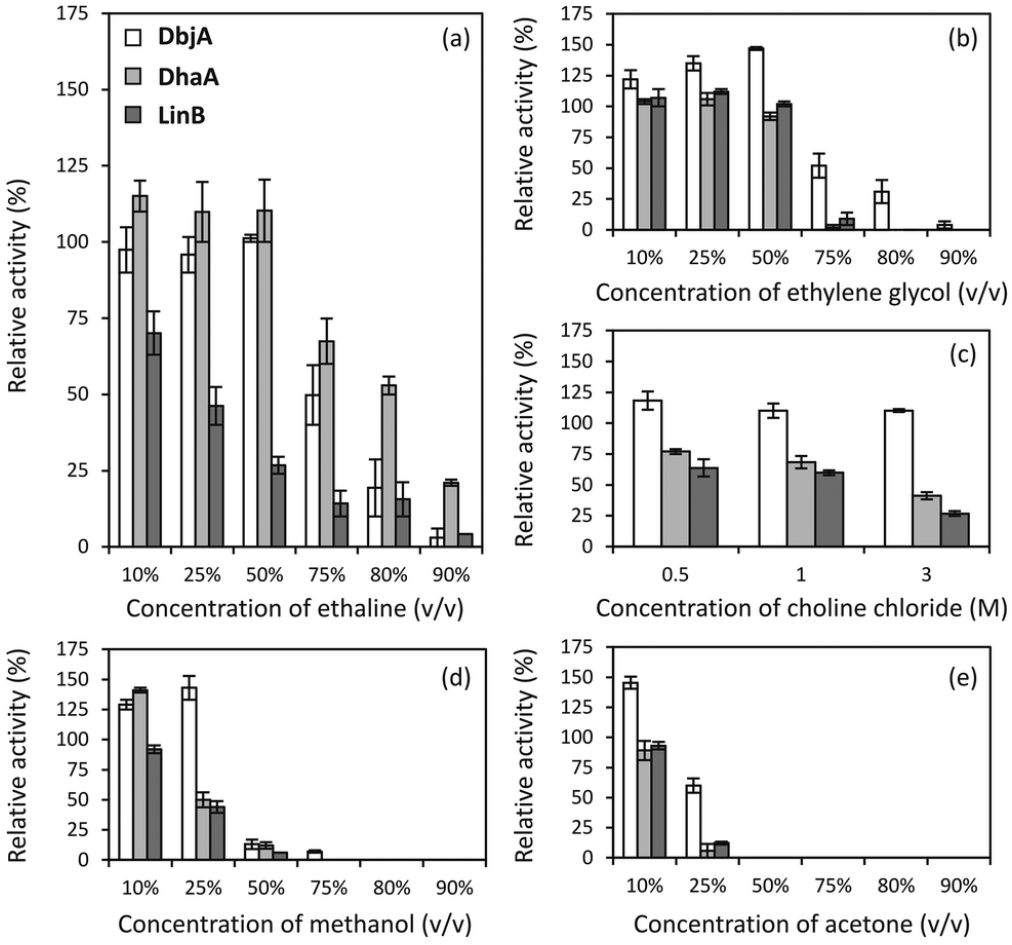

Figure 1.10 The relative activities of DbjA, DhaA, and LinB measured in the presence of various concentrations of (a) ChCl: ethylene glycol (ethaline), (b) ethylene glycol, (c) choline chloride, (d) methanol, and (e) acetone at 37°C and pH 8.6. Reprinted with permission from ref. 101. Copyright © 2014 Royal Society of Chemistry.

All of the KREDS were inactive in 50% (w/w) ChCl: urea (1:2) and ChCl: lactic acid (1:2); however, higher conversions were seen (39–99%) when 50% (w/w) ChCl: sorbitol (1:1) and ChCl: glycerol (1:2) were used. Similar reports have shown steady activity of the alcohol dehydrogenase *Ralstonia* sp. ADH (RasADH) in 70% (v/v) ChCl: glycerol (1:2), an enantiomeric excess between 60–90% at higher DES concentrations, and the enzyme retained half of its original activity in very concentrated (95% v/v) ChCl: glycerol.[104]

Additionally, ChCl: glycerol (1:2) has been successfully used alongside other ADH-catalyzed reactions.[105] The water-immiscible enzyme laccase (benzenediol oxygen oxidoreductase) from *Bacillus* sp. HR03 has also been studied with DESs.[106] Khodaverdian *et al.* found that 20% (v/v) betaine: glycerol (1:2) resulted in an enzyme activity of 300% and 50% (v/v) malic acid: betaine: water (1:1:1) showed an activity of 150%. It was also observed that laccase retained about 92% and 85% of its initial activity in sorbitol: betaine: water (1:1:1) and betaine: glycerol (1:2), respectively, after 120 min at room temperature.

In a recent study, Toledo *et al.* swapped out the chloride ion of ChCl with either dihydrogen citrate (DHC) or dihydrogen phosphate (DHP) in various NADESs and showed that an increase in laccase activity could be achieved over ChCl.[107] When DHP was used, the highest enzyme activity was seen in ChDHP: xylitol (1:2), yielding 170% activity at both 10 and 25 wt% DES. Similar laccase activities were obtained with ChDHC: erythritol (between 120–150% at molar ratios of 2:1, 1:1, or 1:2) and ChDHC: xylitol (between 120–200% at molar ratios of 2:1, 1:1, or 1:2) at DES concentrations of 25 and 50 wt%. Comparing all ChDHC-based DESs at a molar ratio of 2:1 and at 50 wt%, the increase in the enzyme activity followed the order of increasing number of hydroxyl groups in the polyol: ChDHC: ethylene glycol < ChDHC: glycerol < ChDHC: erythritol < ChDHC: xylitol. Interestingly, the activity of laccase in betaine: glycerol regardless of molar ratio and DES concentration was less than 150%, which was lower than the aforementioned report of 300% laccase activity in 20% (v/v) betaine: glycerol (1:2).[106]

Decarboxylases have also been incorporated alongside DESs to improve their reactions. Phenolic acid decarboxylase from *Bacillus subtilis* (BsPAD) was used in the enzymatic decarboxylation of *p*-hydroxycinnamic acid followed by Pd catalyzed Heck-

type C–C coupling to produce biaryl derivatives.[108] The use of ChCl: glycerol (1:2) allowed for much higher yields initially (95% after 20 h) as compared to water which resulted in 87% yield after 24 h. It was also reported that the Pd-catalyzed Heck-type coupling in DES gave an isolated yield of 65% of (*E*)-4-hydroxystilbene after 8 h. Similar results have been observed in a fully integrated two-step continuous flow process resulting in full conversions and yielding 20% product in 16 h.[109] Interestingly, 3D printing techniques have been used to construct custom-built reactors that were shown to be applicable for the decarboxylation of *p*-coumaric acid (*via* BsPAD) and subsequent Pd-catalyzed Heck cross-coupling reaction in a continuous flow method. The use of ChCl: glycerol (1:2) allowed for excellent selectivity (99%), conversion of 70%, and an overall yield of (*E*)-4-hydroxystilbene to be 15% after > 4 h.[110]

Whole-cell biocatalysis

As compared to the use of isolated enzymes, a major advantage of using whole cell catalysts is that they provide a natural environment for enzymes, preventing denaturation and inactivation that might occur more easily in nonaqueous reaction media. Additionally, they do not require any enzyme purification which allows for more cost-efficient applications. Although researchers have begun incorporating DESs into whole cell biotransformations, the amount of water necessary has still been a valid concern. As mentioned earlier, hydration up to a certain percent has been shown to destroy the supramolecular structure of DESs resulting in solutions of their individual components, therefore losing their unique characteristics.[26, 111] To this, Gutiérrez *et al.* devised a unique approach to bypass this issue by incorporating freeze-dried bacteria solutions (*Escherichia coli*; strain TG1/pPBG11) in neat ChCl: glycerol (1:2).[16] Overall, only a few damaged

bacteria were observed resulting in a 2% loss of fluorescence intensity indicating that this system retained the bacteria's viability and integrity. Similar results have been seen with NADESs acting as cryoprotective agents against lactic acid bacteria. The NADESs had a stronger ability to inhibit ice crystal formation during the freeze-drying process, resulting in minimal disruption of cellular metabolic enzyme activities and cell structures after long-term cryostorage.[112]

Hydrated ChCl: glycerol (1:2) has been used with baker's yeast in the enantioselective reduction of ethyl acetoacetate.[113] The presence of DESs with varying water contents (0–50% v/v) led to low conversions after 72 h (4–25% conversion); however, the cells were active for at least 200 h. Therefore, low conversion rates could be related to low concentrations of enzymes in the whole-cell and not due to any type of degradation by the DES. Interestingly, varying the water content in the system led to complete inversion of the enantioselectivity of the reduction reaction, as can be seen in Figure 1.11. In pure water, (no DES) the baker's yeast whole cells displayed high stereoselectivity of the (*S*) enantiomer with an enantiomeric excess (ee) of 95%. As the amount of water decreased (therefore increasing DES content), it was noticed that a high (*R*) enantioselectivity emerged, while still maintaining a 95% ee. At 30% (v/v) water in the DES, a racemic mixture could be achieved.

Similar results have been seen with Vitale *et al.* who observed that at higher water contents (40–50%) with DESs (either ChCl: glycerol or ChCl: fructose), the (*S*) enantiomer was favoured in a baker's yeast bioreduction of aryl-containing ketones. Upon decreasing the water content to ~10%, the stereoselectivity was inverted, favouring the (*R*) enantiomer.[114] When baker's yeast was used alongside various DESs in the reduction of

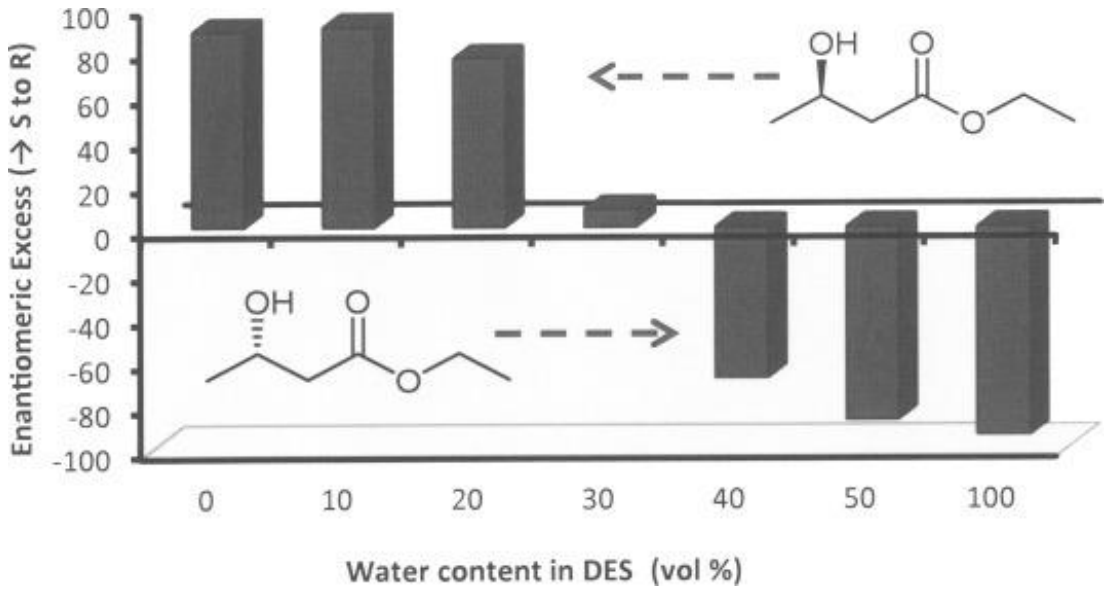

Figure 1.11 Enantioselectivity of the reductive reaction depending on the different water/DES mixtures. Conditions include 50 mM ethyl acetoacetate and 200 mg mL^{-1} baker's yeast in 1:2 molar ratio of ChCl: glycerol at room temperature for 72 h. Reprinted with permission from ref. 109. Copyright © 2014 Wiley.

ethyl-3-oxobutanoate to ethyl-3-hydroxybutanoate, the (*S*) enantiomer was predominantly seen regardless of water content (10–90% w/w), although the (*R*) enantiomer was observed when 10% (w/w) water in ChCl: fructose (3:2) was used.[115] In another interesting report, Yang *et al.* studied the bioconversion of isoeugenol to vanillin catalyzed by Lysinibacillus fusiformis CGMCC1347 cells.[116] Twenty-four DESs were synthesized either with ChCl or ChAc as the HBA along with various HBDs of acetamide, urea, glycerol, ethylene glycol at various molar ratios. All DESs (except for 2:1 ChCl: urea) resulted in high conversions of isoeugenol to vanillin at 1% (v/v) DES concentration, and although the yields did not seem to have any obvious correlation with either the HBD or the salt: HBD molar ratio, the yields obtained in the presence of ChAc-based DESs were overall slightly higher than

those obtained with ChCl-based DESs. In addition, the optimum yield (142%) was obtained when the volume of DES added reached 20% (v/v). When NADESs were investigated on the bioconversion, 20% (v/v) ChCl: lactose (4:1) and ChCl: raffinose (11:2) resulted in high conversions of 132% and 131%, respectively. It is interesting to note that cell viability studies were performed and agreed with similar literature that stated that increasing the amount of DES to over 50% disrupts the cell membranes and leads to apoptosis.[115] Interestingly, the cells treated with ChCl-based DESs survived better than the cells treated with ChAc-based DESs.

Lastly, as a model reaction, Li *et al.* studied the synthesis of (*R*)-[3,5-bis (trifluoromethyl)phenyl]ethanol ((*R*)-BTPE) by asymmetric reduction of 3,5-bis(trifluoromethyl)acetophenone (3,5-BTAP) using whole cells of *Trichoderma asperellum* ZJPH0810 as a biocatalyst in a DES of ChCl: glutathione (1:1).[117] A solution containing 1% DES (w/v) resulted in a yield of 90.7% and enantiomeric excess > 99%. Since glutathione is composed of the amino acids γ-glutamine, cysteine, and glycine, DESs consisting of ChCl and those amino acids were also synthesized in 1:1 molar ratios. As to be expected, when 1% (w/v) ChCl: γ-glutamine, ChCl: cysteine, and ChCl: glycine were investigated in the bioreduction reaction, they resulted in yields lower than the ChCl: glutathione DES (66.0%, 80.7%, 63.1%, respectively), and all enantiomeric excesses were > 99%, which shows that the amino acids had an enhanced effect in glutathione as compared to their individual results.

Acetobacter whole cells

Much research has been done regarding various DESs as cosolvents to help improve the biocatalytic performance of immobilized *Acetobacter* sp. CCTCC M209061 cells. For

example, Xu *et al.* implemented DESs to improve the performance of these cells for the asymmetric oxidation of 1-(4-methoxyphenyl)ethanol (MOPE).[118] The DESs ChCl: urea, ChCl: ethylene glycol and ChCl: glycerol (molar ratios 1:2, 20% v/v) all resulted in similar conversions (42.9–49.4%) to the buffer (47.5%); however, stability of the immobilized *Acetobacter* sp. CCTCC M209061 cells were greatly enhanced with the incorporation of DESs and the enantiomeric excess increased from 91.4% to 98.7% in ChCl: glycerol. Additionally, ChCl: glycerol resulted in the highest cell membrane integrity and was shown to be very biocompatible, as well as allowed the reaction to proceed in only 9 h as compared to 11 h in buffer.

Similar results were seen when the same DESs and cells were used in another reduction, specifically, the asymmetric reduction of 3-chloropropiophenone (CPE) to (*S*)-3-chloro-1-phenylpropanol (CPL).[119] In this reaction, the buffer produced an 85.2% yield and 5% (v/v) DESs yielded results between 79.9–86.0%. Interestingly, ChCl: urea resulted in the highest yield (86.0%) and shortened the reaction time from 10 h in buffer to only 6 h, as well as being the most biocompatible to the cells. The DESs and substrates for both reactions showed slight toxicity against the immobilized *Acetobacter* sp. CCTCC M209061 cells, although the DESs reduced the substrate toxicity when incorporated into the reaction system. Furthermore, the biocatalyst retained nearly 80.0% of its initial activity and the product enantiomeric excess was consistently > 99% in systems containing ChCl: urea after five consecutive batches as compared to the system with no DES, which resulted in 50.4% activity. Interestingly, when the aforementioned DESs were used with *Acetobacter pasteurianus* GIM1.158 cells for the biocatalytic reduction of 2-octanone to

(*R*)-2-octanol, 10% ChCl: ethylene glycol (1:2) resulted in the highest conversion of 85.5% as compared to the buffer, which yielded results of 80.1%.[120]

Biomass Processing

Industrial applications for biomolecules using DESs have become increasingly popular. Since there are multiple reviews that discuss biomass pretreatment and conversions of lignocellulosic material, some of which involve the use of DESs,[121-122] this chapter herein discusses only the most recent literature and compares results from previous reports. Lignocellulosic biomass is a renewable, widely available raw material for fuels (*e.g.*, bioethanol), chemicals and polymeric materials production. It can be obtained from various agricultural sources including wastes such as corn stalks, corn cobs, and sugar cane bagasse, and forest residues such as sawdust, bark, and waste left from paper and wood products. Lignocellulosic material consists of a complex matrix of cellulose, hemicellulose and lignin which makes it highly resistant to depolymerization. Once these components are separated, typically by pretreatment and fractionation processes, they can be converted to valuable fuels and chemicals via various reactions such as hydrolysis, hydrogenation and oxidation.

The pretreatment and fractionation steps generally require excessive use of organic and inorganic acids to aid in loosening the components from the matrix. Some of the most common pretreatment methods include steam/steam explosion, grinding/milling/hot water/autohydrolysis, acid treatment and alkali treatment.[123-126] These pretreatment methods can be energy intensive and may require additional steps for solvent recovery. Therefore, DESs have been implemented to enhance the biomass pretreatment process as they can effectively break down the complex matrix and enhance cellulose enzymatic

hydrolysis.[127-129] A modified liquid hot water (MLHW) pretreatment technique was proposed that involved hemicellulose-derived acids (acetic, formic, and gluconic acid) being produced during the LHW process, which could then synthesize a DES *in situ* when ChCl was loaded into the system due to hydrogen bonding of the substituents to improve the delignification of garden waste.[130]

More than 50 million tons of lignin are produced annually by the global paper industry, but only a small proportion is used; the rest typically gets burned away, which unnecessarily depletes resources and causes environmental pollution. Therefore, developing ways to use lignin effectively is an important project for environmental and commercial reasons. Cellulose and hemicellulose can be converted into fermentable sugars by pretreatment and enzymatic hydrolysis processes. However, due to the recalcitrant structure of lignin in the lignocellulose, the direct conversion of lignocellulosic biomass into products is not energy-favorable because lignin serves as a protective barrier, causing the biomass to be strongly resistant against biological and chemical attacks. Hence, the removal of lignin from the lignocellulosic biomass by pretreatment is necessary to facilitate the conversion into other bio-based products.

Throughout the literature, it has been determined that acidic DESs exhibit a larger affinity toward lignin and hemicellulose dissolution during the pretreatment process.[13, 131] Additionally, Satlewal *et al.* found that ChCl: lactic acid (1:5) successfully removed 50.6% and 63.0% lignin and hemicellulose, respectively, from sugar cane bagasse, as compared to dilute alkali (NaOH) and acid (H_2SO_4) pretreatment which resulted in 59.7% and 10.4% lignin removal, respectively.[132] These results agree with previous literature that have reported high lignin removal with ChCl: lactic acid pretreatment of rice straw and

corncob.[127, 133] In another study, when the molar ratio of ChCl: lactic acid was changed to 1:10, the DES yielded a maximum lignin removal of 64.0% in the pretreatment of *Eucalyptus camaldulensis*.[134] The DES has also been used in the pretreatment of oil palm empty fruit punch to extract 33.5% lignin when the molar ratio was 1:1; however, when it was changed to 1:15, the lignin yield increased to 61.0%.[135] In addition to high lignin extractions, ChCl: lactic acid has been shown to enhance enzymatic hydrolysis/saccharification of cellulose to produce glucose yields between 20–94%,[131-132, 134] which is similar to or better than the typical dilute alkali and acid pretreatments.[136-137] Both conventional acid and alkaline pretreatments are not eco-friendly, as high cost is required on chemical recovery, equipment and neutralization processes. Therefore, implementing DESs can be used as an alternative environmentally friendly solvent for lignocellulosic biomass pretreatment.

Other acidic DESs have shown some lignin and hemicellulose dissolution, namely ChCl: oxalic acid, ChCl: malonic acid and ChCl: succinic acid.[135, 138-139] More specifically, Lee *et al.* found that when the above DESs (neat) were used in a 1:1 molar ratio, enhanced dissolution of hemicellulose was observed to eventually result in furfural from oil palm fronds, yielding the product of 9.74 mol%, 0.36 mol%, and 0.19 mol%, respectively, over 120–300 minutes.[140] When varying water contents were added to each DES, the furfural yields remained fairly consistent with ChCl: malonic acid and ChCl: succinic acid; however, the yields were greatly enhanced to 26.34 mol% in ChCl: oxalic acid with 16.4 wt% water, most likely due to decreased mass transfer limitations. Similar results have been reported when ChCl: urea (1:2) was used in the pretreatment process on the delignification of oil palm fronds.[141] The neat DES only allowed 11.10% lignin removal,

but the addition of 30% water with the DES led to an increase of 16.31% lignin removal. Liang *et al.* implemented ChCl: ethylene glycol (1:2) in a hydrothermal pretreatment to fractionate hemicellulose and lignin from Eucalyptus globulus wood.[142] In this study, biomass pretreatment involved the hemicellulose removal by hydrothermal treatment followed by lignin removal by DES treatment from the hydrothermal residue. After the two-step pretreatment, the removal ratios of lignin and hemicellulose were 90.2% and 97.4%, respectively, while cellulose could be effectively retained with 94.5% of original cellulose in the DES-treated residue.

Chen *et al.* used ChCl: *p*-coumaric acid (PCA) as a DES in a 1:1 molar ratio to effectively pretreat herb residues of *Cortex albiziae* (HRCA).[143] It was observed that neat ChCl: PCA successfully removed 85.25% of hemicellulose at 180°C in only 1 h. When the reaction proceeded for 7 h, 64.03% lignin could be removed. However, at 180°C, > 50% cellulose was removed which hindered enzymatic hydrolysis reactions. When the optimized parameters were determined (ChCl: PCA 1:1, 160°C, 5 h), the enzymatic hydrolysis increased from 48.08% to 84.62%. Interestingly, hemicellulose removal increased from 69.68% to 79.78% with the addition of 5% water in the newly optimized system and the removal of lignin increased to 39.89% with the addition of 50% water.

Alkaline DESs have been shown to enhance the solubility of cellulose due to their ability to break down the intermolecular hydrogen bonding of cellulose. For instance, successful fractionation of cellulose from lignin and hemicellulose was observed when ChCl: KOH (1:4) was used in the pretreatment of beechwood.[138] Lim *et al.* investigated the DES K_2CO_3: glycerol (1:7) as an alternative solvent to the typical kraft pulping pretreatment process that usually involves high temperatures and pressure.[144] Although

kraft pulping is an efficient process, it releases volatile sulphur compounds such as hydrogen sulfide (H_2S), sulfur dioxide (SO_2), dimethyl sulfide (C_2H_6S) and methanethiol (CH_4S) into the atmosphere, in addition to contaminating water sources. Cellulose isolation was successfully achieved from rice straw using the alkaline-DES pulping technique with 73.8% at somewhat lower temperatures (140°C) and 100 minutes. Another example involving the use of 20% (v/v) ChCl: ethylene glycol and ChCl: glycerol (both 1:2 molar ratios) led to increased halophilic cellulase activity, which led to high *in situ* saccharification glucose yields in rice husks.[145] Another interesting pretreatment approach has been to synthesize a ternary DES with two HBD's. Jablonsky *et al.* found that malonic acid: ChCl: propanediol (1:1:3) solubilized 2.09% of cellulose, whereas betaine: urea: glycerol, (1:2:3), betaine: propanediol: lactic acid (1:3:1), and ChCl: acetamide: lactic acid (1:2:3) all solubilized 1.24%, 0.87%, and 0.66% of cellulose, respectively.[139] Additionally, the ternary DESs were investigated in the delignification process of unbleached beech pulp and the authors found that ChCl: acetamide: lactic acid effectively removed 33.80% lignin.

In another example, the addition of *p*-toluenesulfonic acid (PTSA) as a second HBD to the DES of guanidine hydrochloride (GH) and ethylene glycol (EG) was investigated on the pretreatment of switchgrass. The resulting DES GH-EG-PTSA was shown to remove 79% lignin and 82% xylose from switchgrass and < 2% cellulose was lost during this pretreatment, which produced a glucose yield of 90% after enzymatic cellulose hydrolysis after 36 h.[146] Similar sugar yields and lignin removal percentages have been seen with binary DESs in the pretreatment of switchgrass,[127, 147-149] although longer reaction times were necessary. It has been determined that DESs with lower density have an easier time penetrating through the complex lignocellulosic matrix, allowing for better dissolution and

fractionation of lignin, hemicellulose and cellulose. Additionally, it has been observed that the delignification efficiency of a HBD containing a dicarboxylic acid is generally lower than when monocarboxylic acid HBDs are used in various pretreatment processes.[150] D'Agostino *et al.* explained that in DESs containing dicarboxylic acid HBDs, the two COOH groups can form extensive chains of dimers, which can restrict the mobility of solvent molecules.[151] Additionally, it has been observed that lower carbon chain length acids (such as formic and lactic acid) result in higher lignin removal yields as compared to increasing aliphatic chain length (such as butyric, malic and citric acid) that typically result in lower lignin removal yields.[151-152] Although the fractionation of lignocellulose biomass using aqueous DES solutions has shown to be successful, it is still somewhat poorly understood. It is thus important to achieve a deeper understanding of the role of DESs and their aqueous solutions on the selective solubilization of lignin.

Biomedical and Pharmaceutical Applications

Drug solubilization and delivery

Drug delivery is a crucial process in the treatment of illnesses and diseases. There have been many strategies and methods employed to ensure drugs arrive at the location of interest, although the water-solubility of drugs continues to be an issue. Additionally, some drugs such as aspirin can undergo hydrolysis upon prolonged storage in water. Organic solvents have been used to increase drug solubility; however, due to toxicity, flammability, volatility, and environmental concerns, the use of organic solvents is not a practical or a desirable alternative in most pharmaceutical settings. Therefore, DESs have been investigated as a versatile alternative solvent for the solubilization and delivery of pharmaceutical drugs. To this, Morrison *et al.* were among the first to investigate the

solubilization potential of two DESs: one composed of ChCl: urea (1:2 molar ratio) and one of ChCl: malonic acid (1:1 molar ratio).[153] These eutectic systems were studied alongside several poorly water-soluble compounds including benzoic acid, griseofulvin, danazol, itraconazole, and an experimental drug AMG517. Solubility was measured in the neat DES, mixtures of DES and water (75:25 and 50:50 by weight) and pure water. The results indicated that the solubility of the compounds increased by 5- to 22,000-fold in neat DESs when compared with their solubility in water. The solubility of the compounds in aqueous solutions of the individual DES components (ChCl, urea, and malonic acid) were also investigated and, although solubilization of drugs did occur, it was significantly lower than the drugs in the DESs, which confirm the symbiotic nature of the DES components. Li *et al.* also studied the solubilization of itraconazole, along with posaconazole, lidocaine, and piroxicam in several ChCl-based DESs.[154] The solubilities of all four drugs significantly increased in ChCl: glycolic acid (1:2) compared to that of water. For example, lidocaine had a solubility in water of 3.63 mg mL^{-1} but increased to 100.6 mg mL^{-1} in ChCl: glycolic acid. When a third component (oxalic acid) was introduced into the DES to make a ternary DES composed of ChCl: glycolic acid: oxalic acid, (1:1.7:0.3), the solubility of lidocaine was further enhanced to 295.4 mg mL^{-1}. Additionally, the solubilities of itraconazole, piroxicam, and posaconazole all increased in both binary and ternary DESs as compared to their solubilities in water.

The solubility of non-steroidal anti-inflammatory drugs (NSAIDS) in DESs has also been studied. Lu *et al.* studied nineteen different DESs as possible vehicles for drug solubilization and stability of aspirin, acetaminophen, ketoprofen, naproxen and ibuprofen.[155] Overall, the solubility of these drugs increased by 17- to 5477-fold in various

neat DESs as compared to their solubility in water, with tetrapropylammonium bromide: 1,2-propanediol (TPAB: P; 1:2 molar ratio) resulting in the highest solubility of 383.4 ± 4.03 mg mL^{-1} for ibuprofen. Although high drug solubilization was seen when TPAB was used as the HBA, the DES was not considered to be a viable solvent due to its safety issues in both food and pharmaceuticals. Although the DESs ChCl: levulinic acid (1:2) and ChCl: 1,2-propanediol (1:2) resulted in somewhat lower solubilities for acetaminophen and ibuprofen (183.3 – 324.0 mg mL^{-1}), they were ~10-fold higher than the reported solubilities in ILs 1-butyl-3-methylimidazolium hexafluorophosphate [BMIM][PF_6] and 1-hexyl-3-methylimidazolium hexafluorophosphate [HMIM][PF_6] of 10.1–37.2 mg mL^{-1} at room temperature.[156]

The solubility of acetaminophen has also been investigated in DESs of ChCl: urea (1:2), ChCl: malonic acid (1:1), and ChCl: oxalic acid (1:1).[157] The mole fraction of solubility of acetaminophen increased with increasing weight fractions of DESs up to 0.15, yielding solubilities of 3.9887–9.8765, 3.7999–5.8970, and 3.6050–5.2959 in ChCl: malonic acid, ChCl: oxalic acid, and ChCl: urea, respectively, from T = 298.15–313.15 K. In a subsequent paper, the authors were able to increase the weight fraction of DES to 0.90 which showed a > 25-fold enhancement in the acetaminophen solubility in all DESs, with solubility mole fractions of 74.444–140.519, 62.988–103.052, and 52.584–97.302 for ChCl: malonic acid, ChCl: oxalic acid, and ChCl: urea, respectively, in the temperature range of T = 298.15–318.15 K. Interestingly, when the DESs ChCl: glycerol and ChCl: ethylene glycol (molar ratios both 1:2) were implemented, the maximum solubility of acetaminophen was observed when weight fractions of the DESs were 0.80, yielding results of 22.1743–51.6381 and 62.5752–92.2144, respectively from T = 298.15–313.15

K.[158] Structurally speaking, the dicarboxylic acids on malonic and oxalic acid could provide increased hydrogen bonding of the drug to the DES, increasing its solubility, whereas the extra hydroxyl group on glycerol might potentially sterically hinder the acetaminophen-DES interactions, ultimately resulting in lower solubility.

These DESs have been observed to enhance the solubility of other pharmaceutical compounds. For instance, ChCl: malonic acid, ChCl: ethylene glycol, and ChCl: urea all strongly enhanced naproxen solubility up to 3300-fold with DES weight fractions up to 0.90 and temperatures up to 313.15 K.[159] In another study, neat ChCl: urea, ChCl: glycerol, and ChCl: ethylene glycol have successfully enhanced the solubility of the anticonvulsant drug, lamotrigine.[160] Lamotrigine belongs to the bio-pharmaceutical classification system Class II of drugs due to its low water solubility, the generic scheme of which can be seen in Figure 1.12 However, upon the incorporation of the DESs alongside the drug, the results showed a 341-fold solubility enhancement and lamotrigine could be classified as Class I due to the improve solubility.

Natural DESs (NADESs) have also been shown to improve the solubility of drugs. β-lactam antibiotics have a very unstable chemical structure that are prone to β-lactam ring opening resulting from nucleophilic or electrophilic attacks, which can lead to antibiotic degradation or loss of antimicrobial activity. Therefore, a NADES consisting of betaine: urea (1:1.5) has been used to successfully stabilize two β-lactam antibiotics, namely clavulanic acid (CLV) and imipenem (IMP).[161] Both antibiotics displayed no reduction in antimicrobial activity when dissolved in the NADES over at least seven days, as compared to the antibiotics in water which showed significantly decreased activity, further proving that these viable solvents can improve solubility and stability of very important

pharmaceuticals. Lastly, resveratrol, a dietary water-insoluble antioxidant, has been studied with a DES to inhibit matrix metalloprotease-9 in the tumour necrosis factor (TNF-α) activated human leukemia cell line.[162] Resveratrol was successfully dissolved in the DES composed of 1,2-propanediol: ChCl: water (1:1:1), and was able to inhibit matrix

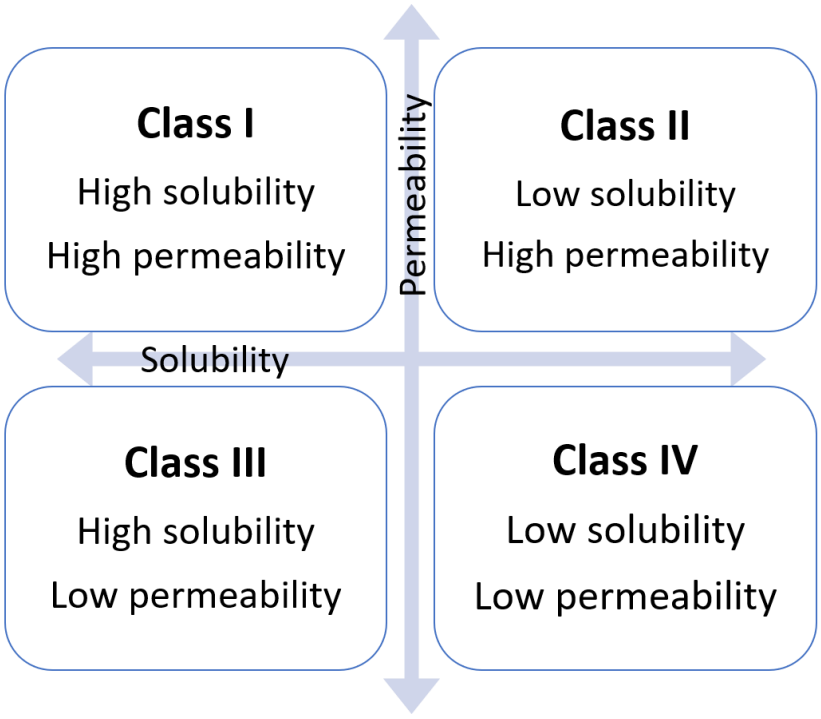

Figure 1.12 Biopharmaceutical classification system of APIs reprinted with permission from ref. 163. Copyright © 2017 Elsevier.

metalloprotease-9 activity by 52% at a remarkable DES concentration of 0.5%. DMSO, the most commonly used solvent for *in vitro* studies, did not reduce the matrix metalloprotease 9 activity at all when the concentration was 0.5%. Overall, this successful resveratrol/DES formulation could allow for lower dosage requirements in future treatments.

Antimicrobial photodynamic therapy (aPDT)

Antibiotic resistance is becoming an increasingly bigger issue due to the misuse and overuse of antibiotics in this modern world.[163] New treatments and techniques are being developed in order to combat this potentially dangerous problem. To this, antimicrobial photodynamic therapy (aPDT) is a relatively new treatment modality that has been shown to overcome several antibiotic resistant strains of bacteria with much success. aPDT utilizes a combination of visible light, a photosensitizer (PS) and oxygen to produce reactive oxygen species which can damage cellular structures of microorganisms and lead to apoptosis. Porphyrins are aromatic heterocyclic compounds that are present in nature and have been widely investigated in photodynamic therapy of tumours and microbial infections as photosensitizers. Interestingly, neutral and anionic porphyrins have been shown to be phototoxic predominantly against Gram-positive bacteria, whereas cationic porphyrins effectively photoinactivate both Gram-positive and Gram-negative microorganisms. The solvents used in these treatments are typically organic in nature and, due to some of their previously discussed disadvantages, have been used less in recent reports. Researchers are now implementing DESs as alternative solvent systems as well as potential porphyrin solubilizers to evaluate these porphyrins as photosensitizers in aPDT treatments.

Some of the work that has come out of the Tønnesen group has investigated the solubilization ability of NADESs on two different porphyrins, specifically the hydrophobic, neutral porphyrin 5,10,15,20-tetrakis(4-hydroxyphenyl) porphyrin (THPP) and the anionic porphyrin meso-tetra-(4-carboxyphenyl)-porphine (TCPP). It was determined that the hydrophilic NADESs composed of citric acid: sucrose (1:1) and

glucose: malic acid (1:1) were the best at solubilizing THPP due to increased hydrogen bonding between the constituents.[164] The photostability of THPP was enhanced in aqueous NADES solutions of containing 22% (w/w) water content as compared to the porphyrin in typical organic solvents. The high viscosity of the NADES resulted in slower reaction rates and helped form a more stable network between the NADES and THPP. Additionally, the NADESs were able to change the neutral porphyrin to a cationic porphyrin due to proton donor–acceptor interactions between the NADES and THPP. The protons in the acids of the NADES (citric acid and malic acid) donate a hydrogen atom to a pyrrole in THPP, thus changing the neutral porphyrin to a cationic porphyrin. This aPDT system resulted in complete photoinactivation of the Gram-negative bacteria *Escherichia coli* and the Gram-positive bacteria *Enterococcus faecalis* using only nanomolar amounts of THPP (0.5–5 nM) in NADES. Interestingly, the fungus *Candida albicans* was least susceptible to any photoinactivation treatment regardless of the NADES or nanomolar THPP amounts used.[165] Further studies implementing higher concentrations of THPP, a different porphyrin, or different NADESs need to be investigated in order to successfully photoinactivate this fungal strain.

Typically, anionic porphyrins have been shown to be ineffective against Gram-negative bacteria due to a thick permeability barrier of the outer membrane surrounding these bacteria. However, 40 nM TCPP and blue light combined with the NADES citric acid: sucrose (1:1) or malic acid: fructose: glucose (1:1:1) both induced *E. coli* reductions of > 90% due to the NADES effectively solubilizing TCPP and changing the anionic porphyrin to cationic.[166] Additionally, > 90% bacterial reduction was seen in Gram-positive microorganisms (including *E. faecalis* and *Staphylococcus aureus*) when

nanomolar concentrations of TCPP (1–10 nM) were solubilized in the NADES with 22% (w/w) water content. The resulting phototoxicities from THPP and TCPP were enhanced when incorporated with NADES and these solvents proved to be viable porphyrin solubilizers that could allow them to be excellent photosensitizers in future aPDT treatments.

Drug Delivery and Extraction

Targeted drug delivery

Successful delivery to the appropriate target of interest in the human body is always a challenge when designing drugs. A hurdle of oral administration of pharmaceuticals is the release of the drug too early and not reaching the area of interest or the degradation of the drug itself in the digestive system. Polymers can behave as vehicles for drug delivery since they can polymerize and self-assemble into micelles which can then be used to encapsulate drugs. DESs have been implemented as functionalizing agents and act as the hydrophobic moiety in the inner core of the micelle allowing for incorporation of hydrophobic drugs while the polymeric carrier forms the hydrophilic outer shell of the polymer allowing it to navigate through the biological environment.[167-168]

Pradeepkumar *et al.* have synthesized micelles using polycaprolactone functionalized with DESs to investigate the controlled release of hydrophobic drugs. Specifically, micelles functionalized with ChCl: citric acid (either 1:1 or 1:2 molar ratio) were used to entrap the anticancer drug camptothecin for successful delivery.[169] It was determined that 93%, 85%, 84%, and 67% of camptothecin was released from the micelle carrier at pH values of 2.6, 5.5, 6.8, and 7.4, respectively, over 8.5 h at 37°C. The drug release was predominantly influenced by the hydrolysis of the ester bonds that were formed

between polycaprolactone and the citric acid component of the DES. The cytotoxicity of the camptothecin-loading micelles was studied in human lung cancer cell line (A549) as well as normal human cell line (L929). The drug-loaded micelles were more cytotoxic to the A549 cells most likely due to the strong negative surface charge on the micelles which disrupted the cancer cell membrane and induced early, and late apoptosis as can be seen in Figure 1.13.

Polycaprolactone has also been conjugated with folic acid and β-alanine to encapsulate the drug doxorubicin using the DES (3-(4-(4-(bis(2-chloroethyl)amino)phenyl)butanoyloxy)-*N*,*N*,*N*-trimethylpropane-1-aminium chloride) (CABAL): 1,4-butanediol in a 1:6 molar ratio.[170] Again, the DES was used to help form the hydrophobic moiety of the micelle to help encapsulate the hydrophobic drug. It was determined that 98% of doxorubicin was released at pH 2.5 within 225 minutes whereas < 50% of the drug was released at pH 5.5 and 6.8, agreeing with the previous results that show that acidic environments can improve drug release. When tested against the breast cancer cell line MDA-MB-231 and normal human cell line L929, the doxorubicin loaded micelle was more cytotoxic to MDA-MB-231 cells. Mechanistically, once the carrier reached the cancer cells, the ester bonds in the micelle were degraded by lysozyme, which has been shown to be highly present in cancer cells. This degradation allowed for the release of doxorubicin into the cancer cell leading to apoptosis.

Another interesting example comes from Mukesh *et al.* who have reported the self-polymerization of 2-hydroxy ethyl methacrylate (HEMA) in the NADES of ChCl: fructose (2:1) in the presence of the NSAID drug indomethacin, where indomethacin was immobilized in the resulting DES/HEMA iongel.[171] The nontoxic and biocompatible gel

was then tested for slow release of the drug at pH 1.2, 4.0, 6.8, and 7.4 in PBS. Pure indomethacin was insoluble in PBS buffer regardless of pH; however, when indomethacin was in incorporated into the DES/HEMA ion gel, it was released up to 96% and 88% at pH 7.4 and 6.8 in 15 h and 20 h, respectively, and the NSAID was found to be structurally stable in the gels for at least six months. Interestingly, indomethacin in the DES/HEMA ion gel was found to be insoluble in acidic pH (pH 1.2 and 4.0). Due to the specificity of these pH-sensitive micellar systems, they show promise as effective delivery systems to target and treat various ailments and diseases.

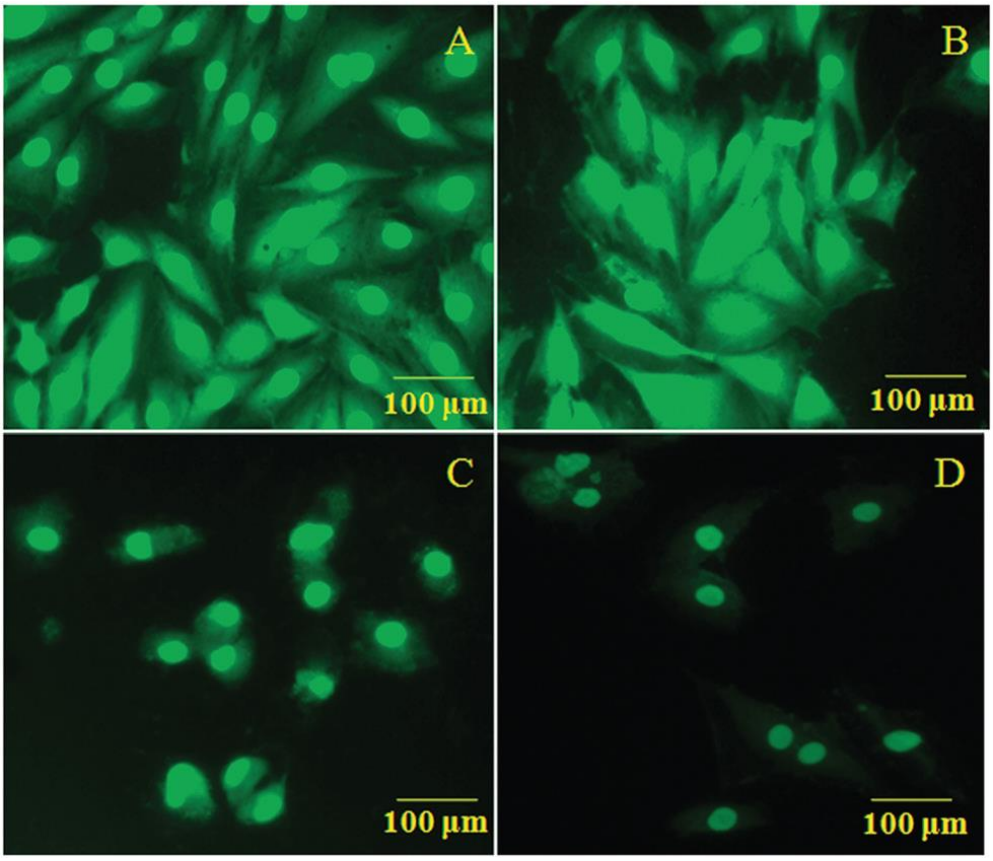

Figure 1.13 Apoptosis of A549 cells cultured with CPT-loaded poly-cp-*co*-CA micelles for (A) 0 min, (B), 24 h, (C) 48 h and (D) 72 h. Reprinted with permission from ref. 172. Copyright © 2018 Royal Society of Chemistry.

Microextraction techniques

Many of the extraction techniques used to extract pharmaceuticals including dispersive liquid–liquid extraction, solid-phase extraction, and hollow-fiber-based liquid–liquid extraction are labour intensive and involve the use organic solvents which violate the principles found in green chemistry. Additionally, these solvents are limited to extracting compounds that have low polarity, which prove to be ineffective at extracting polar media. Microextraction techniques implementing DESs as the extraction solvent have become increasingly popular. For instance, ChCl: phenol (1:4) has been used to successfully extract various antidepressant drugs from biofluid and pharmaceutical wastewater samples using an efficient air-agitated emulsification microextraction technique.[172] In this extraction process, the water miscible DES molecules aggregate and form a cloudy state after the completion of 14 air-agitation cycles in a home-made extraction cell, after which the target analytes become trapped in the aggregated DES and extracted. The percent extraction recovery (% ER) and enrichment factor (EF) are then calculated. At a spiked concentration level of 100 ng mL^{-1}, the % ER and EF values were determined to be 68% and 40 for escitalopram, 42% and 25 for desipramine and 64% and 38 for imipramine, respectively, with a standard deviation lower than 5.7%. When this DES microextraction technique was implemented to test biofluid and pharmaceutical wastewater, the relative recovery percentages were determined to be 88.75–99.45%. Interestingly, this air-agitation microextraction process was also successful in extracting amphetamine and methamphetamine from human plasma and pharmaceutical wastewater, although the DES composed of ChCl: phenethyl alcohol (1:4) was used.[173] The resulting extraction percentages of 63% and 66% and enrichment factors of 47 and 50 were seen in spiked

samples for amphetamine and methamphetamine, respectively, with relative recoveries between 80.5–103.3% for real biofluid and pharmaceutical wastewater samples.

The DES of ChCl: phenethyl alcohol (1:4) has been incorporated into another microextraction technique, namely a hollow-fiber based liquid phase microextraction (HF-LPME) to assist in extracting antiarrhythmic agents.[174] For this technique, the target compounds were penetrated into a supported liquid matrix containing the DES that was fixed inside the pores of a hollow fiber which effectively trapped the drugs of interest, followed by immediate back-extraction into an aqueous phase that was located in the lumen of the hollow fiber. The extraction recoveries of spiked concentration levels of 150 ng mL^{-1} propranolol, carvedilol, verapamil, and amlodipine were determined to be 54%, 48%, 44%, and 44%, respectively, with enrichment factors of 135, 120, 110, 110, which were all higher as compared to the traditional solvent of 1-octanol. Additionally, the relative recoveries of these drugs in real samples of urine, plasma, and pharmaceutical wastewater were found to be in the range of 96.8–103.7%. Liquid–liquid microextraction and solid-phase microextraction are other techniques that have shown enhanced extraction of antibiotics using DESs. The DES of ChCl: glycerol (1:2) mixed with chloroform successfully extracted 87.23% and 83.17% of chloromycetin and thiamphenicol, respectively, using liquid–liquid microextraction. Interestingly, however, these values increased when the DES alone was used in a solid phase extraction to purify and extract these antibiotics from tainted milk, resulting in extraction percentages of 91.23% and 87.02% for chloromycetin and thiamphenicol, respectively.[175]

Additionally, Tang *et al.* successfully extracted the antibiotics levofloxacin and ciprofloxacin using the DES of tricaprylmethylammonium chloride: 1-octanol (1:1) in a

vortex-assisted liquid–liquid microextraction to yield extraction efficiencies > 80% and relative recoveries up to 94.5% in real water samples.[176] Lastly, a DES composed of choline chloride and itaconic acid (1:5) was a functional monomer to synthesize a polymer monolithic column inside a poly(ether ether ketone)(PEEK) tube in order to perform an in-tube solid phase microextraction of NSAIDs.[177] The recoveries of three NSAIDs, specifically ketoprofen, flurbiprofen and diclofenac sodium were determined by HPLC to be between 87.3–113.7% in real lake water samples, while also completing extraction in as little as17 minutes, as compared to other systems which have reported taking anywhere from 30–120 minutes.[178-179]

Therapeutic Deep Eutectic Solvents (THEDES)

Drug solubilization in THEDESs

The ability to form a DES with an active pharmaceutical ingredient (API) as one of the DES components is known as a therapeutic deep eutectic solvent (THEDES). These systems allow for the possibility of developing drug delivery vehicles. The eutectic can prevent recrystallization of the active pharmaceutical ingredient when dispersed in water, leading to more stable and active APIs. Additionally, the preparation of THEDES (and DESs in general) yields 100% pure product, without the need for any purification steps. Stott and coworkers demonstrated for the first time, transdermal drug delivery of ibuprofen through DESs composed of ibuprofen and a range of terpene enhancers including menthol, thymol, menthone, 1,8-cineole, D-limonene, p-cymene.[180] These DESs showed increased solubility, permeability, and absorption of the API of interest.

Aroso *et al.* developed THEDES based on ChCl or menthol as the HBAs conjugated with three different APIs, namely acetylsalicylic acid, benzoic acid, and

phenylacetic acid.[181] Specifically, the DESs investigated were ChCl: phenylacetic acid (1:1), ChCl: acetylsalicylic acid (1:1), menthol: acetylsalicylic acid (3:1), menthol: benzoic acid (3:1), menthol: phenylacetic acid (2:1) and menthol: phenylacetic acid (3:1). Interestingly, the dissolution rate was enhanced in the majority of menthol based THEDES (15–45 min) as compared to ChCl-based THEDES (> 24 h), as well as a few of the individual APIs in buffer (> 24 h). The resulting dissolution efficiencies for all samples tested were in the range of 10–87%, with menthol: benzoic acid providing the highest dissolution efficiency of 87%, although it required 24 h. Interestingly, menthol: phenylacetic acid (3:1) displayed a high efficiency of 81% in only 15 minutes. Additionally, all menthol-based THEDES showed wide inhibitory zones of growth when tested against both Gram-positive and Gram-negative bacteria, as compared to the pure APIs, showing enhanced antibacterial properties when APIs are incorporated into a DES.

In a later work, menthol was combined with ibuprofen in a 3:1 ratio to make a THEDES that enhanced ibuprofen solubility from 2.1 mg mL^{-1} in PBS to 26.8 mg mL^{-1} in THEDES.[182] Ibuprofen in its native form falls into the Class II type of drugs when fitted with the biopharmaceutical classification system, as can be seen in Figure 1.12; however, when it is in combination with menthol, it can now be classified as a Class I type due to its increased solubility and permeability in a THEDES. The anti-tuberculosis drug ethambutol and the amino acid L-arginine have been incorporated as APIs into THEDES using citric acid as the HBA and water to further increase solubility.[183] Impressively, ethambutol solubility increased from 4.64 ± 0.07 mg mL^{-1} in PBS to 127.60 ± 0.69 mg mL^{-1} when incorporated into the THEDES (citric acid: ethambutol: water; 2:1:10). Additionally, the permeability was shown to have a 1.5-fold increase, which altered its classification from a

Class III compound (high solubility, low permeability) to Class I (high solubility, high permeability) when in THEDES. The incorporation of ethambutol in a THEDES could be a potentially better anti-tuberculosis treatment due to the lower dosage that could be implemented for patients. For L-arginine, a slight solubility increase was observed from 99.35 ± 0.54 mg mL^{-1} in PBS to 102.17–107.86 mg mL^{-1} in the THEDES (citric acid: L-arginine) regardless of the molar ratio used. Arginine-based DESs have also been investigated to increase the API lidocaine solubility in various THEDES. Density functional theory and molecular dynamic methods have shown that high solvation of lidocaine with arginine in a THEDES is based on strong solute–solvent intermolecular interactions, with hydrogen bonding playing the key role in the solubilization process.[184-185]

Another interesting study came from Abbott *et al.* who employed ChCl as the HBA along with the following HBDs: phenol, catechol, resorcinol, hydroquinone, 2-methyl-phenol,3,4-dimethyl-phenol, 2,4,6-trimethyl-phenol, thymol, 2,6-di-*tert*butyl-4-methylphenol, salicylic acid, 4-chloro phenol, 4-methoxyphenol, paracetamol, benzoic acid, and aspirin.[186] Among these, ChCl: resorcinol (1:1) displayed the highest solubility of 1110 g dm^{-3}, while 2,6-di-*tert*-butyl-4-methylphenol was insoluble and did not even form a DES. Additionally, the THEDES incorporating benzoic acid and aspirin showed the lowest solubilities of 3.4 g dm^{-3} and 4.6 g dm^{-3}, respectively. Two commonly prescribed drugs, adiphenine and ranitidine, were also investigated in this study and were able to form eutectics with HBDs of glycerol, urea, and aspirin, the latter showing that two active pharmaceutical ingredients can be incorporated together in a DES. Oddly enough, when adiphenine was mixed with glycerol, urea, or aspirin, the solubility remained the same

throughout, at 70 g dm^{-3}, showing that, in this case at least, the HBD did not make a difference.

As this section has discussed, drug solubilization and permeability can be greatly enhanced when the APIs of interest are incorporated into the deep eutectic solvent system. Dissolution and permeation of the APIs depends on the formulation of the THEDES, which, due to their strong intermolecular hydrogen bonding in solution, allows for higher transport rates through membranes than in their solid forms. Additionally, the stoichiometries of THEDES can be fine-tuned to allow for greater specificity and show great potential as new delivery systems.[187] Overall, it's been shown that a wide array of pharmaceuticals can form THEDES that increase the APIs solubility and improve drug delivery while also decreasing the dosage requirements for future treatments.

THEDES in polymers

Biodegradable elastomers have demonstrated a tremendous versatility as polymeric networks for regenerative medicine as well as efficient systems for controlled drug release in biomedical applications.[188] The coupling of THEDES with polymeric material brings new possibilities for alternative pharmaceutical systems. Supercritical fluid technology has opened the door to a variety of applications in recent years. This sintering process takes place at subcritical conditions using carbon dioxide ($scCO_2$) where polymeric particles are fused together by plasticization to create a lightweight and porous 3D structure. The main requirement for the CO_2–foaming process is that a sufficient amount of CO_2 needs to be dissolved in the polymer. By doping polymers with THEDES, this foaming/sintering process can still take place due to the plasticizing properties of the THEDES. These potential plasticizing agents can improve the foaming ability by decreasing the melting

point of the polymers or by enhancing CO_2 solubility in the matrix, while also improving the overall flexibility of the polymer. Additionally, the resulting polymeric matrices can display enhanced porosity that can be exploited as potential alternatives as drug delivery systems. Martins *et al.* have evaluated various NADESs to enhance the $scCO_2$ foaming process to promote the synthesis of 3D porous structures.[189] Although the final polymer porosity increased with all NADESs investigated, it was highly dependent on which NADES was used. In the case of the polymer blended with ChCl: sucrose (1:1) and ChCl: citric acid (1:1), the foamed structures presented large open pores, high homogeneity, and high pore interconnectivity, with ChCl: sucrose resulting in a 52% increase in porosity. As expected, the polymer blend foamed without the presence of NADES showed very low levels of porosity.

Aroso *et al.* have created a polymer based on 70% cornstarch and poly-ε-caprolactone impregnated with the THEDES menthol: ibuprofen (3:1) as a potential drug delivery system.[190] The presence of 20% THEDES impregnated in the polymers enhanced the porosity to 44% and increased the interconnectivity to 28%, which was shown to be 3-fold and 9-fold higher, respectively, than the polymer alone. Additionally, ibuprofen displayed a faster release from the polymeric matrix when it was impregnated with THEDES (~85%) as compared to the polymer containing just ibuprofen (~65%) in 125 h. Similar supercritical fluid sintering results have been shown with ChCl: ascorbic acid (2:1) containing solubilized dexamethasone.[191] An incredible increase in dexamethasone solubility and diffusion rate was seen when the polymer was doped with 10 wt% THEDES (~4000 mg L^{-1}) as compared with the drug in powder form (60 mg L^{-1}).

Poly(diol-*co*-citrates) (PDC) polymers were first described by Yang *et al.* in 2004 as new types of biodegradable and biocompatible polyesters.[192] Over the years, there have been many challenges in regards to incorporating APIs into these polymers mostly due to the prepolymer synthetic step because the high temperatures that are required (several minutes at 160–165°C) can be detrimental to APIs, leading to inactivation or denaturation of these pharmaceuticals. In addition, during the post synthesis steps, it is difficult for the APIs to be homogeneously distributed. Nonetheless, Serrano *et al.* have prepared DESs based on lidocaine and 1,8-octanediol (molar ratio 1:3) to create poly(octanediol-*co*-citrate) elastomers loaded with lidocaine.[193] The DES provided not only one of the polymer precursors and the API, but was also the synthetic media where the second polymer precursor (citric acid) could be solubilized in order for polymerization to take place. The prepolymer synthesis was able to be carried out at 90°C (instead of the typical 160°C), ensuring no lidocaine inactivation or degradation. A burst release of lidocaine occurred within the first hour of the elastomer being in water or PBS after which it continued to slowly increase up to 300 h.

Emerging Biomedical Applications

Alginates, specifically calcium alginates, have been used in the pharmaceutical industry for controlled drug release; however, DESs are more recently being used as reinforcement fillers in calcium alginate beads to further enhance the slow release of drugs. More specifically, ChCl: thiourea (1:2) has been mixed with chitin powder to produce chitin nanofibers in calcium alginate beads to enhance the release of the anticancer drug 5-fluoroaurascil.[194] These DES-chitin nanofibers were able to release 70% of the drug after 24 h at pH 7.4, as compared to the typical DES-free calcium-alginate beads that only

released 39%of the drug after 3 h. Shrimp shells contain calcium carbonate (25–50%), protein (35–50%), and chitin (15–25%), among which, chitin has many beneficial properties such as biocompatibility, biodegradability, bioactivity, and non-toxicity, and can be applied in numerous fields such as biomedicine, agriculture, water treatment and cosmetics. Moreover, chitin derivatives including deacylated, acylated, thiolated, and grafted chitin have attracted more interest because of their high solubility and possess unique properties compared with chitin. The conventional methods to retrieve chitin and obtain its acylated derivative involve removing the calcium carbonate and protein which typically involve time-consuming processes and the use of harsh chemicals that are hazardous to the environment. Hence, DESs have been implemented as a triple threat solvent where decalcification, deproteinization, and acylation of chitin all occur in a one-step process.

For instance, ChCl: DL-malic acid (1:2) has been shown to successfully remove calcium and proteins from shrimp shells while simultaneously causing an acylation reaction in chitin at 130°C in 3 h.[195] The DES had the ability to release H^+, which reacted with calcium carbonate to produce carbon dioxide and water-soluble calcium salts and the acidity of the DES allowed for protein dissolution and degradation. Additionally, the H^+ released from the DES was able to catalyze the acylation of chitin in a nucleophilic type of reaction to produce the acylated product O-malate chitin. The obtained acylated chitin was shown to have good antibacterial and antitumor activity against both *E. coli* and C6 glioma, respectively. Interestingly, Zhao *et al.* found that pretreating shrimp shells first with 10% citric acid to help with demineralization allowed the DESs of betaine hydrochloric acid: urea, ChCl: urea, ChCl: ethylene glycol, and ChCl: glycerol (all in 1:2 molar ratios) to all

successfully retrieve chitin in similar yields of around 20–25%, which was higher than the typical acid/alkali extraction method (17.7%), while also drastically reducing the extraction time to as little as seven minutes using microwave irradiation.[196]

A transdermal drug delivery system (TDDS) has many advantages, such as non-invasiveness, sustained release, and enhanced therapeutic efficiency. However, a low permeation rate of drugs through the skin still continues to be an issue. To this, a DES composed of choline bicarbonate and geranic acid (CAGE; molar ratio 1:2) exhibited broad-spectrum antimicrobial activity against a number of drug-resistant bacteria, fungi, and viruses including *Mycobacterium tuberculosis*, *Staphylococcus aureus* and *Candida albicans* as well as strains of Herpes Simplex Virus.[197] Interestingly, *Pseudomonas aeruginosa* was the most resilient to treatment, requiring ~25% (v/v) CAGE to neutralize it. *Mycobacterium tuberculosis* (TB), on the other hand, was the most susceptible out of all 47 strains tested against CAGE, needing < 0.195% (v/v) CAGE for complete neutralization. Overall, the majority of strains tested including Gram-positive and Gram-negative bacteria, aerobes and anaerobes, and fungi and viruses only required < 1% (v/v) CAGE treatment. Additionally, CAGE resulted in an ~180–14,000-fold improved efficacy/toxicity ratio over currently used antiseptic agents and was shown to penetrate deep into the dermis layer of skin to treat a *Propionibacterium acnes* infection *in vivo*, while also displaying good biocompatibility and no toxicity with healthy tissues. Similar studies have been reported for CAGE to act as an antibacterial agent against the Gram-negative bacteria *Escherichia coli (E. coli)* while also being successful in topical delivery for skin diseases and transdermal drug delivery.[198-200] CAGE has also been used to deliver BSA, ovalbumin, and insulin into the dermis of porcine skin to enhance topical delivery of

therapeutic proteins.[201] A significant enhancement of BSA in CAGE was delivered to the epidermis and dermis of rats (2.84 ± 0.59 μg cm^{-2} and 1.61 ± 0.09 μg cm^{-2}, respectively) after only 12 hours as compared to BSA in PBS (0.08 ± 0.01 μg cm^{-2} and 0.04 ± 0.04 μg cm^{-2} for epidermis and dermis, respectively), as can be seen in Figure 1.14.

When rats were given 10 U mL^{-1} insulin-CAGE (25 U kg^{-1} body weight), an immediate 25% decrease in the blood glucose level was observed within two hours of administration, with the highest decrease in blood glucose seen around 40% (59.5 ± 5.6%) after four hours. In comparison with typical insulin injections, when 1 U kg^{-1} of insulin was administered, an immediate 45% decrease in blood glucose was seen; however, it returned to its original value within four hours. Other reports have observed increased absorption and delivery of insulin and small molecule drugs in CAGE,[202-207] although there have been some conflicting reports as to whether CAGE is a DES or IL. It is important to note that CAGE could be used as a stand-alone drug in the case of mild infections or in synergistic combinations with antibiotics in the case of severe or life-threatening infections. Deep eutectic gels have become increasingly popular over the years in ion gel reports. One of the first involves a resorcinol-formaldehyde gel that was prepared using a polycondensation reaction inside DESs to synthesize carbon monoliths.[208] Interestingly, the ion gel was not the product of the reaction but served only as a template that was discarded after synthesis. Subsequently, publications started to increase where the ion gel was synthesized by incorporating a DES into the synthesis and these ‘‘eutectogels’’ showed good flexibility, conductivity, and shape recovery.[171, 209-211] In a recent report, a eutectogel was formed by incorporating the DES ChCl: glyceline (1:2) within bacterial cellulose.[212] The very high crystallinity of bacterial cellulose remained unaffected by the

DES contained in the gels even at high loadings (98.8% by weight). Overall, the structural behaviors and dynamic properties of this gelatin-like self-supported material was investigated through a multitude of techniques, including X-ray diffraction, nuclear magnetic resonance (NMR), small-angle neutron scattering (SANS), and molecular dynamics (MD) simulations.

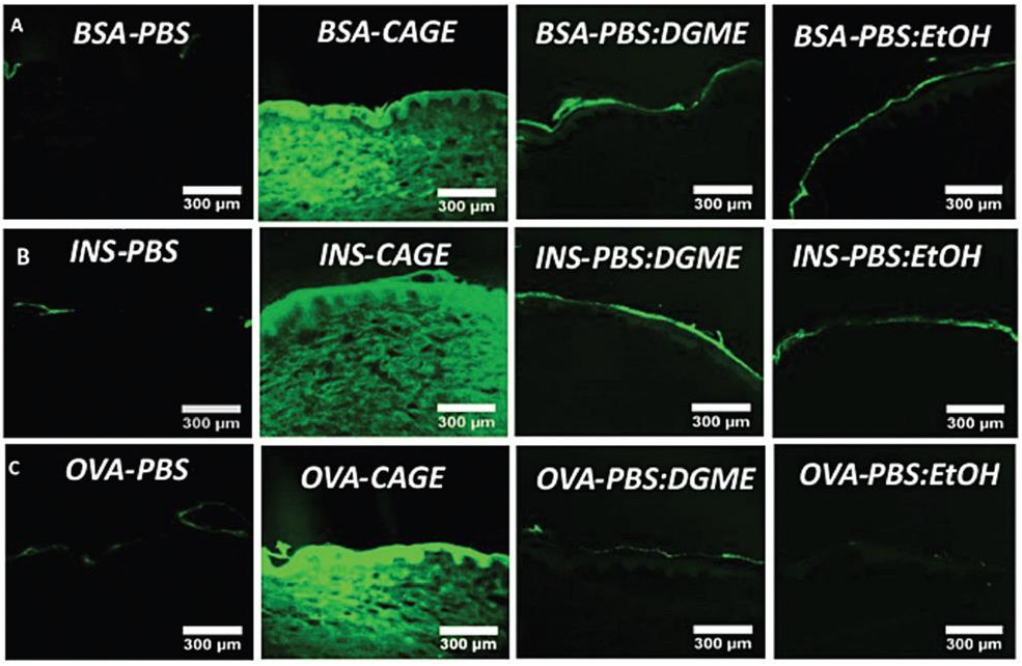

Figure 1.14 Confocal images of skin penetration of fluorescently labeled proteins in PBS, CAGE, 50:50 (v/v) PBS: DGME, or 50:50 (v/v) PBS: ethanol. Reprinted with permission from ref. 203. Copyright® 2017 Wiley.

Conclusions and Outlook

This chapter has discussed the use of DESs in a wide array of biological or biotechnology-oriented applications. These emergent and potentially-green solvents have been shown to greatly improve the thermostability of proteins, to aid in high value biological extractions, and to open the door to steering the self-assembly of various DNA topologies, including the emergence of unique, non-native architectures. In many cases, DESs strongly increase

product yields and conversion rates when incorporated as the solvent, co-solvent, substrate, or catalyst in various biocatalytic scenarios. DESs also allow for the enhanced pretreatment of recalcitrant biomass (*e.g.*, removal of chitin from shrimp shells), effectively separating and breaking down complex lignocellulosic matrices to better utilize the resulting products as fuels or synthetic feedstocks. Furthermore, the improved stability and solubility of various pharmaceuticals and the introduction of therapeutic DESs (THEDES) indicate future promise in oral and transdermal drug delivery, potentially at lower dosing of APIs. In addition to some established avenues for the application of DESs in biologics, there are some less explored but highly exciting avenues that will see increased activity in the coming years. Because DESs frequently comprise natural primary metabolites known to aid in survival at negative temperatures (*e.g.*, sugars, sugar alcohols, organic acids, amino acids, amines), they hold intriguing potential as cryoprotective agents, conversely, as room-temperature preservation media to eliminate the cold-chain storage of therapeutic proteins and vaccines. DESs are likely to be a great asset to the biotechnologist in other ways as well, including as artificial, small-molecule chaperonins aiding in protein refolding,[213] as promoters of rapidly controlled protein fibrillation, and as media for the design of artificialbiosystems[214] and synthetic protocells.

Despite the obvious importance of water content (*e.g.*, key structural waters) in the behavior of DESs, the key molecular details are still awaited. And while, in principle, these solvents can be optimized to the application of interest, the lion's share of studies remain focused on a handful of DESs, particularly the ''notorious three'' (*i.e.*, reline, ethaline, glyceline). Given the enormous interest in these solvents, the ongoing challenges and opportunities discussed herein will very likely be met and exceeded in real time.

Acknowledgements

H. Z. acknowledges the Donors of the American Chemical Society Petroleum Research Fund (PRF# 60077-ND4) for support of this research. K. R. M.-K. is supported by the National Science Foundation under Grant No. CHE-1665157.

References

1. Plechkova, N. V.; Seddon, K. R., Applications of Ionic Liquids in the Chemical Industry. *Chem. Soc. Rev.* **2008,** *37* (1), 123-150.

2. Rogers, R. D.; Seddon, K. R., Ionic Liquids--Solvents of the Future? *Science* **2003,** *302* (5646), 792-793.

3. Petkovic, M.; Seddon, K. R.; Rebelo, L. P. N.; Silva Pereira, C., Ionic Liquids: A Pathway to Environmental Acceptability. *Chem. Soc. Rev.* **2011,** *40* (3), 1383-1403.

4. Deetlefs, M.; Seddon, K. R., Assessing the Greenness of Some Typical Laboratory Ionic Liquid Preparations. *Green Chem.* **2010,** *12* (1), 17-30.

5. Carriazo, D.; Serrano, M. C.; Gutiérrez, M. C.; Ferrer, M. L.; del Monte, F., Deep-Eutectic Solvents Playing Multiple Roles in the Synthesis of Polymers and Related Materials. *Chem. Soc. Rev.* **2012,** *41* (14), 4996-5014.

6. Zhang, Q.; De Oliveira Vigier, K.; Royer, S.; Jérôme, F., Deep Eutectic Solvents: Syntheses, Properties and Applications. *Chem. Soc. Rev.* **2012,** *41* (21), 7108-7146.

7. Ruß, C.; König, B., Low Melting Mixtures in Organic Synthesis – an Alternative to Ionic Liquids? *Green Chem.* **2012,** *14* (11), 2969-2982.

8. Maugeri, Z.; Leitner, W.; Domínguez de María, P., Practical Separation of Alcohol–Ester Mixtures Using Deep-Eutectic-Solvents. *Tetrahedron Lett.* **2012,** *53* (51), 6968-6971.

9. Maugeri, Z.; Domínguez de María, P., Novel Choline-Chloride-Based Deep-Eutectic-Solvents with Renewable Hydrogen Bond Donors: Levulinic Acid and Sugar-Based Polyols. *RSC Adv.* **2012,** *2* (2), 421-425.

10. Abbott, A. P.; Harris, R. C.; Ryder, K. S.; D'Agostino, C.; Gladden, L. F.; Mantle, M. D., Glycerol Eutectics as Sustainable Solvent Systems. *Green Chem.* **2011,** *13* (1), 82-90.

11. Abbott, A. P.; Boothby, D.; Capper, G.; Davies, D. L.; Rasheed, R. K., Deep Eutectic Solvents Formed between Choline Chloride and Carboxylic Acids: Versatile Alternatives to Ionic Liquids. *J. Am. Chem. Soc.* **2004,** *126* (29), 9142-9147.

12. Abbott, A. P.; Capper, G.; Davies, D. L.; Rasheed, R. K.; Tambyrajah, V., Novel Solvent Properties of Choline Chloride/Urea Mixtures. *Chem. Commun.* **2003,** (1), 70-71.

13. Francisco, M.; van den Bruinhorst, A.; Kroon, M. C., New Natural and Renewable Low Transition Temperature Mixtures (Lttms): Screening as Solvents for Lignocellulosic Biomass Processing. *Green Chem.* **2012,** *14* (8), 2153-2157.

14. Hayyan, M.; Hashim, M. A.; Hayyan, A.; Al-Saadi, M. A.; AlNashef, I. M.; Mirghani, M. E. S.; Saheed, O. K., Are Deep Eutectic Solvents Benign or Toxic? *Chemosphere* **2013,** *90* (7), 2193-2195.

15. Gutiérrez, M. C.; Ferrer, M. L.; Mateo, C. R.; del Monte, F., Freeze-Drying of Aqueous Solutions of Deep Eutectic Solvents: A Suitable Approach to Deep Eutectic Suspensions of Self-Assembled Structures. *Langmuir* **2009,** *25* (10), 5509-5515.

16. Gutiérrez, M. C.; Ferrer, M. L.; Yuste, L.; Rojo, F.; del Monte, F., Bacteria Incorporation in Deep-Eutectic Solvents through Freeze-Drying. *Angew. Chem. Int. Ed.* **2010,** *49* (12), 2158-2162.

17. Smith, E. L.; Abbott, A. P.; Ryder, K. S., Deep Eutectic Solvents (Dess) and Their Applications. *Chem. Rev.* **2014,** *114* (21), 11060-11082.

18. Mbous, Y. P.; Hayyan, M.; Hayyan, A.; Wong, W. F.; Hashim, M. A.; Looi, C. Y., Applications of Deep Eutectic Solvents in Biotechnology and Bioengineering—Promises and Challenges. *Biotechnol. Adv.* **2017,** *35* (2), 105-134.

19. Wagle, D. V.; Zhao, H.; Baker, G. A., Deep Eutectic Solvents: Sustainable Media for Nanoscale and Functional Materials. *Acc. Chem. Res.* **2014,** *47* (8), 2299-2308.

20. Choi, Y. H.; van Spronsen, J.; Dai, Y.; Verberne, M.; Hollmann, F.; Arends, I. W. C. E.; Witkamp, G.-J.; Verpoorte, R., Are Natural Deep Eutectic Solvents the Missing Link in Understanding Cellular Metabolism and Physiology? *Plant Physiology* **2011,** *156* (4), 1701-1705.

21. Doukyu, N.; Ogino, H., Organic Solvent-Tolerant Enzymes. *Biochemical Engineering Journal* **2010,** *48* (3), 270-282.

22. Volkin, D. B.; Staubli, A.; Langer, R.; Klibanov, A. M., Enzyme Thermoinactivation in Anhydrous Organic Solvents. *Biotechnol. Bioeng.* **1991,** *37* (9), 843-853.

23. Esquembre, R.; Sanz, J. M.; Wall, J. G.; del Monte, F.; Mateo, C. R.; Ferrer, M. L., Thermal Unfolding and Refolding of Lysozyme in Deep Eutectic Solvents and Their Aqueous Dilutions. *Phys. Chem. Chem. Phys.* **2013,** *15* (27), 11248-11256.

24. Sanchez-Fernandez, A.; Edler, K. J.; Arnold, T.; Alba Venero, D.; Jackson, A. J., Protein Conformation in Pure and Hydrated Deep Eutectic Solvents. *Phys. Chem. Chem. Phys.* **2017,** *19* (13), 8667-8670.

25. Xin, R.; Qi, S.; Zeng, C.; Khan, F. I.; Yang, B.; Wang, Y., A Functional Natural Deep Eutectic Solvent Based on Trehalose: Structural and Physicochemical Properties. *Food Chem.* **2017,** *217*, 560-567.

26. Dai, Y.; van Spronsen, J.; Witkamp, G.-J.; Verpoorte, R.; Choi, Y. H., Natural Deep Eutectic Solvents as New Potential Media for Green Technology. *Anal. Chim. Acta* **2013,** *766*, 61-68.

27. Silva, N. H. C. S.; Pinto, R. J. B.; Freire, C. S. R.; Marrucho, I. M., Production of Lysozyme Nanofibers Using Deep Eutectic Solvent Aqueous Solutions. *Colloid Surface B* **2016,** *147*, 36-44.

28. Wu, B.-P.; Wen, Q.; Xu, H.; Yang, Z., Insights into the Impact of Deep Eutectic Solvents on Horseradish Peroxidase: Activity, Stability and Structure. *J. Mol. Catal. B: Enzyme* **2014,** *101*, 101-107.

29. Sánchez-Leija, R. J.; Torres-Lubián, J. R.; Reséndiz-Rubio, A.; Luna-Bárcenas, G.; Mota-Morales, J. D., Enzyme-Mediated Free Radical Polymerization of Acrylamide in Deep Eutectic Solvents. *RSC Adv.* **2016,** *6* (16), 13072-13079.

30. Papadopoulou, A. A.; Efstathiadou, E.; Patila, M.; Polydera, A. C.; Stamatis, H., Deep Eutectic Solvents as Media for Peroxidation Reactions Catalyzed by Heme-Dependent Biocatalysts. *Ind. Eng. Chem. Res.* **2016,** *55* (18), 5145-5151.

31. Laszlo, J. A.; Compton, D. L., Comparison of Peroxidase Activities of Hemin, Cytochrome C and Microperoxidase-11 in Molecular Solvents and Imidazolium-Based Ionic Liquids. *J. Mol. Catal. B: Enzyme* **2002,** *18* (1), 109-120.

32. Kist, J. A.; Henzl, M. T.; Bañuelos, J. L.; Baker, G. A., Calorimetric Evaluation of the Operational Thermal Stability of Ribonuclease a in Hydrated Deep Eutectic Solvents. *ACS Sustainable Chem. Eng.* **2019,** *7* (15), 12682-12687.

33. Lee, M. S.; Lee, K.; Nam, M. W.; Jeong, K. M.; Lee, J. E.; Kim, N. W.; Yin, Y.; Lim, S. Y.; Yoo, D. E.; Lee, J.; Jeong, J. H., Natural Deep Eutectic Solvents as a Storage Medium for Human Interferon-A2: A Green and Improved Strategy for Room-Temperature Biologics. *Journal of Industrial and Engineering Chemistry* **2018,** *65*, 343-348.

34. Unsal, E.; Irmak, T.; Durusoy, E.; Tuncel, M.; Tuncel, A., Monodisperse Porous Polymer Particles with Polyionic Ligands for Ion Exchange Separation of Proteins. *Anal. Chim. Acta* **2006,** *570* (2), 240-248.

35. Wolschin, F.; Wienkoop, S.; Weckwerth, W., Enrichment of Phosphorylated Proteins and Peptides from Complex Mixtures Using Metal Oxide/Hydroxide Affinity Chromatography (Moac). *PROTEOMICS* **2005,** *5* (17), 4389-4397.

36. Li, Z.; Liu, X.; Pei, Y.; Wang, J.; He, M., Design of Environmentally Friendly Ionic Liquid Aqueous Two-Phase Systems for the Efficient and High Activity Extraction of Proteins. *Green Chem.* **2012,** *14* (10), 2941-2950.

37. Zeng, Q.; Wang, Y.; Huang, Y.; Ding, X.; Chen, J.; Xu, K., Deep Eutectic Solvents as Novel Extraction Media for Protein Partitioning. *Analyst* **2014,** *139* (10), 2565-2573.

38. Xu, K.; Wang, Y.; Huang, Y.; Li, N.; Wen, Q., A Green Deep Eutectic Solvent-Based Aqueous Two-Phase System for Protein Extracting. *Anal. Chim. Acta* **2015,** *864*, 9-20.

39. Li, N.; Wang, Y.; Xu, K.; Huang, Y.; Wen, Q.; Ding, X., Development of Green Betaine-Based Deep Eutectic Solvent Aqueous Two-Phase System for the Extraction of Protein. *Talanta* **2016,** *152*, 23-32.

40. Zeng, C.-X.; Xin, R.-P.; Qi, S.-J.; Yang, B.; Wang, Y.-H., Aqueous Two-Phase System Based on Natural Quaternary Ammonium Compounds for the Extraction of Proteins. *Journal of Separation Science* **2016,** *39* (4), 648-654.

41. Pang, J.; Sha, X.; Chao, Y.; Chen, G.; Han, C.; Zhu, W.; Li, H.; Zhang, Q., Green Aqueous Biphasic Systems Containing Deep Eutectic Solvents and Sodium Salts for the Extraction of Protein. *RSC Adv.* **2017,** *7* (78), 49361-49367.

42. Zhang, H.; Wang, Y.; Xu, K.; Li, N.; Wen, Q.; Yang, Q.; Zhou, Y., Ternary and Binary Deep Eutectic Solvents as a Novel Extraction Medium for Protein Partitioning. *Anal. Methods* **2016,** *8* (46), 8196-8207.

43. Meng, J.; Wang, Y.; Zhou, Y.; Chen, J.; Wei, X.; Ni, R.; Liu, Z.; Xu, F., Development of Different Deep Eutectic Solvent Aqueous Biphasic Systems for the Separation of Proteins. *RSC Adv.* **2019,** *9* (25), 14116-14125.

44. Huang, Y.; Wang, Y.; Pan, Q.; Wang, Y.; Ding, X.; Xu, K.; Li, N.; Wen, Q., Magnetic Graphene Oxide Modified with Choline Chloride-Based Deep Eutectic Solvent for the Solid-Phase Extraction of Protein. *Anal. Chim. Acta* **2015,** *877*, 90-99.

45. Xu, K.; Wang, Y.; Ding, X.; Huang, Y.; Li, N.; Wen, Q., Magnetic Solid-Phase Extraction of Protein with Deep Eutectic Solvent Immobilized Magnetic Graphene Oxide Nanoparticles. *Talanta* **2016,** *148*, 153-162.

46. Xu, K.; Wang, Y.; Li, Y.; Lin, Y.; Zhang, H.; Zhou, Y., A Novel Poly(Deep Eutectic Solvent)-Based Magnetic Silica Composite for Solid-Phase Extraction of Trypsin. *Anal. Chim. Acta* **2016,** *946*, 64-72.

47. Liu, Y.; Wang, Y.; Dai, Q.; Zhou, Y., Magnetic Deep Eutectic Solvents Molecularly Imprinted Polymers for the Selective Recognition and Separation of Protein. *Anal. Chim. Acta* **2016,** *936*, 168-178.

48. Xu, W.; Wang, Y.; Wei, X.; Chen, J.; Xu, P.; Ni, R.; Meng, J.; Zhou, Y., Fabrication of Magnetic Polymers Based on Deep Eutectic Solvent for Separation of Bovine Hemoglobin Via Molecular Imprinting Technology. *Anal. Chim. Acta* **2019,** *1048,* 1-11.

49. Zhang, Y.; Cao, H.; Huang, Q.; Liu, X.; Zhang, H., Isolation of Transferrin by Imprinted Nanoparticles with Magnetic Deep Eutectic Solvents as Monomer. *Anal. Bioanal. Chem.* **2018,** *410* (24), 6237-6245.

50. Zhao, H., DNA Stability in Ionic Liquids and Deep Eutectic Solvents. *J. Chem. Technol. Biot.* **2015,** *90* (1), 19-25.

51. Zhao, C.; Qu, X., Recent Progress in G-Quadruplex DNA in Deep Eutectic Solvent. *Methods* **2013,** *64* (1), 52-58.

52. Mamajanov, I.; Engelhart, A. E.; Bean, H. D.; Hud, N. V., DNA and Rna in Anhydrous Media: Duplex, Triplex, and G-Quadruplex Secondary Structures in a Deep Eutectic Solvent. *Angew. Chem. Int. Ed.* **2010,** *49* (36), 6310-6314.

53. Gállego, I.; Grover, M. A.; Hud, N. V., Folding and Imaging of DNA Nanostructures in Anhydrous and Hydrated Deep-Eutectic Solvents. *Angew. Chem. Int. Ed.* **2015,** *54* (23), 6765-6769.

54. Mondal, D.; Sharma, M.; Mukesh, C.; Gupta, V.; Prasad, K., Improved Solubility of DNA in Recyclable and Reusable Bio-Based Deep Eutectic Solvents with Long-Term Structural and Chemical Stability. *Chem. Commun.* **2013,** *49* (83), 9606-9608.

55. Zhao, H.; Shen, K., DNA-Based Asymmetric Catalysis: Role of Ionic Solvents and Glymes. *RSC Adv.* **2014,** *4* (96), 54051-54059.

56. de La Harpe, K.; Kohl, F. R.; Zhang, Y.; Kohler, B., Excited-State Dynamics of a DNA Duplex in a Deep Eutectic Solvent Probed by Femtosecond Time-Resolved Ir Spectroscopy. *J. Phys. Chem. A* **2018,** *122* (9), 2437-2444.

57. Parkinson, G. N.; Lee, M. P.; Neidle, S., Crystal Structure of Parallel Quadruplexes from Human Telomeric DNA. *Nature* **2002,** *417* (6891), 876-80.

58. Huppert, J. L., Four-Stranded Nucleic Acids: Structure, Function and Targeting of G-Quadruplexes. *Chem. Soc. Rev.* **2008,** *37* (7), 1375-1384.

59. Mashimo, T.; Yagi, H.; Sannohe, Y.; Rajendran, A.; Sugiyama, H., Folding Pathways of Human Telomeric Type-1 and Type-2 G-Quadruplex Structures. *J. Am. Chem. Soc.* **2010,** *132* (42), 14910-14918.

60. Lannan, F. M.; Mamajanov, I.; Hud, N. V., Human Telomere Sequence DNA in Water-Free and High-Viscosity Solvents: G-Quadruplex Folding Governed by Kramers Rate Theory. *J. Am. Chem. Soc.* **2012,** *134* (37), 15324-15330.

61. Zhao, C.; Ren, J.; Qu, X., G-Quadruplexes Form Ultrastable Parallel Structures in Deep Eutectic Solvent. *Langmuir* **2013,** *29* (4), 1183-1191.

62. Pal, S.; Paul, S., Effect of Hydrated and Nonhydrated Choline Chloride–Urea Deep Eutectic Solvent (Reline) on Thrombin-Binding G-Quadruplex Aptamer (Tba): A Classical Molecular Dynamics Simulation Study. *J. Phys. Chem. C* **2019,** *123* (18), 11686-11698.

63. Gorke, J.; Srienc, F.; Kazlauskas, R., Toward Advanced Ionic Liquids. Polar, Enzyme-Friendly Solvents for Biocatalysis. *Biotechnology and Bioprocess Engineering* **2010,** *15* (1), 40-53.

64. Xu, P.; Zheng, G.-W.; Zong, M.-H.; Li, N.; Lou, W.-Y., Recent Progress on Deep Eutectic Solvents in Biocatalysis. *Bioresources and Bioprocessing* **2017,** *4* (1), 34.

65. Guajardo, N.; Müller, C. R.; Schrebler, R.; Carlesi, C.; Domínguez de María, P., Deep Eutectic Solvents for Organocatalysis, Biotransformations, and Multistep Organocatalyst/Enzyme Combinations. *ChemCatChem* **2016,** *8* (6), 1020-1027.

66. Zaks, A.; Klibanov, A., Enzymatic Catalysis in Organic Media at 100 Degrees C. *Science* **1984,** *224* (4654), 1249-1251.

67. Parawira, W., Biotechnological Production of Biodiesel Fuel Using Biocatalysed Transesterification: A Review. *Crit. Rev. Biotechnol.* **2009,** *29* (2), 82-93.

68. Pöhnlein, M.; Ulrich, J.; Kirschhöfer, F.; Nusser, M.; Muhle-Goll, C.; Kannengiesser, B.; Brenner-Weiß, G.; Luy, B.; Liese, A.; Syldatk, C.; Hausmann, R., Lipase-Catalyzed Synthesis of Glucose-6-O-Hexanoate in Deep Eutectic Solvents. *Eur. J. Lipid Sci. Tech.* **2015,** *117* (2), 161-166.

69. Gorke, J. T.; Srienc, F.; Kazlauskas, R. J., Hydrolase-Catalyzed Biotransformations in Deep Eutectic Solvents. *Chem. Commun.* **2008,** (10), 1235-1237.

70. Siebenhaller, S.; Muhle-Goll, C.; Luy, B.; Kirschhöfer, F.; Brenner-Weiss, G.; Hiller, E.; Günther, M.; Rupp, S.; Zibek, S.; Syldatk, C., Sustainable Enzymatic Synthesis of Glycolipids in a Deep Eutectic Solvent System. *J. Mol. Catal. B: Enzyme* **2016,** *133*, S281-S287.

71. Bakar, P. N. M. A.; Gonawan, F. N.; Kamaruddin, A. H., Parameters Study of Lipase-Transesterification Reaction of Ethyl Caffeate and Glycerol in Deep Eutectic Solvent (Des). *IOP Conference Series: Materials Science and Engineering* **2018,** *440*, 012004.

72. Papadopoulou, A. A.; Tzani, A.; Polydera, A. C.; Katapodis, P.; Voutsas, E.; Detsi, A.; Stamatis, H., Green Biotransformations Catalysed by Enzyme-Inorganic Hybrid Nanoflowers in Environmentally Friendly Ionic Solvents. *Environmental Science and Pollution Research* **2018,** *25* (27), 26707-26714.

73. Dahanayake, J. N.; Mitchell-Koch, K. R., How Does Solvation Layer Mobility Affect Protein Structural Dynamics? *Frontiers in Molecular Biosciences* **2018,** *5* (65).

74. Tzialla, A. A.; Pavlidis, I. V.; Felicissimo, M. P.; Rudolf, P.; Gournis, D.; Stamatis, H., Lipase Immobilization on Smectite Nanoclays: Characterization and Application to the Epoxidation of A-Pinene. *Bioresource Technol.* **2010,** *101* (6), 1587-1594.

75. Zhao, H.; Baker, G. A.; Holmes, S., New Eutectic Ionic Liquids for Lipase Activation and Enzymatic Preparation of Biodiesel. *Org. Biomol. Chem.* **2011,** *9* (6), 1908-1916.

76. Huang, Z.-L.; Wu, B.-P.; Wen, Q.; Yang, T.-X.; Yang, Z., Deep Eutectic Solvents Can Be Viable Enzyme Activators and Stabilizers. *J. Chem. Technol. Biot.* **2014,** *89* (12), 1975-1981.

77. Durand, E.; Lecomte, J.; Baréa, B.; Piombo, G.; Dubreucq, E.; Villeneuve, P., Evaluation of Deep Eutectic Solvents as New Media for Candida Antarctica B Lipase Catalyzed Reactions. *Process Biochem.* **2012,** *47* (12), 2081-2089.

78. Durand, E.; Lecomte, J.; Baréa, B.; Dubreucq, E.; Lortie, R.; Villeneuve, P., Evaluation of Deep Eutectic Solvent–Water Binary Mixtures for Lipase-Catalyzed Lipophilization of Phenolic Acids. *Green Chem.* **2013,** *15* (8), 2275-2282.

79. Cvjetko Bubalo, M.; Jurinjak Tušek, A.; VinkoviĿ, M.; RadoševiĿ, K.; Gaurina SrĿek, V.; RadojĿiĿ Redovnikovi Ŀ, I., Cholinium-Based Deep Eutectic Solvents and Ionic Liquids for Lipase-Catalyzed Synthesis of Butyl Acetate. *J. Mol. Catal. B: Enzyme* **2015,** *122*, 188-198.

80. Lindberg, D.; de la Fuente Revenga, M.; Widersten, M., Deep Eutectic Solvents (Dess) Are Viable Cosolvents for Enzyme-Catalyzed Epoxide Hydrolysis. *Journal of Biotechnology* **2010,** *147* (3), 169-171.

81. Guajardo, N.; Domínguez de María, P.; Ahumada, K.; Schrebler, R. A.; Ramírez-Tagle, R.; Crespo, F. A.; Carlesi, C., Water as Cosolvent: Nonviscous Deep Eutectic Solvents for Efficient Lipase-Catalyzed Esterifications. *ChemCatChem* **2017,** *9* (8), 1393-1396.

82. Guajardo, N.; Schrebler, R. A.; Domínguez de María, P., From Batch to Fed-Batch and to Continuous Packed-Bed Reactors: Lipase-Catalyzed Esterifications in Low Viscous Deep-Eutectic-Solvents with Buffer as Cosolvent. *Bioresource Technol.* **2019,** *273*, 320-325.

83. Hümmer, M.; Kara, S.; Liese, A.; Huth, I.; Schrader, J.; Holtmann, D., Synthesis of (-)-Menthol Fatty Acid Esters in and from (-)-Menthol and Fatty Acids – Novel Concept for Lipase Catalyzed Esterification Based on Eutectic Solvents. *Molecular Catalysis* **2018,** *458*, 67-72.

84. Liang, H.; Qin, X.; Tan, C. P.; Li, D.; Wang, Y., Choline-Chloride-Based Eutectic Solvent for the Efficient Production of Docosahexaenoyl and Eicosapentaenoyl Ethanolamides Via an Enzymatic Process. *J. Agr. Food Chem.* **2018,** *66* (46), 12361-12367.

85. Tian, X. Z., Suoqin; Zheng, Liangyu Enzyme-Catalyzed Henry Reaction in Choline Chloride-Based Deep Eutectic Solvents. *J. Microbiol. Biotechnol.* **2016,** *26* (1), 80-88.

86. González-Martínez, D.; Gotor, V.; Gotor-Fernández, V., Application of Deep Eutectic Solvents in Promiscuous Lipase-Catalysed Aldol Reactions. *Eur. J. Org. Chem.* **2016,** *2016* (8), 1513-1519.

87. Zhou, P.; Wang, X.; Yang, B.; Hollmann, F.; Wang, Y., Chemoenzymatic Epoxidation of Alkenes with Candida Antarctica Lipase B and Hydrogen Peroxide in Deep Eutectic Solvents. *RSC Adv.* **2017,** *7* (21), 12518-12523.

88. Lan, D.; Wang, X.; Zhou, P.; Hollmann, F.; Wang, Y., Deep Eutectic Solvents as Performance Additives in Biphasic Reactions. *RSC Adv.* **2017,** *7* (64), 40367-40370.

89. Ranganathan, S.; Zeitlhofer, S.; Sieber, V., Development of a Lipase-Mediated Epoxidation Process for Monoterpenes in Choline Chloride-Based Deep Eutectic Solvents. *Green Chem.* **2017,** *19* (11), 2576-2586.

90. Zhou, P.; Wang, X.; Zeng, C.; Wang, W.; Yang, B.; Hollmann, F.; Wang, Y., Deep Eutectic Solvents Enable More Robust Chemoenzymatic Epoxidation Reactions. *ChemCatChem* **2017,** *9* (6), 934-936.

91. Yang, S.-L.; Duan, Z.-Q., Insight into Enzymatic Synthesis of Phosphatidylserine in Deep Eutectic Solvents. *Catal. Commun.* **2016,** *82*, 16-19.

92. Kim, S. H.; Park, S.; Yu, H.; Kim, J. H.; Kim, H. J.; Yang, Y.-H.; Kim, Y. H.; Kim, K. J.; Kan, E.; Lee, S. H., Effect of Deep Eutectic Solvent Mixtures on Lipase Activity and Stability. *J. Mol. Catal. B: Enzyme* **2016,** *128*, 65-72.

93. Singh, B.; Lobo, H.; Shankarling, G., Selective N-Alkylation of Aromatic Primary Amines Catalyzed by Bio-Catalyst or Deep Eutectic Solvent. *Catal. Lett.* **2011,** *141* (1), 178-182.

94. Sanap, A. K.; Shankarling, G. S., Eco-Friendly and Recyclable Media for Rapid Synthesis of Tricyanovinylated Aromatics Using Biocatalyst and Deep Eutectic Solvent. *Catal. Commun.* **2014,** *49*, 58-62.

95. Monhemi, H.; Housaindokht, M. R.; Moosavi-Movahedi, A. A.; Bozorgmehr, M. R., How a Protein Can Remain Stable in a Solvent with High Content of Urea: Insights from Molecular Dynamics Simulation of Candida Antarctica Lipase B in Urea : Choline Chloride Deep Eutectic Solvent. *Phys. Chem. Chem. Phys.* **2014,** *16* (28), 14882-14893.

96. Xu, W.-J.; Huang, Y.-K.; Li, F.; Wang, D.-D.; Yin, M.-N.; Wang, M.; Xia, Z.-N., Improving B-Glucosidase Biocatalysis with Deep Eutectic Solvents Based on Choline Chloride. *Biochemical Engineering Journal* **2018,** *138*, 37-46.

97. Juneidi, I.; Hayyan, M.; Hashim, M. A.; Hayyan, A., Pure and Aqueous Deep Eutectic Solvents for a Lipase-Catalysed Hydrolysis Reaction. *Biochemical Engineering Journal* **2017,** *117*, 129-138.

98. Weiz, G.; Braun, L.; Lopez, R.; de María, P. D.; Breccia, J. D., Enzymatic Deglycosylation of Flavonoids in Deep Eutectic Solvents-Aqueous Mixtures: Paving the Way for Sustainable Flavonoid Chemistry. *J. Mol. Catal. B: Enzyme* **2016,** *130*, 70-73.

99. Zhao, H.; Baker, G. A.; Holmes, S., Protease Activation in Glycerol-Based Deep Eutectic Solvents. *J. Mol. Catal. B: Enzyme* **2011,** *72* (3), 163-167.

100. Maugeri, Z.; Leitner, W.; Domínguez de María, P., Chymotrypsin-Catalyzed Peptide Synthesis in Deep Eutectic Solvents. *Eur. J. Org. Chem.* **2013,** *2013* (20), 4223-4228.

101. Maugeri, Z.; Domínguez de María, P., Benzaldehyde Lyase (Bal)-Catalyzed Enantioselective Cc Bond Formation in Deep-Eutectic-Solvents–Buffer Mixtures. *J. Mol. Catal. B: Enzyme* **2014,** *107*, 120-123.

102. Stepankova, V.; Vanacek, P.; Damborsky, J.; Chaloupkova, R., Comparison of Catalysis by Haloalkane Dehalogenases in Aqueous Solutions of Deep Eutectic and Organic Solvents. *Green Chem.* **2014,** *16* (5), 2754-2761.

103. Cicco, L.; Ríos-Lombardía, N.; Rodríguez-Álvarez, M. J.; Morís, F.; Perna, F. M.; Capriati, V.; García-Álvarez, J.; González-Sabín, J., Programming Cascade Reactions Interfacing Biocatalysis with Transition-Metal Catalysis in Deep Eutectic Solvents as Biorenewable Reaction Media. *Green Chem.* **2018,** *20* (15), 3468-3475.

104. Müller, C. R.; Lavandera, I.; Gotor-Fernández, V.; Domínguez de María, P., Performance of Recombinant-Whole-Cell-Catalyzed Reductions in Deep-Eutectic-Solvent–Aqueous-Media Mixtures. *ChemCatChem* **2015,** *7* (17), 2654-2659.

105. Huang, L.; Bittner, J. P.; Domínguez de María, P.; Jakobtorweihen, S.; Kara, S., Modeling Alcohol Dehydrogenase Catalysis in Deep Eutectic Solvent/Water Mixtures. *ChemBioChem* **2020,** *21* (6), 811-817.

106. Khodaverdian, S.; Dabirmanesh, B.; Heydari, A.; Dashtban-moghadam, E.; Khajeh, K.; Ghazi, F., Activity, Stability and Structure of Laccase in Betaine Based Natural Deep Eutectic Solvents. *International Journal of Biological Macromolecules* **2018,** *107*, 2574-2579.

107. Toledo, M. L.; Pereira, M. M.; Freire, M. G.; Silva, J. P. A.; Coutinho, J. A. P.; Tavares, A. P. M., Laccase Activation in Deep Eutectic Solvents. *ACS Sustainable Chem. Eng.* **2019,** *7* (13), 11806-11814.

108. Ríos-Lombardía, N.; Rodríguez-Álvarez, M. J.; Morís, F.; Kourist, R.; Comino, N.; López-Gallego, F.; González-Sabín, J.; García-Álvarez, J., Design of Sustainable One-Pot Chemoenzymatic Organic Transformations in Deep Eutectic Solvents for the Synthesis of 1,2-Disubstituted Aromatic Olefins. *Frontiers in Chemistry* **2020,** *8* (139).

109. Grabner, B.; Schweiger, A. K.; Gavric, K.; Kourist, R.; Gruber-Woelfler, H., A Chemo-Enzymatic Tandem Reaction in a Mixture of Deep Eutectic Solvent and Water in Continuous Flow. *Reaction Chemistry & Engineering* **2020,** *5* (2), 263-269.

110. Maier, M. C.; Valotta, A.; Hiebler, K.; Soritz, S.; Gavric, K.; Grabner, B.; Gruber-Woelfler, H., 3d Printed Reactors for Synthesis of Active Pharmaceutical Ingredients in Continuous Flow. *Organic Process Research & Development* **2020**.

111. Domínguez de María, P.; Maugeri, Z., Ionic Liquids in Biotransformations: From Proof-of-Concept to Emerging Deep-Eutectic-Solvents. *Curr. Opin. Chem. Biol.* **2011,** *15* (2), 220-225.

112. Qiao, Y.; Cai, H.-L.; Yang, X.; Zang, Y.-Y.; Chen, Z.-G., Effects of Natural Deep Eutectic Solvents on Lactic Acid Bacteria Viability During Cryopreservation. *Appl. Microbiol. Biotechnol.* **2018,** *102* (13), 5695-5705.

113. Maugeri, Z.; Domínguez de María, P., Whole-Cell Biocatalysis in Deep-Eutectic-Solvents/Aqueous Mixtures. *ChemCatChem* **2014,** *6* (6), 1535-1537.

114. Vitale, P.; Abbinante, V. M.; Perna, F. M.; Salomone, A.; Cardellicchio, C.; Capriati, V., Unveiling the Hidden Performance of Whole Cells in the Asymmetric Bioreduction of Aryl-Containing Ketones in Aqueous Deep Eutectic Solvents. *Advanced Synthesis & Catalysis* **2017,** *359* (6), 1049-1057.

115. Cvjetko Bubalo, M.; Mazur, M.; Radošević, K.; Radojčić Redovniković, I., Baker's Yeast-Mediated Asymmetric Reduction of Ethyl 3-Oxobutanoate in Deep Eutectic Solvents. *Process Biochem.* **2015,** *50* (11), 1788-1792.

116. Yang, T.-X.; Zhao, L.-Q.; Wang, J.; Song, G.-L.; Liu, H.-M.; Cheng, H.; Yang, Z., Improving Whole-Cell Biocatalysis by Addition of Deep Eutectic Solvents and Natural Deep Eutectic Solvents. *ACS Sustainable Chem. Eng.* **2017,** *5* (7), 5713-5722.

117. Li, J.; Wang, P.; He, Y.-S.; Zhu, Z.-R.; Huang, J., Toward Designing a Novel Oligopeptide-Based Deep Eutectic Solvent: Applied in Biocatalytic Reduction. *ACS Sustainable Chem. Eng.* **2019,** *7* (1), 1318-1326.

118. Xu, P.; Cheng, J.; Lou, W.-Y.; Zong, M.-H., Using Deep Eutectic Solvents to Improve the Resolution of Racemic 1-(4-Methoxyphenyl)Ethanol through Acetobacter Sp. Cctcc M209061 Cell-Mediated Asymmetric Oxidation. *RSC Adv.* **2015,** *5* (9), 6357-6364.

119. Xu, P.; Xu, Y.; Li, X.-F.; Zhao, B.-Y.; Zong, M.-H.; Lou, W.-Y., Enhancing Asymmetric Reduction of 3-Chloropropiophenone with Immobilized Acetobacter Sp. Cctcc M209061 Cells by Using Deep Eutectic Solvents as Cosolvents. *ACS Sustainable Chem. Eng.* **2015,** *3* (4), 718-724.

120. Xu, P.; Du, P.-X.; Zong, M.-H.; Li, N.; Lou, W.-Y., Combination of Deep Eutectic Solvent and Ionic Liquid to Improve Biocatalytic Reduction of 2-Octanone with Acetobacter Pasteurianus Gim1.158 Cell. *Sci. Rep.* **2016,** *6*, 26158.

121. Zdanowicz, M.; Wilpiszewska, K.; Spychaj, T., Deep Eutectic Solvents for Polysaccharides Processing. A Review. *Carbohyd. Polym.* **2018,** *200*, 361-380.

122. Chen, Y.; Mu, T., Application of Deep Eutectic Solvents in Biomass Pretreatment and Conversion. *Green Energy & Environment* **2019,** *4* (2), 95-115.

123. Liu, Z.-H.; Chen, H.-Z., Xylose Production from Corn Stover Biomass by Steam Explosion Combined with Enzymatic Digestibility. *Bioresource Technol.* **2015,** *193*, 345-356.

124. Timung, R.; Mohan, M.; Chilukoti, B.; Sasmal, S.; Banerjee, T.; Goud, V. V., Optimization of Dilute Acid and Hot Water Pretreatment of Different Lignocellulosic Biomass: A Comparative Study. *Biomass and Bioenergy* **2015,** *81*, 9-18.

125. Kim, J. S.; Lee, Y. Y.; Park, S. C., Pretreatment of Wastepaper and Pulp Mill Sludge by Aqueous Ammonia and Hydrogen Peroxide. *Appl Biochem Biotechnol* **2000,** *84* (1), 129-139.

126. Choi, W.-I.; Park, J.-Y.; Lee, J.-P.; Oh, Y.-K.; Park, Y. C.; Kim, J. S.; Park, J. M.; Kim, C. H.; Lee, J.-S., Optimization of Naoh-Catalyzed Steam Pretreatment of Empty Fruit Bunch. *Biotechnology for Biofuels* **2013,** *6* (1), 170.

127. Zhang, C.-W.; Xia, S.-Q.; Ma, P.-S., Facile Pretreatment of Lignocellulosic Biomass Using Deep Eutectic Solvents. *Bioresource Technol.* **2016,** *219*, 1-5.

128. Procentese, A.; Raganati, F.; Olivieri, G.; Russo, M. E.; Rehmann, L.; Marzocchella, A., Low-Energy Biomass Pretreatment with Deep Eutectic Solvents for Bio-Butanol Production. *Bioresource Technol.* **2017,** *243*, 464-473.

129. Yu, Q.; Zhang, A.; Wang, W.; Chen, L.; Bai, R.; Zhuang, X.; Wang, Q.; Wang, Z.; Yuan, Z., Deep Eutectic Solvents from Hemicellulose-Derived Acids for the Cellulosic Ethanol Refining of Akebia' Herbal Residues. *Bioresource Technol.* **2018,** *247*, 705-710.

130. Yu, Q.; Qin, L.; Liu, Y.; Sun, Y.; Xu, H.; Wang, Z.; Yuan, Z., In Situ Deep Eutectic Solvent Pretreatment to Improve Lignin Removal from Garden Wastes and Enhance Production of Bio-Methane and Microbial Lipids. *Bioresource Technol.* **2019,** *271*, 210-217.

131. Soares, B.; Silvestre, A. J. D.; Rodrigues Pinto, P. C.; Freire, C. S. R.; Coutinho, J. A. P., Hydrotropy and Cosolvency in Lignin Solubilization with Deep Eutectic Solvents. *ACS Sustainable Chem. Eng.* **2019,** *7* (14), 12485-12493.

132. Satlewal, A.; Agrawal, R.; Das, P.; Bhagia, S.; Pu, Y.; Puri, S. K.; Ramakumar, S. S. V.; Ragauskas, A. J., Assessing the Facile Pretreatments of Bagasse for Efficient Enzymatic Conversion and Their Impacts on Structural and Chemical Properties. *ACS Sustainable Chem. Eng.* **2019,** *7* (1), 1095-1104.

133. Kumar, A. K.; Parikh, B. S.; Pravakar, M., Natural Deep Eutectic Solvent Mediated Pretreatment of Rice Straw: Bioanalytical Characterization of Lignin Extract and Enzymatic Hydrolysis of Pretreated Biomass Residue. *Environmental Science and Pollution Research* **2016,** *23* (10), 9265-9275.

134. Shen, X.-J.; Wen, J.-L.; Mei, Q.-Q.; Chen, X.; Sun, D.; Yuan, T.-Q.; Sun, R.-C., Facile Fractionation of Lignocelluloses by Biomass-Derived Deep Eutectic Solvent (Des) Pretreatment for Cellulose Enzymatic Hydrolysis and Lignin Valorization. *Green Chem.* **2019,** *21* (2), 275-283.

135. Tan, Y. T.; Ngoh, G. C.; Chua, A. S. M., Effect of Functional Groups in Acid Constituent of Deep Eutectic Solvent for Extraction of Reactive Lignin. *Bioresource Technol.* **2019,** *281*, 359-366.

136. Alvarez-Vasco, C.; Ma, R.; Quintero, M.; Guo, M.; Geleynse, S.; Ramasamy, K. K.; Wolcott, M.; Zhang, X., Unique Low-Molecular-Weight Lignin with High Purity Extracted from Wood by Deep Eutectic Solvents (Des): A Source of Lignin for Valorization. *Green Chem.* **2016,** *18* (19), 5133-5141.

137. Zhang, K.; Pei, Z.; Wang, D., Organic Solvent Pretreatment of Lignocellulosic Biomass for Biofuels and Biochemicals: A Review. *Bioresource Technol.* **2016,** *199*, 21-33.

138. Mamilla, J. L. K.; Novak, U.; Grilc, M.; Likozar, B., Natural Deep Eutectic Solvents (Des) for Fractionation of Waste Lignocellulosic Biomass and Its Cascade Conversion to Value-Added Bio-Based Chemicals. *Biomass and Bioenergy* **2019,** *120*, 417-425.

139. Jablonsky, M.; Majova, V.; Ondrigova, K.; Sima, J., Preparation and Characterization of Physicochemical Properties and Application of Novel Ternary Deep Eutectic Solvents. *Cellulose* **2019,** *26* (5), 3031-3045.

140. Lee, C. B. T. L.; Wu, T. Y.; Ting, C. H.; Tan, J. K.; Siow, L. F.; Cheng, C. K.; Md. Jahim, J.; Mohammad, A. W., One-Pot Furfural Production Using Choline Chloride-Dicarboxylic Acid Based Deep Eutectic Solvents under Mild Conditions. *Bioresource Technol.* **2019,** *278*, 486-489.

141. New, E. K.; Wu, T. Y.; Tien Loong Lee, C. B.; Poon, Z. Y.; Loow, Y.-L.; Wei Foo, L. Y.; Procentese, A.; Siow, L. F.; Teoh, W. H.; Nik Daud, N. N.; Jahim, J. M.; Mohammad, A. W., Potential Use of Pure and Diluted Choline Chloride-Based Deep Eutectic Solvent in Delignification of Oil Palm Fronds. *Process Safety and Environmental Protection* **2019,** *123*, 190-198.

142. Liang, X.; Fu, Y.; Chang, J., Effective Separation, Recovery and Recycling of Deep Eutectic Solvent after Biomass Fractionation with Membrane-Based Methodology. *Separation and Purification Technology* **2019,** *210*, 409-416.

143. Chen, L.; Yu, Q.; Wang, Q.; Wang, W.; Qi, W.; Zhuang, X.; Wang, Z.; Yuan, Z., A Novel Deep Eutectic Solvent from Lignin-Derived Acids for Improving the Enzymatic Digestibility of Herbal Residues from Cellulose. *Cellulose* **2019,** *26* (3), 1947-1959.

144. Lim, W.-L.; Gunny, A. A. N.; Kasim, F. H.; AlNashef, I. M.; Arbain, D., Alkaline Deep Eutectic Solvent: A Novel Green Solvent for Lignocellulose Pulping. *Cellulose* **2019,** *26* (6), 4085-4098.

145. Nagoor Gunny, A. A.; Arbain, D.; Javed, M.; Baghaei-Yazdi, N.; Gopinath, S. C. B.; Jamal, P., Deep Eutectic Solvents-Halophilic Cellulase System: An Efficient Route for in Situ Saccharification of Lignocellulose. *Process Biochem.* **2019,** *81*, 99-103.

146. Chen, Z.; Jacoby, W. A.; Wan, C., Ternary Deep Eutectic Solvents for Effective Biomass Deconstruction at High Solids and Low Enzyme Loadings. *Bioresource Technol.* **2019,** *279*, 281-286.

147. Xu, G.-C.; Ding, J.-C.; Han, R.-Z.; Dong, J.-J.; Ni, Y., Enhancing Cellulose Accessibility of Corn Stover by Deep Eutectic Solvent Pretreatment for Butanol Fermentation. *Bioresource Technol.* **2016,** *203*, 364-369.

148. Hou, X.-D.; Feng, G.-J.; Ye, M.; Huang, C.-M.; Zhang, Y., Significantly Enhanced Enzymatic Hydrolysis of Rice Straw Via a High-Performance Two-Stage Deep Eutectic Solvents Synergistic Pretreatment. *Bioresource Technol.* **2017,** *238*, 139-146.

149. Hou, X.-D.; Xu, J.; Li, N.; Zong, M.-H., Effect of Anion Structures on Cholinium Ionic Liquids Pretreatment of Rice Straw and the Subsequent Enzymatic Hydrolysis. *Biotechnol. Bioeng.* **2015,** *112* (1), 65-73.

150. Hou, X.-D.; Li, A.-L.; Lin, K.-P.; Wang, Y.-Y.; Kuang, Z.-Y.; Cao, S.-L., Insight into the Structure-Function Relationships of Deep Eutectic Solvents During Rice Straw Pretreatment. *Bioresource Technol.* **2018,** *249*, 261-267.

151. D'Agostino, C.; Harris, R. C.; Abbott, A. P.; Gladden, L. F.; Mantle, M. D., Molecular Motion and Ion Diffusion in Choline Chloride Based Deep Eutectic Solvents Studied by 1h Pulsed Field Gradient Nmr Spectroscopy. *Phys. Chem. Chem. Phys.* **2011,** *13* (48), 21383-21391.

152. Lynam, J. G.; Kumar, N.; Wong, M. J., Deep Eutectic Solvents' Ability to Solubilize Lignin, Cellulose, and Hemicellulose; Thermal Stability; and Density. *Bioresource Technol.* **2017,** *238*, 684-689.

153. Morrison, H. G.; Sun, C. C.; Neervannan, S., Characterization of Thermal Behavior of Deep Eutectic Solvents and Their Potential as Drug Solubilization Vehicles. *Int. J. Pharm.* **2009,** *378* (1), 136-139.

154. Li, Z.; Lee, P. I., Investigation on Drug Solubility Enhancement Using Deep Eutectic Solvents and Their Derivatives. *Int. J. Pharm.* **2016,** *505* (1), 283-288.

155. Lu, C.; Cao, J.; Wang, N.; Su, E., Significantly Improving the Solubility of Non-Steroidal Anti-Inflammatory Drugs in Deep Eutectic Solvents for Potential Non-Aqueous Liquid Administration. *MedChemComm* **2016,** *7* (5), 955-959.

156. Smith, K. B.; Bridson, R. H.; Leeke, G. A., Solubilities of Pharmaceutical Compounds in Ionic Liquids. *J. Chem. Eng. Data* **2011,** *56* (5), 2039-2043.

157. Shekaari, H.; Zafarani-Moattar, M. T.; Mokhtarpour, M., Solubility, Volumetric and Compressibility Properties of Acetaminophen in Some Aqueous Solutions of Choline Based Deep Eutectic Solvents at T=(288.15 to 318.15) K. *European Journal of Pharmaceutical Sciences* **2017,** *109*, 121-130.

158. Shekaari, H.; Zafarani-Moattar, M. T.; Shayanfar, A.; Mokhtarpour, M., Effect of Choline Chloride/Ethylene Glycol or Glycerol as Deep Eutectic Solvents on the Solubility and Thermodynamic Properties of Acetaminophen. *J. Mol. Liq.* **2018,** *249*, 1222-1235.

159. Mokhtarpour, M.; Shekaari, H.; Martinez, F.; Zafarani-Moattar, M. T., Study of Naproxen in Some Aqueous Solutions of Choline-Based Deep Eutectic Solvents: Solubility Measurements, Volumetric and Compressibility Properties. *Int. J. Pharm.* **2019,** *564*, 197-206.

160. Shekaari, H.; Zafarani-Moattar, M. T.; Mokhtarpour, M.; Faraji, S., Exploring Cytotoxicity of Some Choline-Based Deep Eutectic Solvents and Their Effect on the Solubility of Lamotrigine in Aqueous Media. *J. Mol. Liq.* **2019,** *283*, 834-842.

161. Olivares, B.; Martínez, F.; Rivas, L.; Calderón, C.; M. Munita, J.; R. Campodonico, P., A Natural Deep Eutectic Solvent Formulated to Stabilize B-Lactam Antibiotics. *Sci. Rep.* **2018,** *8* (1), 14900.

162. Shamseddin, A.; Crauste, C.; Durand, E.; Villeneuve, P.; Dubois, G.; Durand, T.; Vercauteren, J.; Veas, F., Resveratrol Formulated with a Natural Deep Eutectic Solvent Inhibits Active Matrix Metalloprotease-9 in Hormetic Conditions. *Eur. J. Lipid Sci. Tech.* **2017,** *119* (11), 1700171.

163. Maisch, T., Resistance in Antimicrobial Photodynamic Inactivation of Bacteria. *Photoch. Photobio. Sci.* **2015,** *14* (8), 1518-1526.

164. Wikene, K. O.; Bruzell, E.; Tønnesen, H. H., Improved Antibacterial Phototoxicity of a Neutral Porphyrin in Natural Deep Eutectic Solvents. *Journal of Photochemistry and Photobiology B: Biology* **2015,** *148*, 188-196.

165. Wikene, K. O.; Rukke, H. V.; Bruzell, E.; Tønnesen, H. H., Investigation of the Antimicrobial Effect of Natural Deep Eutectic Solvents (Nades) as Solvents in Antimicrobial Photodynamic Therapy. *Journal of Photochemistry and Photobiology B: Biology* **2017,** *171*, 27-33.

166. Wikene, K. O.; Rukke, H. V.; Bruzell, E.; Tønnesen, H. H., Physicochemical Characterisation and Antimicrobial Phototoxicity of an Anionic Porphyrin in Natural Deep Eutectic Solvents. *Eur. J. Pharm. Biopharm.* **2016,** *105*, 75-84.

167. Xu, Z.; Liu, S.; Kang, Y.; Wang, M., Glutathione-Responsive Polymeric Micelles Formed by a Biodegradable Amphiphilic Triblock Copolymer for Anticancer Drug Delivery and Controlled Release. *ACS Biomaterials Science & Engineering* **2015,** *1* (7), 585-592.

168. Mao, J.; Li, Y.; Wu, T.; Yuan, C.; Zeng, B.; Xu, Y.; Dai, L., A Simple Dual-Ph Responsive Prodrug-Based Polymeric Micelles for Drug Delivery. *ACS Appl. Mater. Interfaces* **2016,** *8* (27), 17109-17117.

169. Pradeepkumar, P.; Elgorban, A. M.; Bahkali, A. H.; Rajan, M., Natural Solvent-Assisted Synthesis of Amphiphilic Co-Polymeric Nanomicelles for Prolonged Release of Camptothecin Delivery. *New J. Chem.* **2018,** *42* (12), 10366-10375.

170. Pradeepkumar, P.; Rajendran, N. K.; Alarfaj, A. A.; Munusamy, M. A.; Rajan, M., Deep Eutectic Solvent-Mediated Fa-G-B-Alanine-Co-Pcl Drug Carrier for Sustainable and Site-Specific Drug Delivery. *ACS Applied Bio Materials* **2018,** *1* (6), 2094-2109.

171. Mukesh, C.; Upadhyay, K. K.; Devkar, R. V.; Chudasama, N. A.; Raol, G. G.; Prasad, K., Preparation of a Noncytotoxic Hemocompatible Ion Gel by Self-Polymerization of Hema in a Green Deep Eutectic Solvent. *Macromol. Chem. Physic.* **2016,** *217* (17), 1899-1906.

172. Moghadam, A. G.; Rajabi, M.; Asghari, A., Efficient and Relatively Safe Emulsification Microextraction Using a Deep Eutectic Solvent for Influential Enrichment of Trace Main Anti-Depressant Drugs from Complicated Samples. *Journal of Chromatography B* **2018,** *1072*, 50-59.

173. Rajabi, M.; Ghassab, N.; Hemmati, M.; Asghari, A., Emulsification Microextraction of Amphetamine and Methamphetamine in Complex Matrices Using an up-to-Date Generation of Eco-Friendly and Relatively Hydrophobic Deep Eutectic Solvent. *J. Chromatogr. A* **2018,** *1576*, 1-9.

174. Rajabi, M.; Ghassab, N.; Hemmati, M.; Asghari, A., Highly Effective and Safe Intermediate Based on Deep Eutectic Medium for Carrier Less-Three Phase Hollow Fiber Microextraction of Antiarrhythmic Agents in Complex Matrices. *Journal of Chromatography B* **2019,** *1104*, 196-204.

175. Li, G.; Zhu, T.; Row, K. H., Deep Eutectic Solvents for the Purification of Chloromycetin and Thiamphenicol from Milk. *Journal of Separation Science* **2017,** *40* (3), 625-634.

176. Tang, W.; Dai, Y.; Row, K. H., Evaluation of Fatty Acid/Alcohol-Based Hydrophobic Deep Eutectic Solvents as Media for Extracting Antibiotics from Environmental Water. *Anal. Bioanal. Chem.* **2018,** *410* (28), 7325-7336.

177. Wang, R.; Li, W.; Chen, Z., Solid Phase Microextraction with Poly(Deep Eutectic Solvent) Monolithic Column Online Coupled to Hplc for Determination of Non-Steroidal Anti-Inflammatory Drugs. *Anal. Chim. Acta* **2018,** *1018*, 111-118.

178. Racamonde, I.; Rodil, R.; Quintana, J. B.; Sieira, B. J.; Kabir, A.; Furton, K. G.; Cela, R., Fabric Phase Sorptive Extraction: A New Sorptive Microextraction Technique for the Determination of Non-Steroidal Anti-Inflammatory Drugs from Environmental Water Samples. *Anal. Chim. Acta* **2015,** *865*, 22-30.

179. Lyu, D.-Y.; Yang, C.-X.; Yan, X.-P., Fabrication of Aluminum Terephthalate Metal-Organic Framework Incorporated Polymer Monolith for the Microextraction of Non-Steroidal Anti-Inflammatory Drugs in Water and Urine Samples. *J. Chromatogr. A* **2015,** *1393*, 1-7.

180. Stott, P. W.; Williams, A. C.; Barry, B. W., Transdermal Delivery from Eutectic Systems: Enhanced Permeation of a Model Drug, Ibuprofen. *J. Controlled Release* **1998,** *50* (1), 297-308.

181. Aroso, I. M.; Silva, J. C.; Mano, F.; Ferreira, A. S. D.; Dionísio, M.; Sá-Nogueira, I.; Barreiros, S.; Reis, R. L.; Paiva, A.; Duarte, A. R. C., Dissolution Enhancement of Active Pharmaceutical Ingredients by Therapeutic Deep Eutectic Systems. *Eur. J. Pharm. Biopharm.* **2016,** *98*, 57-66.

182. Duarte, A. R. C.; Ferreira, A. S. D.; Barreiros, S.; Cabrita, E.; Reis, R. L.; Paiva, A., A Comparison between Pure Active Pharmaceutical Ingredients and Therapeutic Deep

Eutectic Solvents: Solubility and Permeability Studies. *Eur. J. Pharm. Biopharm.* **2017,** *114*, 296-304.

183. Santos, F.; P.S. Leitão, M. I.; C. Duarte, A. R., Properties of Therapeutic Deep Eutectic Solvents of L-Arginine and Ethambutol for Tuberculosis Treatment. *Molecules* **2018,** *24* (1), 55.

184. Gutiérrez, A.; Aparicio, S.; Atilhan, M., Design of Arginine-Based Therapeutic Deep Eutectic Solvents as Drug Solubilization Vehicles for Active Pharmaceutical Ingredients. *Phys. Chem. Chem. Phys.* **2019,** *21* (20), 10621-10634.

185. Gutiérrez, A.; Atilhan, M.; Aparicio, S., A Theoretical Study on Lidocaine Solubility in Deep Eutectic Solvents. *Phys. Chem. Chem. Phys.* **2018,** *20* (43), 27464-27473.

186. Abbott, A. P.; Ahmed, E. I.; Prasad, K.; Qader, I. B.; Ryder, K. S., Liquid Pharmaceuticals Formulation by Eutectic Formation. *Fluid Phase Equilibria* **2017,** *448*, 2-8.

187. Wang, H.; Gurau, G.; Shamshina, J.; Cojocaru, O. A.; Janikowski, J.; MacFarlane, D. R.; Davis, J. H.; Rogers, R. D., Simultaneous Membrane Transport of Two Active Pharmaceutical Ingredients by Charge Assisted Hydrogen Bond Complex Formation. *Chem. Sci.* **2014,** *5* (9), 3449-3456.

188. Amsden, B. G., Biodegradable Elastomers in Drug Delivery. *Expert Opinion on Drug Delivery* **2008,** *5* (2), 175-187.

189. Martins, M.; Aroso, I. M.; Reis, R. L.; Duarte, A. R. C.; Craveiro, R.; Paiva, A., Enhanced Performance of Supercritical Fluid Foaming of Natural-Based Polymers by Deep Eutectic Solvents. *AIChE Journal* **2014,** *60* (11), 3701-3706.

190. Aroso, I. M.; Craveiro, R.; Rocha, Â.; Dionísio, M.; Barreiros, S.; Reis, R. L.; Paiva, A.; Duarte, A. R. C., Design of Controlled Release Systems for Thedes—Therapeutic Deep Eutectic Solvents, Using Supercritical Fluid Technology. *Int. J. Pharm.* **2015,** *492* (1), 73-79.

191. Silva, J. M.; Reis, R. L.; Paiva, A.; Duarte, A. R. C., Design of Functional Therapeutic Deep Eutectic Solvents Based on Choline Chloride and Ascorbic Acid. *ACS Sustainable Chem. Eng.* **2018,** *6* (8), 10355-10363.

192. Yang, J.; Webb, A. R.; Ameer, G. A., Novel Citric Acid-Based Biodegradable Elastomers for Tissue Engineering. *Adv. Mater.* **2004,** *16* (6), 511-516.

193. Serrano, M. C.; Gutiérrez, M. C.; Jiménez, R.; Ferrer, M. L.; Monte, F. d., Synthesis of Novel Lidocaine-Releasing Poly(Diol-Co-Citrate) Elastomers by Using Deep Eutectic Solvents. *Chem. Commun.* **2012,** *48* (4), 579-581.

194. Mukesh, C.; Mondal, D.; Sharma, M.; Prasad, K., Choline Chloride–Thiourea, a Deep Eutectic Solvent for the Production of Chitin Nanofibers. *Carbohyd. Polym.* **2014,** *103*, 466-471.

195. Feng, M.; Lu, X.; Zhang, J.; Li, Y.; Shi, C.; Lu, L.; Zhang, S., Direct Conversion of Shrimp Shells to O-Acylated Chitin with Antibacterial and Anti-Tumor Effects by Natural Deep Eutectic Solvents. *Green Chem.* **2019,** *21* (1), 87-98.

196. Zhao, D.; Huang, W.-C.; Guo, N.; Zhang, S.; Xue, C.; Mao, X., Two-Step Separation of Chitin from Shrimp Shells Using Citric Acid and Deep Eutectic Solvents with the Assistance of Microwave. *Polymers (Basel)* **2019,** *11* (3), 409.

197. Zakrewsky, M.; Banerjee, A.; Apte, S.; Kern, T. L.; Jones, M. R.; Sesto, R. E. D.; Koppisch, A. T.; Fox, D. T.; Mitragotri, S., Choline and Geranate Deep Eutectic Solvent as a Broad-Spectrum Antiseptic Agent for Preventive and Therapeutic Applications. *Adv. Healthc. Mater.* **2016,** *5* (11), 1282-1289.

198. Ibsen, K. N.; Ma, H.; Banerjee, A.; Tanner, E. E. L.; Nangia, S.; Mitragotri, S., Mechanism of Antibacterial Activity of Choline-Based Ionic Liquids (Cage). *ACS Biomaterials Science & Engineering* **2018,** *4* (7), 2370-2379.

199. Dharamdasani, V.; Mandal, A.; Qi, Q. M.; Suzuki, I.; Bentley, M. V. L. B.; Mitragotri, S., Topical Delivery of Sirna into Skin Using Ionic Liquids. *J. Controlled Release* **2020,** *323*, 475-482.

200. Tanner, E. E. L.; Curreri, A. M.; Balkaran, J. P. R.; Selig-Wober, N. C.; Yang, A. B.; Kendig, C.; Fluhr, M. P.; Kim, N.; Mitragotri, S., Design Principles of Ionic Liquids for Transdermal Drug Delivery. *Adv. Mater.* **2019,** *31* (27), 1901103.

201. Banerjee, A.; Ibsen, K.; Iwao, Y.; Zakrewsky, M.; Mitragotri, S., Transdermal Protein Delivery Using Choline and Geranate (Cage) Deep Eutectic Solvent. *Adv. Healthc. Mater.* **2017,** *6* (15), 1601411.

202. Banerjee, A.; Ibsen, K.; Brown, T.; Chen, R.; Agatemor, C.; Mitragotri, S., Ionic Liquids for Oral Insulin Delivery. *Proc. Natl. Acad. Sci. U.S.A* **2018,** *115* (28), 7296-7301.

203. Peng, K.; Shi, Y.; LaBarbiera, A.; Mitragotri, S., Mucoadhesive Ionic Liquid Gel Patches for Oral Delivery. *ACS Biomaterials Science & Engineering* **2020**.

204. Qi, Q. M.; Mitragotri, S., Mechanistic Study of Transdermal Delivery of Macromolecules Assisted by Ionic Liquids. *J. Controlled Release* **2019,** *311-312*, 162-169.

205. Tanner, E. E. L.; Ibsen, K. N.; Mitragotri, S., Transdermal Insulin Delivery Using Choline-Based Ionic Liquids (Cage). *J. Controlled Release* **2018,** *286*, 137-144.

206. Shi, Y.; Zhao, Z.; Gao, Y.; Pan, D. C.; Salinas, A. K.; Tanner, E. E. L.; Guo, J.; Mitragotri, S., Oral Delivery of Sorafenib through Spontaneous Formation of Ionic Liquid Nanocomplexes. *J. Controlled Release* **2020,** *322*, 602-609.

207. Vaidya, A.; Mitragotri, S., Ionic Liquid-Mediated Delivery of Insulin to Buccal Mucosa. *J. Controlled Release* **2020,** *327*, 26-34.

208. Gutiérrez, M. C.; Rubio, F.; del Monte, F., Resorcinol-Formaldehyde Polycondensation in Deep Eutectic Solvents for the Preparation of Carbons and Carbon−Carbon Nanotube Composites. *Chem. Mater.* **2010,** *22* (9), 2711-2719.

209. Mukesh, C.; Gupta, R.; Srivastava, D. N.; Nataraj, S. K.; Prasad, K., Preparation of a Natural Deep Eutectic Solvent Mediated Self Polymerized Highly Flexible Transparent Gel Having Super Capacitive Behaviour. *RSC Adv.* **2016,** *6* (34), 28586-28592.

210. Marullo, S.; Meli, A.; Giannici, F.; D'Anna, F., Supramolecular Eutecto Gels: Fully Natural Soft Materials. *ACS Sustainable Chem. Eng.* **2018,** *6* (10), 12598-12602.

211. Qin, H.; Owyeung, R. E.; Sonkusale, S. R.; Panzer, M. J., Highly Stretchable and Nonvolatile Gelatin-Supported Deep Eutectic Solvent Gel Electrolyte-Based Ionic Skins for Strain and Pressure Sensing. *J. Mater. Chem. C* **2019,** *7* (3), 601-608.

212. Smith, C. J.; Wagle, D. V.; Bhawawet, N.; Gehrke, S.; Hollóczki, O.; Pingali, S. V.; O'Neill, H.; Baker, G. A., Combined Small-Angle Neutron Scattering, Diffusion Nmr, and Molecular Dynamics Study of a Eutectogel: Illuminating the Dynamical Behavior of Glyceline Confined in Bacterial Cellulose Gels. *J. Phys. Chem. B* **2020,** *124* (35), 7647-7658.

213. Niknaddaf, F.; Shahangian, S. S.; Heydari, A.; Hosseinkhani, S.; Sajedi, R. H., Deep Eutectic Solvents as a New Generation of Chemical Chaperones. *ChemistrySelect* **2018,** *3* (38), 10603-10607.

214. Nardecchia, S.; Gutiérrez, M. C.; Ferrer, M. L.; Alonso, M.; López, I. M.; Rodríguez-Cabello, J. C.; del Monte, F., Phase Behavior of Elastin-Like Synthetic Recombinamers in Deep Eutectic Solvents. *Biomacromolecules* **2012,** *13* (7), 2029-2036.

Chapter 2: Calorimetric Evaluation of the Operational Thermal Stability of Ribonuclease A in Hydrated Deep Eutectic Solvents†

†This chapter is based on a published manuscript in ACS Sustainable Chem. Eng. The information contained herein is adapted with permission from **Kist, J. A.**; Henzl, M. T.; Bañuelos, J. L.; and Baker, G. A., Calorimetric Evaluation of the Operational Thermal Stability of Ribonuclease A in Hydrated Deep Eutectic Solvents. ACS Sustainable Chem. Eng. **2019**, 7, 12682-12687. Copyright © 2019 American Chemical Society.

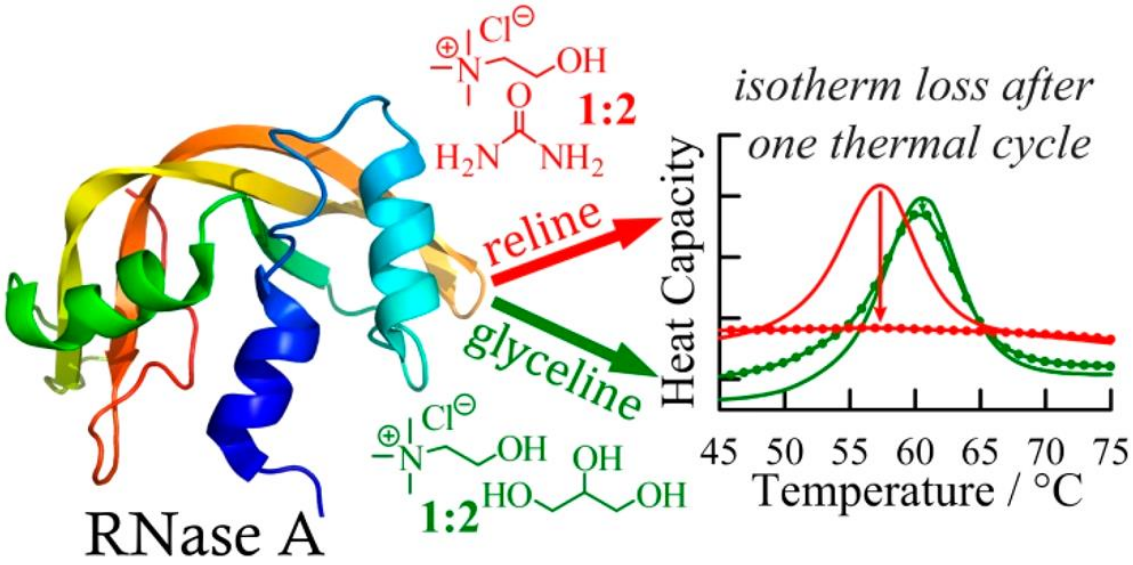

Scheme 2.1 Graphical abstract showing the thermodynamic differences in RNase A when it interacts with various deep eutectic solvents.

Abstract

Deep eutectic solvents (DESs), and particularly their mixtures with water, have been postulated as progressive, sustainable biocatalytic media. Currently, however, knowledge of biomolecular stability within DES media, such as protein folding reversibility, remains quite limited. In this chapter, we present the findings of a study of bovine ribonuclease A (RNase A) unfolding/refolding within aqueous media containing 5−35 wt% of illustrative DESs comprising 1:2 molar ratios of choline chloride plus urea (so-called reline), ethylene glycol (ethaline), or glycerol (glyceline). Using differential scanning calorimetry, iterative thermal cycling of RNase A in the presence of reline is shown to result in rapid and complete loss in folding reversibility, tentatively linked to ammonia evolution, whereas the addition of glyceline actually improves the RNase A thermodynamic stability beyond the native, purely aqueous milieu.

Introduction

Solvent engineering to improve upon the biomolecular activity and stability displayed in the natural, aqueous milieu remains a topic of great interest both in academe and industry.[1] Ionic liquid-based media have received considerable interest for their ability to intensify biocatalytic capabilities in terms of improved enantioselectivity, reusability, thermal stability, and substrate promiscuity, among other areas.[1-10] Despite substantial developments, the appeal of ionic liquids is sometimes hampered by legitimate concerns over cytotoxicity and biodegradability, as well as obstacles related to the economic viability of certain classes of ionic liquids,[11-13] although the development of low-cost ionic liquids is an active area of inquiry.[14]

Deep eutectic solvents (DESs) are beginning to attract attention as sustainable solvents for biotransformations,[15] biocomposite synthesis,[16] and the extraction of biomolecules and bioactive phytochemicals.[17-18] The most commonly studied DESs comprise a quaternary ammonium salt paired with a hydrogen bond donor species to yield a eutectic mixture displaying a melting point depressed well below that of the individual constituents.[19] Significantly, DESs share a number of attractive solvent features in common with ionic liquids (*e.g.*, tunability, low volatility, wide electrochemical window), in addition to offering certain additional advantages in terms of favorable economics, cytotoxicity, biodegradability, and ease of synthesis, making them attractive for large-scale applications.[20-27] Besides, environmentally benign cosolvents can be added alongside DESs to yield interesting properties of DES based solubilizing media.[28] Esquembre *et al.* were among the first to study protein thermostability in DESs, using circular dichroism (CD) spectroscopy to probe the thermal (un)folding behavior of hen egg white lysozyme in two popular cholinium-based DESs, choline chloride: urea (*i.e.*, reline) and choline chloride: glycerol (*i.e.*, glyceline), employing 1:2 molar ratios in both cases.[7] Upon thermal treatment of lysozyme, CD spectra confirmed a stable secondary structure and largely reversible tertiary structural changes within glyceline, while both secondary and tertiary structures were irreversibly lost upon heating for lysozyme dissolved in reline. Ultimately, the authors decided that reline qualitatively destabilized the protein, whereas glyceline improved stability, although the underlying mechanism and energetics remain unknown.

Xin *et al.* investigated the thermostability of lysozyme in a DES composed of trehalose and choline chloride.[29] Differential scanning calorimetry (DSC) measurements performed from 30 to 90°C were used to evaluate the thermostability of lysozyme in water

containing 25 and 50 wt% 3:1 choline chloride: trehalose. The DSC-determined transition temperature (T_m) for lysozyme in water was reported to be 70.2°C, while the protein showed transition temperatures of 74.4 and 80.6°C in 25 and 50 wt% DES, respectively. The conformations of lysozyme and bovine serum albumin were recently determined by Sanchez-Fernandez and co-workers using small-angle neutron scattering (SANS).[30] It was concluded that in the case of a hydrated DES, water may form a solvation shell around active sites, allowing the protein to adopt a more native conformation with better retention of enzyme activity. As another example, Wu *et al.* used fluorescence and CD spectroscopies to examine the stability and structure of horseradish peroxidase in cholinium-based DESs.[31] Overall, the protein activity was apparently favored in choline chloride-based DESs over their choline acetate analogues. While these studies have made important contributions to our understanding, direct measures of the thermodynamic stability for any biomolecule within a DES system remain elusive.

In this chapter, we make the first step toward spanning this knowledge gap by offering a preliminary examination of the energetics of protein folding using bovine ribonuclease A (RNase A) as a biomolecular model in hydrated DESs using calorimetry, the only tool available for the direct measurement of thermodynamics. A small, single-domain enzyme containing 124 amino acid residues (13.6 kDa), RNase A represents one of the most rigorously studied proteins,[1, 32-35] including past investigations in ionic liquid media, offering useful benchmarks for comparison. For example, inspired by seminal work by von Hippel and Wong elucidating thermal stability effects of various salts on RNase A,[34] Weingärtner and co-workers used DSC to systematically investigate the impact of

various cation−anion pairings on the thermostability of RNase A in aqueous imidazolium halides.[1, 33]

In the current study, three cholinium-based DESs were investigated, namely, those comprising 1:2 molar mixtures of choline chloride: urea (reline), choline chloride: ethylene glycol (ethaline), and choline chloride: glycerol (glyceline).[20, 35-36] These three examples represent the most popular DESs being studied currently and are completely miscible with water in all proportions. RNase A unfolding and refolding were monitored using DSC at several DES levels in water (5, 10, 20, 25, and 35 wt%) over multiple heating/cooling cycles. The experimental RNase A concentration used was consistently in the 3.5−4.7 mg mL^{-1} range (complete sample details are supplied in Tables A.1 and A.2). The unfolding transitions were analyzed using a two-state model to extract estimates of the thermal transition temperature (T_m) and van't Hoff enthalpy (ΔH_{vH}). The unfolding/refolding of RNase A in aqueous solutions of the individual DES components (*i.e.*, urea, ethylene glycol, glycerol, and choline chloride), at concentrations corresponding to their contents in 5 and 35 wt% solutions of the respective DESs, were also studied for comparison. DSC experiments demonstrate that RNase A is increasingly stabilized at higher ethaline and glyceline contents relative to the protein in water. In contrast, RNase A is completely denatured under thermal cycling in aqueous solutions containing more than 5 wt% reline. As a benchmark, DSC analysis was also performed for RNase A in water containing 25 wt% 1-butyl-3-methylimidazoliumchloride ([bmim]Cl) since this ionic liquid has previously been reported to be as potent a denaturant as the well-known guanidine hydrochloride on a molar basis.[1, 9-10]

Experimental

Materials and reagents

Ribonuclease A from bovine pancreas (RNase A) (R5500, ≥ 90%), ammonium acetate (238074,97%), and 1,3-dimethylurea (15450, ≥ 99%) were purchased from Sigma-Aldrich (St. Louis, MO). Reline (1:2 choline chloride: urea), ethaline (1:2 choline chloride: ethylene glycol), and glyceline (1:2 choline chloride: glycerol) were prepared following previously reported procedures. For the individual component studies, urea (U5378), ethylene glycol (P3015), and glycerol (G9012, ≥ 99.5%) were obtained from Sigma-Aldrich. Choline chloride (99%) was purchased from Acros Organic (Morris Plains, NJ). Cellulose dialysis membrane with molecular weight cut off (MWCO) of 8 kDa (Spectra/Por® 7, 132116) was acquired from Spectrum Labs (Rancho Dominguez, CA). All chemicals were used as received and all experiments were performed using Ultrapure Millipore water (18.2 MΩ cm).

Methods

A stock solution of 10 mg mL^{-1} RNase A was used throughout all experiments. Briefly, 1.0 mL of various concentrations of deep eutectic solvents (DESs; 5, 10, 20, 25, and 35 wt%), denoted as the reference, was dialyzed against a solution comprising 0.5 mL of 10 mg mL^{-1} RNase A plus 0.5 mL of DES at twice the desired wt%. For example, for dialysis of RNase A in 35 wt% glyceline, one side of the dialysis chamber held 1.0 mL of 35 wt% glyceline (reference) and the other side contained 0.5 mL of 10 mg mL^{-1} RNase A and 0.5 mL of 70 wt% glyceline (sample). The set up was dialyzed for at least 12 h at 4°C. Once dialyzed, differential scanning calorimetry (DSC) was performed on both the sample and the reference with a heating/cooling range of 10–80°C, with a scan rate of 1°C min^{-1} and

a constant pressure of 2.5 atm. The protein scans were background corrected for DES by subtraction of DES-only scans obtained under the same conditions. For the individual component studies, the procedure and dialysis were performed similarly, studying urea, ethylene glycol, glycerol, and choline chloride. The wt% (5 or 35) for the individual component was considered as per its respective wt% DES; *i.e.,* urea as per 35 wt% reline.

For the 1-butyl-3-methylimidazolium chloride ([bmim]Cl) study, the ionic liquid was synthesized following an earlier report. A 1.0 mL solution of 25 wt% [bmim]Cl was dialyzed (MWCO: 8 kDa) against 0.5 mL of 10 mg mL^{-1} RNase A solution plus 0.5 mL of 50 wt% [bmim]Cl for at least 12 h at 4°C. For 25 wt% [bmim]Cl, the equivalent molar concentration was 1.43 M. Following dialysis, DSC was performed as described earlier.

For the ammonium acetate control study, a 50 mM ammonium acetate and 25 wt% reline stock (equivalent molar concentration was 0.96 M) solution was made. 5 mL of the stock solution was added to 25 mg RNase A to give a protein concentration before dialysis of 5 mg mL^{-1}. A 1.0 mL aliquot of the stock solution was dialyzed against the protein-stock solution for at least 12 h at 4°C. After dialysis, the procedure was the same as mentioned above. The procedure was followed in the same manner with 1.0 M ammonium acetate.

For the direline study, the DES of choline chloride:1,3-dimethylurea (1:2, 25 wt%) was synthesized in the lab. A 1.0 mL solution of 25 wt% direline was dialyzed against 0.5 mL of 10 mg mL^{-1} RNase A solution plus 0.5 mL of 50 wt% direline for at least 12 h at 4°C. After dialysis, the DSC measurements proceeded in the same manner as mentioned above.

Instrumentation

To determine the final RNase A concentration following dialysis, absorbance spectra were measured in quartz cuvettes using a Cary Bio 50 UV-Vis spectrophotometer scanning from 800–200 nm, using a medium scan speed of 600 nm min^{-1}. Beer's law was used to calculate the final concentration of RNase A after dialysis, using the absorbance at 278 nm, a 0.2 cm pathlength, and an extinction coefficient of 0.72 mg mL^{-1} cm^{-1}. The protein concentration ranged from 3.5-4.5 mg mL^{-1}. Thermal transitions were characterized by differential scanning calorimetry (DSC) using a CSC 5100 Nano Differential Scanning Calorimeter and the calorimetric data were analyzed using the program CpCalc (Calorimetry Sciences Corp, Lindon, UT).

Results and Discussion

Figure 2.1 displays consecutive heating and cooling DSC scans between 10 and 80°C for RNase A in 5 wt% aqueous ethaline, glyceline, and reline. Thermal unfolding is highly reversible in the ethaline and glyceline systems. For these samples, the shapes of the DSC profiles are symmetric and can be fitted to two-state unfolding model. The endothermic unfolding transition is followed by an exothermic refolding transition of comparable magnitude during the subsequent cooling scan. The traces are characterized only by the peak for RNase A (un)folding at different temperatures. The minor losses in experimental heat capacity observed during successive cycles reflect a small degree of irreversible protein unfolding. In contrast, as illustrated in Figure 2.1C, the 5 wt% reline exerts a significant impact on RNase A thermal unfolding behavior, revealing an irreversible loss of the majority of the protein after a single thermal cycle and complete deactivation within four cycles.

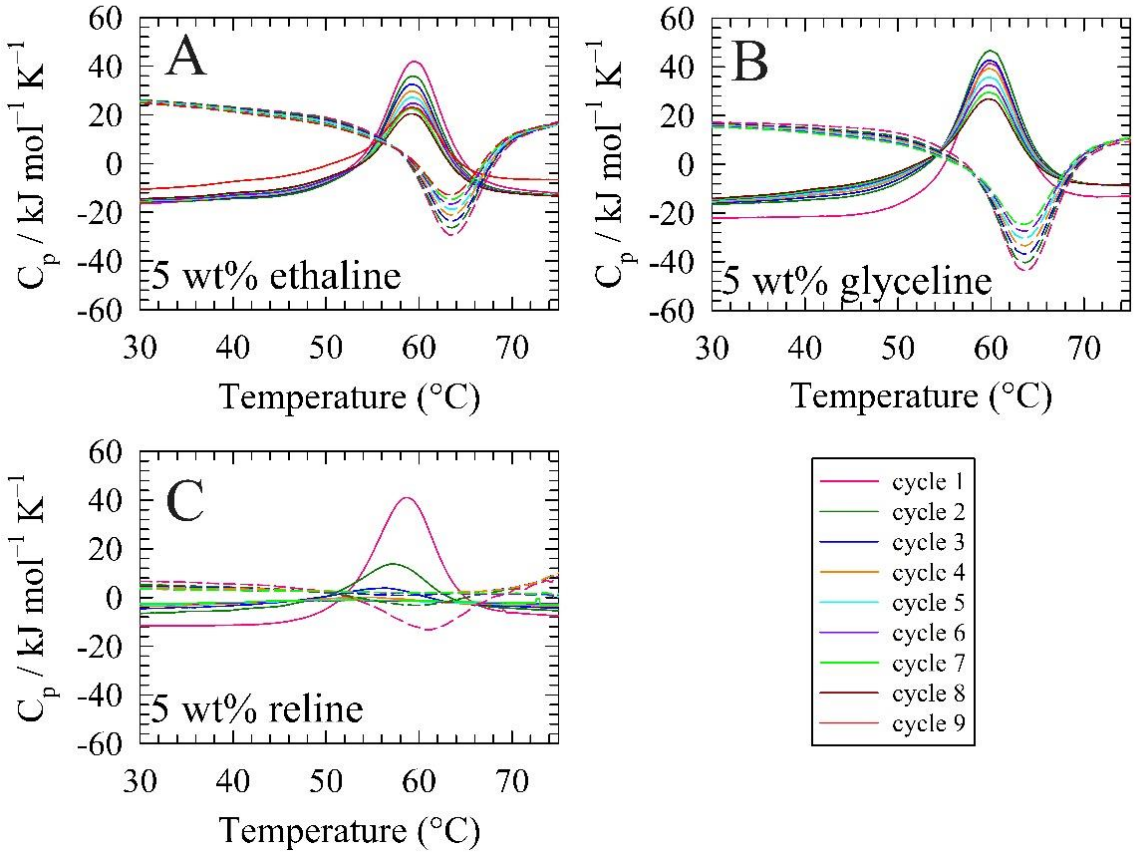

Figure 2.1 DSC scans for RNase A in 5 wt% (A) ethaline, (B) glyceline, and (C) reline. The precise concentrations of RNase A used in each experiment are provided in Tables A.1 and A.2. The cycle number shown in the legend refers to the corresponding heating scan from 10-80°C at a rate of 1°C min^{-1}. The dashed lines represent the cooling cycle for their respective cycle number. The peaks for the solid profiles indicate that RNase A unfolding as the temperature increases, and the dashed profiles denote RNase A refolding as the temperature is decreased. The average of at least three trials for each cycle is shown. In Panel C, for clarity, data are omitted for cycles five and beyond.

Typical DSC scans for RNase A in aqueous media containing higher amounts of DES (10, 20, 25, and 35 wt% ethaline, glyceline, or reline) are shown in Figures A.1-3. Notably, all concentrations of ethaline and glyceline showed a stabilizing effect on RNase A, relative to water, for up to eight repetitive DSC scans. Meanwhile, for 10 wt% reline and above, RNase A was completely and irreversibly thermally denatured after one DSC scan to 80°C (Figure A.3), indicating the denaturing tendency of reline.

In an effort to separate the influence of individual DES constituents, the thermal unfolding/refolding behavior of RNase A in aqueous solutions of the individual DES components (*i.e.*, urea, ethylene glycol, glycerol, and choline chloride) was investigated at concentrations corresponding to those present in 5 and 35 wt% solutions of their respective parent DESs. The resulting DSC profiles are presented in Figures A.4 and A.5. RNase A displayed good unfolding reversibility in both 5 and 35 wt% solutions of the individual DES components over eight repetitive DSC scans with the exception of urea which clearly destabilizes RNase A, reflected in the progressive loss in the area under the peak for repetitive DSC scans. The loss in the enthalpy of unfolding in repetitive DSC scans, computed from the area under the DSC peaks, provide a measure of the reversibility of unfolding. In this way, the fraction of irreversible unfolding ($f_{un,ir}$) after each cycle can be estimated from equation 1

$$F_{un,ir} = 1 - (\Delta H_{vH} / \Delta H_{0,vH}) \qquad (1)$$

where ΔH_{vH} is the van't Hoff unfolding enthalpy of a particular up scan, and $\Delta H_{0,vH}$ is the van't Hoff enthalpy of the first scan. This index was computed for repetitive DSC scans employing a scan rate of 1°C and a maximum temperature of 80°C for RNase A in the various DES systems. Figure 2.2 provides plots of the fraction of irreversibly unfolded

RNase A measured during the upscans of repetitive DSC cycles in the three DES systems, alongside results for DES-free water. During the eighth consecutive DSC cycle, the fraction of irreversibly unfolded RNase A in water was determined to be ~40%. For all concentrations of ethaline and glyceline explored, the fraction of irreversibly unfolded RNase A was 25%−35% during the eighth successive DSC scan, demonstrating the ability of ethaline and glyceline to suppress RNase A deactivation relative to water. In 5 wt% reline, the fraction of irreversibly unfolded RNase A varied between 60% and 80% during the third upscan, and an unfolding transition could no longer be observed during the fourth upscan. On the other hand, in 10 wt% or higher reline, RNase A unfolding is essentially irreversible after the very first DSC scan. As Figure A.3 shows, no exothermic refolding transition can be seen for the cooling segment of the DSC scan during the first cycle for RNase A in 10, 20, 25, or 35 wt% reline. Consistent with this notion, $f_{un,ir}$ is 100% by the second upscan (heating segment) for reline solutions of 10 wt% or more (Figure 2.2).

The fraction of irreversible unfolding was also computed for RNase A in aqueous solutions of the individual DES components present at concentrations corresponding to those present in 5 and 35 wt% solutions of the corresponding DESs. The results for RNase A in glycerol, ethylene glycol, and choline chloride generally revealed a similar or a lower content of irreversibly unfolded RNase A compared to that seen in water (Figure A.6). Choline chloride and glycerol individually showed protein stabilizing effects, notably with fractions of irreversibly unfolded protein between 20% and 30% at the eight consecutive DSC cycles. However, for urea present in water at an amount akin to that present in 5 and 35 wt% reline, RNase A was associated with a fraction of irreversibly unfolded protein between 40% and 60% during the third upscan. Note, although minor peaks can be

observed in the fourth upscans of the DSC analysis (Panels A and B of Figure A.4), the enthalpy of unfolding could not be reliably determined. Figure A.7 compares the van't Hoff unfolding enthalpy (ΔH_{vH}) for RNase A dissolved in various wt% solutions of aqueous ethaline,

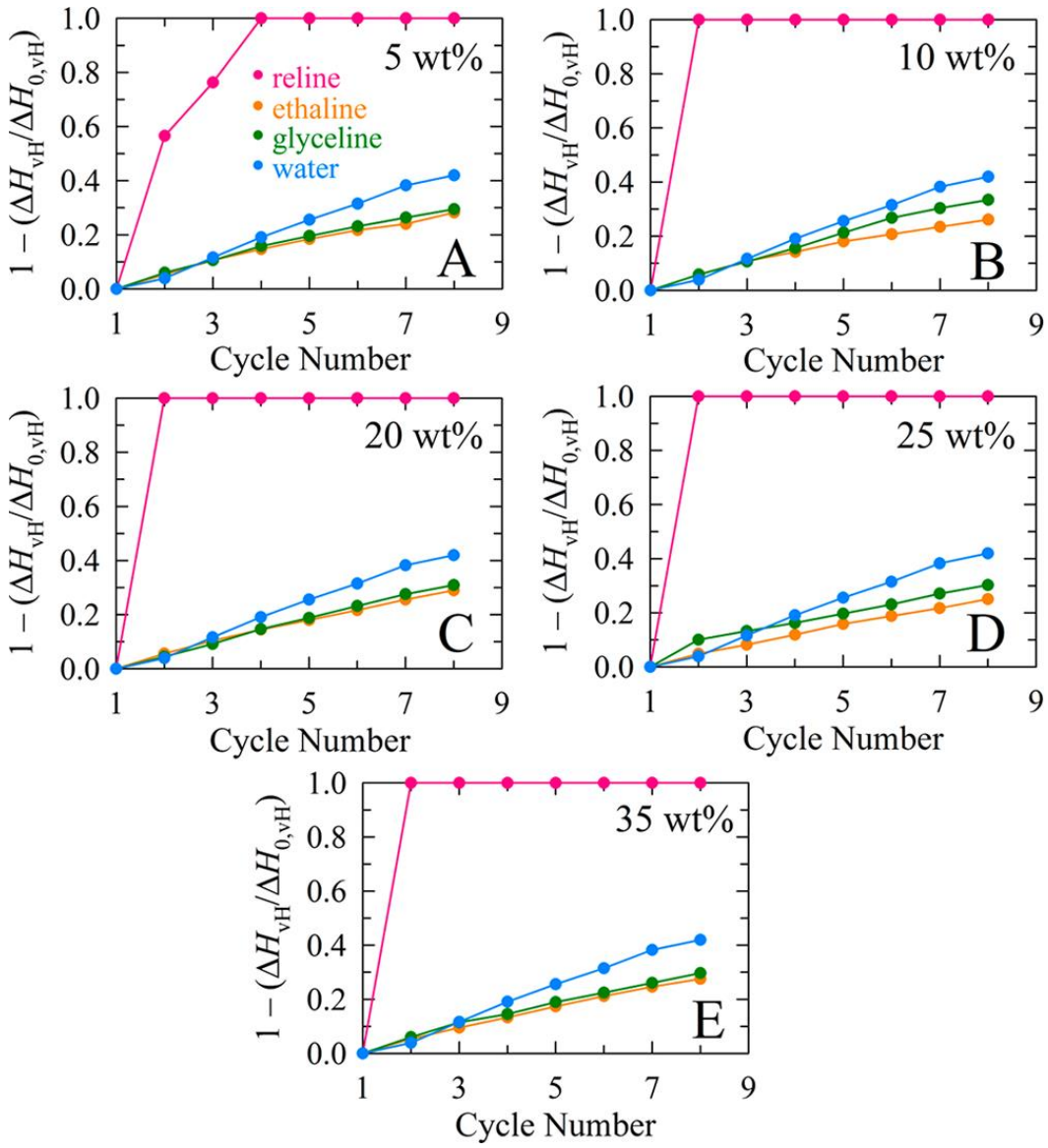

Figure 2.2 Fraction of irreversible RNase A unfolding displayed during the upscan of each heating/cooling cycle in (A) 5 wt%, (B) 10 wt%, (C) 20 wt%, (D) 25 wt% and (E) 35 wt% aqueous solutions of reline, ethaline, and glyceline, alongside results for RNase A in water.

Ethaline and glyceline media both show lower amounts of irreversible RNase A unfolding compared to RNase A in water. In contrast, reline-containing water is incompatible with RNase A thermal stability. In fact, for 10 wt% or higher reline, irreversible thermal denaturation is observed during a single cycle to 80°C.

glyceline,and reline. The drop in ΔH_{vH} per repetitive DSC cycle for RNase A in 5 wt % ethaline, 5 wt% glyceline, and 5 wt% reline was determined to be 3.9, 4.6, and 26.9 kcal mol^{-1}/cycle, respectively (Table A.3). The van't Hoff enthalpies were also compared thermal cycle-wise for RNase A in the individual DES components (Figure A.8). The decrement in ΔH_{vH} per cycle for RNase A in all other wt% DES media is compiled in Table A.3. Note that these enthalpic losses are proportional to the fraction of irreversible protein unfolding.

The ionic liquid 1-butyl-3-methylimidazolium chloride ([bmim]Cl), known to be a potent denaturant, was also examined as a cosolvent for RNase A unfolding using DSC analysis. Figure 2.3 summarizes the midpoint temperature of the unfolding transition (melting temperature, T_m) for RNase A dissolved in aqueous media containing the three representative DESs. Benchmark values for RNase A in water (T_m = 59.7°C) and 25 wt% [bmim]Cl (T_m = 44.5°C) are also provided for reference. Higher amounts of glyceline were found to progressively shift the denaturation transition for RNase A to higher temperatures, with T_m increasing from 59.9 to 63.0°C as glyceline increases from 5 to 35 wt%. Of the three DES hydrogen bond donors (urea, ethylene glycol, glycerol), glycerol clearly induces the highest protein stability (Figure A.6), possibly linked to the presence of a greater number of hydrogen-bond donor groups.[37] The T_m for RNase A in ethaline remained

constant across the range from 5 to 35 wt% ethaline, with an average transition temperature of 59.6°C, essentially identical to the native value observed in water. According to D'Agostino *et al.*, the diffusion coefficients of the hydroxyl protons of choline and ethylene glycol as a function of water content are almost identical to that for water,[37] which may offer a rationale for the consistency between the T_m values for RNase A in ethaline and in water. Figure 2.3 also shows that T_m for the thermal denaturation of RNase A decreases as the reline concentration is increased showing a T_m value of 57.0°C at 5 wt% reline which further drops to 51.8°C by the time 35 wt% reline is reached.

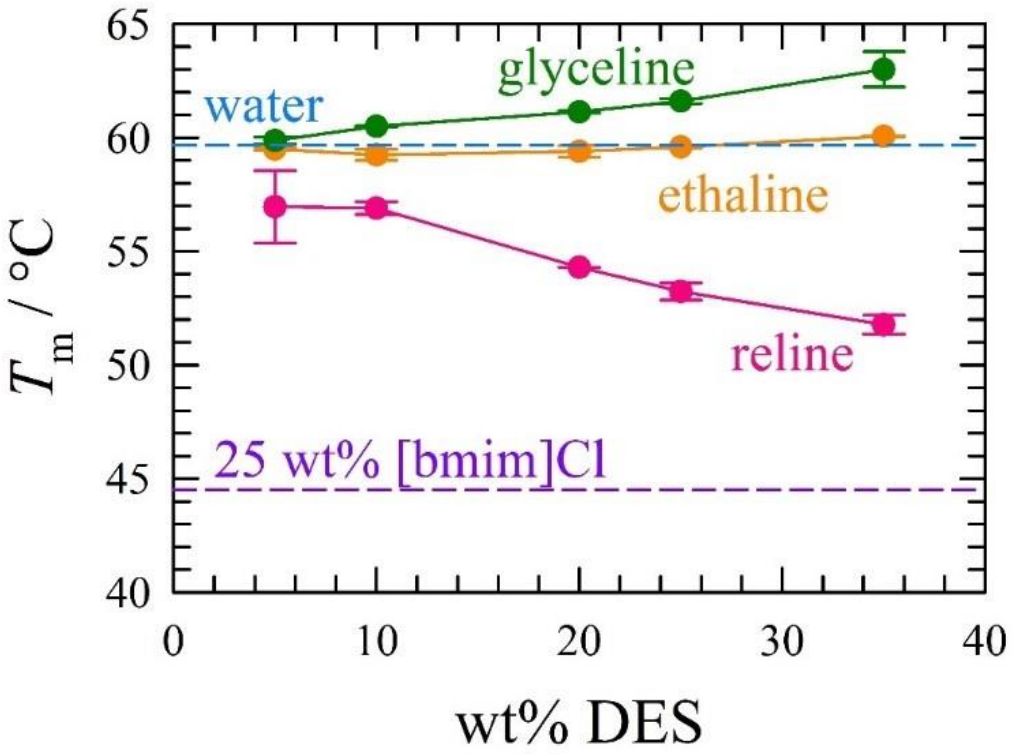

Figure 2.3 Plot of transition temperature T_m for RNase A thermal unfolding versus wt% of the DES (reline, ethaline, or glyceline) in water. Horizontal dashed lines show reference T_m values for RNase A in water and 25 wt% [bmim]Cl.

It is apparent from these data that reline destabilizes RNase A. Within this context, it should be remarked that such behavior is typical of aqueous solutions of conventional ionic liquids.[1, 33] As an illustration of this fact, the T_m value measured for RNase A in 25 wt% [bmim]Cl (equivalent to ~1.43 M) was 44.5°C, even lower than the value of 53.2°C observed for RNase A in 25 wt% reline. Interestingly, Weingärtner and coworkers reported a T_m of ~46°C for RNase A in 1.5 M [bmim]Br,[33] and the similarity in T_m at comparable molarity suggesting that $[bmim]^+$ exerts the dominant role in controlling RNase A thermal destabilization, not the halide.

The T_m values determined for RNase A in solutions of the individual DES components are summarized in Figure A.9. For RNase A in ethylene glycol, T_m for RNase A was similar to that in water. The stabilizing role of glycerol is once again apparent, with T_m values higher than the benchmark value in water. In the case of urea, while a low concentration yields an RNase A T_m similar to water, when the urea content in water matches that present in a 35 wt% reline solution the T_m has fallen to 50°C, a temperature even lower than the 51.8°C seen in 35 wt% reline. For RNase A in choline chloride (ChCl) solutions matched to their respective lowest- and highest-concentration DES samples, T_m is akin to water or slightly above, respectively, indicating a weakly stabilizing behavior. For ease of visual comparison, a plot compiling T_m data for RNase A in the three DESs together with results in solutions of the individual DES components is provided as Figure A.10. Referring to Figure A.10, it is found that, at the highest concentration studied, glyceline produces a stabilizing effect on RNase A that is practically additive from its individual components. Meanwhile, urea itself appears to be more destabilizing toward RNase A than the same amount of urea formulated within a DES, again suggesting a

mediation effect from the ChCl component. Finally, RNase A transition temperatures in ethaline and ethylene glycol solutions are similar to values for the native protein in water.

It has been reported that urea decomposition in DESs can lead to the liberation of ammonia, especially in the presence of polyalcohols via the formation of cyclic carbonates.[38] Similarly, accumulation of cyanate in urea solutions is known to occur, with the resulting cyanate ion being reactive toward amino and sulfhydryl groups to form carbamylated products which may irreversibly inactivate proteins. Many strategies have been followed to avoid protein carbamylation, including reducing the generation of cyanates or removing active cyanates from solution, freshly preparing urea which is further deionized prior to use, removing urea prior to sample digestion, acidifying samples, and maintaining a low reaction temperature to decrease the rate of urea decomposition. Sun *et al.* recently reported the inhibition of protein carbamylation in urea solutions by using ammonium-containing buffers (*e.g.,* NH_4HCO_3), the logic being that NH_4^+ from these buffers should (according to Le Chatelier's principle) drive the equilibrium of the urea dissociation reaction (*i.e.,* $(NH_2)_2CO \leftrightarrow NH_4^+ + [NCO]^-$) to favor urea over isocyanic acid (HNCO), the product that causes carbamylation.[39]

To test urea decomposition as a primary vehicle for RNase A deactivation in reline, DSC was performed on a sample of RNase A in 25 wt% reline supplemented with 50 mM ammonium acetate (NH_4OAc). Figure 2.4 shows the results of this experiment over iterative DSC cycles. Comparing Panels 2.4A and 2.4B, it is evident that the inclusion of 50 mM NH_4OAc had a positive effect on RNase A unfolding reversibility (also compare profiles 1 and 2 in Panels E and F), although beyond two DSC cycles denaturation remained wholly irreversible. Based on this positive result, however, we performed an experiment

with RNase A in 25 wt% reline containing 1.0 MNH_4OAc. As shown in Figure 4C, this resulted in vastly improved RNase A unfolding reversibility. Indeed, an endothermic peak is now evident even during the sixth upscan, and the improved reversibility is accompanied by an increase in T_m (measured during the first upscan) to 58.2°C in relation to a value of 53.2°C in 25 wt % reline. It should be noted that while supported by prior analytical work,[39] the suppression of urea dissociation remains speculative in our system, and it is likewise possible that the acetate anion forms hydrogen bonds with urea, minimizing its chaotropic nature and denaturing impact.

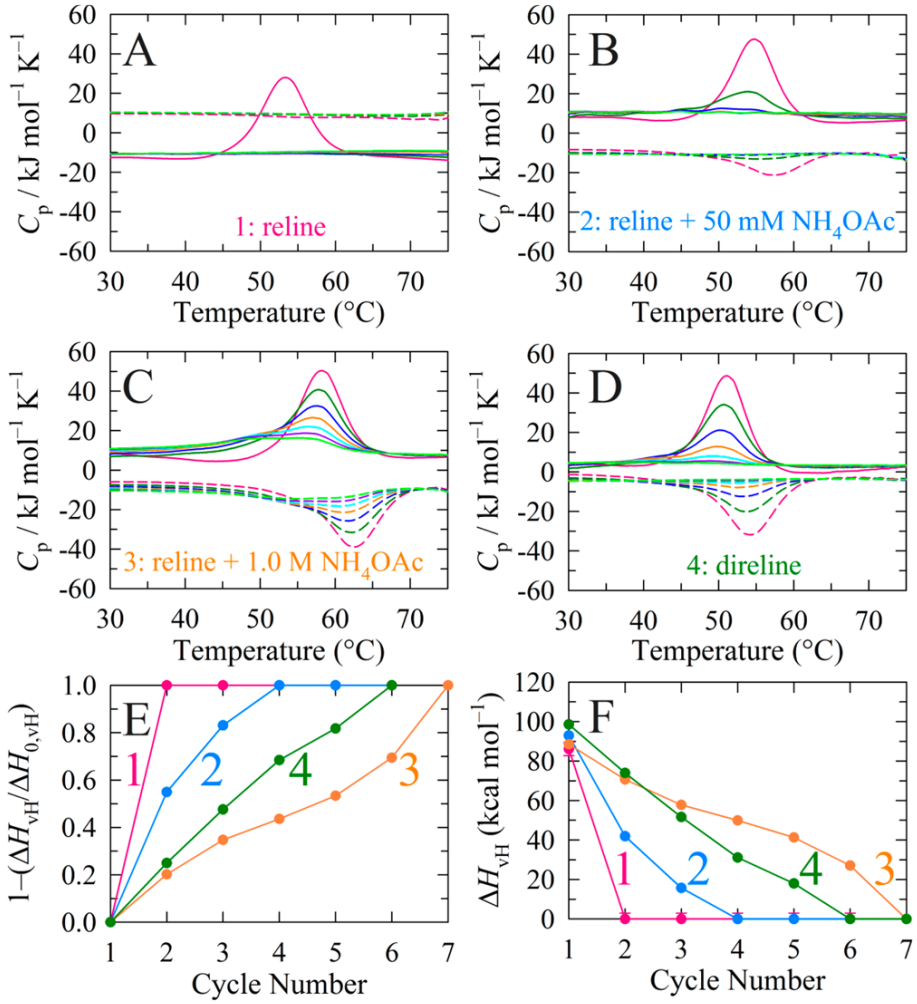

Figure 2.4 Representative DSC scans for RNase A in (A) 25 wt% reline, (B) 25 wt% reline + 50 mM NH_4OAc, (C) 25 wt% reline + 1.0 M NH_4OAc and (D) 25 wt% direline (1:2 choline chloride: 1,3-dimethylurea). The direline appears to impart greater operational stability to RNase A in solutions, as judged by the rate of loss of ΔH_{vH} with iterative cycles, although T_m is concomitantly shifted from 53.2°C in 25 wt% reline (Panel A) to 51.1°C in 25 wt% direline (Panel D). Thermal cycle-dependent (E) fractions of irreversible RNase A unfolding and (F) van't Hoff enthalpies are also provided. The numerals 1-4 denote the four solvent systems presented in panels A-D, respectively.

Revisiting the concept of urea decomposition, since the products of urea dissociation (*i.e.*, cyanate and ammonia) are problematic, we decided to employ a more stable urea analog in an attempt to avoid ammonia and cyanate by-production. To accomplish this, we prepared a DES consisting of a 1:2 choline chloride:1,3-dimethylurea mixture, a DES denoted direline herein. DSC traces for iterative thermal cycles of RNase A in 25 wt% direline are provided in Panel D of Figure 2.4. Interestingly, while direline showed significantly improved reversibility for RNase A unfolding relative to reline (*i.e.*, five consecutive heating/cooling cycles are required for complete inactivation of RNase A within direline versus a single cycle within reline), T_m decreased slightly from 53.2°C in 25 wt% reline to 51.1°C in 25 wt% direline. The improved operational stability, however, supports the utilization of direline over reline as an aqueous cosolvent due to the relative suppression of irreversible protein deactivation during thermal cycling. Finally, Figure 2.4F presents plots of ΔH_{vH} versus DSC cycle number. Compared to the drop in ΔH_{vH}/cycle for RNase A in 25 wt% reline (nearly 80 kJ mol^{-1}/cycle), the decrement for RNase A in 25 wt% reline + 50 mM NH_4OAc, 25 wt reline + 1.0 M NH_4OAc, and 25 wt% direline are 19,

12, and 20 kJ mol^{-1}/cycle, respectively, emphasizing the improved operational stability afforded by these supplemented or alterative reline media.

Conclusions

In conclusion, the thermostability of RNase A in three hydrated cholinium chloride-based deep eutectic solvent systems has been studied using DSC analysis. These measurements reveal that RNase A stabilization increases with increasing ethaline or glyceline concentration up to at least 35 wt%, consistent with the low fraction of irreversibly unfolded protein observed after iterative thermal cycles and increased transition temperature compared to RNase A in water. In contrast, RNase A was completely denatured in systems comprising 10 wt% or higher reline after a single thermal cycle to 80°C. Indeed, under these thermal conditions (*i.e.*, heating to 80°C at a 1°C min^{-1} ramp, followed by immediate cooling to room temperature), RNase A is quantitatively and irreversibly unfolded. Experiments attempting to reduce cyanate and ammonia production were also performed by (i) supplementing reline with ammonium acetate buffer or (ii) employing a more stable alternative to urea (*i.e.*, 1,3-dimethylurea), leading to better outcomes for RNase A operational stability compared with reline. Overall, this work offers the first thermodynamic assessment of model protein (re)folding energetics in a deep eutectic solvent system, setting the stage for the deeper understanding of biomolecular behavior and stability within these emerging solvent systems.

Acknowledgements

This study was supported by the Research Corporation for Science Advancement. We thank one reviewer for kindly suggesting a possible role for acetate in mediating the efficacy of urea as a denaturant.

References

1. Constantinescu, D.; Herrmann, C.; Weingärtner, H., Patterns of Protein Unfolding and Protein Aggregation in Ionic Liquids. *Phys. Chem. Chem. Phys.* **2010,** *12* (8), 1756-1763.

2. Erbeldinger, M.; Mesiano, A. J.; Russell, A. J., Enzymatic Catalysis of Formation of Z-Aspartame in Ionic Liquid − an Alternative to Enzymatic Catalysis in Organic Solvents. *Biotechnol. Progr.* **2000,** *16* (6), 1129-1131.

3. Baker, S. N.; McCleskey, T. M.; Pandey, S.; Baker, G. A., Fluorescence Studies of Protein Thermostability in Ionic Liquids. *Chem. Commun.* **2004,** (8), 940-941.

4. Zhao, H.; Baker, G. A.; Song, Z.; Olubajo, O.; Crittle, T.; Peters, D., Designing Enzyme-Compatible Ionic Liquids That Can Dissolve Carbohydrates. *Green Chem.* **2008,** *10* (6), 696-705.

5. Page, T. A.; Kraut, N. D.; Page, P. M.; Baker, G. A.; Bright, F. V., Dynamics of Loop 1 of Domain I in Human Serum Albumin When Dissolved in Ionic Liquids. *J. Phys. Chem. B* **2009,** *113* (38), 12825-12830.

6. Weaver, K. D.; Vrikkis, R. M.; Van Vorst, M. P.; Trullinger, J.; Vijayaraghavan, R.; Foureau, D. M.; McKillop, I. H.; MacFarlane, D. R.; Krueger, J. K.; Elliott, G. D., Structure and Function of Proteins in Hydrated Choline Dihydrogen Phosphate Ionic Liquid. *Phys. Chem. Chem. Phys.* **2012,** *14* (2), 790-801.

7. Esquembre, R.; Sanz, J. M.; Wall, J. G.; del Monte, F.; Mateo, C. R.; Ferrer, M. L., Thermal Unfolding and Refolding of Lysozyme in Deep Eutectic Solvents and Their Aqueous Dilutions. *Phys. Chem. Chem. Phys.* **2013,** *15* (27), 11248-11256.

8. Brogan, A. P. S.; Bui-Le, L.; Hallett, J. P., Non-Aqueous Homogenous Biocatalytic Conversion of Polysaccharides in Ionic Liquids Using Chemically Modified Glucosidase. *Nat. Chem.* **2018,** *10* (8), 859-865.

9. Baker, G. A.; Heller, W. T., Small-Angle Neutron Scattering Studies of Model Protein Denaturation in Aqueous Solutions of the Ionic Liquid 1-Butyl-3-Methylimidazolium Chloride. *Chem. Eng. J.* **2009,** *147* (1), 6-12.

10. Baker, S. N.; Zhao, H.; Pandey, S.; Heller, W. T.; Bright, F. V.; Baker, G. A., Fluorescence Energy Transfer Efficiency in Labeled Yeast Cytochrome C: A Rapid Screen for Ion Biocompatibility in Aqueous Ionic Liquids. *Phys. Chem. Chem. Phys.* **2011,** *13* (9), 3642-3644.

11. Romero, A.; Santos, A.; Tojo, J.; Rodríguez, A., Toxicity and Biodegradability of Imidazolium Ionic Liquids. *J. Hazard. Mater.* **2008,** *151* (1), 268-273.

12. Plechkova, N. V.; Seddon, K. R., Applications of Ionic Liquids in the Chemical Industry. *Chem. Soc. Rev.* **2008,** *37* (1), 123-150.

13. Radošević, K.; Cvjetko Bubalo, M.; Gaurina Srček, V.; Grgas, D.; Landeka Dragičević, T.; Radojčić Redovniković, I., Evaluation of Toxicity and Biodegradability of Choline Chloride Based Deep Eutectic Solvents. *Ecotoxicol. Environ. Saf.* **2015,** *112*, 46-53.

14. Gschwend, F. J. V.; Malaret, F.; Shinde, S.; Brandt-Talbot, A.; Hallett, J. P., Rapid Pretreatment of Miscanthus Using the Low-Cost Ionic Liquid Triethylammonium Hydrogen Sulfate at Elevated Temperatures. *Green Chem.* **2018,** *20* (15), 3486-3498.

15. Guajardo, N.; Müller, C. R.; Schrebler, R.; Carlesi, C.; Domínguez de María, P., Deep Eutectic Solvents for Organocatalysis, Biotransformations, and Multistep Organocatalyst/Enzyme Combinations. *ChemCatChem* **2016,** *8* (6), 1020-1027.

16. Feng, M.; Lu, X.; Jiang, K.; Zhang, J.; Xin, J.; Shi, C.; Wang, K.; Zhang, S., One-Step Preparation of an Antibacterial Chitin/Zn Composite from Shrimp Shells Using Urea-Zn(Oac)2·2h2o Aqueous Solution. *Green Chem.* **2018,** *20* (10), 2212-2217.

17. Zeng, Q.; Wang, Y.; Huang, Y.; Ding, X.; Chen, J.; Xu, K., Deep Eutectic Solvents as Novel Extraction Media for Protein Partitioning. *Analyst* **2014,** *139* (10), 2565-2573.

18. Cao, J.; Chen, L.; Li, M.; Cao, F.; Zhao, L.; Su, E., Two-Phase Systems Developed with Hydrophilic and Hydrophobic Deep Eutectic Solvents for Simultaneously Extracting Various Bioactive Compounds with Different Polarities. *Green Chem.* **2018,** *20* (8), 1879-1886.

19. Smith, E. L.; Abbott, A. P.; Ryder, K. S., Deep Eutectic Solvents (Dess) and Their Applications. *Chem. Rev.* **2014,** *114* (21), 11060-11082.

20. Abbott, A. P.; Capper, G.; Davies, D. L.; Rasheed, R. K.; Tambyrajah, V., Novel Solvent Properties of Choline Chloride/Urea Mixtures. *Chem. Commun.* **2003,** (1), 70-71.

21. Zhang, Q.; De Oliveira Vigier, K.; Royer, S.; Jérôme, F., Deep Eutectic Solvents: Syntheses, Properties and Applications. *Chem. Soc. Rev.* **2012,** *41* (21), 7108-7146.

22. Carriazo, D.; Serrano, M. C.; Gutiérrez, M. C.; Ferrer, M. L.; del Monte, F., Deep-Eutectic Solvents Playing Multiple Roles in the Synthesis of Polymers and Related Materials. *Chem. Soc. Rev.* **2012,** *41* (14), 4996-5014.

23. Zhao, H.; Baker, G. A., Ionic Liquids and Deep Eutectic Solvents for Biodiesel Synthesis: A Review. *J. Chem. Technol. Biot.* **2013,** *88* (1), 3-12.

24. Wagle, D. V.; Zhao, H.; Baker, G. A., Deep Eutectic Solvents: Sustainable Media for Nanoscale and Functional Materials. *Acc. Chem. Res.* **2014,** *47* (8), 2299-2308.

25. Soares, B.; Tavares, D. J. P.; Amaral, J. L.; Silvestre, A. J. D.; Freire, C. S. R.; Coutinho, J. A. P., Enhanced Solubility of Lignin Monomeric Model Compounds and Technical Lignins in Aqueous Solutions of Deep Eutectic Solvents. *ACS Sustainable Chem. Eng.* **2017,** *5* (5), 4056-4065.

26. Juneidi, I.; Hayyan, M.; Hashim, M. A., Intensification of Biotransformations Using Deep Eutectic Solvents: Overview and Outlook. *Process Biochem.* **2018,** *66*, 33-60.

27. dos Santos, N. V.; Martins, M.; Santos-Ebinuma, V. C.; Ventura, S. P. M.; Coutinho, J. A. P.; Valentini, S. R.; Pereira, J. F. B., Aqueous Biphasic Systems Composed of Cholinium Chloride and Polymers as Effective Platforms for the Purification of Recombinant Green Fluorescent Protein. *ACS Sustainable Chem. Eng.* **2018,** *6* (7), 9383-9393.

28. Kadyan, A.; Behera, K.; Pandey, S., Hybrid Green Nonaqueous Media: Tetraethylene Glycol Modifies the Properties of a (Choline Chloride + Urea) Deep Eutectic Solvent. *RSC Adv.* **2016,** *6* (36), 29920-29930.

29. Xin, R.; Qi, S.; Zeng, C.; Khan, F. I.; Yang, B.; Wang, Y., A Functional Natural Deep Eutectic Solvent Based on Trehalose: Structural and Physicochemical Properties. *Food Chem.* **2017,** *217*, 560-567.

30. Sanchez-Fernandez, A.; Edler, K. J.; Arnold, T.; Alba Venero, D.; Jackson, A. J., Protein Conformation in Pure and Hydrated Deep Eutectic Solvents. *Phys. Chem. Chem. Phys.* **2017,** *19* (13), 8667-8670.

31. Wu, B.-P.; Wen, Q.; Xu, H.; Yang, Z., Insights into the Impact of Deep Eutectic Solvents on Horseradish Peroxidase: Activity, Stability and Structure. *J. Mol. Catal. B: Enzyme* **2014,** *101*, 101-107.

32. Almarza, J.; Rincon, L.; Bahsas, A.; Brito, F., Molecular Mechanism for the Denaturation of Proteins by Urea. *Biochemistry* **2009,** *48* (32), 7608-7613.

33. Constantinescu, D.; Weingärtner, H.; Herrmann, C., Protein Denaturation by Ionic Liquids and the Hofmeister Series: A Case Study of Aqueous Solutions of Ribonuclease A. *Angew. Chem. Int. Ed.* **2007,** *46* (46), 8887-8889.

34. von Hippel, P. H.; Wong, K.-Y., On the Conformational Stability of Globular Proteins: The Effects of Various Electrolytes and Nonelectrolytes on the Thermal Ribonuclease Transition. *J. Biol. Chem.* **1965,** *240* (10), 3909-3923.

35. Gutiérrez, M. C.; Ferrer, M. L.; Yuste, L.; Rojo, F.; del Monte, F., Bacteria Incorporation in Deep-Eutectic Solvents through Freeze-Drying. *Angew. Chem. Int. Ed.* **2010,** *49* (12), 2158-2162.

36. Abbott, A. P.; Harris, R. C.; Ryder, K. S.; D'Agostino, C.; Gladden, L. F.; Mantle, M. D., Glycerol Eutectics as Sustainable Solvent Systems. *Green Chem.* **2011,** *13* (1), 82-90.

37. D'Agostino, C.; Gladden, L. F.; Mantle, M. D.; Abbott, A. P.; Ahmed, E. I.; Al-Murshedi, A. Y. M.; Harris, R. C., Molecular and Ionic Diffusion in Aqueous – Deep Eutectic Solvent Mixtures: Probing Inter-Molecular Interactions Using Pfg Nmr. *Phys. Chem. Chem. Phys.* **2015,** *17* (23), 15297-15304.

38. Simeonov, S. P.; Afonso, C. A. M., Basicity and Stability of Urea Deep Eutectic Mixtures. *RSC Adv.* **2016,** *6* (7), 5485-5490.

39. Sun, S.; Zhou, J.-Y.; Yang, W.; Zhang, H., Inhibition of Protein Carbamylation in Urea Solution Using Ammonium-Containing Buffers. *Anal. Biochem.* **2014,** *446*, 76-81.

Appendix A: Supporting Figures for Chapter 2-Calorimetric Evaluation of the Operational Thermal Stability of Ribonuclease A in Hydrated Deep Eutectic Solvents

Jennifer A. Kist, Michael T. Henzl, José L. Bañuelos, and Gary A. Baker

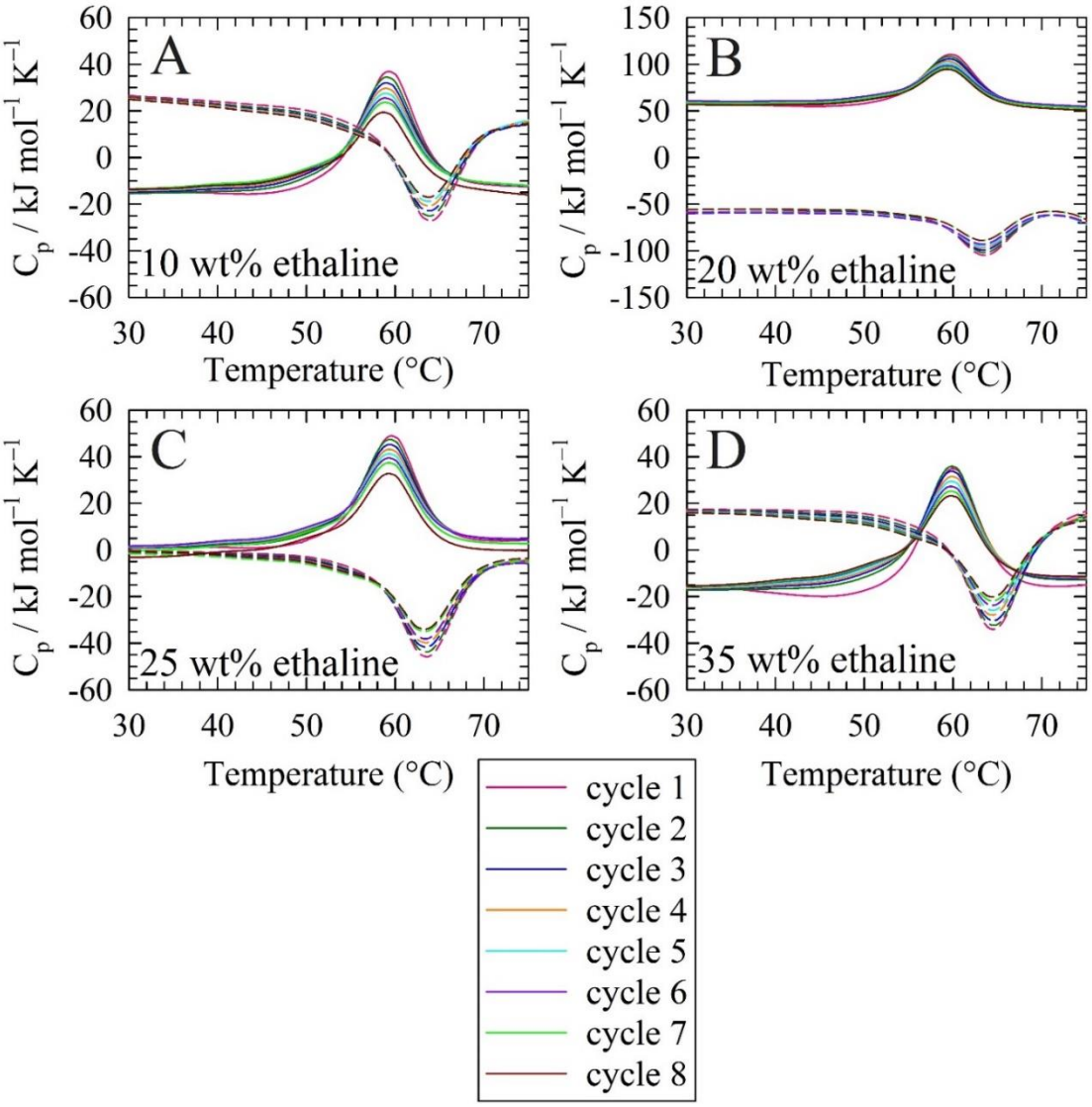

Figure A.1 DSC scans for RNase A in aqueous solutions containing various wt% ethaline (1:2 choline chloride: ethylene glycol). The cycle number refers to the corresponding heating scan from 10-80°C at a rate of 1°C min^{-1}. The dashed lines represent cooling cycles. The average of at least three trials for each heating/cooling cycle is shown.

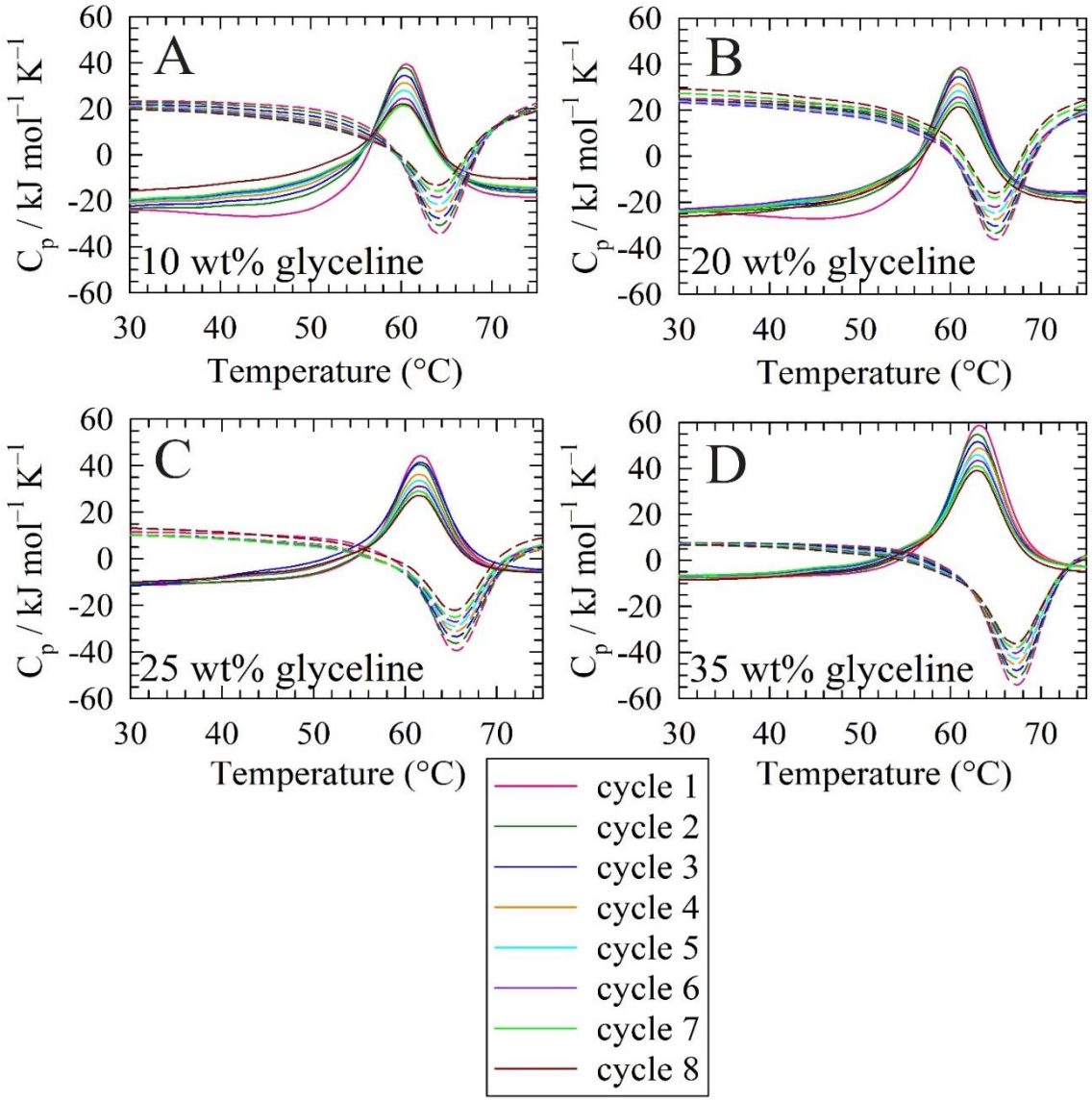

Figure A.2 DSC scans for RNase A in aqueous solutions containing various wt% glyceline (1:2 choline chloride: glycerol). The cycle number refers to the corresponding heating scan from 10–80°C at a rate of 1°C min^{-1}. The dashed lines represent cooling cycles. The average of at least trials for each heating/cooling cycle is shown.

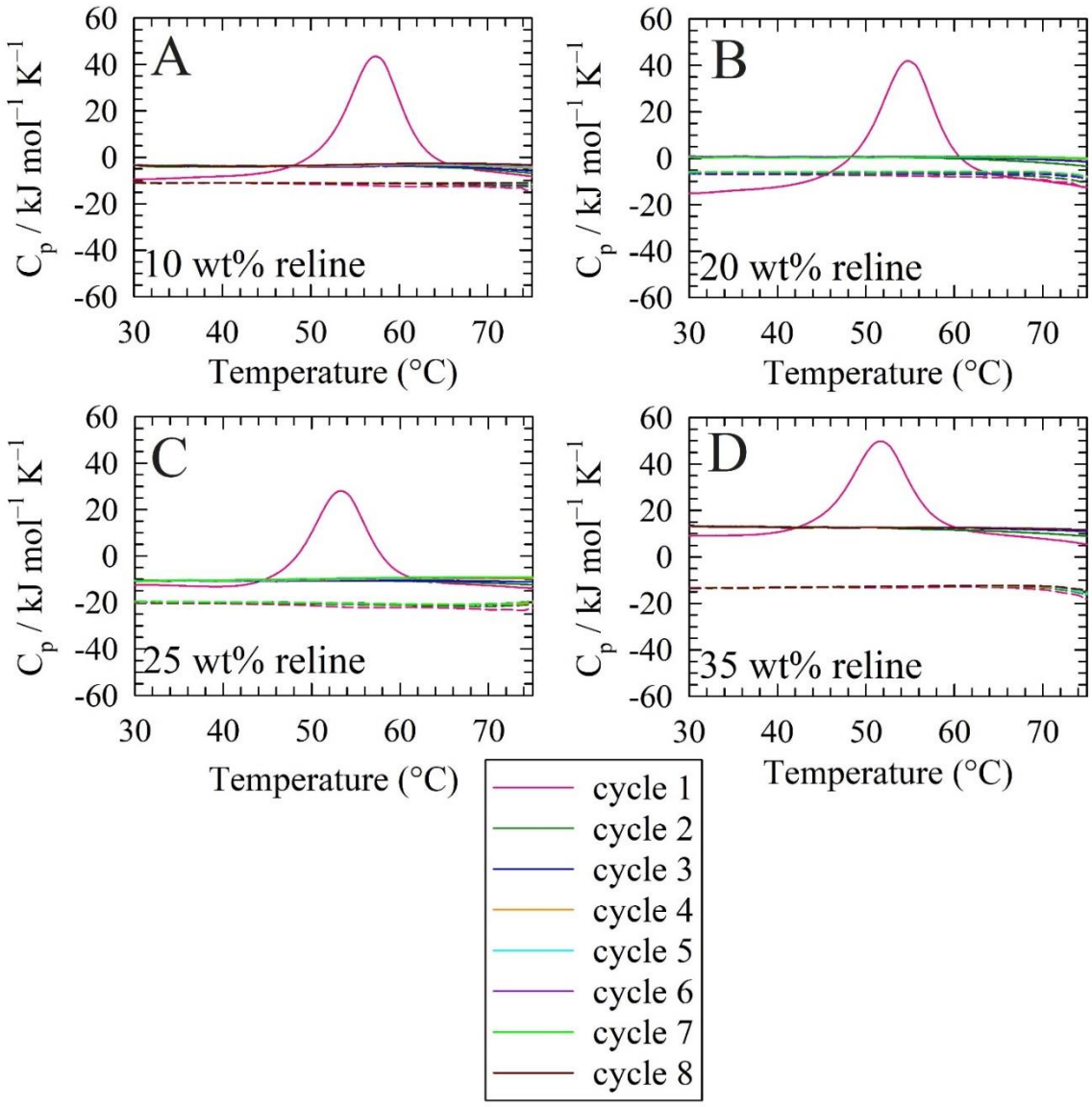

Figure A.3 DSC scans for RNase A in aqueous solutions containing various wt% reline (1:2 choline chloride: urea). The cycle number refers to the corresponding heating scan from 10–80°C at a rate of 1°C min^{-1}. The dashed lines represent cooling cycles. After one heating cycle, the protein is fully denatured in solutions of 10 wt% reline and above. The average of at least trials for each heating/cooling cycle is shown.

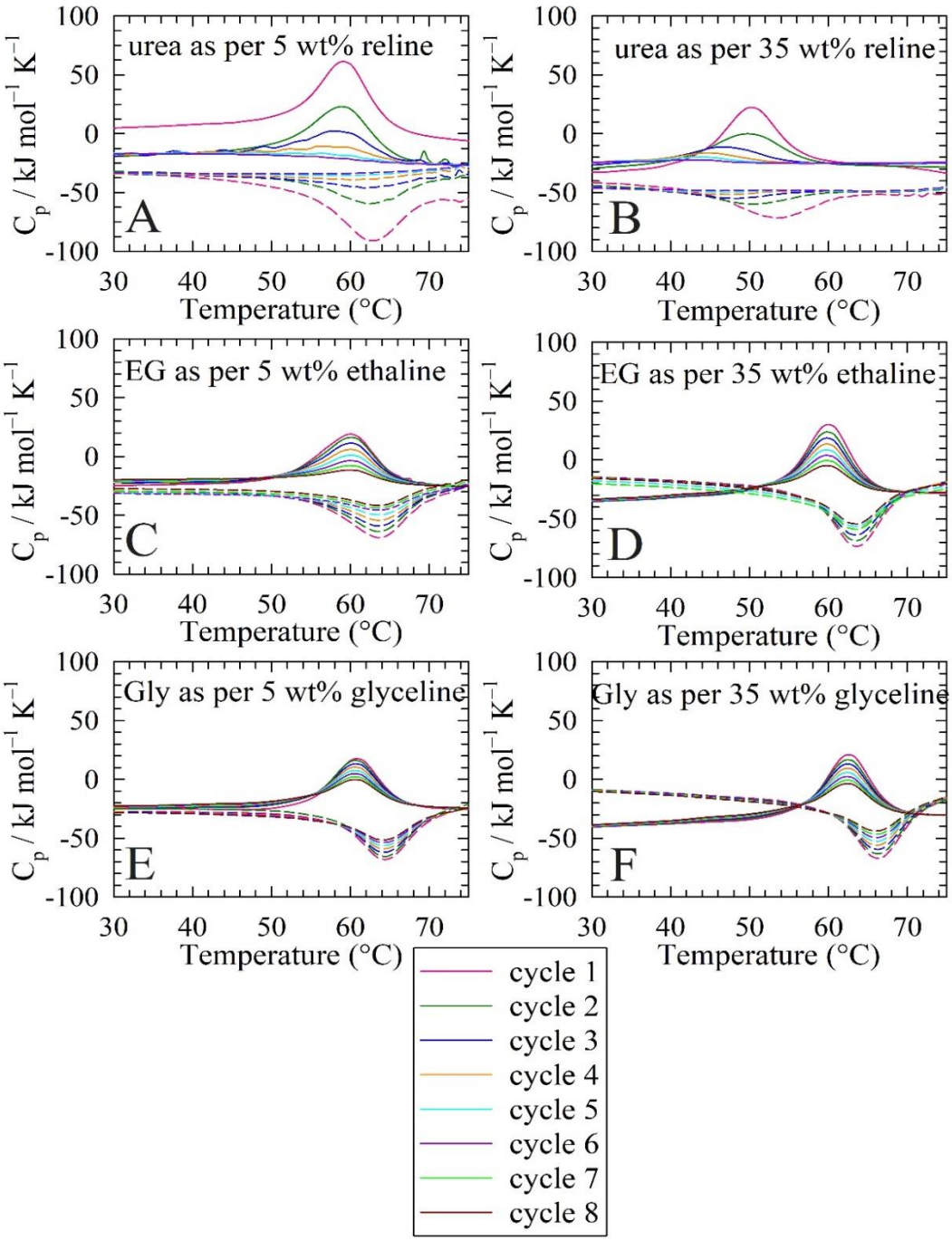

Figure A.4 DSC scans for RNase A in aqueous solutions containing individual components as per 5 and 35 wt% of their respective DES. EG is abbreviated for ethylene glycol and Gly is the abbreviation for glycerol. The cycle number refers to the corresponding heating scan from 10–80°C at a rate of 1°C min^{-1}. The average of at least trials for each heating/cooling cycle is shown.

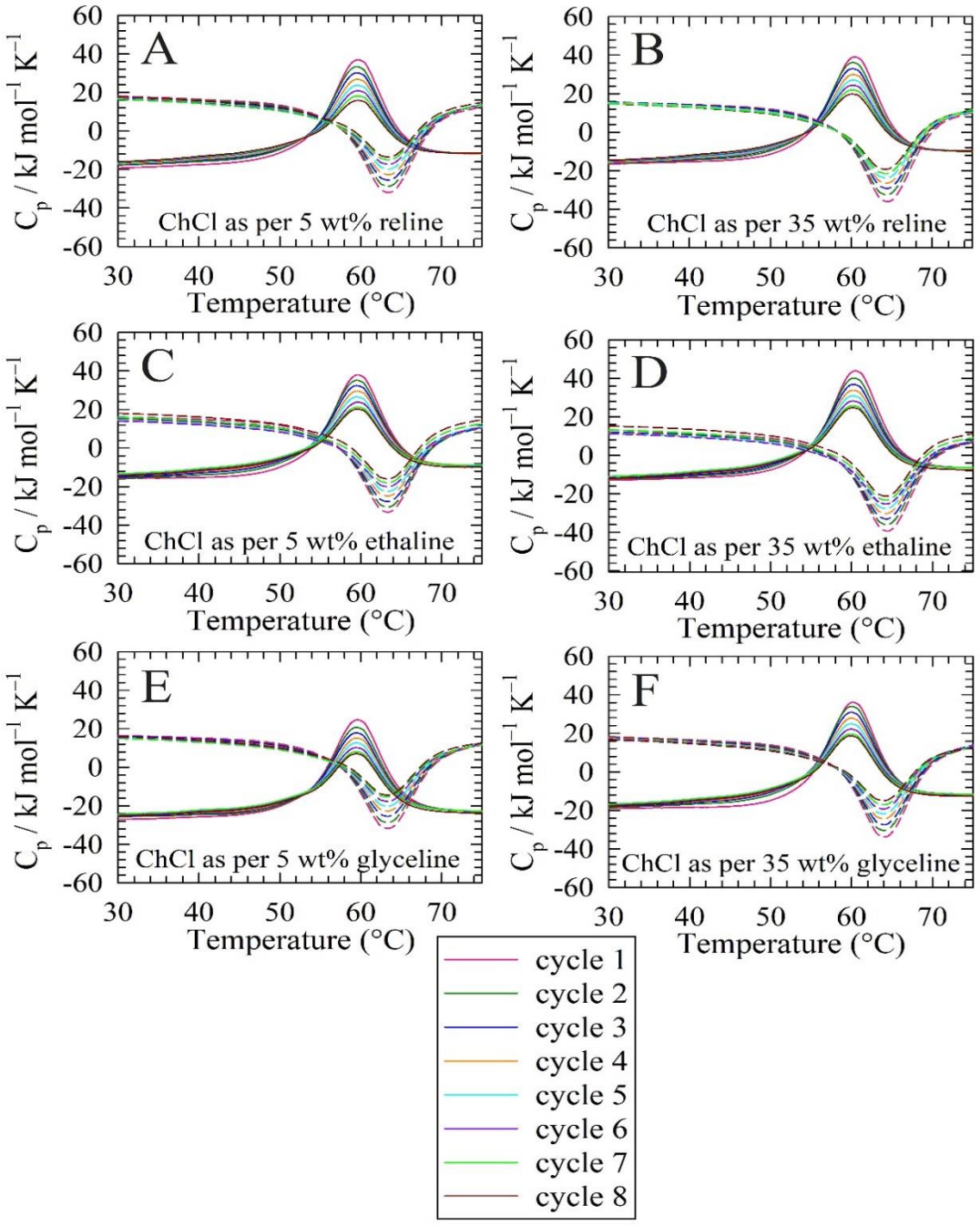

Figure A.5 DSC scans for RNase A in aqueous solutions containing choline chloride (ChCl) as per 5 and 35 wt% of its respective DES. The cycle number refers to the corresponding heating scan from 10–80°C at a rate of 1°C min^{-1}. The dashed lines represent cooling cycles. The average of at least trials for each heating/cooling cycle is shown.

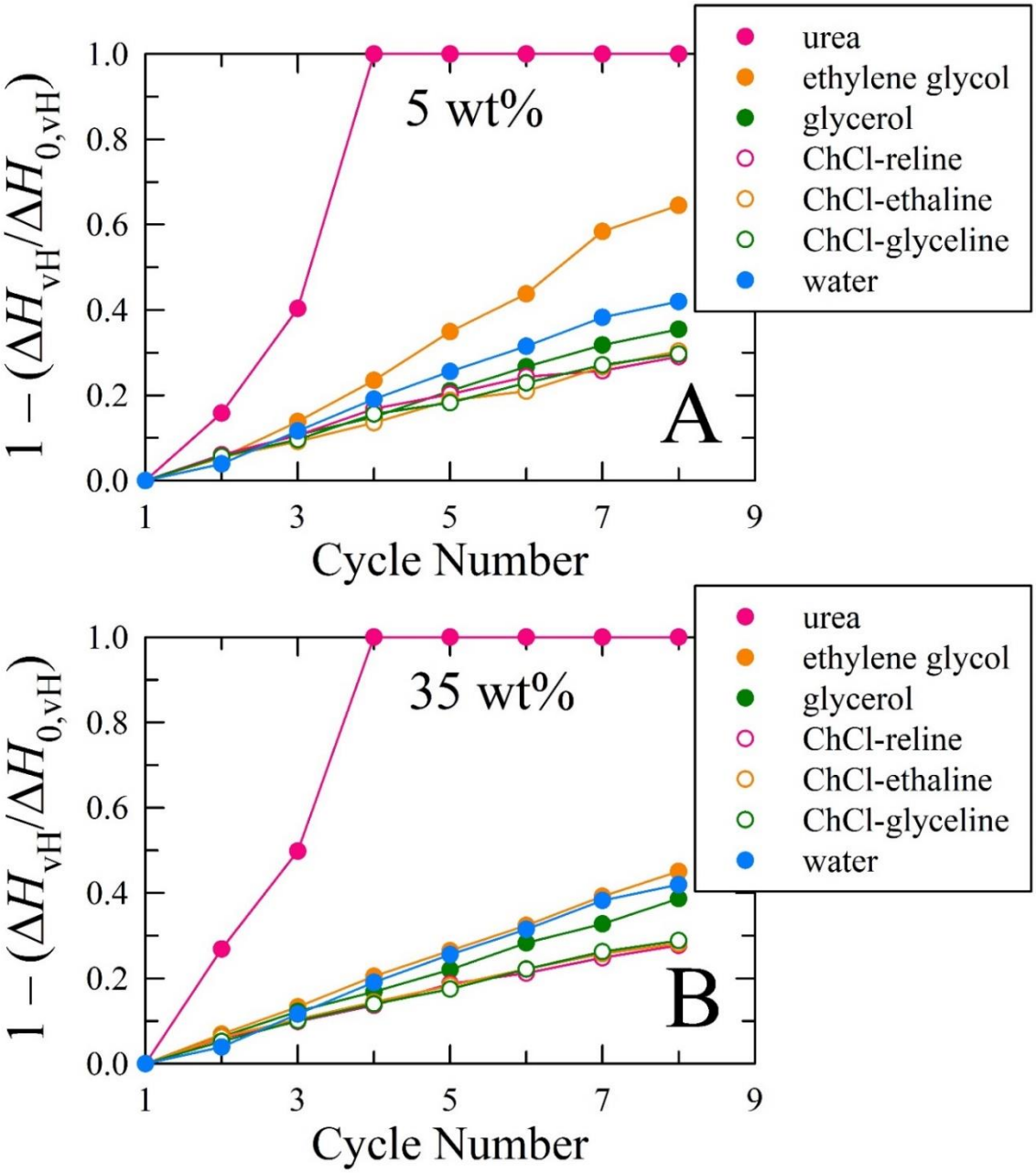

Figure A.6 The fraction of RNase A irreversibly unfolded after each heating/cooling cycle in the wt% of individual components as per their respective DES: (A) 5 wt% and (B) 35 wt%. ChCl stands for choline chloride.

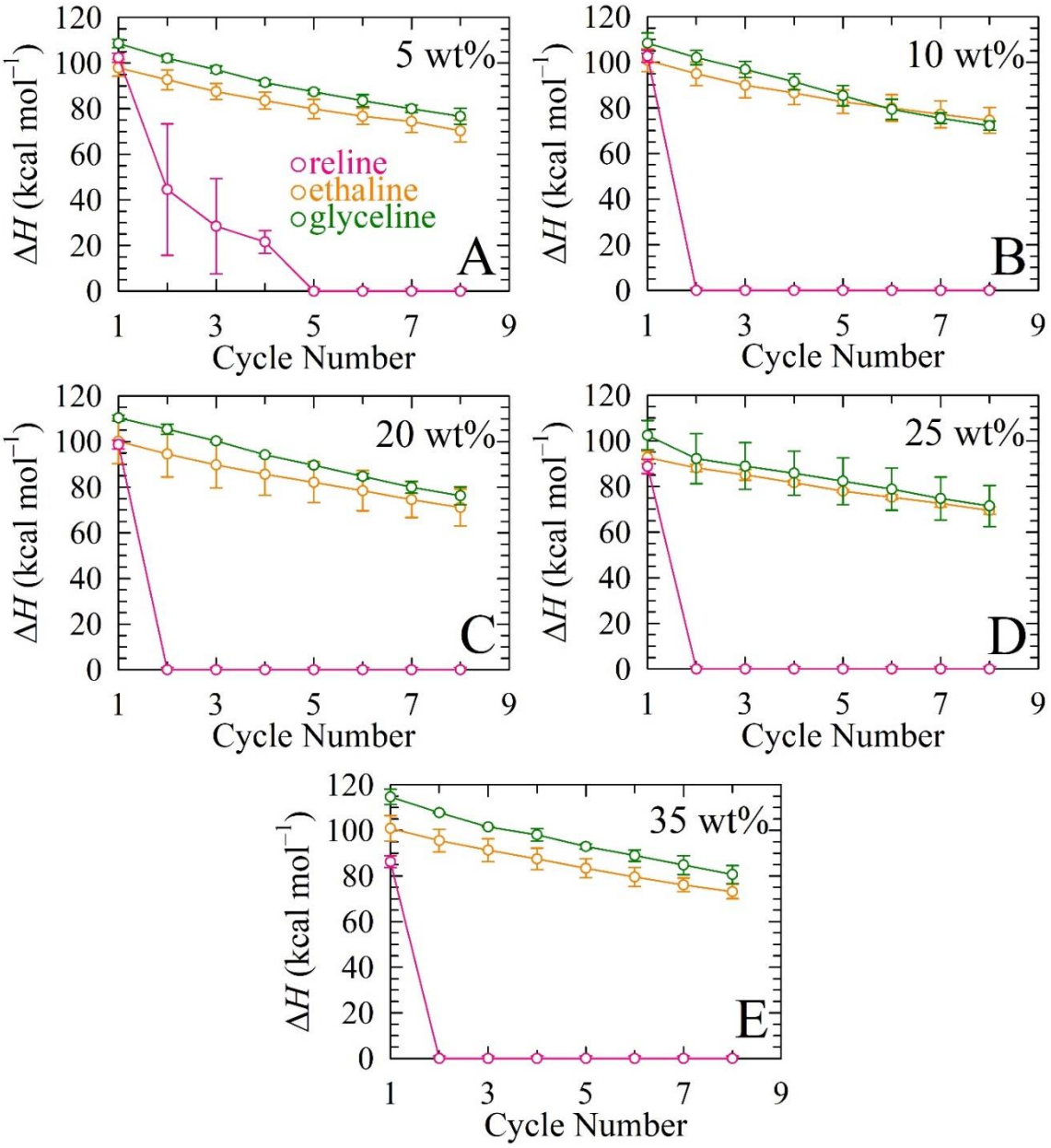

Figure A.7 Comparison of the van't Hoff enthalpies for RNase A in aqueous solutions containing reline (pink), ethaline (orange), and glyceline (green) at various wt% over eight consecutive heating/cooling cycles.

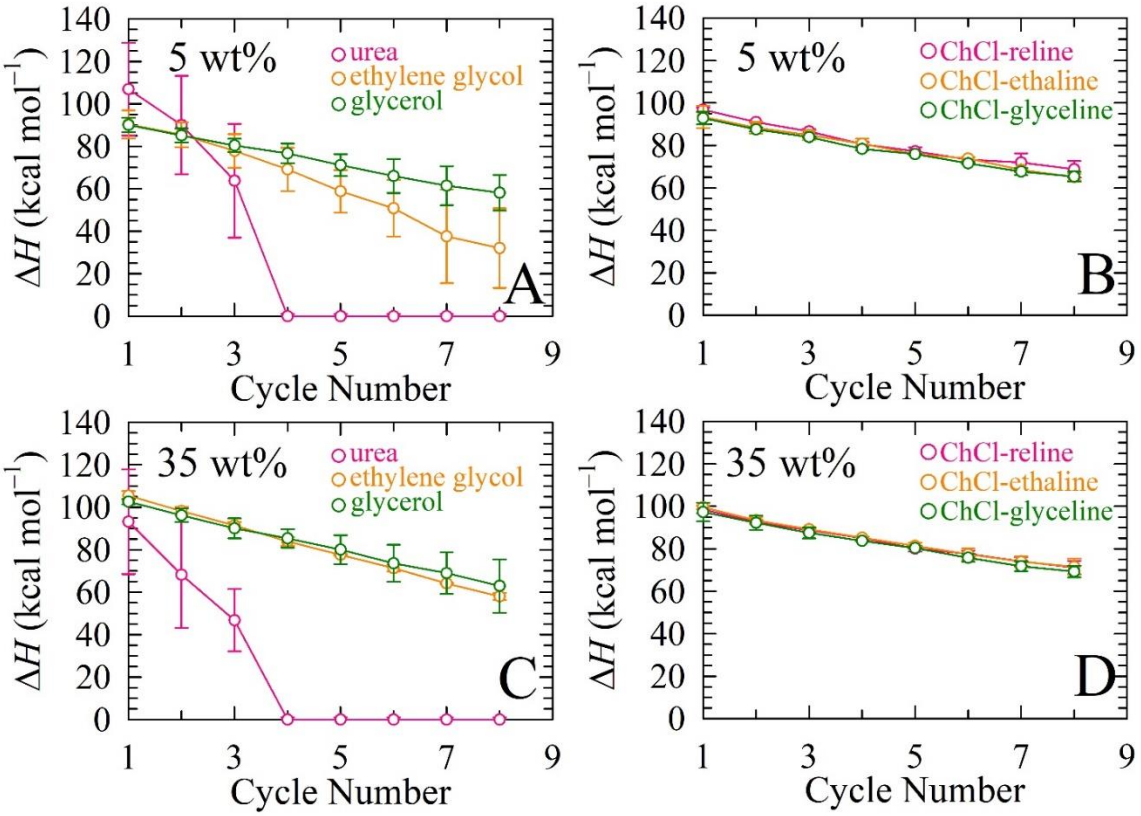

Figure A.8 Comparison of the van't Hoff enthalpies (ΔH_{vH}) for RNase A in aqueous solutions containing individual components: urea (pink), ethylene glycol (orange) and glycerol (green) over eight consecutive heating/cooling cycles. ChCl is abbreviated for choline chloride. All Panels show the individual component as per 5 and 35 wt% of their respective DES.

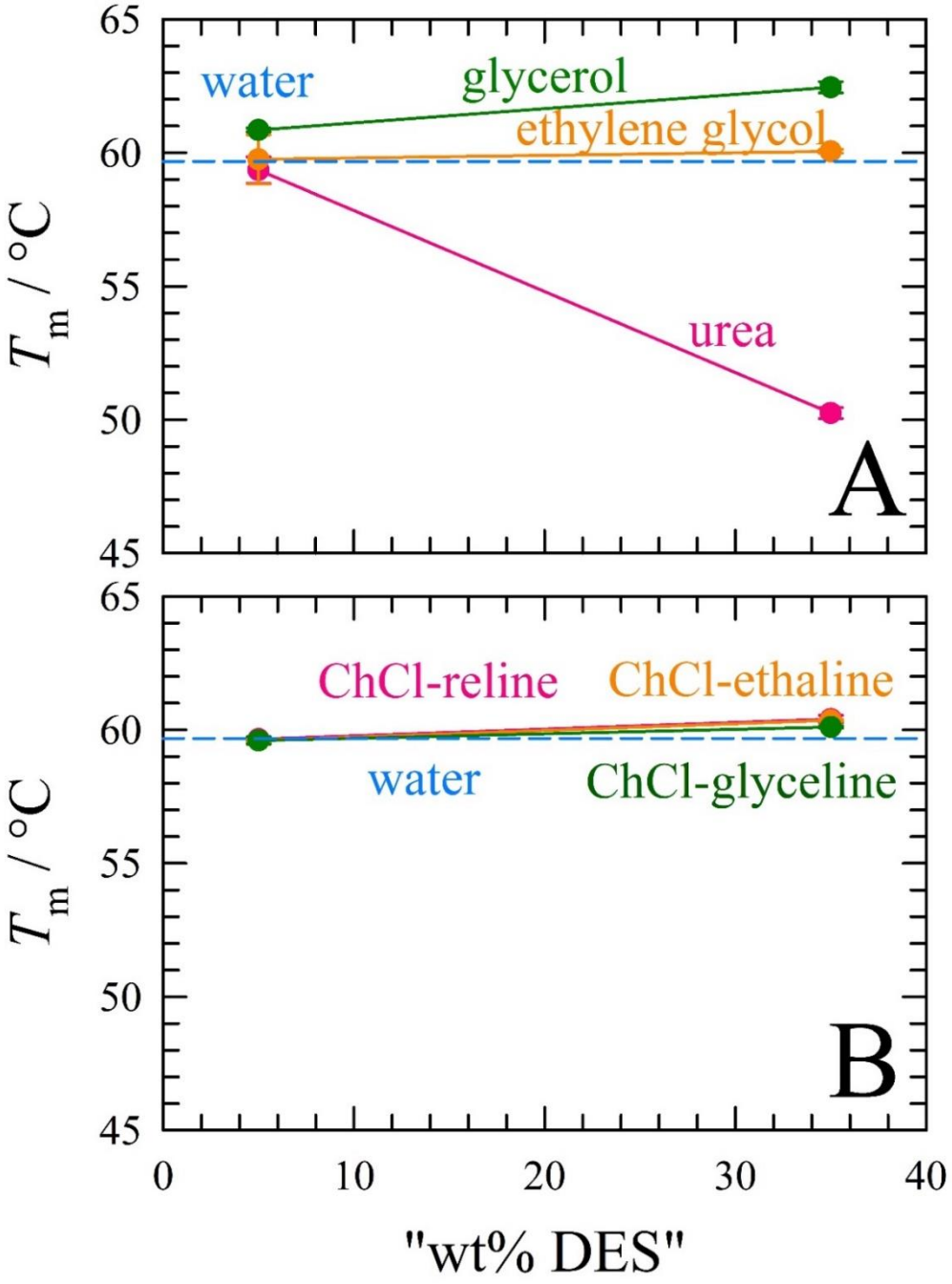

Figure A.9 Plot of the transition temperature, T_m, versus "wt% DES" for RNase A in aqueous solutions containing individual DES components. The "wt% DES" represents the individual component as per its respective DES. ChCl stands for choline chloride. The T_m for RNase A in water is shown for reference.

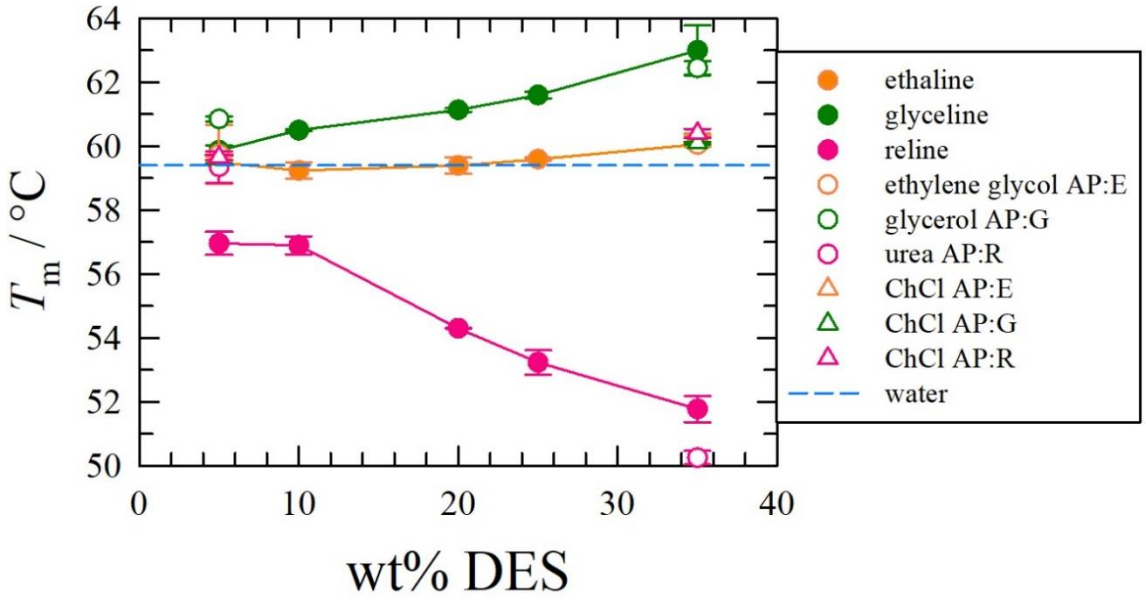

Figure A.10 A plot of the transition temperature, T_m, versus the wt% DES. RNase A in the three DESs (reline, ethaline, and glyceline) are shown with closed circles. The protein in individual DES components (ethylene glycol, glycerol, urea, and choline chloride) is shown with open circles and triangles. The abbreviation AP stands for as per, which corresponds to the same wt% in which the individual component participates in their respective DES (in this case, 5 and 35 wt%). E, G, and R stand for ethaline, glyceline, and reline, respectively. RNase A in ethylene glycol (open orange circle) is in line with the DES ethaline (closed orange circle). All the samples of RNase A in choline chloride (ChCl; open triangles) show a very similar T_m as compared with RNase A in ethaline.

Table A.1 The average RNase A concentration in various wt% DES after dialysis for at least three trials. The average concentration of RNase A in water after dialysis is also shown.

	5wt%	**10wt%**	**20wt%**	**25wt%**	**35wt%**
reline	4.16 mg mL^{-1}	3.85 mg mL^{-1}	3.90 mg mL^{-1}	4.32 mg mL^{-1}	4.28 mg mL^{-1}
ethaline	4.15 mg mL^{-1}	4.17 mg mL^{-1}	4.53 mg mL^{-1}	4.67 mg mL^{-1}	4.47 mg mL^{-1}
glyceline	3.59 mg mL^{-1}	3.61 mg mL^{-1}	3.72 mg mL^{-1}	3.79 mg mL^{-1}	3.98 mg mL^{-1}
water 3.96 mg mL^{-1}					

Table A.2 The average concentration of RNase A in individual DES components after dialysis for at least three trials.

	5 wt%	**35 wt%**
urea	3.99 mg mL^{-1}	4.10 mg mL^{-1}
ethlyene glycol	4.12 mg mL^{-1}	3.87 mg mL^{-1}
glycerol	4.21 mg mL^{-1}	3.96 mg mL^{-1}
ChCl-reline	4.1 mg mL^{-1}	4.21 mg mL^{-1}
ChCl-ethaline	4.18 mg mL^{-1}	4.25 mg mL^{-1}
ChCl-glyceline	4.18 mg mL^{-1}	4.27 mg mL^{-1}

Table A.3 The drop in ΔH_{vH} per cycle (kcal mol^{-1}/cycle) for RNase A in each of the various wt% DES.

	5 wt%	**10 wt%**	**20 wt%**	**25 wt%**	**35 wt%**
ethaline	3.9	3.8	4.1	3.3	4.0
glyceline	4.6	5.2	4.9	4.4	4.9
reline	26.9	86.5	82.0	76.0	58.2

Appendix B: Silver-mediated Squaric Acid Reduction as a Facile, Ambient-temperature and Seedless Route to Tunable Bimetallic Au/Ag Nanostars and Nanosnowflakes

†This chapter is based on a published manuscript in Chemistry of Nanomaterials for Energy, Biology, and More. The information contained herein is adapted with permission from **Kist, J. A.**; Essner, J. B.; Woodward, J. D.; and Baker, G. A., Silver-mediated squaric acid reduction as a facile, ambient-temperature and seedless route to tunable bimetallic Au/Ag nanostars and nanosnowflakes. Chem. Nano. Mat. **2022**, 8, e202200189. Copyright © 2022 Wiley Online Library.

As first author of this publication, I performed all experiments where I synthesized and characterized the bimetallic nanoparticles (except for TEM, EDX, XRD, and SAED analyses). I also wrote multiple drafts of the manuscript and created the figures.

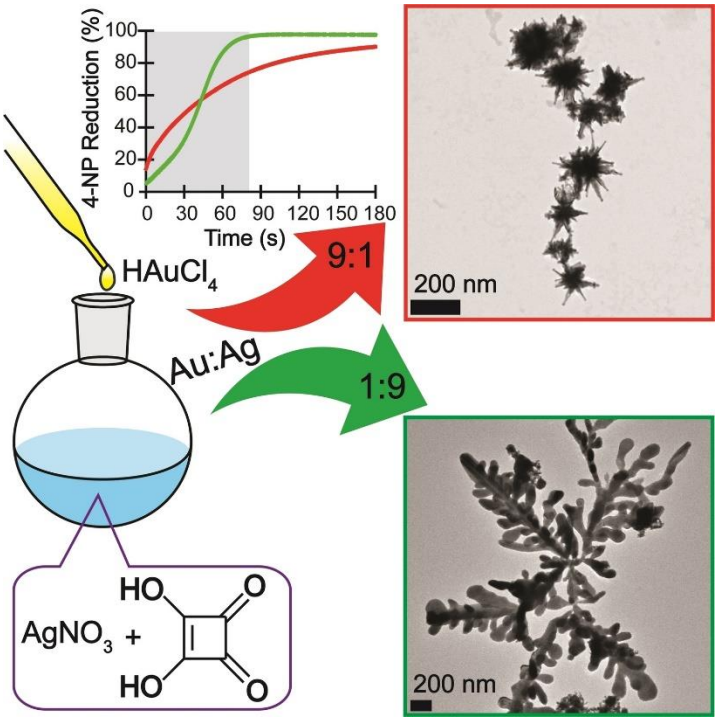

Scheme B.1 We report a simple, ambient-temperature, and single-pot route to bimetallic Au:Ag nanoparticles that employs squaric acid as the reducing and capping agent. Variation in the synthetic Au:Ag ratio reveals striking consequences for the nanoparticle morphology with related impact on the nanocatalytic activity toward nitroarene reduction.

Abstract

Bimetallic Au/Ag nanoparticles were successfully synthesized using a facile and reproducible method involving rapid, room-temperature mixing of aqueous solutions of $HAuCl_4$ and $AgNO_3$ in the presence of squaric acid as both the reducing agent and surface capping ligand. Variation in the initial Au:Ag molar ratio yielded a tunable anisotropic shape and affiliated surface plasmon resonance. The nanoparticles displayed excellent stability in water for at least 10 weeks and showed robust catalytic activity in the borohydride-assisted reduction of the model substrate 4-nitrophenol.

Introduction

Metal nanoparticles (NPs) have received great attention due to their unique optical, thermal, and chemical properties. These distinct properties directly result from the size, shape, and composition of the NPs, which also dictate how the nanoparticles interact with incident light. This gives rise to an energy-dependent resonance known as the localized surface plasmon resonance (LSPR).[1-2] Due to the tailorability of the size and shape of metal NPs, they have shown great success in a number of fields including surface-enhanced Raman spectroscopy (SERS), biomedicine, sensors, catalysis, and photovoltaics.[3-12] Interestingly, the properties of bimetallic NPs (BMNPs) often result in enhanced performance over their monometallic counterparts due to a synergistic coupling between the individual metals' LSPRs.[1, 13-17] A variety of approaches have been utilized to produce stable and high-performing NPs, including laser ablation,[18] microwave irradiation,[19] wet chemical reduction ($NaBH_4$,[20] hydrazine[21]), and use of organic solvents;[17] however, most of these techniques involve multi-step, tedious or time-consuming procedures, or entail the use of hazardous chemicals to aid in the reduction. Additionally, most anisotropic NPs rely

on a seed-mediated approach which has been shown to be labor intensive and can include intricate, difficult-to-replicate steps. Furthermore, the use of surfactants (*e.g.*, hexadecyltrimethylammonium bromide; CTAB) has been reported to stabilize NPs, although high toxicity to cells is a known limitation, ultimately hindering their use in biomedical applications. Therefore, it is of high importance to synthesize highly catalytically active and stable BMNPs, especially anisotropic structures, through environmentally friendly, facile, seedless, and surfactant- free routes.

In this appendix, bimetallic Au/Ag NPs were successfully synthesized at room temperature using a facile, seedless approach implementing the cyclic oxocarbon diacid, squaric acid (SA), as both the reducing and capping agent. The synthesis of Au NPs in the presence of SA has been recently reported;[2, 22] however, bimetallic Au/Ag NPs synthesized with this reducing agent have not been investigated, which further motivated this work. The LSPR and colloidal stability of the resultant BMNPs were monitored over 10 weeks via UV-Vis spectroscopy. Excitingly, varying the Au:Ag synthetic ratio resulted in tailored morphologies and surface plasmon resonances. High-resolution transmission electron microscopy (HRTEM) and energy dispersive X-ray spectroscopy (EDX) were performed to further examine the nanoscale morphologies and determine the relative incorporation of the metals. The crystal structures were investigated using X-ray diffraction (XRD) and selected area electron diffraction (SAED). In an additional set of experiments (herein denoted as Set 2), the initial [Au^{3+}] concentration was held constant while incremental volumes of $AgNO_3$ were added alongside a constant volume of SA, resulting in interesting plasmonic shifts. Lastly, the catalytic activities of as-synthesized and aged (1–10 weeks)

BMNPs were evaluated using the model borohydride-assisted 4-nitrophenol (4-NP) reduction reaction and compared against benchmark nanocatalysts.[23-24]

Experimental Section

Materials and reagents.

Squaric acid (SA; C-7254, ≥ 98%), tetrachloroauric acid ($HAuCl_4$; 520918, ≥ 99.9%), silver (I) nitrate ($AgNO_3$;204390, 99.9999%), 4-nitrophenol (4-NP; 241326, ≥ 99%), and sodium borohydride ($NaBH_4$; 480886, 99.99%) were all purchased from Sigma-Aldrich (St. Louis, Missouri). The numbers shown parenthetically are the catalog numbers and vendor-reported purities. All chemicals were used as received and all experiments were performed using Ultrapure Millipore water (18.2 MΩ · cm).

Characterization techniques.

Absorbance spectra were measured in disposable PMMA cuvettes using a Cary Bio 60 UV-Vis spectrophotometer scanning from 1100–200 nm, using a medium scan speed of 600 nm/min. Absorbance spectra were collected on samples every week over the course of 10 weeks to determine stability. Nitroarene reduction catalysis experiments were measured using the same UV-Vis spectrophotometer scanning from 800–200 nm, using a survey scan speed of 24,000 nm/min. Transmission electron microscopy (TEM) studies were performed on carbon coated and formvar-coated copper grids (Ted Pella, Inc., 01822-F, ultrathin carbon type-A, 400 mesh copper grid) using a FEI Technai (F30 G2, Twin) microscope operated at an accelerating voltage of 300 keV. As-prepared samples (within 10 min of synthesis) were drop-casted onto the grid and allowed to air dry before imaging. Bright field imaging and high-resolution TEM (HRTEM) were conducted. Energy-dispersive X-ray spectroscopy (EDX) was performed in STEM mode at 300 keV. EDX

spectra were collected on the areas of interest for at least two minutes to ensure adequate counts. To assess the elemental compositions of the bimetallic nanoparticles, EDX spectra from at least five different areas of particles were analyzed for the Au:Ag ratios using only the L lines of Au and Ag. The Au:Ag ratios for the spectra were calculated using TEM Imaging and Analysis (TIA), software provided by FEI, and the resultant values were averaged together to generate the % Au (or %Ag). Note that the TIA software determines %Au and %Ag values on an atomic % basis rather than a weight % basis. The composite elemental mapping images were generated in ImageJ, a public domain, open source, Java-based image processing program developed at the National Institutes of Health (NIH). PXRD analysis was performed using a Rigaku SmartLab X-ray diffractometer equipped with monochromatic Cu-kα source (λ = 1.541826 A) and operated at 40 kV and 44 mA over a scanning range of 15–90° 2θ. The size of the nanoparticles was determined using dynamic light scattering (Zetasizer Nano-ZS).

Bimetallic nanoparticle synthesis.

(Set 1) In a typical synthesis of squaric acid-reduced bimetallic NPs (SA-BMNPs), aliquots of 5 mM chloroauric acid ($HAuCl_4$) (0.9–0.1 mL) were added to falcon tubes filled with deionized water (9.1–9.9 mL) to bring the total volume to 10.0 mL. In a second set of falcon tubes, 0.1–0.9 mL of 5 mM silver(I) nitrate ($AgNO_3$) were added to 1 mL of 17 mM SA and 8.9–8.1 mL of water to give a total volume of 10.0 mL. The $HAuCl_4$ (*aq*) solution was then added to the SA/Ag solution via vortexing to ensure homogenous mixing at room temperature to give Au:Ag initial molar ratios of 9:1, 8:2, 7:3, 6:4, 5:5, 4:6, 3:7, 2:8, and 1:9. For Set 1, the total ([Au]+[Ag]) metal concentration was fixed at 0.25 mM.

(Set 2) For the studies employing a constant $HAuCl_4$ concentration, the final concentration and total volume of 5 mM $HAuCl_4$ used in the synthesis was held constant at 0.25 mM and 1.0 mL, respectively, and was incorporated with 9.0 mL water in one falcon tube. The volume of $AgNO_3$ (5.0 or 0.5 mM) was systematically varied alongside 1.0 mL 17 mM SA and water to give a total volume of 10.0 mL in a second falcon tube. The aqueous Au solution was added to the aqueous SA/$AgNO_3$ solution via vortexing at room temperature just as previously described and the final solution volume was 20.0 mL. The initial molar ratios for Au:Ag were 1: *x*, where *x* = 1.0, 0.10, 0.050, 0.030, 0.025, 0.020, 0.016, 0.014, 0.012, 0.011, 0.010, 0.005, 0.0033, 0.0025, 0.0020, 0.00010, and 0. Note, the samples implementing Au:Ag 1: *x* ratios of 1: 200 - 1: 1000 (*x* = 0.005, 0.0033, 0.0025, 0.0020, 0.00010), 0.5 mM $AgNO_3$ was used in place of 5 mM $AgNO_3$. For Set 2, the total metal concentration varied from 0.5 mM (1:1 Au:Ag) to 0.25 mM (1:0 Au:Ag). All samples were stored at room temperature in 50 mL centrifuge tubes, protected from light. Note, all stock solutions were freshly prepared prior to experiments.

Catalytic activity measurements

To assess the catalytic activity of the SA-BMNPs towards 4-nitrophenol (4-NP) reduction, 0.9 mL of freshly prepared 0.1 M aqueous $NaBH_4$ was added to 2.1 mL of aqueous 0.2 mM 4-NP solution in a 4 mL PMMA cuvette to yield a deep yellow solution, indicative of the formation of the 4-nitrophenolate ion (4-NPO). Upon addition of an effective nanocatalyst, the absorption decreased in real time, the pale-yellow color disappeared, and 4-aminophenol (4-AP) was produced, which was apparent due to the formation of an absorbance peak at 300 nm. To initiate the reaction, 84 μL of 0.25 mM aqueous SA-BMNP solution prepared using Set 1 conditions was added to the above mixture and gently

homogenized (slow manual inversion five times) to avoid bubble generation. The samples were tested within ten minutes of preparation except for the aged studies. The reduction of 4-NP to 4-AP was monitored at room temperature using a Cary Bio 60 UV-Vis spectrophotometer, collecting spectra every 15 s in the scanning range of 800–200 nm at a scan speed of 24,000 nm/min. To test catalytic rates of SA-BMNPs over time, NP solutions aged for 12 h, 24 h, 1 week, 2 weeks, 5 weeks and 10 weeks were investigated with Au:Ag ratios of 9:1, 1:1, and 1:9.

Control experiments were also conducted where 4-NP and $NaBH_4$ were used in the absence of SA-BMNP metal catalyst (just SA was used), and no decrease in 4-NPO was observed, confirming that catalysis resulted from the SA-BMNPs and not the reducing agent. To test the recyclability of SA-BMNPs as catalysts over multiple reaction cycles, as-synthesized and aged (12 h, 24 h, 1 week, 2 weeks) SA-BMNPs (Au:Ag 1:9) were used in the 4-NP reduction process, with 84 μL of 5 mM 4-NP and 90 μL of 1 M $NaBH_4$ (both freshly prepared) added to the cuvette once the previous reaction had gone to completion (the solution was no longer yellow and the peak at 400 nm disappeared). This process was repeated for a total of five times. For all catalysis experiments, apparent rate constants (k_{app}) were calculated from the linear correlation of $\ln(A_0/A_t)$ versus time plots, where A_0 and A_t denote the initial 400 nm absorbance for 4-NPO and the time-dependent absorbance at 400 nm, respectively. Of note, all assessments of catalytic rates were conducted at 5 mol% total metal (Au + Ag) relative to 4-NP.

Results and Discussion

The detailed experimental procedures for synthesizing and characterizing the SA-reduced Au/Ag BMNPs (herein, SA-BMNPs) are provided in the experimental section above as Set 1. Briefly, appropriate aliquots of $HAuCl_4(aq)$ were added to falcon tubes containing water while aliquots of $AgNO_3(aq)$ were added alongside SA(aq) and water in another set of falcon tubes. The $HAuCl_4(aq)$ and $AgNO_3$/SA(aq) solutions of appropriate concentrations were mixed together at room temperature via vortexing to yield Au:Ag molar ratios of 9:1, 8:2, 7:3, 6:4, 5:5, 4:6, 3:7, 2:8, and 1:9. Note, the aqueous metal solutions were generated in separate falcon tubes to avoid the formation of AgCl(s) prior to reduction and $AgNO_3$ was paired with SA as no reduction or NP formation was evident at room temperature, even after weeks of storage.

As a preliminary assessment of BMNP formation, the resultant SA-BMNPs were spectroscopically analyzed using UV-Vis spectroscopy. Figure B.1A shows the absorbance spectra for the as-synthesized SA-BMNPs (measured within 10 min of synthesis) and the appearance of the corresponding solutions is provided in Figure B.1B. Varying the initial Au:Ag ratio in the reaction resulted in tunable LSPR maxima in the range of 740–950 nm. The broad, single plasmon absorption band widths and resulting blue solutions are consistent with nanostar formation.

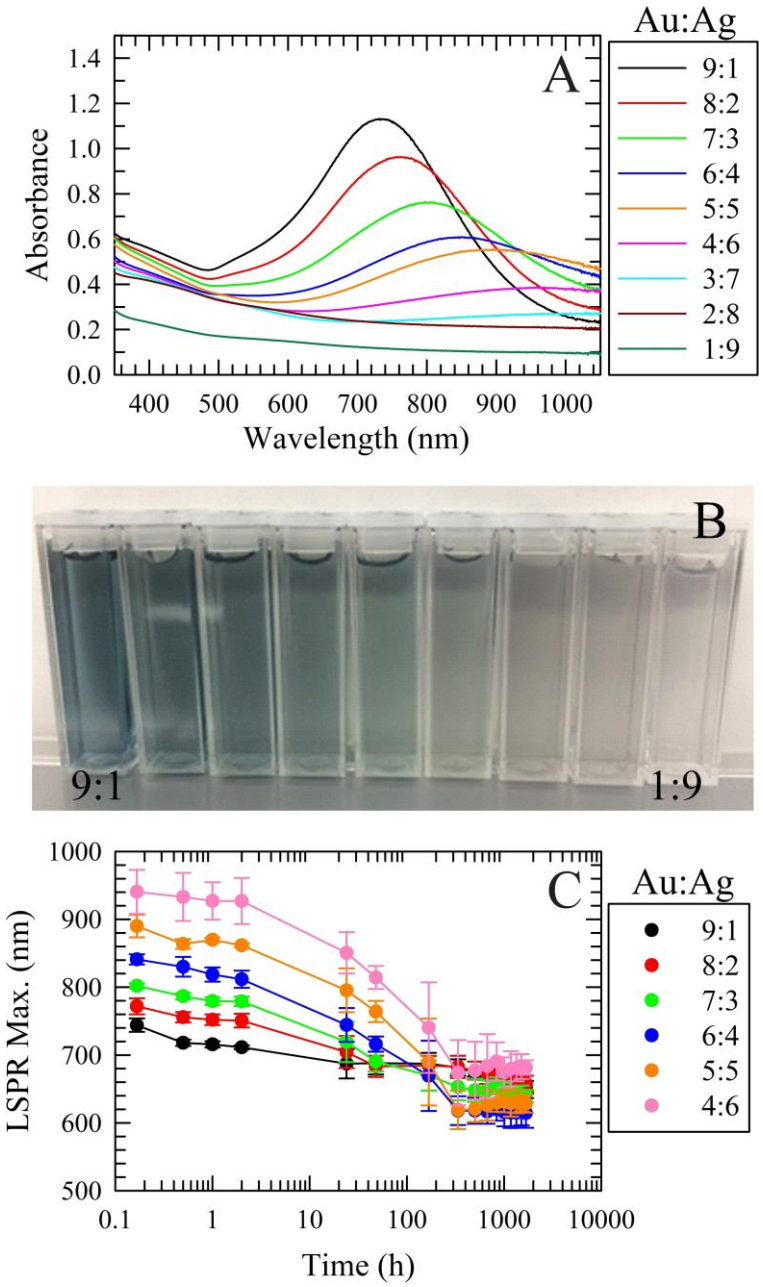

Figure B.1 (Panel A) Absorbance spectra of as-synthesized Au/Ag bimetallic NPs using squaric acid as a dual reducing and stabilizing agent. Measurements were taken within 10 min after synthesis. The shifting LSPR bands of the resultant SA-BMNPs show the evident tunability achieved simply by modulating the initial Au:Ag ratio (shown in the legend). Note, the total metal concentration (Au + Ag) was 0.25 mM for all samples. Panel B shows the corresponding SA-BMNP solutions for all tested ratios, with the Au:Ag ratio proceeding from 9:1 to 1:9 left to right. The stability of the solutions was evaluated over

10 weeks (1680 h) and the LSPR maxima were extracted and plotted in Panel C. Even though a hypsochromic shift is seen in the absorbance spectra, the solutions remain blue in color. Note, the Au:Ag ratios of 3:7, 2:8, and 1:9 are not represented in Panel C due to lack of distinguishable band features in their absorbance spectra (refer to Panel A).

As the proportion of Au decreased, the intensity of the absorption for the as-prepared SA-BMNPs showed a pronounced bathochromic shift. Incorporating higher concentrations of Ag^+ (in the form of $AgNO_3$) has been shown to progressively red-shift the plasmon band to longer wavelengths, most likely due to the formation of interior hollows and hierarchical (*e.g.*, more branched) NPs,[25-26] allowing for tunability among the samples. The stability of the SA-BMNPs was monitored via UV-Vis spectroscopy over the course of 10 weeks. Note, all samples were stored in a lab drawer devoid of light until time of characterization. The associated LSPR maxima are summarized in Figure B.1C. Initially (*i.e.*, after 24 h), the LSPR maxima of all samples exhibited hypsochromic shifts ranging from 57 to 97 nm, after which, the LSPR continued to blue shift until finally stabilizing after three weeks of aging (504 h). Throughout the 10 weeks, Au:Ag 9:1 displayed the smallest temporal shift in LSPR starting at 744 nm and ending at 653 nm (91 nm shift).

The plasmonic shifts were more dramatic for equimolar samples or those containing excess Ag, with Au:Ag 5:5 starting at 890 nm and ending at 629 nm (261 nm shift) and Au:Ag 4:6 starting at 940 nm and ending at 682 nm (258 nm shift) after 10 weeks. Notably, for plasmonic nanostructures with a single peak, a change in the LSPR wavelength often indicates a change in the NP size, shape, or dielectric property.[27-30] Note, SA-BMNPs employing Au:Ag ratios of 3:7, 2:8, and 1:9 are not shown in Figure B.1C due to lack of distinguishable LSPR peaks in their absorbance spectra (refer to Panel A). Figure B.2A

displays a representative transmission electron microscopy (TEM) image for SA-BMNPs derived from a 9:1 stoichiometric Au:Ag experimental ratio, revealing a spiny nanostar morphology. The average particle size was determined to be 208 nm, with spike lengths and widths averaging 76.1 nm and 17.4 nm, respectively.

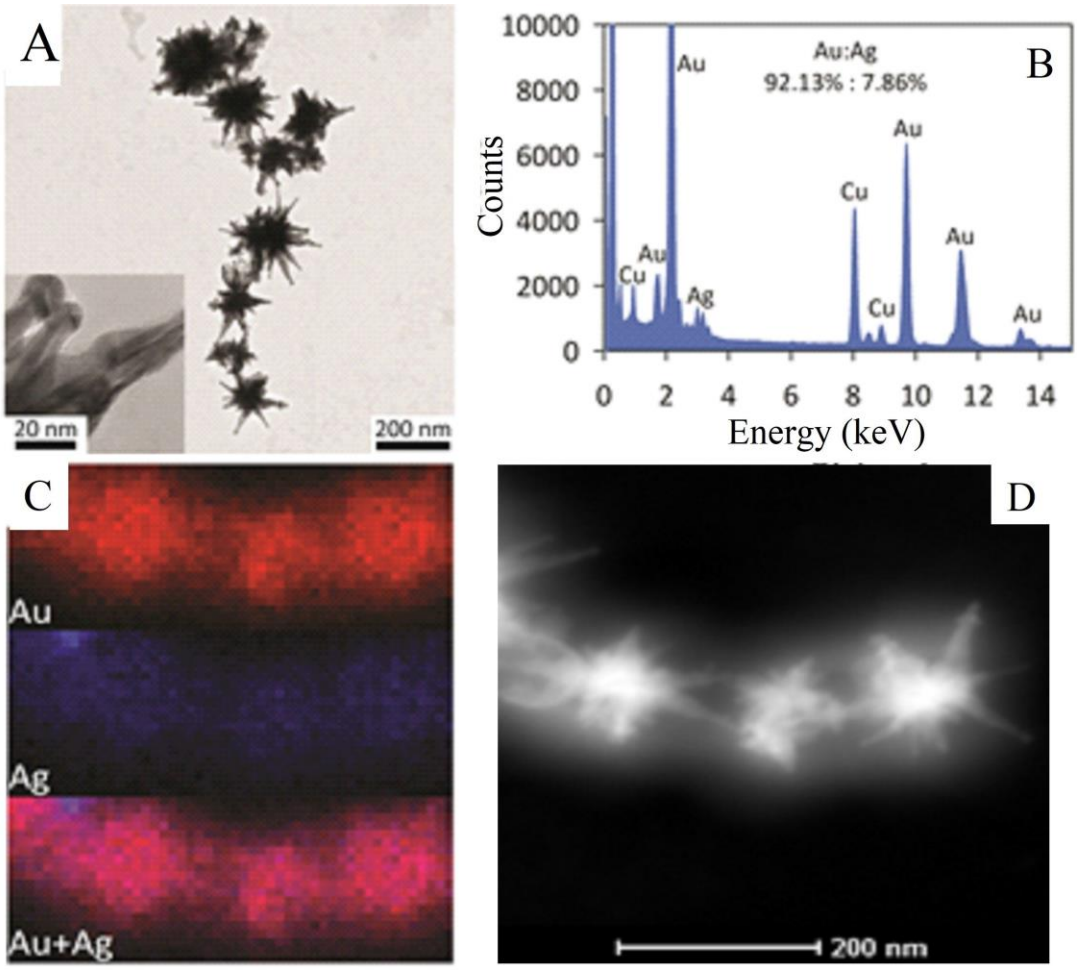

Figure B.2 (A) Representative TEM image of as-synthesized SA-BMNPs for a 9:1 Au:Ag ratio displaying a spiky nanostar morphology. The inset in Panel A shows one of the spikes on the nanoparticles. (B) EDX results indicating 92% Au and 7.9% Ag, resulting from a 9:1 Au:Ag experimental ratio. The presence of Cu results from the TEM grid. (C) The EDX elemental mapping of Au and Ag which suggests their uniform distribution throughout the SA-BMNPs. (D) Reference image from which the elemental mapping was taken.

Energy-dispersive X-ray (EDX) microanalysis of the Au:Ag 9:1 nanostars was performed to determine the composition of the bimetallic colloids, the results of which are given in Figure B.2B. The percentages of metals present were determined to be 92% Au and 7.9% Ag, in good agreement with the 9:1 Au:Ag ratio employed. Elemental mapping, shown in Figure B.2C–D, suggests the two metals appear to be homogeneously dispersed throughout the SA-BMNPs. EDX microanalysis was also performed on samples employing Au:Ag ratios of 1:1 and 1:9, which yielded results of 41% Au and 59% Ag and 14% Au and 86% Ag, respectively. The elemental mapping and EDX results for Au:Ag 1:1 and 1:9 can be seen in Figures C.1 and C.2, respectively.

To monitor evolution in morphology, TEM was performed on SA-BMNP samples with Au:Ag ratios of 9:1 (Figure B.3 top row, Panels A–C), 5:5 (*i.e.*, 1:1; middle row, Panels D–F) and 1:9 (bottom row, Panels G–I) at different time points including as synthesized (as-synth; < 30 min after synthesis), 24 h post-synthesis, and six weeks post-synthesis. The nanostar morphology seen in Au:Ag 9:1 compares well with previous literature examples of nanostar or nanourchin-like particles, although their syntheses typically implemented ascorbic acid as a reducing agent and a separate surfactant as a stabilizing/capping agent.[31-35] The Au:Ag 1:1 sample exhibited more nanocube-like structures over nanostars, with minor quasi-spherical SA-BMNPs formation observed 24 h after synthesis (Panel E). Interestingly, the SA-BMNPs with a 1:9 Au:Ag ratio displayed large dendritic morphologies somewhat reminiscent of a nanosnowflake shape.

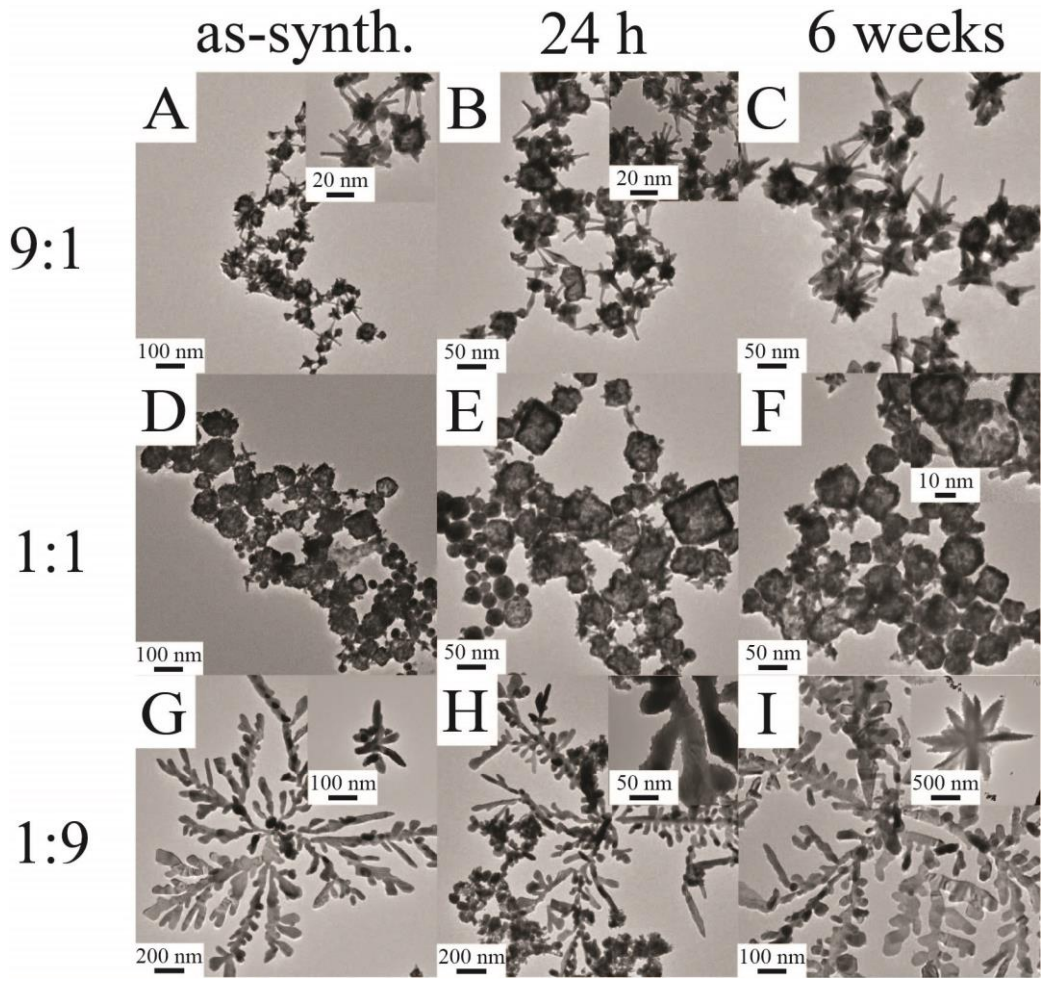

Figure B.3. Representative TEM images for SA-BMNPs with Au:Ag ratios of 9:1 (top row), 1:1 (middle row), and 1:9 (bottom row) throughout various aging time points. The SA-BMNPs employing a 9:1 Au:Ag ratio showed a nanostar morphology even after 6 weeks post-synthesis. The as-synthesized SA-BMNPs with a 1:1 Au:Ag ratio displayed a mixture of nanostars, nanocubes, and a few quasi-spherical NPs but displayed mostly nanocubes after 24 h and remained consistent throughout 6 weeks after synthesis. Lastly, the 1:9 Au:Ag SA-BMNPs exhibited nanosnowflake morphologies regardless of aging time.

These SA-BMNPs exhibited fractal morphologies ranging from hundreds of nanometers to microns in size. Garcia-Leis *et al.* have reported similar snowflake morphologies by reducing Ag^+ with hydroxylamine and citrate and adjusting the reducing agent/Ag^+ ratio.[36]

Additionally, Ag^+ has been shown to promote the growth of anisotropic gold NPs due to Ag blocking select facets on gold limiting further growth to specific directions, resulting in spikey, branched structures.[33, 37] Herein, Ag^+ is most likely behaving as a directional growth agent based on the data presented.

Dynamic light scattering (DLS) was performed on as-synthesized (< 1 h) SA-BMNPs with Au:Ag ratios of 9:1, 1:1, and 1:9 and yielded average sizes of 86 nm, 120 nm, and 320 nm, respectively. To investigate the crystal structure, X-ray diffraction (XRD) patterns were measured and recorded on select BMNP systems that had been lyophilized 1 h after synthesis (Figure C.3, Panel A) and lyophilized 24 h after synthesis (Figure C.3, Panel B), which resulted in five reflections in the 2θ range of 15–85°. According to these results, all of the SA-BMNPs had diffraction peaks, located at 38.20°, 44.40°, and 64.80°, corresponding to the (111), (200), and (220) planes, although the intensities lessened as the amount of Au decreased. The (111) diffraction plane typically corresponds to a d spacing value of 0.238 nm for the lattice fringes of gold nanostars, suggesting a polycrystalline face-centered cubic (fcc) structure of the SA-BMNPs.[38] The structure is in agreement with the data for Joint Committee on Powder Diffraction Standard (JCPDS; file no. 04-0784).[39] Additionally, the peak associated with the (111) plane in the Au:Ag 9:1 sample was much sharper and stronger compared to the other peaks. For samples that were lyophilized 1 h after synthesis, the ratios between the relative intensity of the (200) and (111) planes were calculated to be 0.38, 0.32, and 0.34 for Au:Ag 9:1, 1:1, and 1:9, respectively, while, for the samples that were lyophilized 24 h after synthesis, the ratios were determined to be 0.33, 0.29, and 0.36. These values are lower than the typical value observed (0.52), which suggests that the (111) plane is the predominant orientation in the growth of these NPs.[38,

[40-41] Diffraction peaks at 77.57° and 81.75° corresponding to (311) and (222) planes were also observed throughout all samples, although the intensities were the greatest in Au:Ag 9:1. These peaks also confirmed the fcc lattice structure for the bimetallic NPs.[42-47] The selected area electron diffraction (SAED) patterns further confirmed that the SA-BMNPs particles were polycrystalline due to the diffraction rings shown in Figure C.4.

In another set of experiments (known as Set 2 in the experimental section), the concentrations of Au and SA were kept constant while the Ag concentration was incrementally decreased to yield a Au:Ag ratio of 1:0 from the initial ratio of 1:1. The resulting absorbance spectra (Figure B.4A) reveal that as the amount of Ag decreased, the plasmon band hypsochromically shifted towards that of monometallic Au NPs (*i.e.*, LSPR of 520 nm). The corresponding solutions are shown in Figure B.4B, with the Au:Ag ratio of 1:1 resulting in a bluish-gray solution, transitioning through green-blue and purple solutions when less Ag was used, and ending with pink-red solutions for the lowest Ag content (1:0.001 Au:Ag). The stability of the SA-BMNPs was monitored over five weeks by following the LSPR maxima (Figure C.5, Panel A). Overall, a > 100 nm blue shift was observed after one week in some samples, transitioning to pink/red-colored solutions from their initial blue- or purple-colored solutions, as shown in Figure C.5, panel B. Note, total metal concentration varied from 0.5 mM (1:1 Au:Ag) to 0.25 mM (1:0 Au:Ag). This is different than Set 1 where the total metal concentration was held static at 0.25 mM. This concentration difference resulted in two different plasmon bands for the samples of Au:Ag 1:1. The initial LSPR maximum for Au:Ag 1:1 using Set 1 conditions was 890 nm, whereas 767 nm was the initial LSPR maximum for the same ratio using Set 2 parameters. These results clearly show that the LSPR maxima can be tuned by adjusting the [Ag]/[Au], further

evidenced by fitting the data to a 4-parameter sigmoidal curve, which can be seen in Figure. C.6.

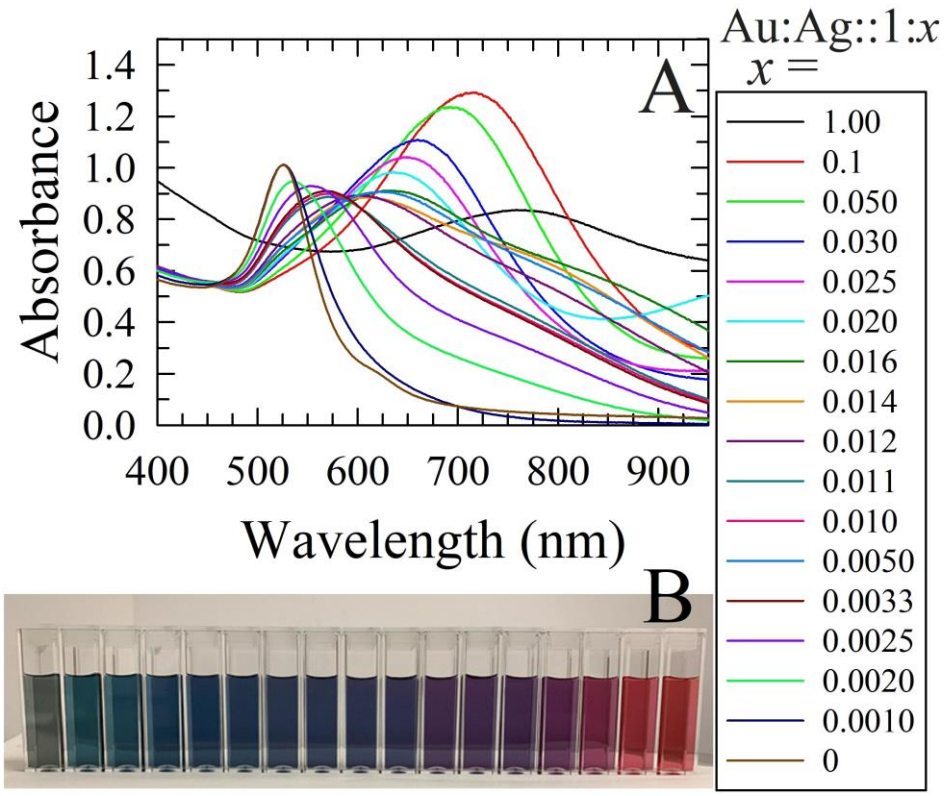

Figure B.4 (A) Absorbance spectra of as-synthesized (10 min after synthesis) SA-BMNPs made employing various Au:Ag mole fractions (see legend) at a fixed $HAuCl_4$ precursor concentration of 0.25 mM. An increase in the relative amount of Ag lead to a bathochromic shift away from 520 nm (the LSPR peak for AuNPs). Note: the total metal concentration varied from 0.5 mM (1:1 Au:Ag) to 0.25 mM (1:0 Au:Ag). (B) The appearance of the corresponding samples, displaying a visually distinct color transition from teal/blue (1:1 Au:Ag, left) to red (1:0 Au: Ag, right) taken 1 h after synthesis.

Lastly, the catalytic activities of as-synthesized and aged SA-BMNPs were evaluated using the model borohydride-assisted 4-nitrophenol (4-NP) reduction reaction. Typically, 4-NP in water exhibits an absorbance peak centered around 320 nm (Figure

C.7A, black line) and displays a pale-yellow color. Addition of $NaBH_4$ to 4-NP induces a deep dark yellow coloration, accompanying a shift to 400 nm, arising from the deprotonation of 4-NP to produce the 4-nitrophenolate ion (4-NPO), shown in Figure C.7A (red line). In the absence of catalyst, the 4-NPO absorbance peak at 400 nm remains unaltered with time. However, upon addition of an appropriate catalyst (such as Au or Ag NPs), a drastic decrease in absorbance at 400 nm is observed, eventually resulting in a complete loss of yellow color, while simultaneously, the emergence of a new peak at 300 nm arises from the 4-aminophenol (4-AP) product. Due to these colorimetric changes, this assay is easily monitored through UV-Vis spectroscopy (the exact procedure can be found in the experimental section). Control experiments were first performed to rule out catalytic contribution from the reducing agent itself. An aqueous solution of squaric acid was tested for BH_4-assisted 4-NP reduction over a 3000 s monitoring period. As can be in seen in Figure C.7B, the 400 nm peak for the 4-NPO ion remained unchanged, verifying that any contribution to the catalytic reduction of 4-NP from the reducing agent was negligible.

The catalytic activities of the SA-BMNPs were then evaluated, and the conversion of 4-NP to 4-AP was essentially complete within 300 s, 141 s, and 74 s for as-synthesized SA-BMNPs employing Au:Ag ratios of 9:1, 1:1, and 1:9, respectively, as shown in Figure C.8. It has been discussed previously that catalytic activity increases with increased spike lengths in NPs.[48] Additionally, dendritic nanostructures have been reported to have excellent electrocatalytic activities due to their very high surface-to-volume ratio, high specific surface area, and abundant active sites.[49-51] These unique morphological properties are most likely the reason why the nanosnowflakes seen in Au:Ag 1 :9 SA-BMNPs herein resulted in much faster catalytic rates. The concentration of $NaBH_4$ employed far exceeded

that of 4-NP (by a factor of ~500), which allowed us to safely assume that the conversion followed pseudo-first order kinetics. In this fashion, the apparent rate constant (k_{app}) could be estimated from the slope of the linear correlation between $\ln(A_0/A_t)$ and time (t) where A_0 and A_t denote the initial absorbance measured at 400 nm and the time-dependent absorbance at 400 nm, respectively. The k_{app} values determined for the as-synthesized SA-BMNP catalysts with Au:Ag ratios of 9:1, 1 :1, and 1:9 were 1.39 (± 0.002) × 10^{-2} s^{-1}, 2.08 (± 0.001) × 10^{-2} s^{-1}, and 9.76 (± 0.019) × 10^{-2} s^{-1}, respectively (Figure B.5A). The activities of these catalysts were excellent considering the modest catalyst dosage used (5 mol%) with respect to the 4-NP. Indeed, examinations of catalytic efficiency using this model reaction are sometimes performed at catalyst dosages of 20–50 mol%.[52] Additionally, these catalytic rates were faster or comparable to several previously reported examples of bimetallic Au/Ag nanocatalysts tested for 4-NP reduction.[1, 43, 53-59] Turnover frequency (TOF) should be reported alongside (or in place of k_{app}) as it allows for more reliable and straightforward comparisons to be made between catalysts.[60] TOF can be calculated using the following expression:

$$TOF = \frac{n_{4-NP}}{(n_m)(t_{rxn})} x \frac{completion\ \%}{100}$$

where $n_{4\text{-NP}}$ and n_m denote the moles of 4-NP and moles of total metal (Au + Ag) in the nanocatalyst, respectively, and t_{rxn} is the reaction time in hours. As per our previous recommendations, we define t_{rxn} as the time required to attain an $\ln(A_0/A_t)$ of 3 (95% reaction completion).[60] The resulting TOFs of the as-synthesized SA-BMNPs with Au:Ag ratios of 9:1, 1:1, and 1:9 were 228 h^{-1}, 485 h^{-1}, and 924 h^{-1}, respectively. From a previous report, the TOFs for 30.4 nm squarate-reduced Au NPs and 15.8 nm citrate-capped AuNPs

were 57 h^{-1} and 161 h^{-1}, respectively.[2] Additionally, 33 nm ascorbate-reduced Au NPs have resulted in a TOF of 84 h^{-1}.[60]

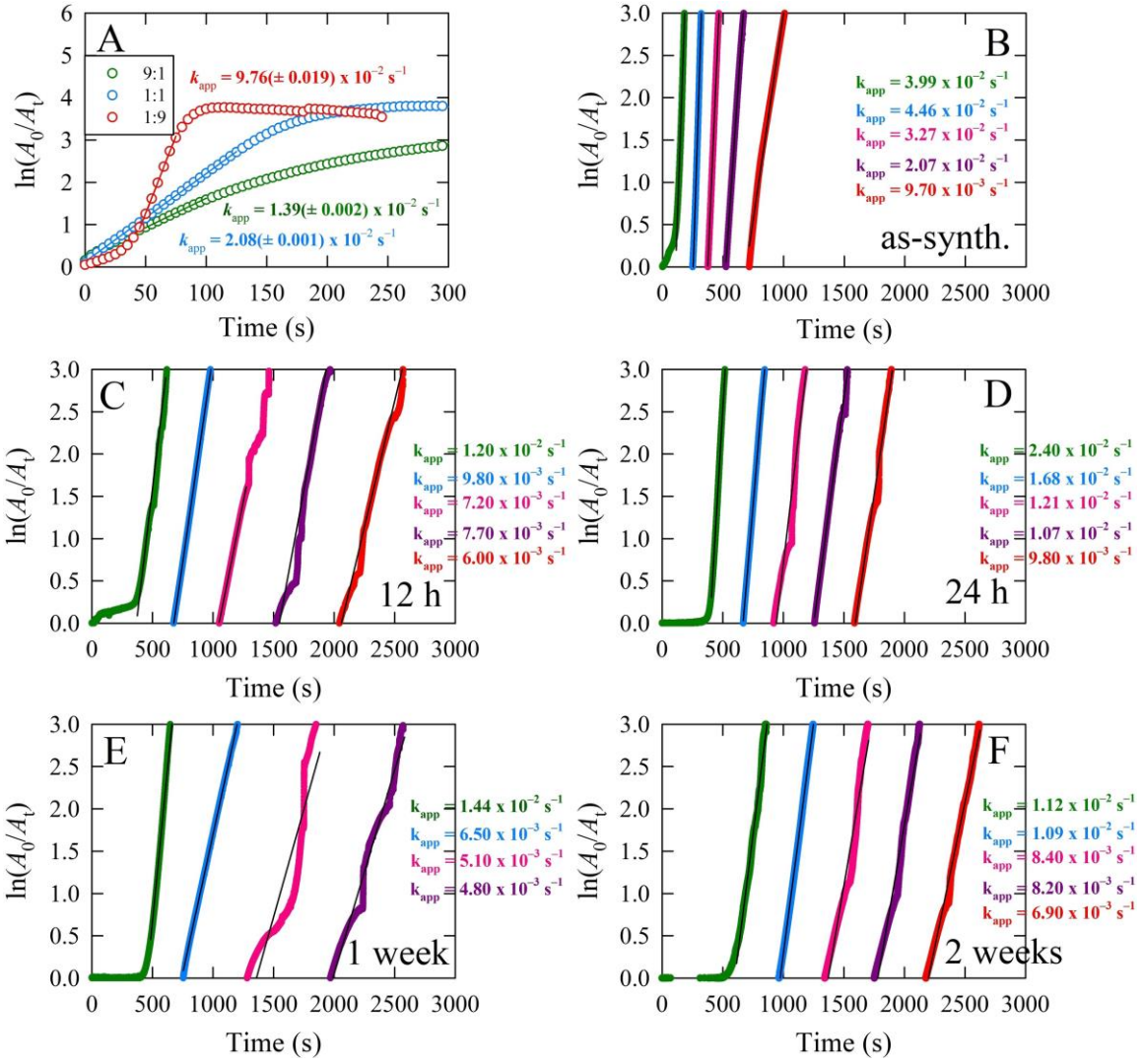

Figure B.5 Panel A shows the ln(A_0/A_t) of 4-NP against time for SA-BMNPs with Au:Ag ratios of 9:1, 1:1, and 1:9, monitored at 400 nm. The apparent rate constant, k_{app} was determined by the slope of the linear region. Each catalyst was tested within ten minutes of preparation using a 5 mol% catalyst concentration. Panels B–F display the influence of the number of repeated uses of fresh and aged SA-BMNP catalysts (Au:Ag ratio of 1:9) on the apparent 4-NP reduction rate. For these latter studies, the metal catalyst concentration was lowered to one-fifth of the original catalyst concentration (1 mol%) in order to slow down the kinetics to more readily capture the initial rate via UV-Vis.

These results demonstrate how the synergistic effects of BMNPs can lead to faster catalytic rates over their monometallic counterparts.[1, 15-16] This improvement in catalytic activity could be accounted for by the electronic charge transfer effects between the elements. For Au/Ag BMNPs, the ionization potentials of Au and Ag are 9.22 and 7.58 eV, respectively. The electronic charges could transfer from Ag atoms to Au atoms in a particle and lead to an increase in electron density on the Au, which would then act as catalytically active sites for the redox reaction to proceed in a kinetically favorable manner.[61] The primary role of the catalyst is to facilitate electron transfer from BH_4^- to 4-NPO ion at the nanoparticle surface.[62]

A lag phase or induction period can be observed in some samples (Panel A of Figure B.5, red line), likely due to the slow transfer of electrons from the metal hydride to the 4-NPO as well as the time required for dissolved oxygen to fall below a critical level.[63-65] This phenomenon can be considered a rate-determining step of this reaction. Such an induction time has been observed previously for different carrier systems.[53] Interestingly, 9:1, 1:1, and 1:9 SA-BMNPs from Set 1 continued to display promising catalytic efficacy after 12 h of aging, despite the observed LSPR shifts. Specifically, these samples displayed apparent catalytic rates of 1.05 ($\pm$ 0.001) $\times$ 10^{-2} s^{-1}, 1.80 ($\pm$ 0.002) $\times$ 10^{-2} s^{-1}, 9.79 ($\pm$ 0.011) $\times$ 10^{-2} s^{-1}, respectively, as shown in Figure C.9. The corresponding TOFs were 210 h^{-1}, 382 h^{-1}, and 547 h^{-1}. It is important to note that the manifest reduction in TOF for the 1:9 SA-BMNP catalyst relative to the as-synthesized sample, in spite of essentially identical apparent rates, is accounted for by the observation of a lag time before the reaction proceeds. Catalysis was also performed on samples that had been aged for 24 h, 1 week, 2 weeks, 5 weeks, and 10 weeks, the results of which are shown in Figures C.10–C.14. Note,

the Au:Ag 1:9 sample started to aggregate after 5 weeks, so catalytic assessment was not performed beyond that time. Additionally, the resulting k_{app} and TOF values for all aged samples can be found in Table C.1. To evaluate the robustness and stability of the SA-BMNPs as catalysts for 4-NP reduction, the activity over several consecutive reactive cycles for as-synthesized SA-BMNPs employing the Au:Ag ratio of 1:9 was measured, the results of which can be seen in Figure B.5B. When the original metal catalyst concentration was implemented, the initial rate was difficult to capture through UV-Vis measurements for the iterative cycles due to the very rapid catalysis, so it was determined that one fifth of the original metal catalyst concentration (1 mol%) was needed in order to successfully capture the initial rate. Recyclability studies were performed on Au:Ag 1:9 SA-BMNPs that were aged 12 h, 24 h, 1 week and 2 weeks (Figure B.5C–F). Even after 2 weeks, the nanoparticles were able to successfully complete five iterative cycles with very good rates. It is important to note, though, the rate decreased after each cycle. The resulting k_{app} and TOF values of the samples for each cycle are given in Table C.2.

Conclusions

In summary, this work presents a facile, room-temperature method to rapidly synthesize Au/Ag BMNPs using squaric acid as a dual reducing and mild stabilizing agent. The sizes and morphologies showed broad tailorability by altering the Au:Ag ratio. These SA-BMNPs displayed good stability in aqueous solutions and exhibited strong catalytic activity. We also showed that they could be reused as catalysts for 4-NP reduction even after multiple consecutive reaction cycles. The plasmonic tailorability of these NIR-absorbing bimetallic nanoparticles bodes well for future applications in surface-enhanced spectroscopies, such as SERS, and biomedical purposes (*e.g.*, photothermal therapy).

References

1. Essner, J. B.; Laber, C. H.; Baker, G. A., Carbon Dot Reduced Bimetallic Nanoparticles: Size and Surface Plasmon Resonance Tunability for Enhanced Catalytic Applications. *J. Mater. Chem. A* **2015,** *3* (31), 16354-16360.

2. Larm, N. E.; Essner, J. B.; Pokpas, K.; Canon, J. A.; Jahed, N.; Iwuoha, E. I.; Baker, G. A., Room-Temperature Turkevich Method: Formation of Gold Nanoparticles at the Speed of Mixing Using Cyclic Oxocarbon Reducing Agents. *J. Phys. Chem. C* **2018,** *122* (9), 5105-5118.

3. Chang, J.; Zhang, A.; Huang, Z.; Chen, Y.; Zhang, Q.; Cui, D., Monodisperse Au@Ag Core-Shell Nanoprobes with Ultrasensitive Sers-Activity for Rapid Identification and Raman Imaging of Living Cancer Cells. *Talanta* **2019,** *198*, 45-54.

4. Mu, Z.; Zhao, X.; Xie, Z.; Zhao, Y.; Zhong, Q.; Bo, L.; Gu, Z., In Situ Synthesis of Gold Nanoparticles (Aunps) in Butterfly Wings for Surface Enhanced Raman Spectroscopy (Sers). *J. Mater. Chem. B* **2013,** *1* (11), 1607-1613.

5. Sharma, V. K.; Yngard, R. A.; Lin, Y., Silver Nanoparticles: Green Synthesis and Their Antimicrobial Activities. *Adv. Colloid Interface Sci.* **2009,** *145* (1), 83-96.

6. Chernousova, S.; Epple, M., Silver as Antibacterial Agent: Ion, Nanoparticle, and Metal. *Angew. Chem. Int. Ed.* **2013,** *52* (6), 1636-1653.

7. Lee, K.-S.; El-Sayed, M. A., Gold and Silver Nanoparticles in Sensing and Imaging: Sensitivity of Plasmon Response to Size, Shape, and Metal Composition. *J. Phys. Chem. B* **2006,** *110* (39), 19220-19225.

8. Yu, C.; Irudayaraj, J., Multiplex Biosensor Using Gold Nanorods. *Anal. Chem.* **2007,** *79* (2), 572-579.

9. Sarina, S.; Waclawik, E. R.; Zhu, H., Photocatalysis on Supported Gold and Silver Nanoparticles under Ultraviolet and Visible Light Irradiation. *Green Chem.* **2013,** *15* (7), 1814-1833.

10. Standridge, S. D.; Schatz, G. C.; Hupp, J. T., Distance Dependence of Plasmon-Enhanced Photocurrent in Dye-Sensitized Solar Cells. *J. Am. Chem. Soc.* **2009,** *131* (24), 8407-8409.

11. Chen, M.; Goodman, D. W., Catalytically Active Gold: From Nanoparticles to Ultrathin Films. *Acc. Chem. Res.* **2006,** *39* (10), 739-746.

12. Siegel, A. L.; Baker, G. A., Bespoke Nanostars: Synthetic Strategies, Tactics, and Uses of Tailored Branched Gold Nanoparticles. *Nanoscale Advances* **2021,** *3* (14), 3980-4004.

13. Chang, H.; Kang, H.; Yang, J.-K.; Jo, A.; Lee, H.-Y.; Lee, Y.-S.; Jeong, D. H., Ag Shell–Au Satellite Hetero-Nanostructure for Ultra-Sensitive, Reproducible, and Homogeneous Nir Sers Activity. *ACS Appl. Mater. Interfaces* **2014,** *6* (15), 11859-11863.

14. Haldar, K. K.; Kundu, S.; Patra, A., Core-Size-Dependent Catalytic Properties of Bimetallic Au/Ag Core–Shell Nanoparticles. *ACS Appl. Mater. Interfaces* **2014,** *6* (24), 21946-21953.

15. Ravula, S.; Essner, J. B.; La, W. A.; Polo-Parada, L.; Kargupta, R.; Hull, G. J.; Sengupta, S.; Baker, G. A., Sunlight-Assisted Route to Antimicrobial Plasmonic Aminoclay Catalysts. *Nanoscale* **2015,** *7* (1), 86-91.

16. Larm, N. E.; Thon, J. A.; Vazmitsel, Y.; Atwood, J. L.; Baker, G. A., Borohydride Stabilized Gold–Silver Bimetallic Nanocatalysts for Highly Efficient 4-Nitrophenol Reduction. *Nanoscale Advances* **2019,** *1* (12), 4665-4668.

17. Liu, S.; Chen, G.; Prasad, P. N.; Swihart, M. T., Synthesis of Monodisperse Au, Ag, and Au–Ag Alloy Nanoparticles with Tunable Size and Surface Plasmon Resonance Frequency. *Chem. Mater.* **2011,** *23* (18), 4098-4101.

18. Lee, I.; Han, S. W.; Kim, K., Production of Au–Ag Alloy Nanoparticles by Laser Ablation of Bulk Alloys. *Chem. Commun.* **2001,** (18), 1782-1783.

19. Pal, A.; Shah, S.; Devi, S., Synthesis of Au, Ag and Au–Ag Alloy Nanoparticles in Aqueous Polymer Solution. *Colloids Surf. A Physicochem. Eng. Asp.* **2007,** *302* (1), 51-57.

20. Liz-Marzan, L. M.; Philipse, A. P., Stable Hydrosols of Metallic and Bimetallic Nanoparticles Immobilized on Imogolite Fibers. *J. Phys. Chem.* **1995,** *99* (41), 15120-15128.

21. Chen, D.-H.; Chen, C.-J., Formation and Characterization of Au–Ag Bimetallic Nanoparticles in Water-in-Oil Microemulsions. *J. Mater. Chem.* **2002,** *12* (5), 1557-1562.

22. Islam, M. T.; Padilla, J. E.; Dominguez, N.; Alvarado, D. C.; Alam, M. S.; Cooke, P.; Tecklenburg, M. M. J.; Noveron, J. C., Green Synthesis of Gold Nanoparticles Reduced and Stabilized by Squaric Acid and Supported on Cellulose Fibers for the Catalytic Reduction of 4-Nitrophenol in Water. *RSC Adv.* **2016,** *6* (94), 91185-91191.

23. Ciganda, R.; Li, N.; Deraedt, C.; Gatard, S.; Zhao, P.; Salmon, L.; Hernández, R.; Ruiz, J.; Astruc, D., Gold Nanoparticles as Electron Reservoir Redox Catalysts for 4-Nitrophenol Reduction: A Strong Stereoelectronic Ligand Influence. *Chem. Commun.* **2014,** *50* (70), 10126-10129.

24. Herves, P.; Perez-Lorenzo, M.; Liz-Marzan, L. M.; Dzubiella, J.; Lu, Y.; Ballauff, M., Catalysis by Metallic Nanoparticles in Aqueous Solution: Model Reactions. *Chem. Soc. Rev.* **2012,** *41* (17), 5577-5587.

25. Hsiangkuo, Y.; Christopher, G. K.; Hanjun, H.; Christy, M. W.; Gerald, A. G.; Tuan, V.-D., Gold Nanostars: Surfactant-Free Synthesis, 3d Modelling, and Two-Photon Photoluminescence Imaging. *Nanotechnology* **2012,** *23* (7), 075102.

26. Li, J.; Zhou, J.; Jiang, T.; Wang, B.; Gu, M.; Petti, L.; Mormile, P., Controllable Synthesis and Sers Characteristics of Hollow Sea-Urchin Gold Nanoparticles. *Phys. Chem. Chem. Phys.* **2014,** *16* (46), 25601-25608.

27. Shuai, H.; Malvin Wei Cherng, K.; Fahima Jaleel, K.; Eddie Khay Ming, T.; Miguel Arnold, R.; James Chen Yong, K., Optimizing Gold Nanostars as a Colloid-Based Surface-Enhanced Raman Scattering (Sers) Substrate. *J. Opt.* **2015,** *17* (11), 114013.

28. Njoki, P. N.; Lim, I. I. S.; Mott, D.; Park, H.-Y.; Khan, B.; Mishra, S.; Sujakumar, R.; Luo, J.; Zhong, C.-J., Size Correlation of Optical and Spectroscopic Properties for Gold Nanoparticles. *J. Phys. Chem. C* **2007,** *111* (40), 14664-14669.

29. Anker, J. N.; Hall, W. P.; Lyandres, O.; Shah, N. C.; Zhao, J.; Van Duyne, R. P., Biosensing with Plasmonic Nanosensors. *Nat. Mater.* **2008,** *7*, 442.

30. Ghosh, S. K.; Pal, T., Interparticle Coupling Effect on the Surface Plasmon Resonance of Gold Nanoparticles: From Theory to Applications. *Chem. Rev.* **2007,** *107* (11), 4797-4862.

31. Silvestri, A.; Lay, L.; Psaro, R.; Polito, L.; Evangelisti, C., Fluidic Manufacture of Star-Shaped Gold Nanoparticles. *Chem.-Eur. J.* **2017,** *23* (41), 9732-9735.

32. He, S.; Kang, M. W. C.; Khan, F. J.; Tan, E. K. M.; Reyes, M. A.; Kah, J. C. Y., Optimizing Gold Nanostars as a Colloid-Based Surface-Enhanced Raman Scattering. *J. Opt.* **2015,** *17* (11), 114013.

33. Cheng, L.-C.; Huang, J.-H.; Chen, H. M.; Lai, T.-C.; Yang, K.-Y.; Liu, R.-S.; Hsiao, M.; Chen, C.-H.; Her, L.-J.; Tsai, D. P., Seedless, Silver-Induced Synthesis of Star-Shaped Gold/Silver Bimetallic Nanoparticles as High Efficiency Photothermal Therapy Reagent. *J. Mater. Chem.* **2012,** *22* (5), 2244-2253.

34. Krajczewski, J.; Kołątaj, K.; Pietrasik, S.; Kudelski, A., Silica-Covered Star-Shaped Au-Ag Nanoparticles as New Electromagnetic Nanoresonators for Raman Characterisation of Surfaces. *Spectrochim. Acta A* **2018,** *193*, 1-7.

35. He, S.; Chua, J.; Tan, E. K. M.; Kah, J. C. Y., Optimizing the Sers Enhancement of a Facile Gold Nanostar Immobilized Paper-Based Sers Substrate. *RSC Adv.* **2017,** *7* (27), 16264-16272.

36. Garcia-Leis, A.; Rivera-Arreba, I.; Sanchez-Cortes, S., Morphological Tuning of Plasmonic Silver Nanostars by Controlling the Nanoparticle Growth Mechanism: Application in the Sers Detection of the Amyloid Marker Congo Red. *Colloids Surf. A Physicochem. Eng. Asp.* **2017,** *535* (Supplement C), 49-60.

37. Atta, S.; Beetz, M.; Fabris, L., Understanding the Role of Agno3 Concentration and Seed Morphology in the Achievement of Tunable Shape Control in Gold Nanostars. *Nanoscale* **2019,** *11* (6), 2946-2958.

38. Ma, H.; Liu, Z.; Wei, Y.; Jiang, L., Controlled Morphology Evolution of Branched Au Nanostructures and Their Shape-Dependent Catalytic and Photo-Thermal Properties. *Colloids Surf. A Physicochem. Eng. Asp.* **2019,** *582*, 123889.

39. Bayliss, P., Mineral Powder Diffraction File Date Book. *JCPDS* **1986**.

40. Jena, B. K.; Raj, C. R., Synthesis of Flower-Like Gold Nanoparticles and Their Electrocatalytic Activity Towards the Oxidation of Methanol and the Reduction of Oxygen. *Langmuir* **2007,** *23* (7), 4064-4070.

41. Wu, H.-Y.; Liu, M.; Huang, M. H., Direct Synthesis of Branched Gold Nanocrystals and Their Transformation into Spherical Nanoparticles. *J. Phys. Chem. B* **2006,** *110* (39), 19291-19294.

42. Yuan, C.-G.; Huo, C.; Gui, B.; Cao, W.-P., Green Synthesis of Gold Nanoparticles Using Citrus Maxima Peel Extract and Their Catalytic/Antibacterial Activities. *IET Nanobiotechnology* **2017,** *11* (5), 523-530.

43. Cui, Q.; Xia, B.; Mitzscherling, S.; Masic, A.; Li, L.; Bargheer, M.; Möhwald, H., Preparation of Gold Nanostars and Their Study in Selective Catalytic Reactions. *Colloids Surf. A Physicochem. Eng. Asp.* **2015,** *465*, 20-25.

44. Song, C. Y.; Yang, B. Y.; Chen, W. Q.; Dou, Y. X.; Yang, Y. J.; Zhou, N.; Wang, L. H., Gold Nanoflowers with Tunable Sheet-Like Petals: Facile Synthesis, Sers Performances and Cell Imaging. *J. Mater. Chem. B* **2016,** *4* (44), 7112-7118.

45. Chatterjee, S.; Ringane, A. B.; Arya, A.; Das, G. M.; Dantham, V. R.; Laha, R.; Hussian, S., A High-Yield, One-Step Synthesis of Surfactant-Free Gold Nanostars and Numerical Study for Single-Molecule Sers Application. *J. Nanopart. Res.* **2016,** *18* (8), 242.

46. Jafari, M.; Rokhbakhsh-Zamin, F.; Shakibaie, M.; Moshafi, M. H.; Ameri, A.; Rahimi, H. R.; Forootanfar, H., Cytotoxic and Antibacterial Activities of Biologically Synthesized Gold Nanoparticles Assisted by Micrococcus Yunnanensis Strain J2. *Biocatalysis and Agricultural Biotechnology* **2018,** *15*, 245-253.

47. Chan, J. Z.; Rasit Ali, R.; Shameli, K.; Salleh, M. S. N.; Lee, K. X.; Mohamed Isa, E. D., Green Synthesis of Gold Nanoparticles Using Aqueous Extract of Clitoria Ternatea Flower. *IOP Conference Series: Materials Science and Engineering* **2020,** *808*, 012036.

48. Ma, T.; Yang, W.; Liu, S.; Zhang, H.; Liang, F., A Comparison Reduction of 4-Nitrophenol by Gold Nanospheres and Gold Nanostars. *Catalysts* **2017,** *7* (2), 38.

49. Huang, D.; Bai, X.; Zheng, L., Ultrafast Preparation of Three-Dimensional Dendritic Gold Nanostructures in Aqueous Solution and Their Applications in Catalysis and Sers. *J. Phys. Chem. C* **2011,** *115* (30), 14641-14647.

50. Liang, Y.; Ma, T.; Xiong, Y.; Qiu, L.; Yu, H.; Liang, F., Highly Efficient Blackberry-Like Trimetallic Pdaucu Nanoparticles with Optimized Pd Content for Ethanol Electrooxidation. *Nanoscale* **2021,** *13* (22), 9960-9970.

51. Ma, T.; Liang, F., Au–Pd Nanostars with Low Pd Content: Controllable Preparation and Remarkable Performance in Catalysis. *J. Phys. Chem. C* **2020,** *124* (14), 7812-7822.

52. Dinda, E.; Rashid, M. H.; Biswas, M.; Mandal, T. K., Redox-Active Ionic-Liquid-Assisted One-Step General Method for Preparing Gold Nanoparticle Thin Films: Applications in Refractive Index Sensing and Catalysis. *Langmuir* **2010,** *26* (22), 17568-17580.

53. Wright, A. R.; Li, M.; Ravula, S.; Cadigan, M.; El-Zahab, B.; Das, S.; Baker, G. A.; Warner, I. M., Soft- and Hard-Templated Organic Salt Nanoparticles with the Midas Touch: Gold-Shelled Nanogumbos. *J. Mater. Chem. C* **2014,** *2* (42), 8996-9003.

54. Hareesh, K.; Sunitha, D. V.; Dhole, S. D.; Bhoraskar, V. N.; Phase, D. M.; Williams, J., One-Step Gamma Radiation Aided Diffusion of Ag-Au Alloy Nanoparticles into Polycarbonate and Its Application Towards the Reduction of 4-Nitrophenol. *Radiat. Phys. Chem.* **2019,** *162*, 126-130.

55. Rodríguez, R. C.; Troiani, H.; Moya, S. E.; Bruno, M. M.; Angelomé, P. C., Bimetallic Ag-Au Nanoparticles inside Mesoporous Titania Thin Films: Synthesis by Photoreduction and Galvanic Replacement, and Catalytic Activity. *Eur. J. Inorg. Chem.* **2020,** *2020* (6), 568-574.

56. Ulker, D.; Kocak, G.; Tuncer, C.; Butun, V., Preparation of Monometallic and Bimetallic Alloy Nanoparticles Stabilized with Sulfobetaine-Based Block Copolymer and Their Catalytic Activities. *Colloid Polym. Sci.* **2019,** *297* (7), 1067-1078.

57. Zafer, Ç.; Ceren, G.; Bengü, G.; Atila, Y.; Nuray, Y., Catalytic Performance of Ag, Au and Ag-Au Nanoparticles Synthesized by Lichen Extract. *Green Processing and Synthesis* **2018,** *7* (5), 433-440.

58. Hu, D.; Xiao, Y.; Liu, H.; Wang, H.; Li, J.; Zhou, B.; Liu, P.; Shen, M.; Shi, X., Loading of Au/Ag Bimetallic Nanoparticles within Electrospun Pva/Pei Nanofibers for Catalytic Applications. *Colloids Surf. A Physicochem. Eng. Asp.* **2018,** *552*, 9-15.

59. Arora, N.; Mehta, A.; Mishra, A.; Basu, S., 4-Nitrophenol Reduction Catalysed by Au-Ag Bimetallic Nanoparticles Supported on Ldh: Homogeneous Vs. Heterogeneous Catalysis. *Appl. Clay Sci.* **2018,** *151*, 1-9.

60. Larm, N. E.; Bhawawet, N.; Thon, J. A.; Baker, G. A., Best Practices for Reporting Nanocatalytic Performance: Lessons Learned from Nitroarene Reduction as a Model Reaction. *New J. Chem.* **2019,** *43* (46), 17932-17936.

61. Zhang, H.; Toshima, N., Fabrication of Catalytically Active Agau Bimetallic Nanoparticles by Physical Mixture of Small Au Clusters with Ag Ions. *Appl. Catal. A: Gen.* **2012,** *447-448*, 81-88.

62. Lam, E.; Hrapovic, S.; Majid, E.; Chong, J. H.; Luong, J. H. T., Catalysis Using Gold Nanoparticles Decorated on Nanocrystalline Cellulose. *Nanoscale* **2012,** *4* (3), 997-1002.

63. Wunder, S.; Polzer, F.; Lu, Y.; Mei, Y.; Ballauff, M., Kinetic Analysis of Catalytic Reduction of 4-Nitrophenol by Metallic Nanoparticles Immobilized in Spherical Polyelectrolyte Brushes. *J. Phys. Chem. C* **2010,** *114* (19), 8814-8820.

64. Menumerov, E.; Hughes, R. A.; Neretina, S., Catalytic Reduction of 4-Nitrophenol: A Quantitative Assessment of the Role of Dissolved Oxygen in Determining the Induction Time. *Nano Lett.* **2016,** *16* (12), 7791-7797.

65. Neal, R. D.; Inoue, Y.; Hughes, R. A.; Neretina, S., Catalytic Reduction of 4-Nitrophenol by Gold Catalysts: The Influence of Borohydride Concentration on the Induction Time. *J. Phys. Chem. C* **2019,** *123* (20), 12894-12901.

Appendix C: Supporting Figures for Appendix B- Silver-mediated Squaric Acid Reduction as a Facile, Ambient-temperature and Seedless Route to Tunable Bimetallic Au/Ag Nanostars and Nanosnowflakes

Jennifer A. Kist, Jeremy B. Essner, Jonathan D. Woodward, and Gary A. Baker

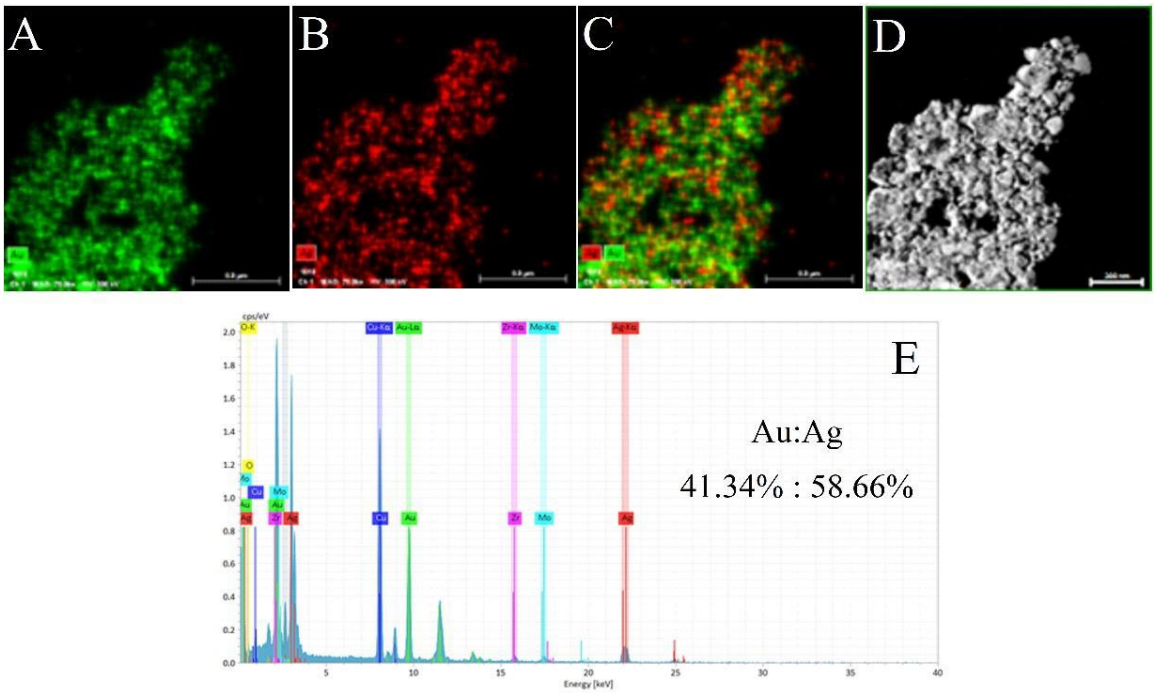

Figure C.1 Elemental mapping for as-synthesized Au:Ag BMNPs with ratio 1:1, showing Au in Panel A, Ag in Panel B, and both metals in Panel C. Panel D is the reference image from which the elemental mapping was taken. The EDX results in Panel E indicate 41.34% Au and 58.66% Ag, resulting from a 1:1 Au:Ag experimental ratio.

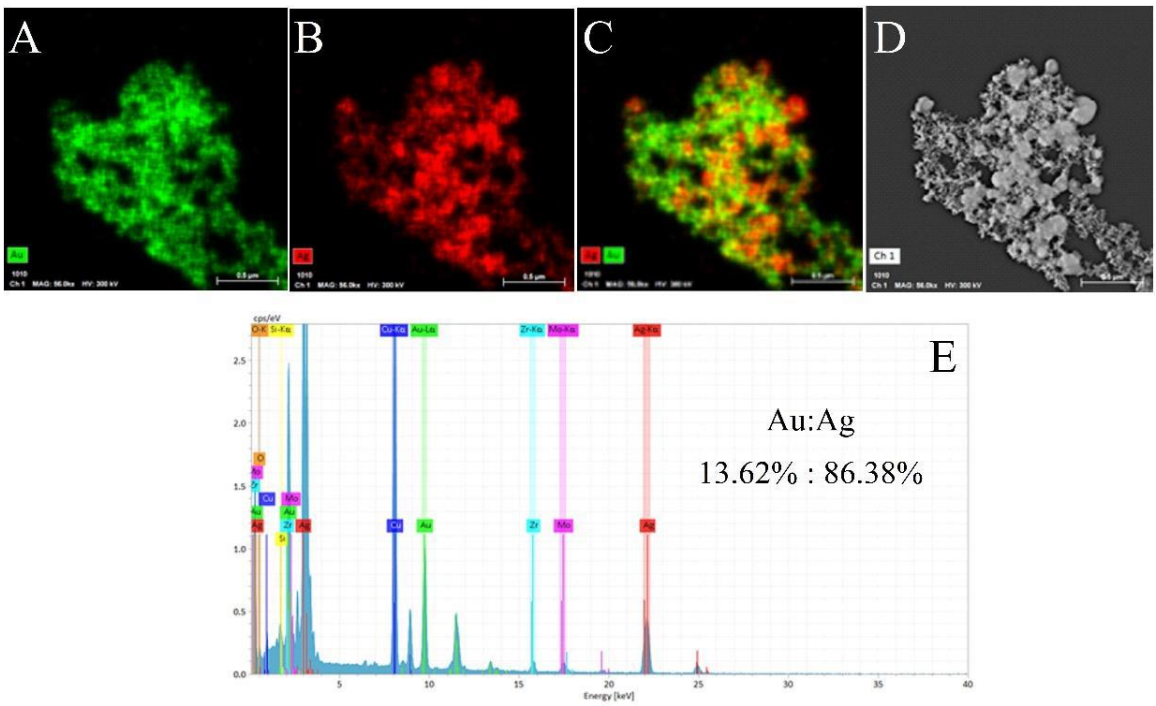

Figure C.2 Elemental mapping for as-synthesized Au:Ag BMNPs with ratio 1:9, showing Au in Panel A, Ag in Panel B, and both metals in Panel C. Panel D is the reference image from which the elemental mapping was taken. The EDX results in Panel E indicate 13.62% Au and 86.38% Ag, resulting from a 1:9 Au:Ag experimental ratio.

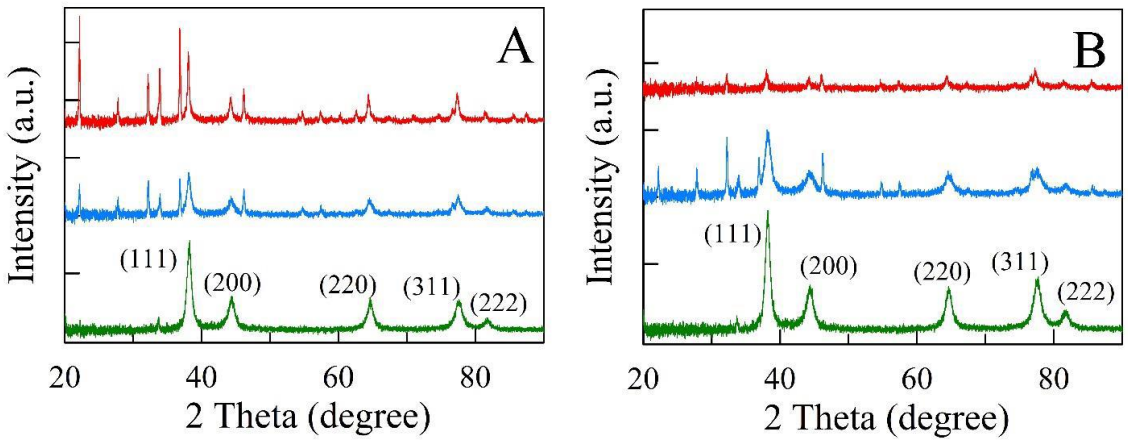

Figure C.3 XRD pattern of the squaric acid bimetallic nanoparticles (SA-BMNPs) that were lyophilized 1 h after synthesis (Panel A) and 24 h after synthesis (Panel B). The Au:Ag ratios investigated were 9:1 (green lines), 1:1 (blue lines), and 1:9 (red lines).

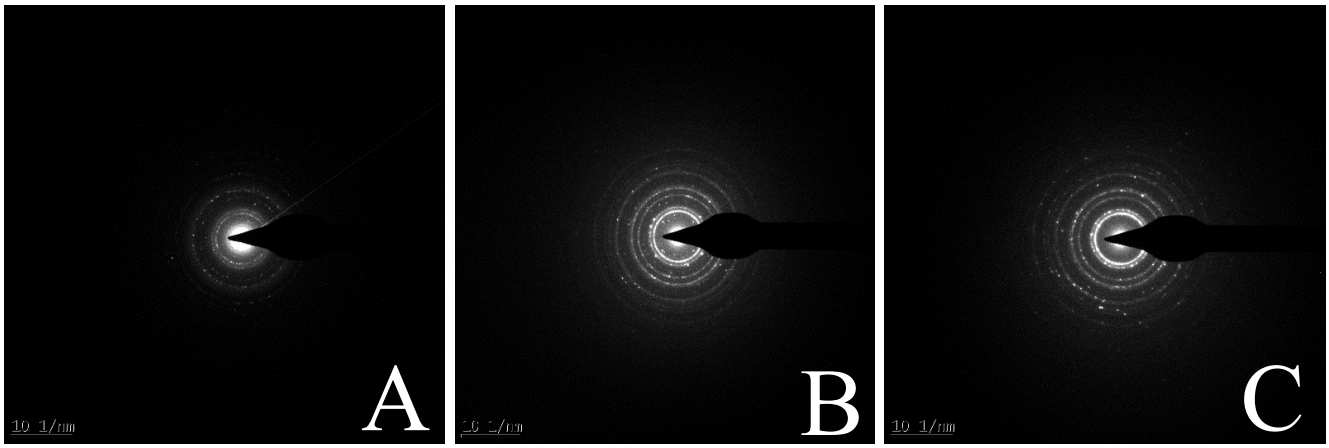

Figure C.4 Small angle electron diffraction (SAED) patterns for as-synthesized SA-BMNPs for Au:Ag ratios of 9:1 (Panel A), 1:1 (Panel B), and 1:9 (Panel C).

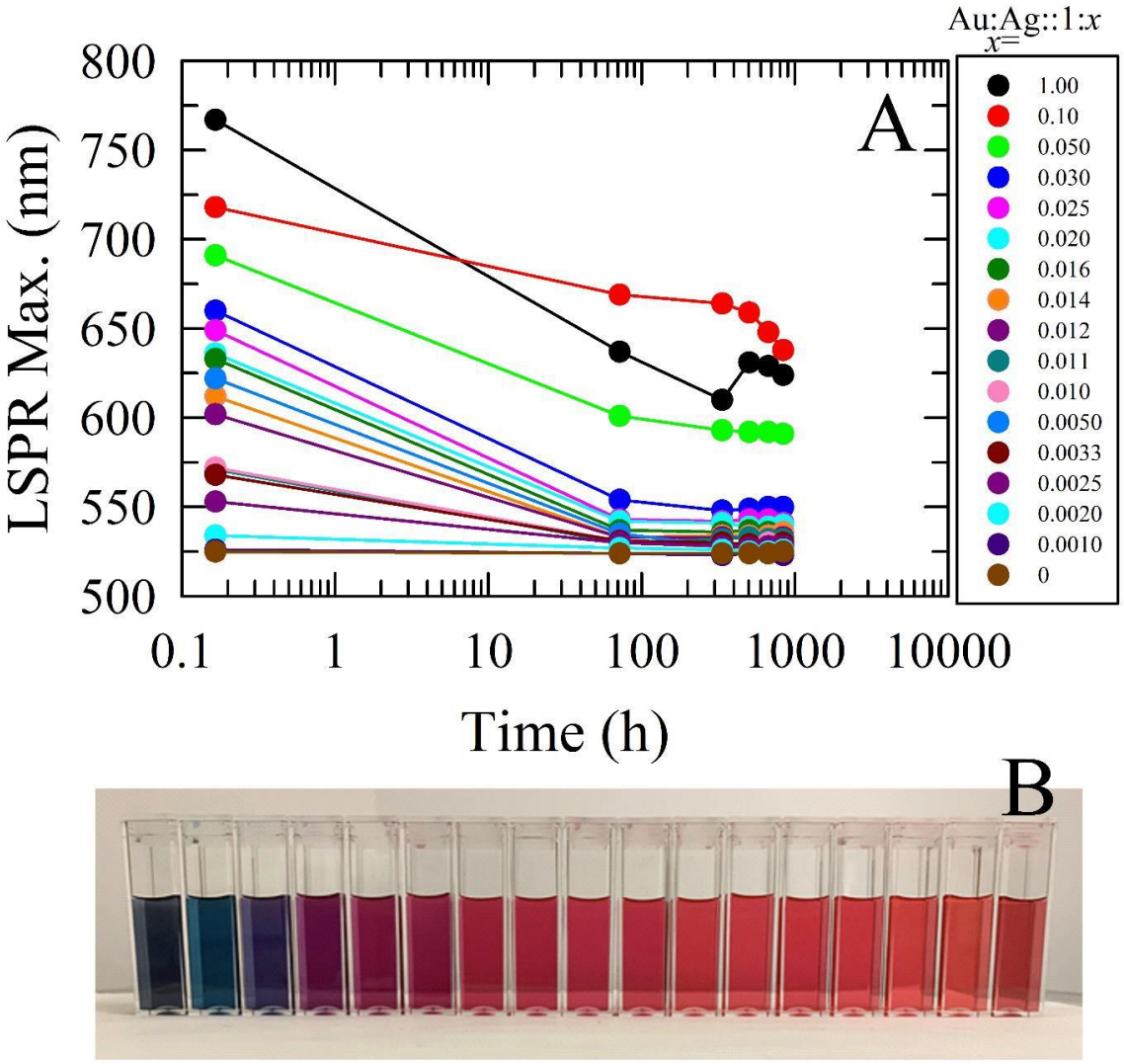

Figure C.5 The localized surface plasmon resonance (LSPR) maxima over five weeks for samples employing various mole fractions of Au:Ag (as seen in the legend in Panel A) with a fixed Au precursor concentration. Panel B shows the corresponding solutions after five weeks.

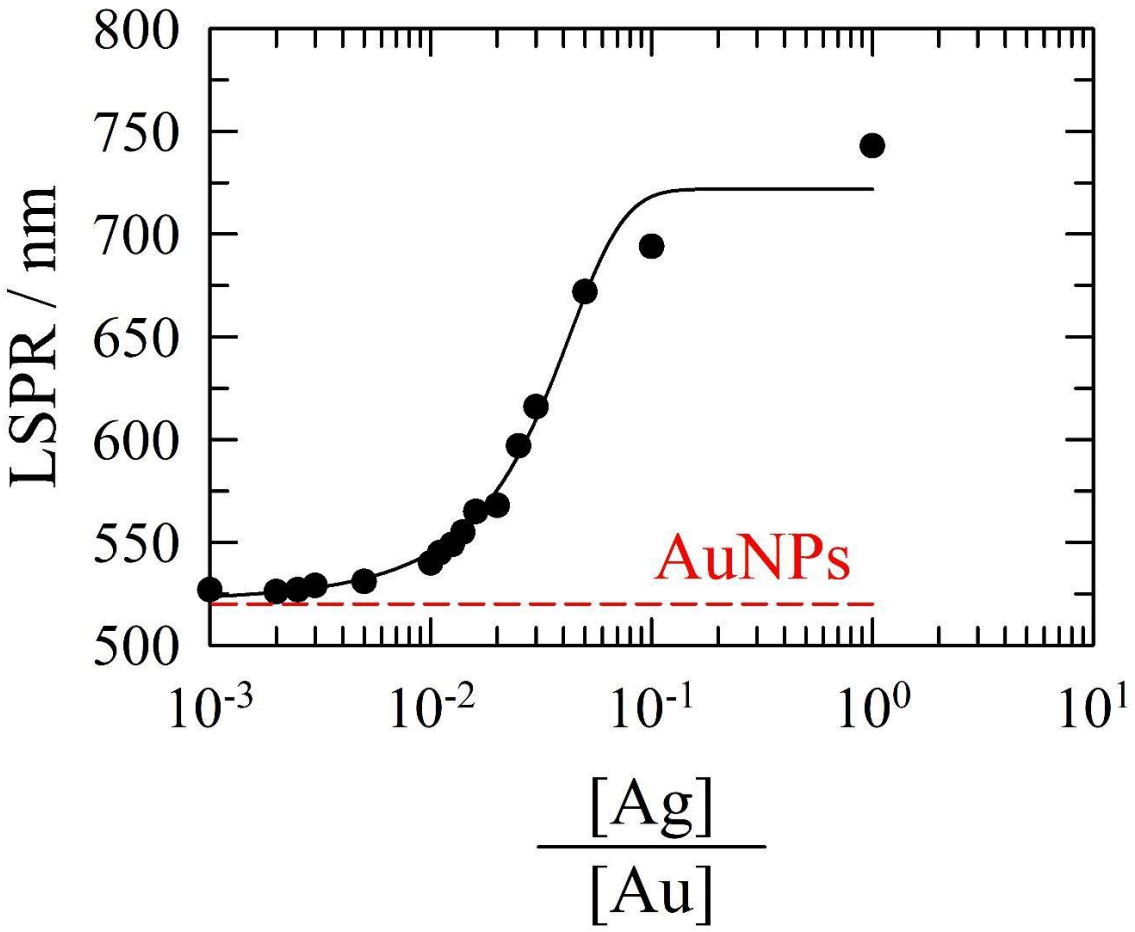

Figure C.6 Plot of LSPR vs. [Ag]/[Au] fitted to a 4-parameter sigmoidal curve for [Ag]/[Au] showing the tunability of the plasmon band when varying [Ag].

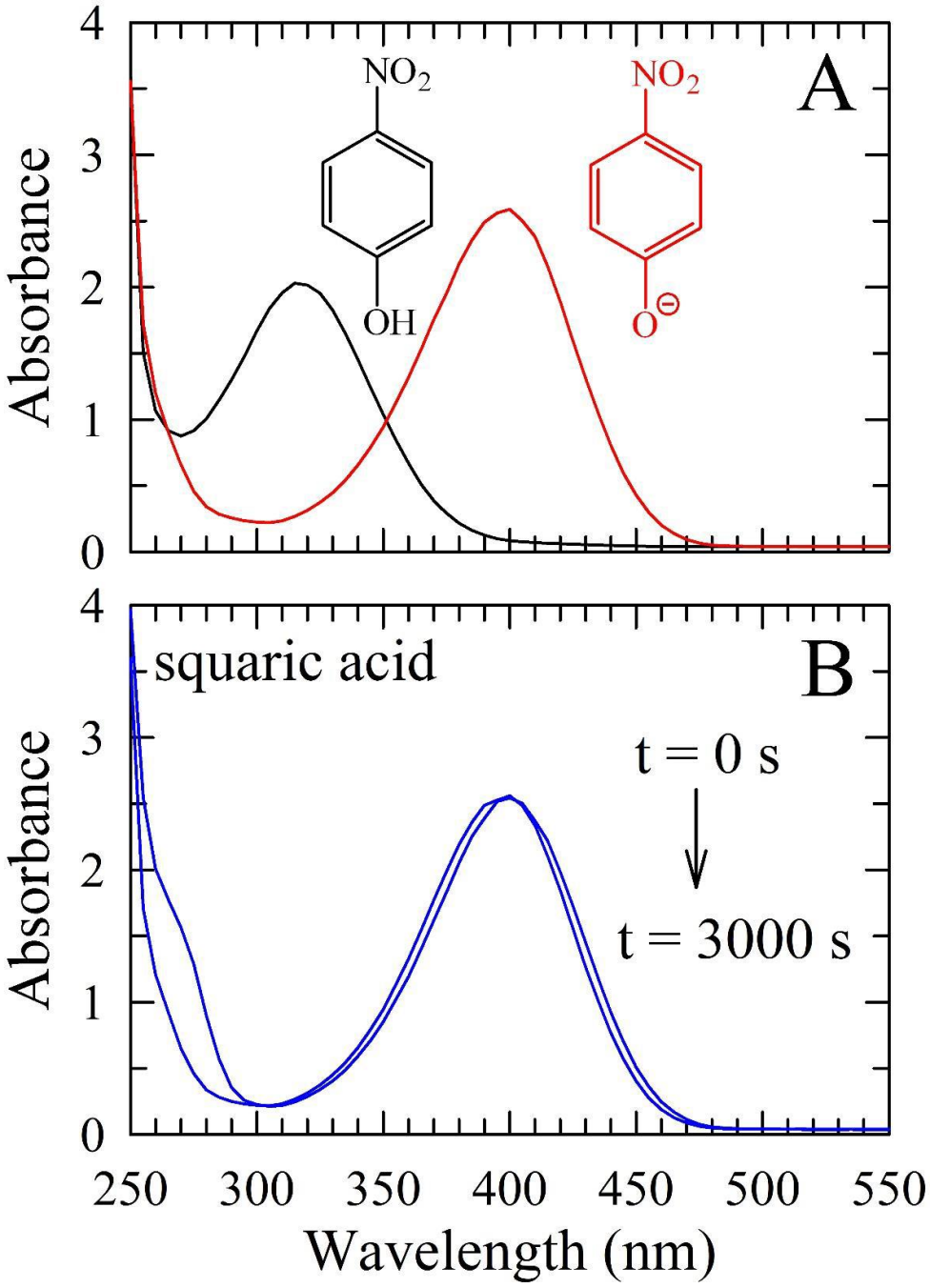

Figure C.7 (Panel A) Absorbance spectra for aqueous 4-nitrophenol (4-NP, black line; 320 nm peak) and 4-nitrophenolate ion (4-NPO, red line; 400 nm peak) produced upon after addition of sodium borohydride ($NaBH_4$). Absent catalyst, the absorbance will remain essentially unchanged indefinitely. (Panel B) The control experiment showing that squaric acid alone did not participate in the catalytic reduction of 4-NP.

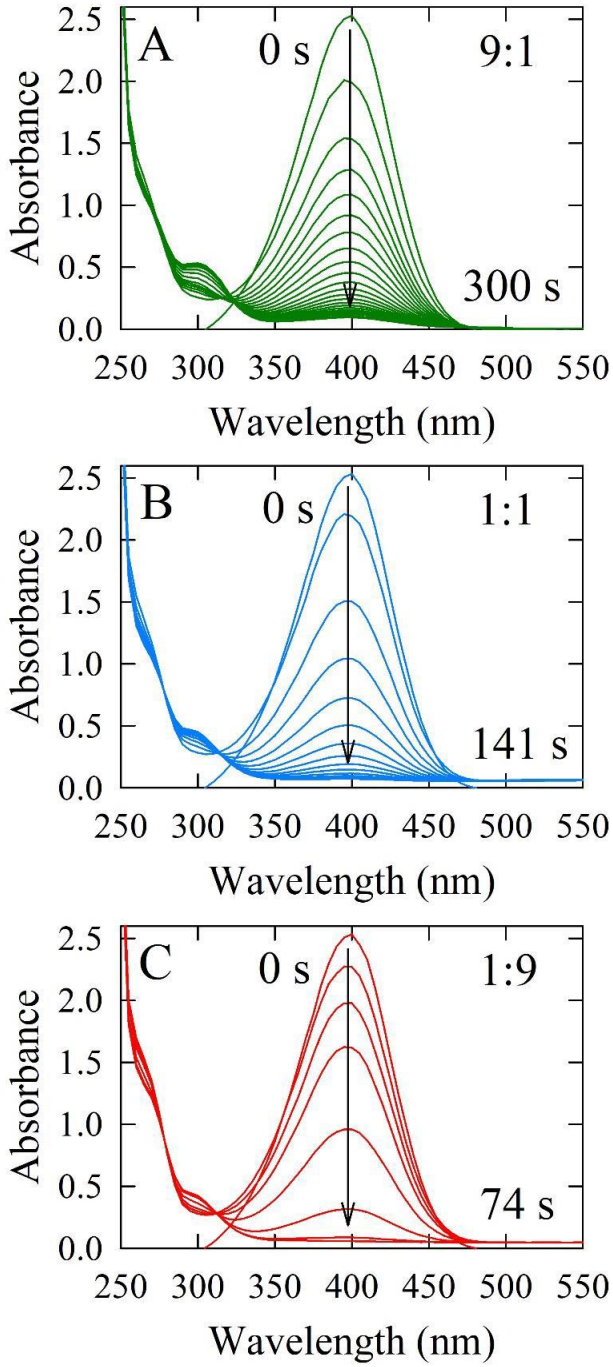

Figure C.8 SA-BMNP nanocatalysts were tested less than 10 minutes after preparation. Time-dependent absorption spectra for $NaBH_4$-assisted 4-NP reduction catalyzed by SA-BMNPs with Au:Ag ratios of 9:1 (Panel A, green), 1:1 (Panel B, blue), and 1:9 (Panel C, red). Spectra were collected every 15 s but, for clarity, spectra are only shown for illustrative times.

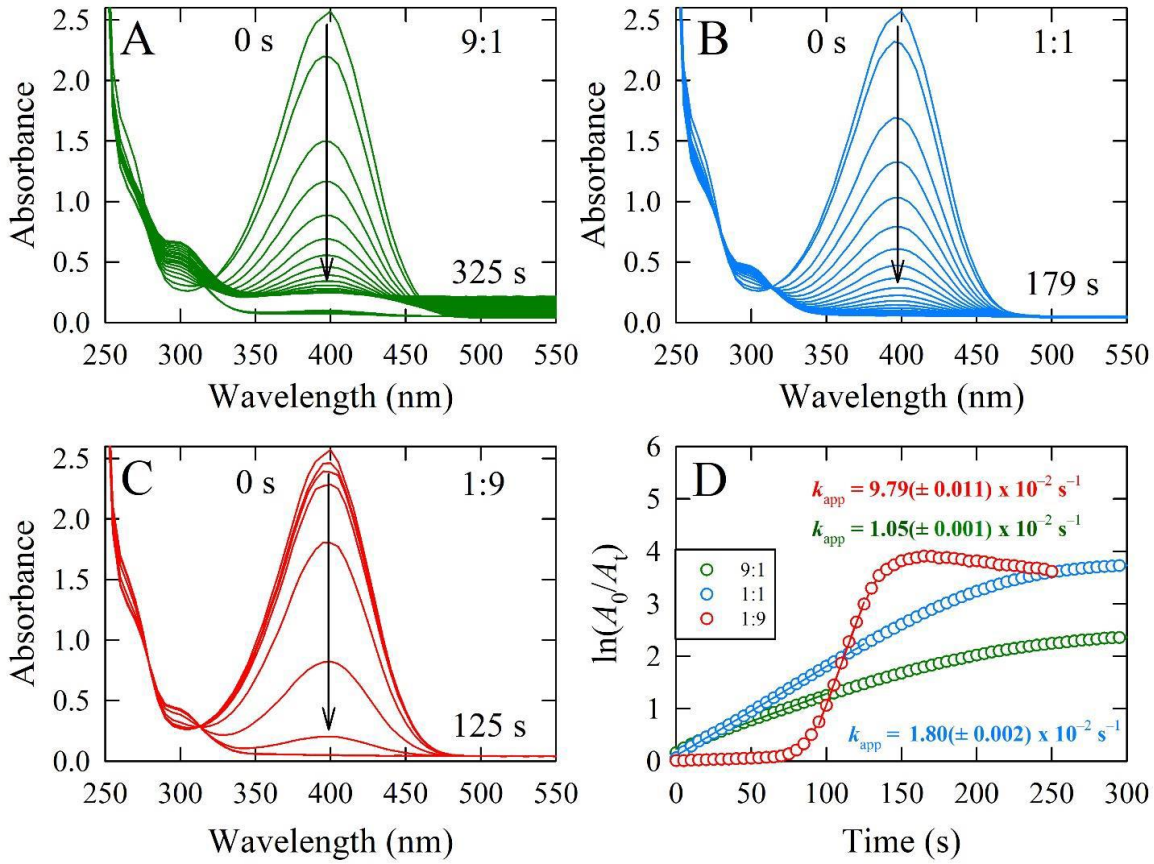

Figure C.9 SA-BMNP nanocatalysts tested 12 h after preparation. Time-dependent absorption spectra for $NaBH_4$-assisted 4-NP reduction catalyzed by SA-BMNPs with Au:Ag ratios of 9:1 (Panel A, green), 1:1 (Panel B, blue), and 1:9 (Panel C, red). Spectra were collected every 15 s but, for clarity, spectra are only shown for illustrative times. Panel D shows the $\ln(A_0/A_t)$ of 4-NP against time for the same catalysts, monitored at 400 nm. The apparent rate constant, k_{app}, were taken from the slope of the linear region of the corresponding plots.

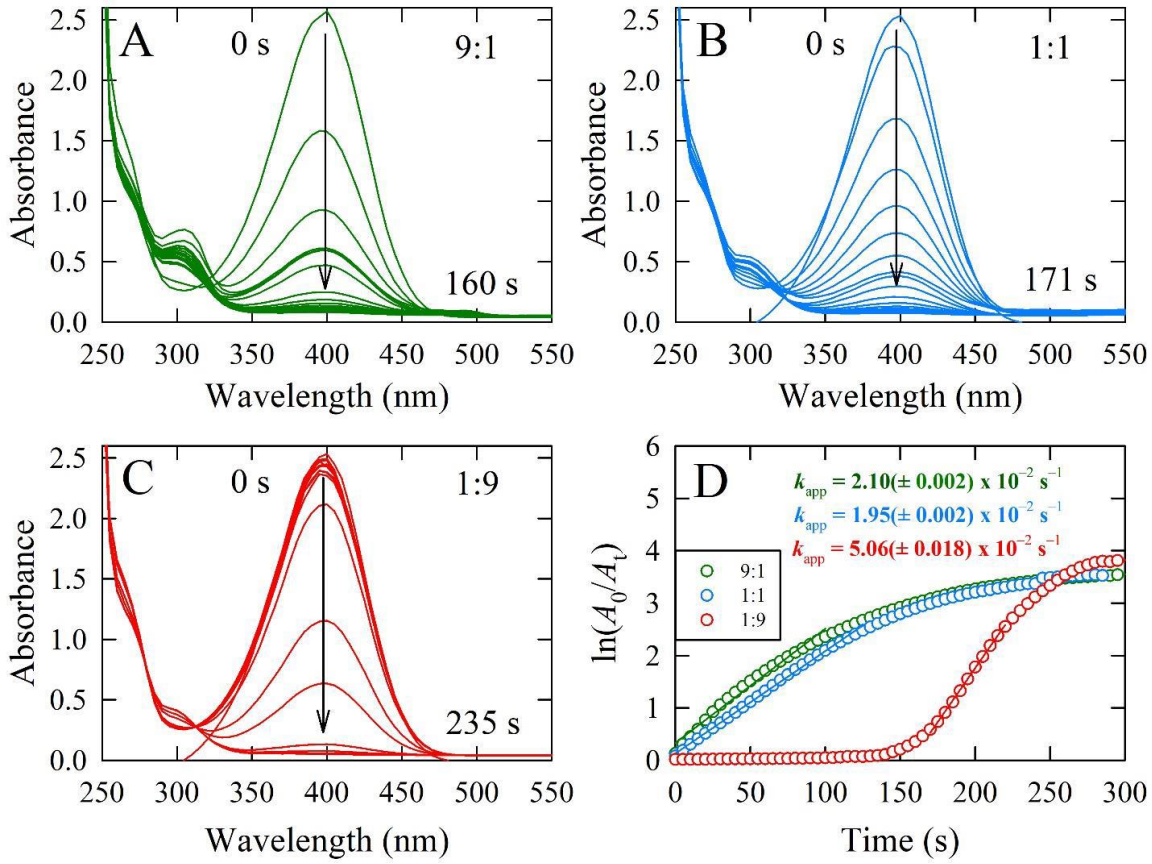

Figure C.10 SA-BMNP nanocatalysts tested 24 h after preparation. Time-dependent absorption spectra for $NaBH_4$-assisted 4-NP reduction catalyzed by SA-BMNPs with Au:Ag ratios of 9:1 (Panel A, green), 1:1 (Panel B, blue), and 1:9 (Panel C, red). Spectra were collected every 15 s but, for clarity, spectra are only shown for illustrative times. Panel D shows the $\ln(A_0/A_t)$ of 4-NP against time for the same catalysts, monitored at 400 nm. The apparent rate constants, k_{app}, were taken from the slope of the linear region of the corresponding plots.

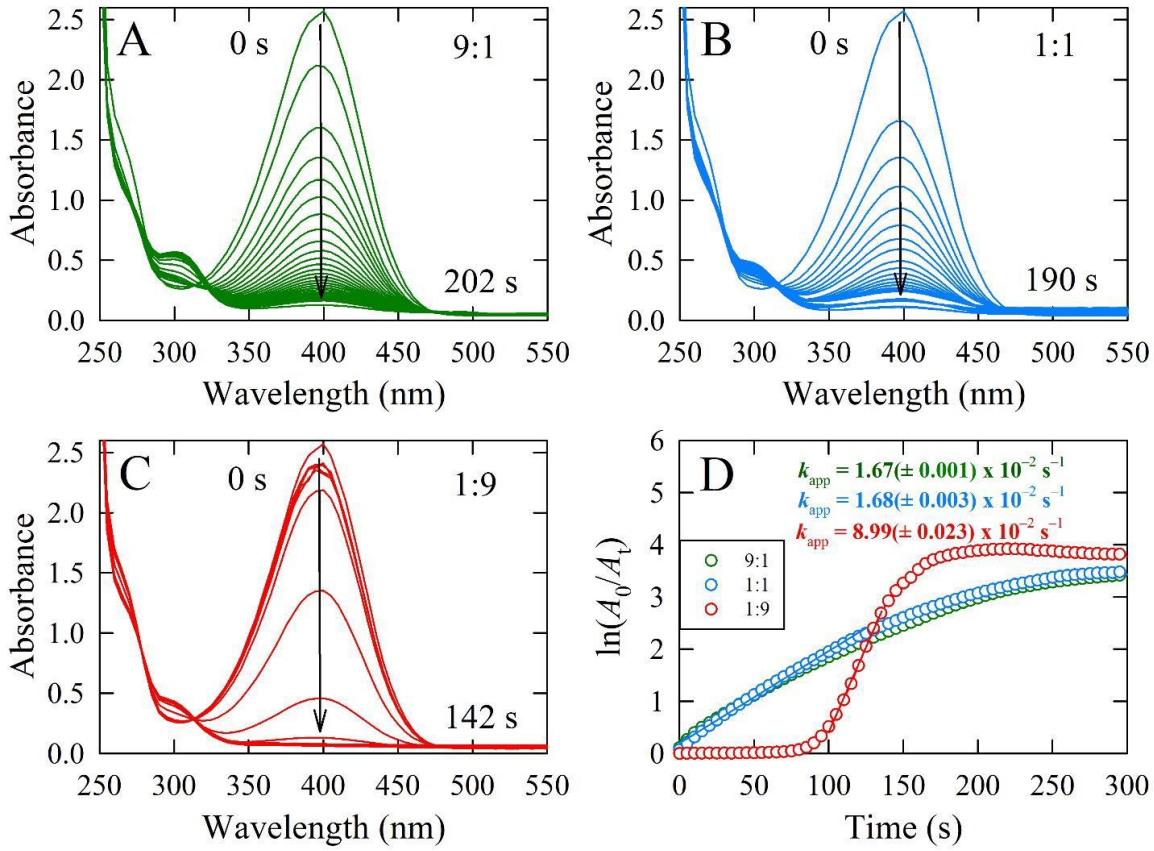

Figure C.11 SA-BMNP nanocatalysts tested 1 week after preparation. Time-dependent absorption spectra for $NaBH_4$-assisted 4-NP reduction catalyzed by SA-BMNPs with Au:Ag ratios of 9:1 (Panel A, green), 1:1 (Panel B, blue), and 1:9 (Panel C, red). Spectra were collected every 15 s but, for clarity, spectra are only shown for illustrative times. Panel D shows the $\ln(A_0/A_t)$ of 4-NP against time for the same catalysts, monitored at 400 nm. The apparent rate constant, k_{app}, were taken from the slope of the linear region of the corresponding plots.

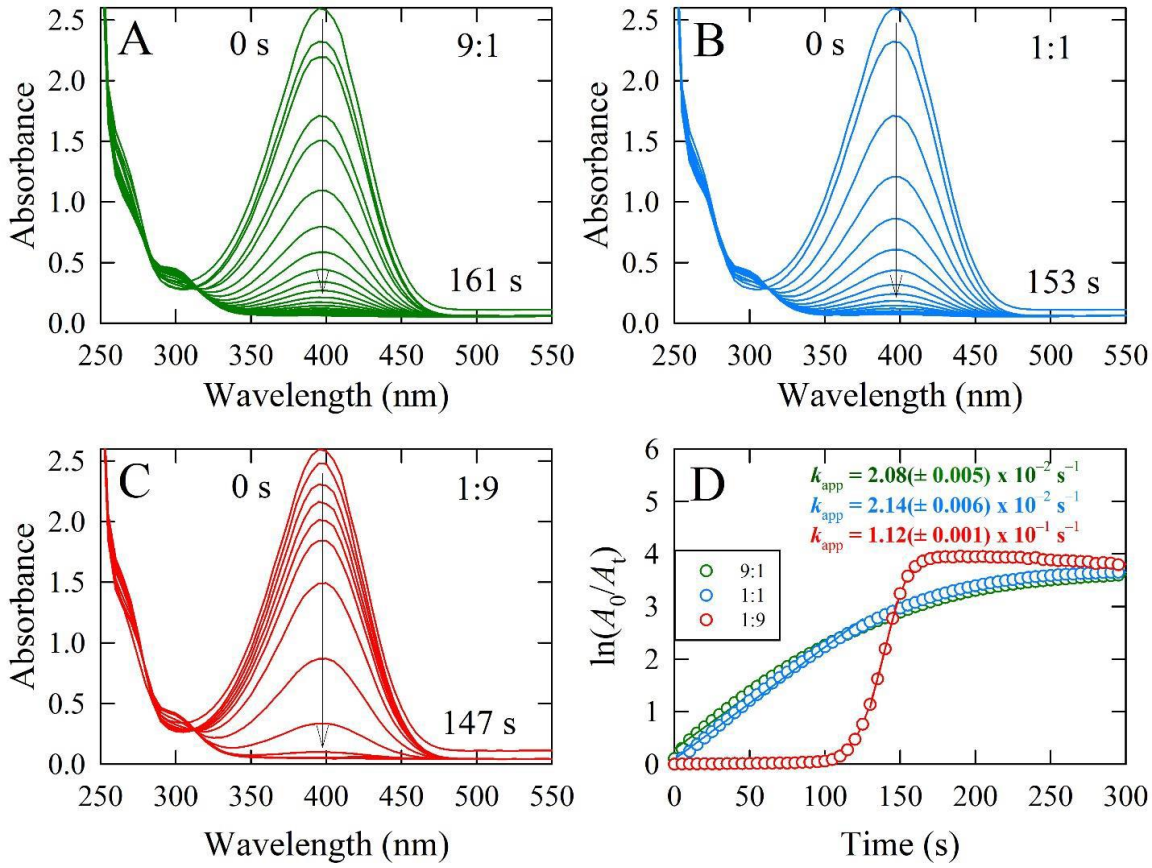

Figure C.12 SA-BMNP nanocatalysts tested 2 weeks after preparation. Time-dependent absorption spectra for $NaBH_4$-assisted 4-NP reduction catalyzed by SA-BMNPs with Au:Ag ratios of 9:1 (Panel A, green), 1:1 (Panel B, blue), and 1:9 (Panel C, red). Spectra were collected every 15 s but, for clarity, spectra are only shown for illustrative times. Panel D shows the $\ln(A_0/A_t)$ of 4-NP against time for the same catalysts, monitored at 400 nm. The apparent rate constants, k_{app}, were taken from the slope of the linear region of the corresponding plots.

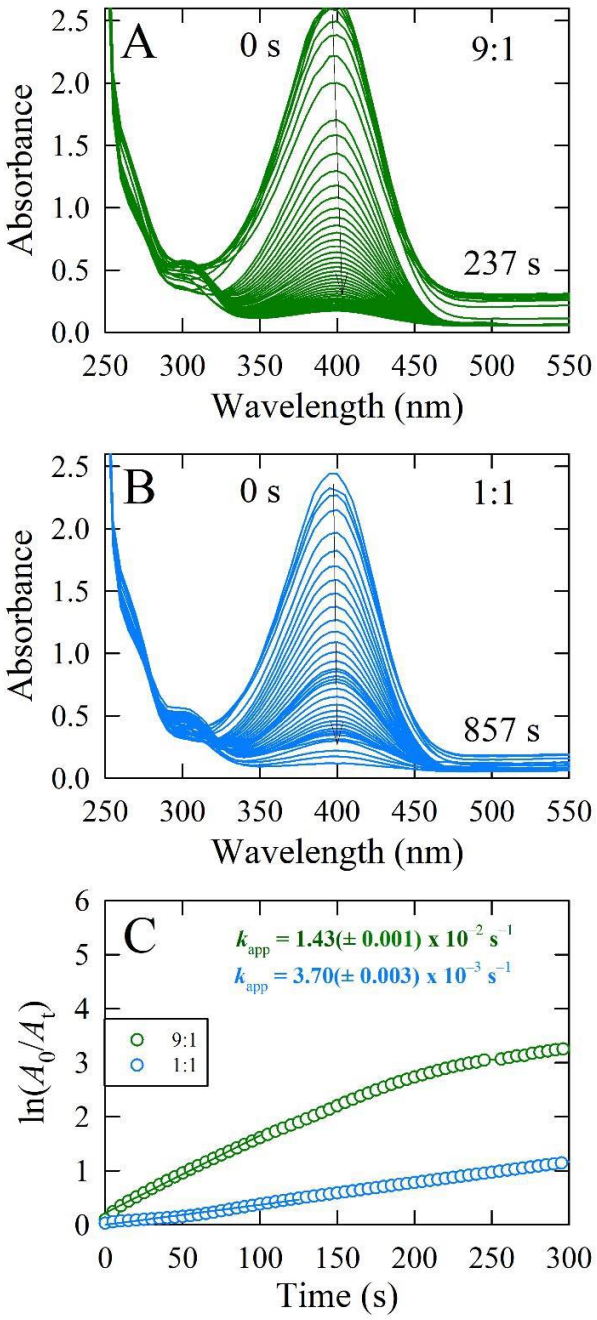

Figure C.13 SA-BMNP nanocatalysts tested 5 weeks after preparation. Time-dependent absorption spectra for $NaBH_4$-assisted 4-NP reduction by SA-BMNPs with Au:Ag ratios of 9:1 (Panel A, green) and 1:1 (Panel B, blue). Spectra were collected every 15 s but, for clarity, spectra are only shown for illustrative times. Panel C shows the $\ln(A_0/A_t)$ of 4-NP against time for the same catalysts, monitored at 400 nm. The apparent rate constants, k_{app}, were taken from the slope of the linear region of the corresponding plots.

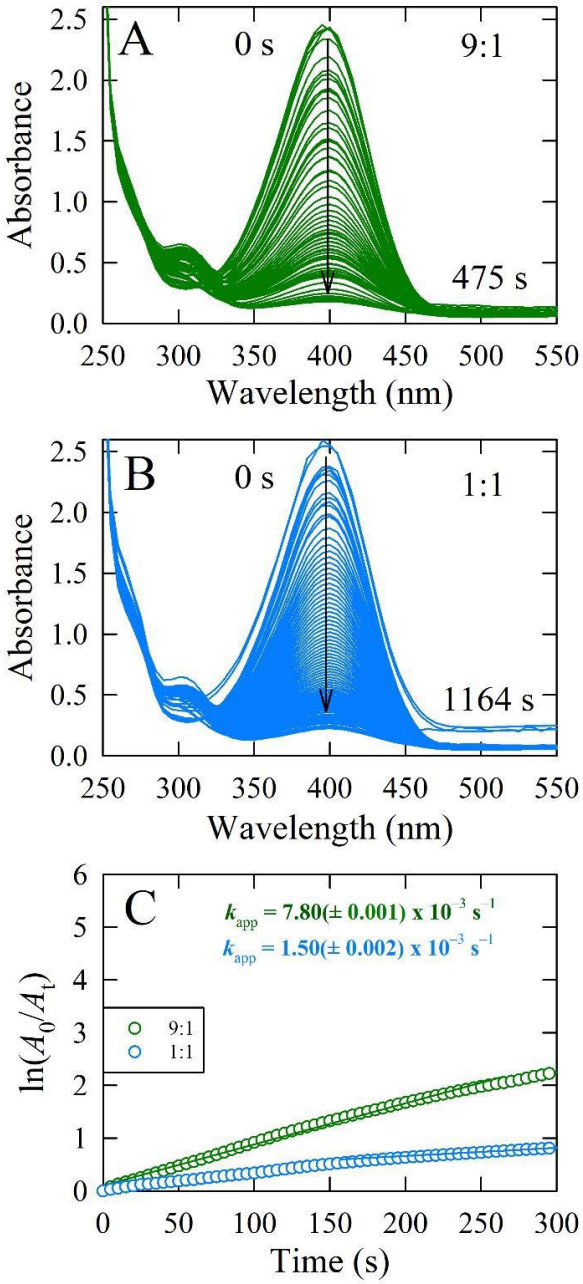

Figure C.14 SA-BMNP nanocatalysts tested 10 weeks after preparation. Time-dependent absorption spectra for $NaBH_4$-assisted 4-NP reduction catalyzed by SA-BMNPs with Au:Ag ratios of 9:1 (Panel A, green) and 1:1 (Panel B, blue). Spectra were collected every 15 s but, for clarity, spectra are only shown for illustrative times. Panel C shows the $\ln(A_0/A_t)$ of 4-NP against time for the same catalysts, monitored at 400 nm. The apparent rate constants, k_{app}, were taken from the slope of the linear region of the corresponding plots.

Table C.1 Apparent catalytic rates and turnover frequencies for the SA-BMNP-catalyzed reduction of 4-NP.

Aging time	**Au:Ag 9:1**		**Au:Ag 1:1**		**Au:Ag 1:9**	
	k_{app} (s^{-1})	TOF (h^{-1})	k_{app} (s^{-1})	TOF (h^{-1})	k_{app} (s^{-1})	TOF (h^{-1})
24 h	2.10×10^{-2}	428	1.95×10^{-2}	400	5.06×10^{-2}	291
1 week	1.67×10^{-2}	339	1.68×10^{-2}	360	8.99×10^{-2}	482
2 weeks	2.08×10^{-2}	425	2.14×10^{-2}	447	1.12×10^{-1}	465
5 weeks	1.43×10^{-2}	289	3.70×10^{-3}	79.8	--	--
10 weeks	7.80×10^{-3}	144	1.50×10^{-3}	58.8	--	--

Table C.2 Apparent catalytic rates and turnover frequencies for the recycling studies at various aging times of Au:Ag 1:9 SA-BMNPs for the catalyzed reduction of 4-NP.

Aging time	**Initial cycle**		**Cycle 2**		**Cycle 3**		**Cycle 4**		**Cycle 5**	
	k_{app} (s^{-1})	TOF (h^{-1})	k_{app} (s^{-1})	TOF (h^{-1})	k_{app} (s^{-1})	TOF (h^{-1})	k_{app} (s^{-1})	TOF (h^{-1})	k_{app} (s^{-1})	TOF (h^{-1})
As-synth.	3.99×10^{-2}	189	4.46×10^{-2}	489	3.27×10^{-2}	380	2.07×10^{-2}	234	9.70×10^{-3}	117
12 h	1.20×10^{-2}	55.2	9.80×10^{-3}	112	7.20×10^{-3}	83.2	7.70×10^{-3}	76.2	6.00×10^{-3}	65.1
24 h	2.40×10^{-2}	65.9	1.68×10^{-2}	192	1.21×10^{-2}	132	1.07×10^{-2}	126	9.80×10^{-3}	113
1 week	1.44×10^{-2}	52.9	6.50×10^{-3}	76.2	5.10×10^{-3}	60.1	4.80×10^{-3}	56.8	--	--
2 weeks	1.12×10^{-2}	39.8	1.09×10^{-2}	122	8.40×10^{-3}	96.3	8.20×10^{-3}	92.2	6.90×10^{-3}	77.9

Appendix D: Laser-Induced Sound Pinging (LISP): A Rapid Photoacoustic Method to Determine the Speed of Sound in Microliter Fluid Volumes.

†This chapter is based on a published manuscript in Sensors & Actuators B: Chemical. The information contained herein is adapted with permission from Polo-Parada, L.; Gutiérrez-Juárez, G.; **Kist, J. A.**; Adhikari, L.; Bhawawet, N.; and Baker, G. A., Laser-induced sound pinging (LISP): A rapid photoacoustic method to determine the speed of sound in microliter fluid volumes. Sensors & Actuators B: Chemical, 291, **2019**, 401-410. Copyright © 2019 Elsevier.

As third author (and first graduate student) on this publication, I assisted with speed of sound measurements on various ionic liquids, milk, and saline solutions. I also helped with the writing of the publication.

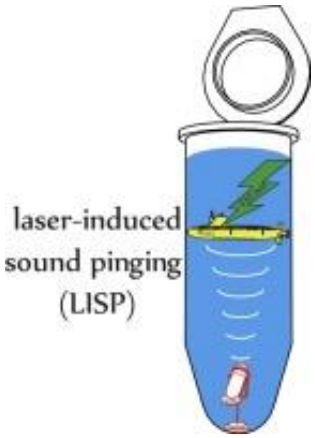

Scheme D.1 Graphical representation illustrating the laser-induced sound pinging (LISP) method.

Abstract

Laser-induced ultrasound detection is a well-known technique for diverse applications, including medical analysis, materials characterization, industrial quality control, and environmental monitoring. The measurement of the speed of sound in liquids is frequently performed using a single-crystal ultrasonic interferometer, a device which requires a substantial volume of liquid (≥ 10 mL), hindering its utility in low-volume applications (*e.g.*, biomedical screening). Other specialized techniques, such as the transient grating approach, exist and while some provide additional useful information (*e.g.*, thermal diffusivity and damping parameters), they are costly and complex to implement, frequently requiring a specialist. In response to these instrumental limitations, we introduce a simple, inexpensive, and convenient laser-based approach to directly measure the speed of sound in minute liquid volumes (≥ 25 μL) with a high degree of accuracy (percent relative standard deviation in determining sound speed better than ± 0.15%).

This new technique, termed laser-induced sound pinging (LISP) owing to the inspiration drawn from submarine sonar pinging, is demonstrated using an inexpensive tattoo removal Nd:Ce:YAG laser. In this appendix, we validate the concept of LISP and demonstrate its unique capabilities by analyzing a variety of samples on the basis of the speed of sound: the salinity of water, dilutions of bovine milk, and the characterization of representative ionic liquids. Given the rapid nature of measurement, ease of operation, simplicity of analysis (model-free), and microliter sample volume requirements, we anticipate that LISP will progress as a beneficial and practically-relevant analytical tool for answering a broad range of liquid forensic questions, with potential applications in drinking water quality evaluation, food safety and authentication, bioanalysis, and quality-control

(*e.g.*, measuring sugar contents in soft drinks). Fieldable and real time, in-line versions of this instrument can also be envisaged in the near future.

Introduction

Ultrasound detection is a well-known technique for materials characterization.[1-2] The speed of sound, sound velocity, and ultrasonic velocity are frequently-used terms that describe the speed at which an ultrasound wave propagates in a fluid.[3] Ultrasound velocity or speed of sound measurements provide further access to other key thermodynamic properties such as isentropic and isothermal compressibilities, isobaric thermal expansion coefficients, cohesive energy barriers, Joule–Thomson coefficients, isobaric and isochoric heat capacities, viscosities, and bulk moduli.[4-5] Velocity measurement, in its most elemental form, depends upon the accurate determination of distance (using a "ruler") and time (using a "clock"). There have been various methods used previously to determine the speed of sound, including time-of-flight, interferometric, transient grating, pulse-echo overlap, and sing-around methods.

Speed of sound determinations have also been performed in a wide array of media, including water, seawater, alcohols, dairy products, and fuels (*e.g.*, biodiesel).[6-9] Indeed, in addition to employing the speed of sound to derive fundamental parameters, the speed of sound represents an important analytical tool in a number of areas. One area of great research over the past few decades has been the measurement of the speed of sound as a function of ocean depth and salinity, an area that has seen both significant experimental and computational effort.[10-13] For example, Leonard *et al.* refined a commonly-used technique to remotely determine subsurface temperature and salinity using Raman scatter.[14] Liu *et al.* determined the speed of sound in water spanning a temperature range

of 0–30°C for salinities of 0% and 3.5% (the latter being the typical salinity of sea water) based on Brillouin scattering using a Q-switched Nd:YAG laser, reporting a maximum speed of sound error of 13 m/s.[15] Ultrasound methods have also been used to characterize dairy-based food products to explore their functional and physical properties. For instance, Elvira *et al.* studied the speed of sound and density of milk, reporting that the speed of sound in skim milk at 40°C was 1552 m/s but decreased to 1548 m/s when tainted with 0.25% melamine.[16] As a final example of the relevance of speed of sound measurements, this is a topic of growing interest in fundamental ionic liquid (IL) research. Fully composed of ions, ILs frequently display melting points below 100°C[17-18] and possess a unique set of attractive features (*e.g.*, low volatility, large electrochemical potential window, wide liquid range, tunability) accounting for their popularity in varied areas ranging from energy and catalysis to the analytical sciences.[19-22]

Preliminary measurements of the speed of sound in ILs were reported by Arce *et al.* in 2004 and comprised measurements made at 298 K for 1-octyl-3-methylimidazolium chloride and 1-butyl-3-methylimidazolium trifluoromethanesulfonate.[23-24] More recently, Frez and coworkers used the transient grating technique to measure thermal diffusivities, making possible the determination of thermal conductivities and the speeds of sound in various 1-butyl-3-methylimidazolium- and bis(trifluoromethylsulfonyl)imide-based ILs.[25] One possible drawback of this approach (which frankly delivers a wealth of information beyond just the speed of sound), apart from its complexity, is the requirement to add a small concentration of inert dye (ferroin) due to the intrinsic transparency of the IL samples studied at 532 nm (the frequency- doubled output of the Nd:YAG laser employed). And while laser-based techniques, such as the transient grating method of Frez and co-workers,

are elegant and can provide useful data beyond the speed of sound, they are frequently complex and require costly, sophisticated laser systems, underscoring the need for more accessible methods to measure the speed of sound. We note that Wu *et al.* specifically reported a correlation between the speed of sound and thermal conductivity of ILs,[26] further pointing to its relevance as a tool in the area of solvent engineering.

In line with this, speed of sound measurements have emerged as useful tools to estimate many thermophysical properties of ILs, a topic which has been reviewed recently.[3] In this appendix we discuss a versatile photoacoustic analysis technique with a facile setup that allows for the accurate determination of the speed of sound in various liquids, an approach we term laser-induced sound pinging (LISP), so-named for the conceptual inspiration loosely drawn from submarine sonar pinging. The LISP method relies primarily on the accurate estimation of the delay in time required for an ultrasound wave to propagate through a liquid of interest. To accurately measure the time delay, a single-mode optical fiber was employed to deliver laser pulses toward the sample, the position of the fiberoptic tip being subject to micromanipulation using an XYZ translation stage. Instead of allowing the direct propagation of light into the sample, the terminus of the fiberoptic was instead capped with a layer of optically dense material that generated an acoustic pulse (*i.e.*, ultrasonic pinging transducer) which impinged on the liquid within the sample cell. The arrival of the acoustic wave was detected by an ultrasonic microphone positioned some distance (*i.e.*, the effective analytical pathlength) away from the transducer and the electronic signal sent to a digital storage oscilloscope for data analysis. Due to the flexibility in the geometry and dimensions of the pinging ultrasound transducer and the sample cell, it is possible to determine the speed of sound within liquid volumes down to

~25 μL, a clear advantage when analyzing precious, hazardous, or scarce (*e.g.*, biological) fluids. In this appendix, we demonstrate the analytical merits and generality of LISP analysis by measuring the speed of sound in a number of representative liquids, including water of varying salinity, bovine milk, and a number of representative ionic liquids, making comparison to previously reported literature values whenever possible.

Materials and Methods

Materials

Sodium chloride (NaCl) (S7653, ≥ 99.5%) was purchased from Sigma-Aldrich (St. Louis, MO). The ionic liquids 1-ethyl-3-methylimidazolium bis(trifluoromethylsulfonyl)imide ($[Emim^+][Tf_2N^-]$), 1-hexyl-3- methylimidazolium bis(trifluoromethylsulfonyl)imide ($[Hmim^+]$ $[Tf_2N^-]$), 1-methyl-1-propylpyrrolidinium bis(trifluoromethylsulfonyl) imide ($[C_3mpy^+][Tf_2N^-]$) and dimethyl(isopropyl)propylammonium bis (trifluoromethylsulfonyl)imide ($[Nip_{311}^+][Tf_2N^-]$) were synthesized in-house following previously reported synthesis, purification, and drying procedures.[27-30] Whole milk was sourced from a local Hy-Vee, an employee-owned chain of supermarkets located throughout the Midwestern United States. All chemicals and reagents were used as received, without further purification. Experiments were carried out using Millipore Milli-Q® Type 1 ultrapure water polished to a resistivity of 18.2 MΩ · cm at 25°C.

LISP experiment

For all experiments and trials performed, 150 μL of sample was used. A micrometer, with a working range of 25 mm, was attached to the ultrasonic pinging transducer, and was used to systematically manipulate the distance between the distal end of the optical fiber and the ultrasonic microphone. Iterative measurements were carried out after completing one full

turn of the micrometer, changing the transducer-to-microphone distance (*i.e.*, effective pathlength) by 0.5 mm. A total of at least five micrometer turns was performed, with the time delay recorded from the oscilloscope after each turn, to yield one trial. A plot of distance change versus time delay was generated in this fashion, allowing the speed of sound to be straightforwardly determined as the slope of this line.

Salinity studies

A stock solution of 1.0 M NaCl was prepared by dissolving 0.10 moles of NaCl in 100 mL of Milli-Q water. This stock solution was volumetrically diluted to various concentrations ranging from 0.025 to 0.9 M. Each saline sample was measured at least three discrete times, using a fresh aliquot for each measurement. Trials were performed at room temperature.

Milk studies

Bovine whole milk was diluted with Milli-Q water to yield a series of samples that were 5, 10, 25, 50, 75, and 100% milk by volume. Milk samples were stored refrigerated (4°C) and then allowed to warm to room temperature for 30 min before performing LISP analysis. Each vol% milk was analyzed three times, using a fresh sample each time. Ultrapure Milli-Q water was employed as a benchmark for comparison.

Ionic liquid studies

The temperature-dependent speed of sound was determined in four representative ILs: 1-ethyl-3-methylimidazolium bis(trifluoromethylsulfonyl) imide ($[Emim^+][Tf_2N^-]$), 1-methyl-1-propylpyrrolidinium bis(trifluoromethylsulfonyl)imide ($[C_3mpy^+]$ $[Tf_2N^-]$), 1-hexyl-3-methylimidazolium bis(trifluoromethylsulfonyl) imide ($[Hmim^+][Tf_2N^-]$), and dimethyl(isopropyl)propylammonium bis(trifluoromethylsulfonyl)imide ($[Nip_{311}^+][Tf_2N^-]$). These ILs were synthesized following known procedures.[27-30] Ionic liquids

were dried on a vacuum line for 24 h at 70°C prior to LISP analysis. Water contents of the ILs were determined using coulometric Karl Fischer (KF) titration (Metrohm 831 KF coulometer) with Aqualine electrolyte AG (Fisher; AL2520-500) as analyte solution (typical sample size ~0.1 g). After drying, the KF-determined water contents for $[Emim^+][Tf_2N^-]$, $[C_3mpy^+][Tf_2N^-]$, $[Hmim^+][Tf_2N^-]$, and $[Nip_{311}^+][Tf_2N^-]$ were 112, 142, 138, and 39 ppm, respectively. Speed of sound measurements were carried out in the temperature range from 293 to 323 K, with measurements taken every 5 K, averaging a total of four measurements taken at each temperature. The temperature was controlled using a Peltier controller to within 0.1°C.

Theory

In the thermoelastic regime, the generation and propagation of photoacoustic pressure in an inviscid medium is described by

$$\left(\frac{\partial^2}{\partial z^2} - \frac{1}{c^2}\frac{\partial^2}{\partial t^2}\right) p(z,t) = -\frac{\beta}{C_p}\frac{\partial H(z,t)}{\partial t} \qquad (1)$$

where $p(z, t)$ is the acoustic pressure at location z and time t, c is the speed of sound, β is the thermal coefficient of volume expansion, C_p is the specific heat capacity at constant pressure, and $H(z, t)$ is the energy density per unit time deposited by the optical source in the sample. Equation (1) applies only in thermal confinement regime. If the optical absorption length across the absorber is smaller than the width of the laser spot size, the shape of the sound source is essentially planar. Considering this situation over an absorber of thickness L, and if the energy distribution within the thickness of the absorber obeys the Beer-Lambert law, then at any position inside the sample, the energy density per unit time absorbed by the sample can be written as

$$H\ (z,t) = \ \alpha F_0 e^{-\alpha z}\ f\ (t) \qquad (2)$$

where α is the absorption coefficient of the heated region, F_0 is the laser fluence, and $f\ (t)$ is the temporal profile of the laser beam. To include the region where the optical absorption can occur, equation (2) must be multiplied by a rectangular function, Π(*z*), centered at *L*/2 and width *L*, yielding

$$H\ (z,t) = \ \alpha F_0 e^{-\alpha z} \Pi[\tfrac{z-\frac{L}{2}}{L}]\ \text{f (t)} \qquad (3)$$

equation (3) represents the energy distribution per unit time that must be substituted into equation (1). For a pulsed beam with a Gaussian temporal profile of width 1/e equal to τ, the solution of equation (1) in the region - ∞ < *z* < ∞, is given by:[31]

$$p\ (z,t) = \tfrac{P_0}{2}\Theta(t)\exp[\left(\tfrac{\alpha c\tau}{4}\right)2\{\exp\left[-\alpha c\left(t-\tfrac{z}{c}\right)\right]P_+(z,t) + \exp[+\alpha c\ (t + \tfrac{z}{c})]P\_(z,t) \qquad (4)$$

where $P_0 \equiv \Gamma\alpha F_0$, $\Gamma \equiv c^2\beta\ /Cp$ is the Grüneisen parameter, Θ(*t*) is the step function defined by

$$\Theta(t) = \begin{cases} 1, if\ t > 0, \\ 0, if\ t < 0 \end{cases}$$

and for brevity, we have defined the function $P \pm (z, t)$ as

$$P \pm (z,t) = \ \pm\{\text{erf}\left[\frac{2}{\tau}\left(t\ \pm\ \frac{z}{c}\right) \pm\ \frac{\alpha c\tau}{4}\ \pm \frac{2L}{c\tau}\right] - \text{erf}[\frac{2}{\tau}\left(t\ \pm\ \frac{z}{c}\right) \pm \frac{\alpha c\tau}{4}]\} \qquad (5)$$

A numerical calculation of equation (4) is provided in Figure D.2D. A planar sample with L = 4 mm, $\alpha = 10^4\ \mathrm{m}^{-1}$, $c = 1.5 \times 10^3$ m/s (water), $\beta = 207 \times 10^{-6}\ \mathrm{K}^{-1}$, and $C_\mathrm{p} = 4.1813 \times 10^3$ J/(kg·K) was assumed as the pinging ultrasound source (in our device, a thin layer of quick-drying black liquid tape was the pinging transducer, see next subsection). The pulse duration in this simulation was = 6 ns. This numerical analysis shows that we can use any point in the LISP signal to measure the retardation in time between two contiguous positions in the transducer. Experimentally, this distance is controlled by executing complete turns of a micrometer on the XYX translation stage, moving the end of the black tape-covered end of the optical fiber (*i.e.*, ultrasonic pinging transducer) precisely in the Z-direction.

A final mention of the dispersive nature of materials is in order. In general, all materials studied here are dispersive, meaning that their thermodynamic properties (*e.g.*, density, compressibility, and shear modulus, which are correlated with the speed of sound) may be frequency-dependent and, consequently, ultrasound (acoustic energy) might be absorbed. Ultrasound absorption is manifested by attenuation in sound intensity. For water, the attenuation of ultrasound is 1 dB/MHz/cm).[32-33] We note, however, that these effects become significant only at long distances in the range of centimeters, so are not a concern in our current experiments which utilize short path lengths within liquids for the determination of the speed of sound. We note that, by maintaining a short distance between the pinging transducer and the microphone (ultrasound path length < 9 mm), employing ~6 ns duration laser pulses, and utilizing a single laser pulse at each transducer position (< 1 Hz), our proposed experimental setup guarantees an isentropic system such that

ultrasound is not absorbed. In other words, the LISP system is adiabatic, because there is negligible transfer from the ultrasound pinging transducer to the sample.

LISP device fabrication and measurement setup

A simplified schematic representation of our LISP experimental setup is presented in Figure D.1. The illumination source in our experimental system is a Sheshou-8 type Q-switched solid-state Nd:Ce:YAG laser (typically used for tattoo removal) with a 532 nm adapter and operated with a fluence of 10.2 ± 0.4 mJ cm^{-2} and a pulse duration of ~6 ns. It was determined that this was the minimal fluence necessary to produce a reliable acoustic signal. A 1-mm diameter optical fiber (ThorLabs, Newton, NJ) encased in an intramedic polyethylene tube (1.1mm diameter) was capped on the distal end with a thin, opaque layer of black brush-on liquid tape (#LTB-400, Gardner Bender, Milwaukee, WI). That is, laser pulses were delivered to the black liquid tape which acts as an ultrasonic pinging transducer, producing strong, localized ultrasonic waves. The terminus of the optical fiber was mounted within a micromanipulator to allow fine positional control.

When the coated fiberoptic tip is immersed into the sample cell, the so-generated ultrasonic wave propagates through the liquid under study and the resulting signal is detected— after a time lag determined by the transducer-to microphone distance—by an inexpensive lead-zirconate-titanate (PZT) piezoelectric ultrasonic microphone embedded at the bottom of the sample chamber. The output signal of the microphone is connected to a digital oscilloscope (Rigol DS1302CA) to measure the timing between the generation of the laser pulse and the arrival of the peak of the ultrasonic signal after propagation throughout the liquid medium of interest. A calibrated QE12 energy detector (Gentec-EO, Lake Oswego, OR) was used to monitor the energy delivered to the system. By using a

calibrated micrometer, the position of the pinging transducer with respect to the fixed position of the ultrasonic microphone was varied in precise, stepwise fashion. This is illustrated in Figure D.2 for three different positions of the pinging transducer (*i.e.*, black liquid tape end-coated optical fiber) relative to the immobile piezoelectric sensor. The delay in the arrival of the photoacoustic signal resulting from upward (Z-direction) translation of the pinging transducer away from the piezoelectric sensor in a precise manner via micromanipulation using an XYZ translation stage allows for the expedient calculation of the speed of sound. In this example (Figure D.2D), a 3-mm upward shift (δd) yields a retardation in the arrival time (time delay, δt) of the acoustic signal by 2 μs, directly yielding a speed of sound of 1500 m/s; viz.: $\delta d/\delta t = (3 \times 10^{-3}\ \text{m})/(2 \times 10^{-6}\ \text{s})$.

It should be appreciated that the actual distance between the pinging transducer and the piezoelectric sensor need not be known (although it can certainly be estimated by employing a reference medium with a known speed of sound) in order to calculate the speed of sound, so long as one has intimate knowledge of the time lag (δt) resulting from a change (δd) in this distance. Since the former is measured directly and the latter is micrometer-controlled, both with high accuracy and precision, the speed of sound may be easily calculated, as illustrated later in Figure D.3. The piezoelectric PZT sensor (*i.e.*, acoustic detector), represented as an ultrasonic microphone in Figure D.1, was constructed in-house and comprises a piezoceramic transducer (5 MHz, 20 × 0.4mm disc, Steiner & Martins, Inc.) with a sensitivity of 8.2 mV/psi.

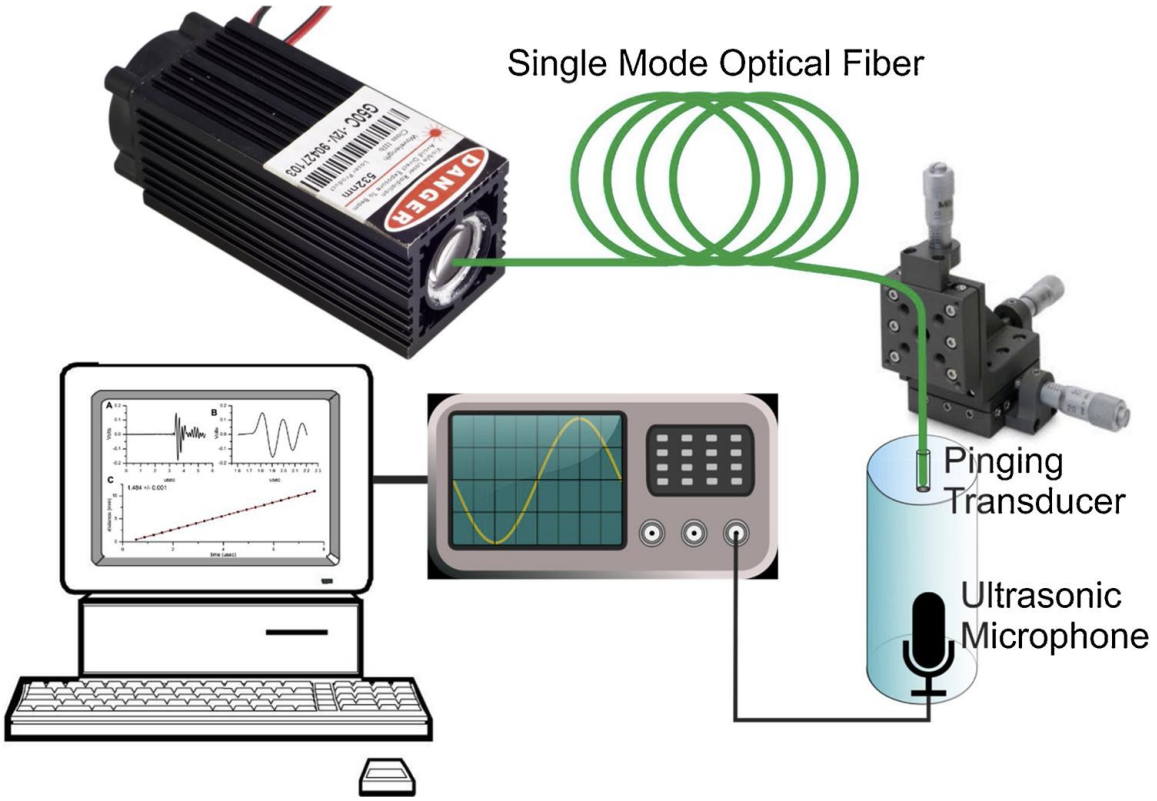

Figure D.1 Simplified schematic of laser-induced sound pinging (LISP) measurement setup. The Nd:Ce:YAG laser beam was directed toward the sample by means of a 1-mm diameter optical fiber covered on the distal end by a thin layer of paint-on rubber-based black liquid tape, serving as ultrasonic pinging transducer to generate ultrasound waves to probe the liquid sample. An XYZ micromanipulation stage allows for the systematic variation in the distance from the transducer to the detector (*i.e.*, PZT ultrasonic microphone). The output signal of the microphone was connected to a digital storage oscilloscope to measure the timing between the generation of the laser pulse and the arrival of the peak ultrasonic signal reaching the microphone. The data received from the oscilloscope were transferred to a personal computer for analysis.

The effective sensing area of the acoustic detector has a 6-mm radius. The detector was calibrated with a certified commercial ICP Pressure Sensor Model 138M146 (PCB Piezotronics Inc., Depew, NY, USA). A low-noise coaxial amplifier (ZFL-500, 21.36 dB gain, Mini-Circuits, Brooklyn, NY) was connected in series with the detector. The signal was digitized at 2 GSa/s and stored on a digital oscilloscope and the data were transferred to a PC for further analysis and processing using Origin 8.5 scientific software (OriginLab, Northampton, MA). A fast response (14 ns rise time), 13mm^2 Si biased detector (DET36 A ThorLabs) was used to trigger the oscilloscope each time a Nd:Ce:YAG laser pulse was delivered.

Results and Discussion

Preliminary LISP analysis: appearance and analysis of data

The LISP system was initially evaluated by measuring the velocity at room temperature of the propagation of sound in water, a medium whose sound speed has been rigorously studied. During the measurement, a single Nd:Ce:YAG laser pulse triggered the oscilloscope (at $t = 0$) to begin recording the acoustic signal detected by the piezoelectric sensor. The laser pulse continued down a single-mode optical fiber and impinged on the black tape (effectively, a beam stop and photoacoustic generator) at its terminus, generating an acoustic wave which propagated into the medium being analyzed (*e.g.*, water). In this manner, a slower speed of sound in the medium at a particular sound path length (*i.e.*, distance from pinging transducer to microphone) resulted in a correspondingly longer time delay before the appearance of the photoacoustic signal. The recorded signal was characterized by the appearance of a series of consecutive crests and valleys that damped in amplitude over time. The recorded signal was highly reproducible and the observed time

delay was linked to the distance between the pinging transducer and the microphone for a specific medium. The appearance of a typical photoacoustic signal waveform measured during a LISP experiment is shown in Figure D.3A. In Figure D.3B, an observed photoacoustic signal is expanded to view only the initial portion of the signal. We note that, for all LISP measurements described herein, the time delay was consistently calculated on the basis of the appearance of the first (most intense) peak of the recorded photoacoustic signal, designated by the asterisk in Figure D.3B. For completeness, it should be noted that this was simply a matter of convenience and any relative position along the waveform could have been used to no detriment so long as it were applied consistently. As shown in Figure D.3C, a series of photoacoustic signals could be generated simply by stepped Z-translation of the coated optical fiber tip (*i.e.*, pinging transducer) away from the microphone.

In these experiments, a micromanipulator was used to move the fiberoptic upward 0.50 mm (corresponding to one full turn of the micrometer used) each time before firing the laser. In this manner, by correlating the precise (micrometer-controlled) interval changes in the distance the sound must travel from genesis to detection at the fixed microphone with the observed time delay of the photoacoustic signal on the oscilloscope, a change in distance versus time delay plot can be generated. Figure D.3D shows the results of such an analysis carried out for room temperature water, using the experimental data provided in Figure D.3C. The slope of such a plot directly yields the speed of sound, as shown in Figure D.3D. In this case, we determined a speed of sound in water at 20°C of 1484.4 ± 1.6 m/s (an average based on five independent sets of measurements with our LISP device made over multiple days), in excellent agreement with the widely-accepted

value. Indeed, the most commonly reported value for the speed of sound in water at room temperature is 1484 m/s, although literature values can vary from 1482 to 1498 m/s, depending on the water source and quality and the precise temperature control.[34-35] Repeated recordings at the same micrometer setting produced highly repeatable time delays, with variations of ± 0.5 ns. This variation can be attributed to normal fluctuations in the trigger sensor response time and to intrinsic limitations in the oscilloscope digitization rate (*i.e.*, non-interpolated data points will be 0.5 ns apart for a 2 GSa/s oscilloscope).

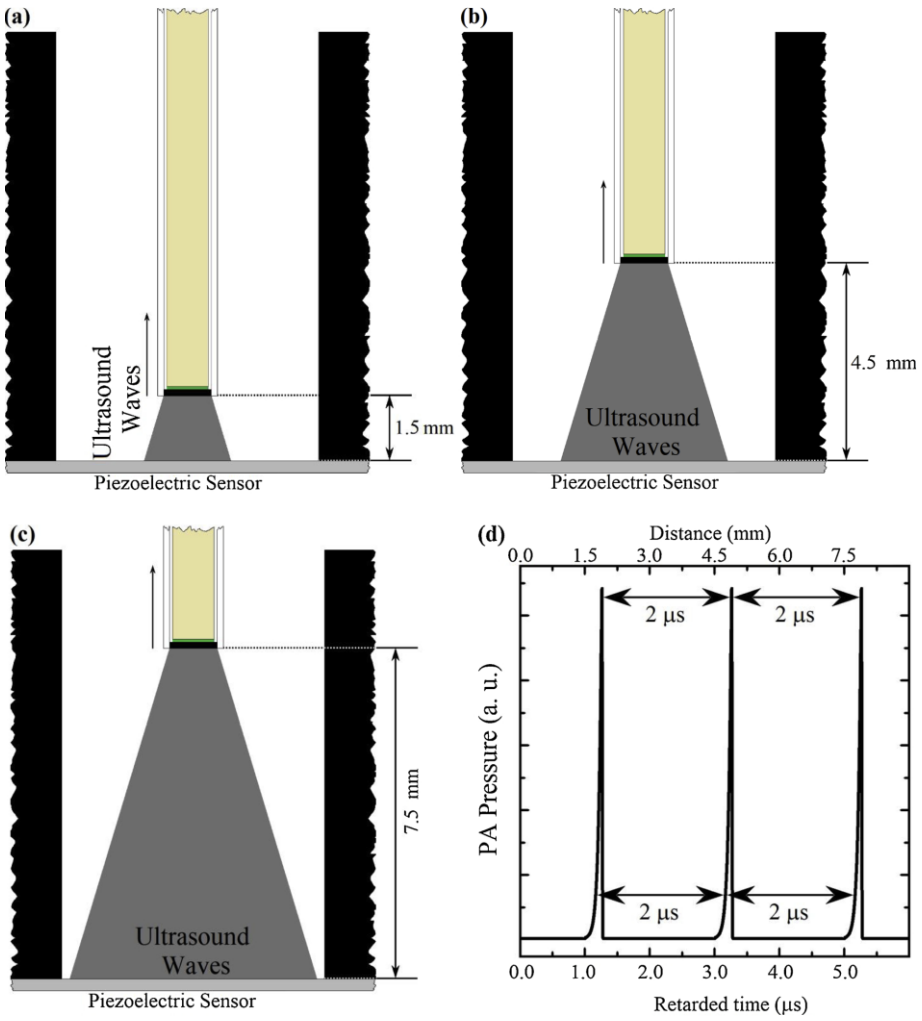

Figure D.2 Schematic representation of the LISP experiment illustrating three different ultrasonic transducer positions (1.5, 4.5, and 7.5 mm) relative to the immobile piezoelectric sensor. Panel A shows the initial position of the LISP experiment, with a distance of 1.5mm between the black liquid tape capping the optical fiber and the planar piezoelectric sensor). Panels B and C show two subsequent positions (4.5 and 7.5 mm, respectively). Panel D shows the LISP signal calculated numerically for each position. It is importantly to note that it does not matter which point on the signal waveform is selected to determine the time delay arising from displacement of the ultrasound source (controlled by Z-translation of the fiberoptic tip using a micrometer), so long as it is always performed at the same relative amplitude.

Significantly, although we fit results using 22 discrete micrometer positions in Figure D.3D (for a net change in the sound-traveled distance of 10.5 mm), in practice, only three to five measurements (micrometer positions) are sufficient to produce a highly reliable speed of sound, beyond which an increase in the number of measurements does not significantly alter the value determined.

Salinity of water

Another set of experiments was carried out to illustrate the utility of LISP in the evaluation of water quality on the basis of estimating its salinity (Figure D.4). For this demonstration, we chose to examine a wide range of aqueous NaCl solutions varying in concentration from 0 to 1000 mM. This range is pertinent for assessing the potability of drinking water (beyond ca. 20 mM [NaCl], water is unpalatable), the suitability for irrigation purposes (the salinity tolerance for crops varies widely from ~6 mM for certain sensitive vegetables to > 50 mM for barley, cotton, and sugarbeet), and fitness for watering livestock (guidelines are roughly

~35 mM for poultry and dairy cattle and nearly twice that for beef cattle, sheep and horses). It should be noted that sometimes much higher salinities can be tolerated for mining or industrial purposes, use by the thermoelectric-power industry to cool electricity- generating equipment being one such example.

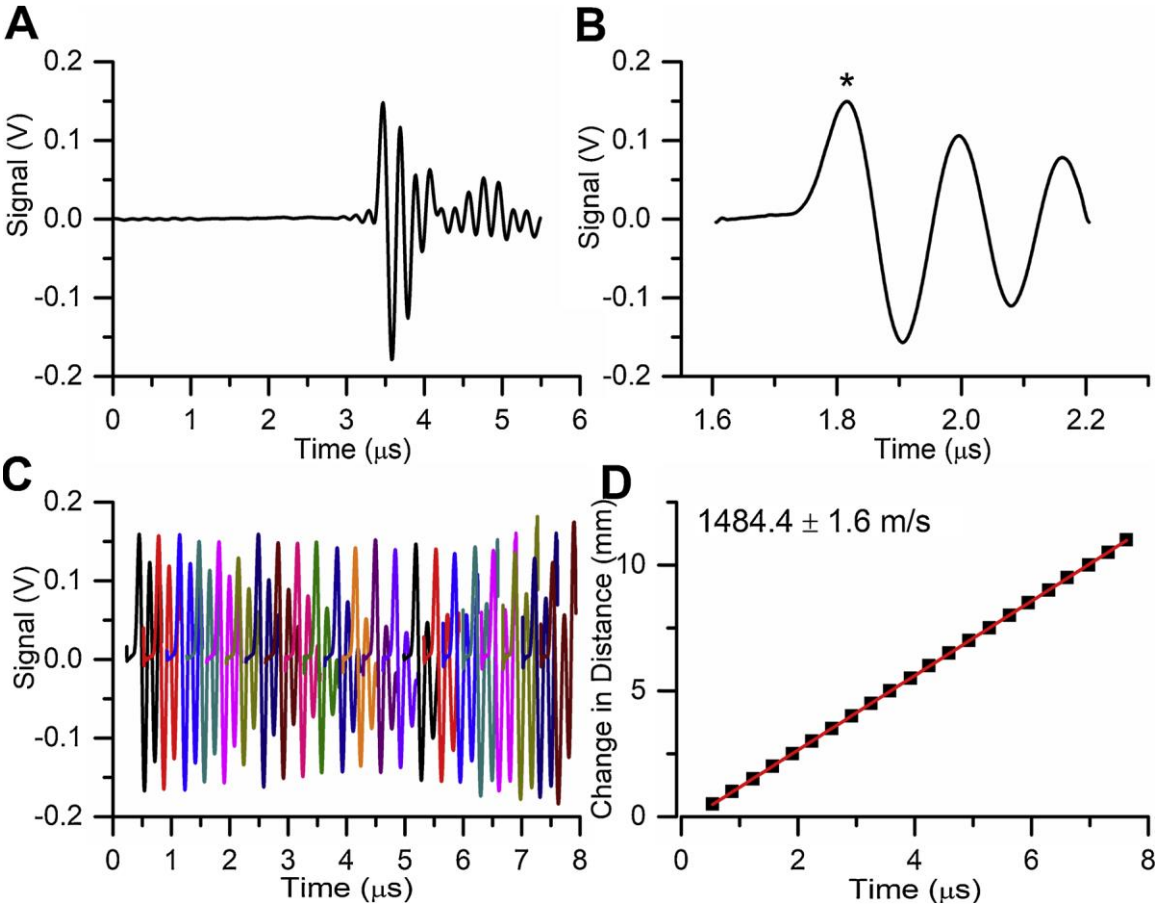

Figure D.3 Typical appearance and analysis of LISP data illustrated using measurements of the propagation of a photogenerated acoustic signal in distilled water at 20°C. Panel A illustrates a time delay (flat profile) prior to detection of the generated photoacoustic signal at the ultrasonic microphone. Panel B shows an example of an expanded photoacoustic signal. In the experiments described herein, for consistency, the time at the apex of the first peak of the photoacoustic signal was used to denote the arrival time of the signal at the microphone. Panel C presents a series of 22 measured photoacoustic waveforms generated by moving the black rubber coated tip of the optical fiber (ultrasonic pinging transducer)

recurrently in 0.50 mm steps upward (*i.e.*, away from the piezoelectric detector). Panel D shows linear regression results for stepped changes in transducer-to-detector distance (δd) versus the corresponding time delay (δt) observed on the basis of the first peak of the photoacoustic signal for each waveform given in Panel C.

Speed of sound measurements to evaluate salinity were made at room temperature and data points represent average values from three independent measurements, using fresh samples for each measurement. Figure D.4 demonstrates that the speed of sound is highly correlated with the content of NaCl dissolved in water, verifying the utility of LISP for estimating salinity. Compared with the speed of sound in water absent NaCl (1484 m/s) as a reference, LISP is able to distinguish water containing low levels of salinity that remain fully potable (1488 m/s for 10 mM NaCl). The speed of sound increases essentially linearly from 1484 to 1500 m/s between 0 and 100 mM NaCl and then monotonically increases more gradually proceeding from 100 to 1000 mM NaCl, at which point the speed of sound reaches 1546 m/s. As a counterpart or alternative to current analytical tools[15,36], there are a number of potential applications that would benefit from the ease of operation and convenient, real-time measures of salinity that LISP can provide, ranging from drinking water compliance assurance programs to environmental research and monitoring.

Analysis of dairy milk

Experiments were next conducted to establish the relevance of the LISP method toward complex food matrices, using speed of sound determinations for dilutions of bovine milk to illustrate utility. For these measurements, refrigerated whole milk was diluted with freshly-drawn Milli-Q water (18.2 MΩ · cm) to yield mixtures containing 5, 10, 25, 50,

and 75 vol% milk for analysis alongside undiluted whole milk and water. Replicate samples for each vol% milk were freshly prepared and measured to obtain a plot of the speed of sound versus vol% milk. As shown in Figure D.5, the speed of sound is linearly correlated with the percent whole milk, allowing for the estimation of the milk content within arbitrary samples. Indeed, the speed of sound increases from 1484 m/s in water, in agreement with literature data,[34-35] to a value of 1514 m/s for whole milk. Overall, these results suggest a broader usefulness of the LISP approach for making facile speed of sound determinations within small fluid volumes of beverages and other complicated milieu.

Ionic liquid analysis

In a final collection of experiments to further determine the capabilities and limitations of the LISP method, the temperature dependence of the speed of sound was measured in four representative ILs ($[Emim^+][Tf_2N^-]$, $[C_3mpy^+][Tf_2N^-]$, $[Hmim^+][Tf_2N^-]$, and $[Nip_{311}^+][Tf_2N^-]$) whose chemical structures are provided in Figure D.6. Speed of sound measurements were performed in the temperature range from 293 to 323 K, at 5 K intervals, independently analyzing four different samples of each particular IL. The results are summarized in Figure D.7A, alongside comparisons to literature values. Numerical values for LISP-determined speeds of sound and referenced literature values can be found in Table E.1.

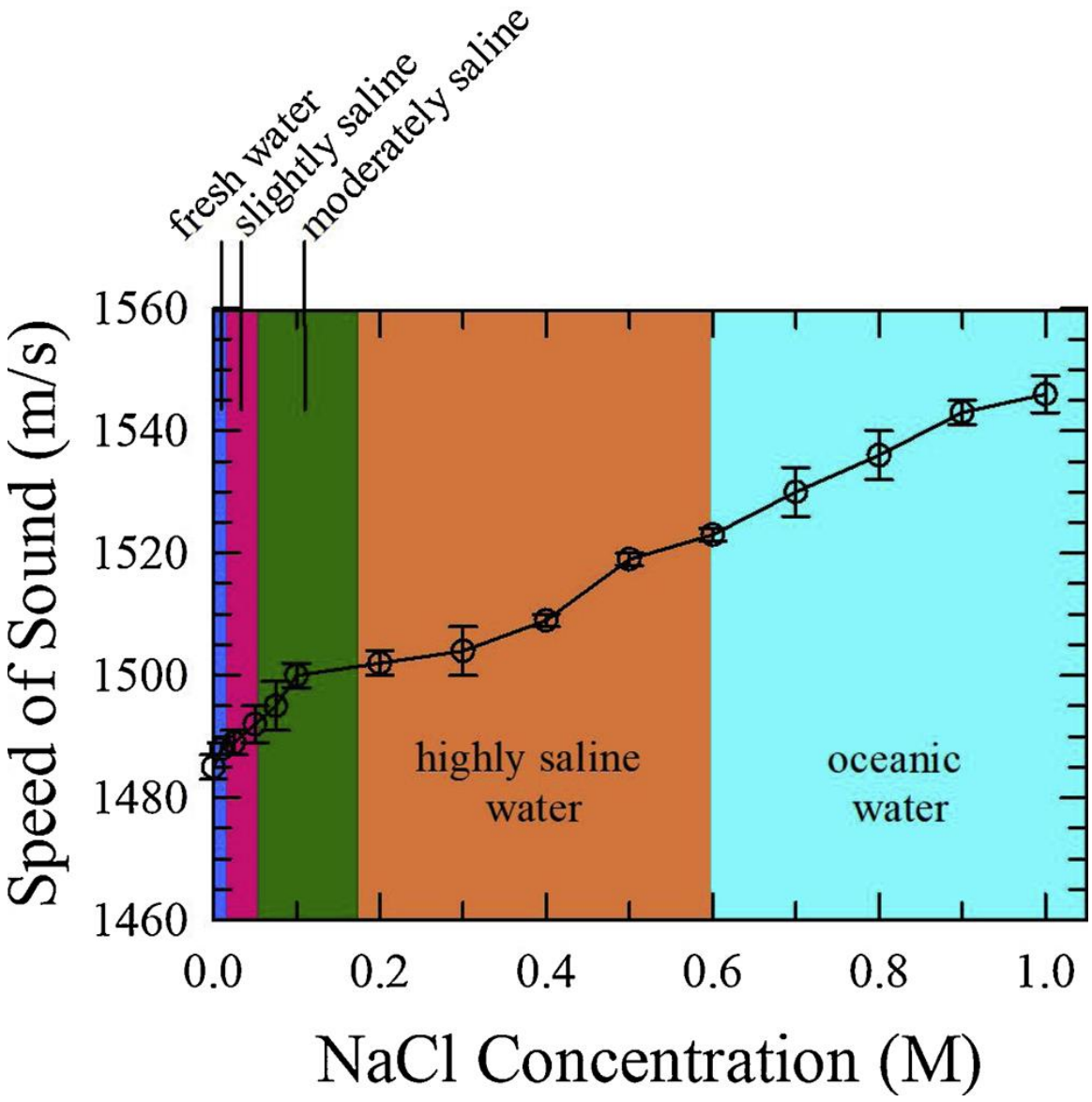

Figure D.4 LISP analysis of the salinity of water based on the speed of sound in the range of 0–1000 mM NaCl. This range is pertinent for assessing the suitability of water for drinking, irrigation, watering livestock, or industrial or mining usage. Samples were measured at room temperature and data points represent average values from at least three independent measurements.

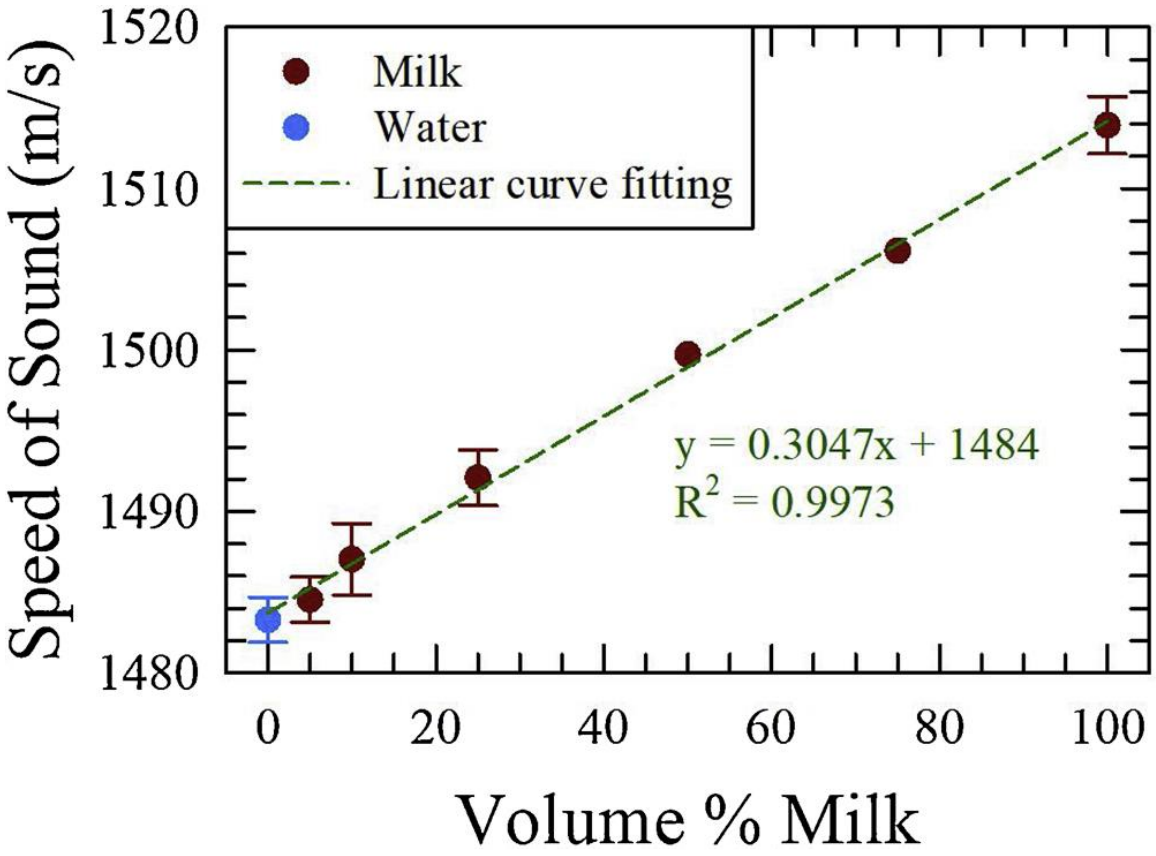

Figure D.5 Plot correlating the speed of sound with the volume percent of whole milk in aqueous-diluted samples. Neat water is included as a benchmark for comparison. Measurements were made at room temperature and data points represent average values from three independent measurements, using fresh samples for each measurement.

For the studied ILs, the speed of sound decreases steadily with increasing temperature with an average sensitivity to temperature slightly lower than that of water. That is, in water, the sound speed changes ~2.4 m/s per degree Kelvin while the rate of change determined for these ILs ranges from 1.91 m/s per degree (for ($[Emim^+][Tf_2N^-]$) to 2.43 m/s per degree ($[Nip_{311}^+][Tf_2N^-]$), a magnitude similar to that observed for most molecular liquids. We note that a linear function is fully adequate to describe the temperature dependence of the speed of sound in these four ILs. The speed of sound for three of these ILs have been

reported previously, providing a useful comparison to the present measurements. In the cases of the two imidazolium-based ILs ([$Emim^+$][Tf_2N^-] and [$Hmim^+$][Tf_2N^-]), our data are highly consistent with published values, differing by ± 0.18%, on average. In the case of [C_3mpy^+][Tf_2N^-], our measured speeds of sound were consistently 0.6–1.0% lower than reported speeds[4, 25, 28, 37-41] discrepancies we preliminarily attribute to differences in sample purity (*e.g.*, residual halide), but particularly water content (*vide infra*). Consistent with literature observations,[39, 42] elongation of the alkyl chain pendant on the imidazolium ring is seen to yield a lower speed of sound in the IL (compare results for [$Emim^+$][Tf_2N^-] and [$Hmim^+$][Tf_2N^-] in Figure D.7A). Likewise, for comparable chain lengths, sound propagates faster in ILs based on the pyrrolidinium cation compared with the imidazolium cation,[3, 39] and our observations with [C_3mpy^+][Tf_2N^-] certainly bear this out. Dzida *et al.* pointed out the relatively high speed of sound measured in tetraalkylammonium hydroxides[3], rousing us to additionally include an acyclic ammonium-based IL in this study.

To this end, we also measured the speed of sound in dimethyl(isopropyl)propylammonium bis(trifluoromethylsulfonyl) imide ([Nip_{311}^+][Tf_2N^-]). The experimental speed of sound in [Nip_{311}^+][Tf_2N^-] was roughly 16.5 m/s faster than in [C_3mpy^+][Tf_2N^-] across the temperature range from 293 to 323 K (*i.e.*, ∼1.3% faster), highlighting the effect of the cationic headgroup sterics and geometry (cyclic versus acyclic ammonium) on packing and induced interactions with the [Tf_2N^-] anion. In this head-to-head comparison, we further note that the ammonium cations [Nip_{311}^+] and [C_3mpy^+] contain the same number of carbon atoms and, in fact, the same calculated molecular volume (166 $Å^3$).[30] This outcome points to the possibility of using the

speed of sound in general, and LISP in particular, to elucidate subtle changes in structure and packing in analogous ILs. We now briefly return to the small but statistically-significant discrepancy between our measured sound speeds in $[C_3mpy^+][Tf_2N^-]$ and available values in the open literature. Given that water is (at least at *some* level) omnipresent in ILs, we carried out a control study seeking to reveal the extent to which this impurity impacts the speed of sound in an architype IL. In this preliminary study, speed of sound was measured in two $[C_3mpy^+][Tf_2N^-]$ samples which had spent disparate periods of time drying under heated (70°C) evacuation to yield two different water contents. Immediately following rapid (~1 min) LISP analysis, the samples were assayed using coulometric Karl Fischer titration procedures to validate water contents of 142 and 1073 ppm. As can be seen in Figure D.7B, despite both samples being relatively dry by conventional standards, an increase in water content from 142 to 1073 ppm resulted in a measurable increase in the speed of sound (by ~0.45%, on average), highlighting the necessity of reporting water levels alongside speed of sound quantities in ILs. Certainly, the influence of water content in ILs on the speed of sound (and on a multitude of physicochemical parameters, for that matter)[43] has been discussed in the literature.[4] Our findings corroborate the need to carefully dry and analyze ILs for water content to improve reliability and reproducibility and remove uncertainties due to ignorance about

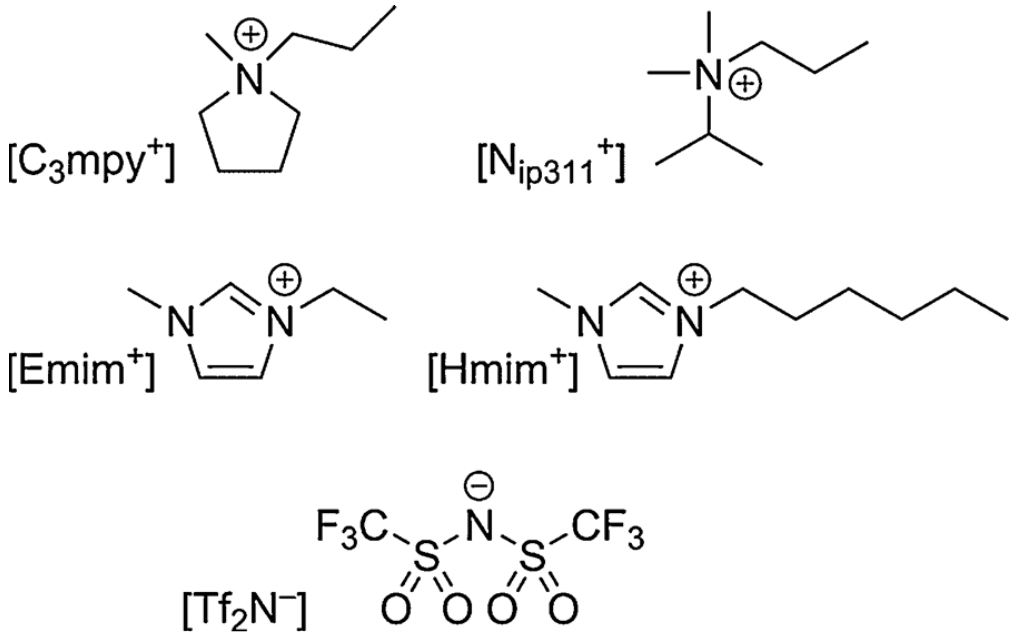

Figure D.6 Chemical structures and shorthand designations of the ions comprising the ionic liquids investigated in this study.

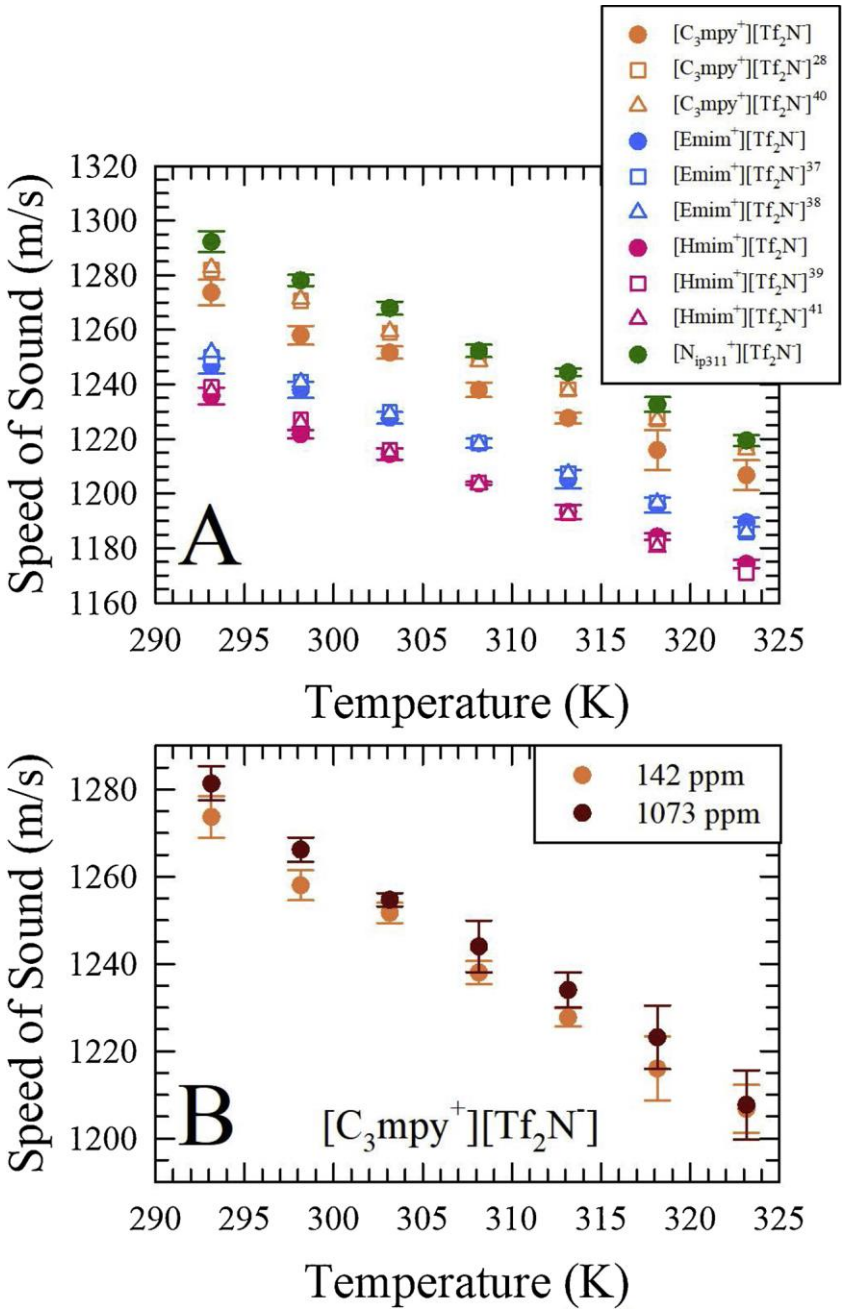

Figure D.7 (A) Temperature-dependent speed of sound results for four representative ionic liquids in the range from 293 to 323 K. Filled circular data points represent values measured in the current study using the LISP approach (samples were dried beforehand *in vacuo* for 24 h at 70°C). Error bars represent the standard deviation from four independent measurements of the indicated ionic liquid made on different days. The measured sound speeds are compared to the indicated literature reported values denoted by open symbols. An example for which no literature data are available is included alongside

([N_{ip311}^{+}][Tf_2N^{-}]), an open invitation for other researchers to use existing or commercial instrumentation (*e.g.*, a Mittal Enterprises ultrasonic interferometer or an Anton Paar DSA series pulsed excitation instrument) to independently determine values for this liquid. (B) In order to illustrate the impact of impurities on this property, the speed of sound in [C_3mpy^{+}][Tf_2N^{-}] was measured after the intentional inclusion of a tiny additional amount of water, an omnipresent impurity in ionic liquids. Despite both samples being relatively dry by conventional standards, an increase in water content from 142 to 1073 ppm manifests in an apparent increase in the speed of sound, highlighting the necessity of knowing the water content when reporting the speed of sound in an ionic liquid. Numerical values for the speed of sound in [C_3mpy^{+}][Tf_2N^{-}] at the two water contents shown are tabulated in Table E.2.

water content. Conversely, it appears that the speed of sound provides an analytical tool to determine gross water content within an ILs, the minimal sample-volume requirements of LISP being a significant benefit in this regard.

Conclusions

Current methods to identify the speed of sound in liquids are cumbersome, expensive, and/or require large sample volumes. In this communication, we demonstrate laser-induced sound pinging (LISP) as a new photoacoustic method to accurately determine the speed of sound in a number of representative liquids, including water of varying salinity (0.0–1.0 M NaCl) and whole and diluted milk samples, as well as temperature-dependent speed of sound determinations from 293 to 323 K made in four illustrative ionic liquids. Typical sample volumes employed for analysis were 150 μL. The operation of LISP relies on the accurate estimation of delays in the time of travel of an acoustic ultrasound wave which are computed with respect to the micrometer-controlled change in the distance between

fiberoptic-delivered acoustic generation in the sample and a PZT piezoelectric detector (microphone). Constructed from off-the-shelf components, LISP is model-independent and offers clear advantages in the determination of the speed of sound, with the added benefits of requiring very small sample volumes, no sample pre-processing or treatment, and low cost per analysis. For example, in contrast to state-of-the-art multi-frequency ultrasonic interferometry (*e.g.*, Mittal Enterprises), which is constrained by the need for ca. 10 mL sample volumes, LISP can be implemented for volumes down to 25 μL which is a significant benefit for analyzing precious, sparse, or hazardous liquids.

The LISP procedure is rapid (assay time of 2–3 min) and is well suited for the repeated analysis of large numbers of samples in small consecutive batches or may be modified for a continuous-flow format to monitor changes of a sample occurring over time (*e.g.*, process control during fermentation). We note that, unless excessive, the laser power exerts no influence on the speed of sound determination, because the light does not directly interact with the sample but instead impinges only on the ultrasonic pinging transducer. For the results reported here, the typical pulse energy was 1 mJ, which neither showed gas bubble production within the tested samples nor damaged the ultrasonic transducer. Although not studied in detail, excessive pulse energies (> 20 mJ) are unnecessary and should in fact be avoided, because they can degrade the transducer after iterative (< 10) pulses. Likewise, the wavelength of light is immaterial as the light does not directly impinge on the liquid sample. This is another key attribute of the proposed LISP approach: a pulsed laser of any wavelength can be applied. For convenience, we have used the 532 nm frequency-doubled output of a Nd:Ce:YAG tattoo-removal laser, since this wavelength is easily transmitted using a standard optical fiber and is fully absorbed by our ultrasonic

pinging transducer. However, in principle, we could have just as readily used the 1064 nm (fundamental) Nd:Ce:YAG output.

Overall, LISP offers a simple, inexpensive, easy-to-use method for measuring the speed of sound in arbitrary or unknown fluids and solutions, fostering the development of rapid and reliable analytical approaches to screen for food adulteration (*e.g.*, fraudulent olive oils) or intentional product contamination, commercial beverage quality control (*e.g.*, alcohol content in beer), water monitoring, and urinalysis, among other possible applications. The capabilities of LISP can be further extended in the future by developing miniaturized, fully fieldable LISP platforms which employ pulsed LED excitation to create inexpensive, small-footprint devices coupled to smartphone technology.

Notes

The authors declare no competing financial interest.

Acknowledgements

This research was partially supported by Consejo Nacional de Ciencia y Tecnología-México (Fronteras de la Ciencia-2016, Grant No. 2029).

References

1. McClements, D. J., Advances in the Application of Ultrasound in Food Analysis and Processing. *Trends in Food Science & Technology* **1995,** *6* (9), 293-299.

2. Sikdar, S.; Shah, J. P.; Gebreab, T.; Yen, R.-H.; Gilliams, E.; Danoff, J.; Gerber, L. H., Novel Applications of Ultrasound Technology to Visualize and Characterize Myofascial Trigger Points and Surrounding Soft Tissue. *Archives of Physical Medicine and Rehabilitation* **2009,** *90* (11), 1829-1838.

3. Dzida, M.; Zorębski, E.; Zorębski, M.; Żarska, M.; Geppert-Rybczyńska, M.; Chorążewski, M.; Jacquemin, J.; Cibulka, I., Speed of Sound and Ultrasound Absorption in Ionic Liquids. *Chem. Rev.* **2017,** *117* (5), 3883-3929.

4. Widegren, J. A.; Magee, J. W., Density, Viscosity, Speed of Sound, and Electrolytic Conductivity for the Ionic Liquid 1-Hexyl-3-Methylimidazolium Bis(Trifluoromethylsulfonyl)Imide and Its Mixtures with Water. *J. Chem. Eng. Data* **2007,** *52* (6), 2331-2338.

5. Zorębski, E.; Dzida, M., The Effect of Temperature and Pressure on Acoustic and Thermodynamic Properties of 1,4-Butanediol. The Comparison with 1,2-, and 1,3-Butanediols. *J. Chem. Thermodynamics* **2012,** *54*, 100-107.

6. Xue, B.; Wang, Z.; Zhang, K.; Zhang, H.; Chen, Y.; Jia, L.; Wu, H.; Zhai, J., Direct Measurement of the Sound Velocity in Seawater Based on the Pulsed Acousto-Optic Effect between the Frequency Comb and the Ultrasonic Pulse. *Opt. Express* **2018,** *26* (17), 21849-21860.

7. Baesso, R. M.; Oliveira, P. A.; Morais, G. C.; Alvarenga, A. V.; Costa-Felix, R. P. B., Using Ultrasonic Velocity for Monitoring and Analysing Biodiesel Production. *Fuel* **2018,** *226*, 389-399.

8. Yebra, F.; Troncoso, J.; Romaní, L., Fully Automatized Apparatus for Determining Speed of Sound for Liquids in the Temperature and Pressure Interval (283.15–343.15)K and (0.1–95)Mpa. *J. Chem. Thermodynamics* **2017,** *104*, 102-109.

9. Cho, B. K.; Irudayaraj, J. M. K., A Noncontact Ultrasound Approach for Mechanical Property Determination of Cheeses. *J. Food Sci.* **2003,** *68* (7), 2243-2247.

10. Leroy, C. C.; Robinson, S. P.; Goldsmith, M. J., A New Equation for the Accurate Calculation of Sound Speed in All Oceans. *The Journal of the Acoustical Society of America* **2008,** *124* (5), 2774-2782.

11. Sallarès, V.; Biescas, B.; Buffett, G.; Carbonell, R.; Dañobeitia, J. J.; Pelegrí, J. L., Relative Contribution of Temperature and Salinity to Ocean Acoustic Reflectivity. *Geophysical Research Letters* **2009,** *36* (24).

12. Lago, S.; Giuliano Albo, P. A.; von Rohden, C.; Rudtsch, S., Speed of Sound Measurements in North Atlantic Seawater and Iapso Standard Seawater up to 70mpa. *Marine Chemistry* **2015,** *177*, 662-667.

13. Rohden, C. v.; Fehres, F.; Rudtsch, S., Capability of Pure Water Calibrated Time-of-Flight Sensors for the Determination of Speed of Sound in Seawater. *The Journal of the Acoustical Society of America* **2015,** *138* (2), 651-662.

14. Leonard, D. A.; Caputo, B.; Hoge, F. E., Remote Sensing of Subsurface Water Temperature by Raman Scattering. *Appl. Opt.* **1979,** *18* (11), 1732-1745.

15. Liu, D.; Xu, J.; Li, R.; Dai, R.; Gong, W., Measurements of Sound Speed in the Water by Brillouin Scattering Using Pulsed Nd:Yag Laser. *Optics Communications* **2002,** *203* (3), 335-340.

16. Elvira, L.; Rodríguez, J.; Lynnworth, L. C., Sound Speed and Density Characterization of Milk Adulterated with Melamine. *The Journal of the Acoustical Society of America* **2009,** *125* (5), EL177-EL182.

17. MacFarlane, D. R.; Tachikawa, N.; Forsyth, M.; Pringle, J. M.; Howlett, P. C.; Elliott, G. D.; Davis, J. H.; Watanabe, M.; Simon, P.; Angell, C. A., Energy Applications of Ionic Liquids. *Energ. Environ. Sci.* **2014,** *7* (1), 232-250.

18. Rogers, R. D.; Seddon, K. R., Ionic Liquids--Solvents of the Future? *Science* **2003,** *302* (5646), 792-793.

19. Baker, G. A.; Baker, S. N.; Pandey, S.; Bright, F. V., An Analytical View of Ionic Liquids. *Analyst* **2005,** *130* (6), 800-808.

20. Ho, T. D.; Canestraro, A. J.; Anderson, J. L., Ionic Liquids in Solid-Phase Microextraction: A Review. *Anal. Chim. Acta* **2011,** *695* (1), 18-43.

21. Wishart, J. F., Energy Applications of Ionic Liquids. *Energ. Environ. Sci.* **2009,** *2* (9), 956-961.

22. Karadas, F.; Atilhan, M.; Aparicio, S., Review on the Use of Ionic Liquids (Ils) as Alternative Fluids for Co2 Capture and Natural Gas Sweetening. *Energ. Fuel* **2010,** *24* (11), 5817-5828.

23. Arce, A.; Rodríguez, O.; Soto, A., Experimental Determination of Liquid−Liquid Equilibrium Using Ionic Liquids: Tert-Amyl Ethyl Ether + Ethanol + 1-Octyl-3-Methylimidazolium Chloride System at 298.15 K. *J. Chem. Eng. Data* **2004,** *49* (3), 514-517.

24. Arce, A.; Rodríguez, O.; Soto, A., Tert-Amyl Ethyl Ether Separation from Its Mixtures with Ethanol Using the 1-Butyl-3-Methylimidazolium Trifluoromethanesulfonate Ionic Liquid: Liquid−Liquid Equilibrium. *Ind. Eng. Chem. Res.* **2004,** *43* (26), 8323-8327.

25. Frez, C.; Diebold, G. J.; Tran, C. D.; Yu, S., Determination of Thermal Diffusivities, Thermal Conductivities, and Sound Speeds of Room-Temperature Ionic Liquids by the Transient Grating Technique. *J. Chem. Eng. Data* **2006,** *51* (4), 1250-1255.

26. Wu, K.-J.; Chen, Q.-L.; He, C.-H., Speed of Sound of Ionic Liquids: Database, Estimation, and Its Application for Thermal Conductivity Prediction. *AIChE Journal* **2014,** *60* (3), 1120-1131.

27. Burrell, A. K.; Sesto, R. E. D.; Baker, S. N.; McCleskey, T. M.; Baker, G. A., The Large Scale Synthesis of Pure Imidazolium and Pyrrolidinium Ionic Liquids. *Green Chem.* **2007,** *9* (5), 449-454.

28. González, B.; González, E. J., Physical Properties of the Pure 1-Methyl-1-Propylpyrrolidinium Bis(Trifluoromethylsulfonyl)Imide Ionic Liquid and Its Binary Mixtures with Alcohols. *J. Chem. Thermodynamics* **2014,** *68*, 109-116.

29. Nockemann, P.; Binnemans, K.; Driesen, K., Purification of Imidazolium Ionic Liquids for Spectroscopic Applications. *Chem. Phys. Lett.* **2005,** *415* (1), 131-136.

30. Jin, H.; O'Hare, B.; Dong, J.; Arzhantsev, S.; Baker, G. A.; Wishart, J. F.; Benesi, A. J.; Maroncelli, M., Physical Properties of Ionic Liquids Consisting of the 1-Butyl-3-Methylimidazolium Cation with Various Anions and the Bis(Trifluoromethylsulfonyl)Imide Anion with Various Cations. *J. Phys. Chem. B* **2008,** *112* (1), 81-92.

31. Bravo-Miranda, C. A.; González-Vega, A.; Gutiérrez-Juárez, G., Influence of the Size, Geometry and Temporal Response of the Finite Piezoelectric Sensor on the Photoacoustic Signal: The Case of the Point-Like Source. *Applied Physics B* **2014,** *115* (4), 471-482.

32. Laugier, P.; Haïat, G., Introduction to the Physics of Ultrasound. In *Bone Quantitative Ultrasound*, Laugier, P.; Haïat, G., Eds. Springer Netherlands: Dordrecht, 2011; pp 29-45.

33. Hendee, W. R.; Ritenour, E. R., Medical Imaging Physics, 4th Ed. Wiley-Liss, New York. 2002. *American Journal of Neuroradiology* **2003,** *24* (5), 1023-1024.

34. Lin, C.-W.; Trusler, J. P. M., The Speed of Sound and Derived Thermodynamic Properties of Pure Water at Temperatures between (253 and 473) K and at Pressures up to 400 Mpa. *J. Chem. Phys.* **2012,** *136* (9), 094511.

35. Chávez, M.; Sosa, V.; Tsumura, R., Speed of Sound in Saturated Pure Water. *The Journal of the Acoustical Society of America* **1985,** *77* (2), 420-423.

36. Carman, J. C., Classroom Measurements of Sound Speed in Fresh/Saline Water. *The Journal of the Acoustical Society of America* **2012,** *131* (3), 2455-2458.

37. Dzida, M.; Chorążewski, M.; Geppert-Rybczyńska, M.; Zorębski, E.; Zorębski, M.; Żarska, M.; Czech, B., Speed of Sound and Adiabatic Compressibility of 1-Ethyl-3-Methylimidazolium Bis(Trifluoromethylsulfonyl)Imide under Pressures up to 100 Mpa. *J. Chem. Eng. Data* **2013,** *58* (6), 1571-1576.

38. Zorębski, E.; Geppert-Rybczyńska, M.; Zorębski, M., Acoustics as a Tool for Better Characterization of Ionic Liquids: A Comparative Study of 1-Alkyl-3-Methylimidazolium Bis[(Trifluoromethyl)Sulfonyl]Imide Room-Temperature Ionic Liquids. *J. Phys. Chem. B* **2013,** *117* (14), 3867-3876.

39. Seoane, R. G.; Corderí, S.; Gómez, E.; Calvar, N.; González, E. J.; Macedo, E. A.; Domínguez, Á., Temperature Dependence and Structural Influence on the Thermophysical Properties of Eleven Commercial Ionic Liquids. *Ind. Eng. Chem. Res.* **2012,** *51* (5), 2492-2504.

40. Geppert-Rybczyńska, M.; Lehmann, J. K.; Heintz, A., Physicochemical Properties of Two 1-Alkyl-1-Methylpyrrolidinium Bis[(Trifluoromethyl)Sulfonyl]Imide Ionic Liquids and of Binary Mixtures of 1-Butyl-1-Methylpyrrolidinium Bis[(Trifluoromethyl)Sulfonyl]Imide with Methanol or Acetonitrile. *J. Chem. Thermodynamics* **2014,** *71*, 171-181.

41. Zorębski, M.; Zorębski, E.; Dzida, M.; Skowronek, J.; Jężak, S.; Goodrich, P.; Jacquemin, J., Ultrasonic Relaxation Study of 1-Alkyl-3-Methylimidazolium-Based Room-Temperature Ionic Liquids: Probing the Role of Alkyl Chain Length in the Cation. *J. Phys. Chem. B* **2016,** *120* (14), 3569-3581.

42. Esperança, J. M. S. S.; Visak, Z. P.; Plechkova, N. V.; Seddon, K. R.; Guedes, H. J. R.; Rebelo, L. P. N., Density, Speed of Sound, and Derived Thermodynamic Properties of Ionic Liquids over an Extended Pressure Range. 4. $[C_3mim][Ntf_2]$ and $[C_5mim][Ntf_2]$. *J. Chem. Eng. Data* **2006,** *51* (6), 2009-2015.

43. Pandey, S.; Fletcher, K. A.; Baker, S. N.; Baker, G. A., Correlation between the Fluorescent Response of Microfluidity Probes and the Water Content and Viscosity of Ionic Liquid and Water Mixtures. *Analyst* **2004,** *129* (7), 569-573.

Appendix E: Supporting Information for Appendix D: Laser-induced Sound Pinging (LISP): A Rapid Photoacoustic Method to Determine the Speed of Sound in Microliter Fluid Volumes

Luis Polo-Parada, Gerardo Gutiérrez-Juárez, **Jennifer A. Kist**, Laxmi Adhikari, Nakara Bhawawet, and Gary A. Baker

Table E.1 Speed of sound in four different ILs over a temperature range of 293.15 to 323.15 K.

Ionic liquid	Temperature (K)	Speed of sound (m/s)			
		Our data	Std. Dev.	Literature value	
$[Emim^+][Tf_2N^-]$	293.15	1246.75	2.75	1249.98[37]	1251.83[38]
	298.15	1238.00	2.94	1240.96[37]	1240.78[38]
	303.15	1227.75	2.06	1229.85[37]	1229.10[38]
	308.15	1218.50	1.73	1218.50[37]	1218.13[38]
	313.15	1205.25	3.30	1207.47[37]	1207.25[38]
	318.15	1195.75	2.75	1196.80[37]	1196.58[38]
	323.15	1189.50	1.73	1185.92[37]	1185.96[38]
$[C_3mpy^+][Tf_2N^-]$	293.15	1273.67	4.73	1281.90[28]	1282.77[40]
	298.15	1258.00	3.46	1270.60[28]	1271.34[40]
	303.15	1251.67	2031	1259.00[28]	1259.53[40]

	308.15	1238.00	2.65	1249.10[28]	1248.56[40]
	313.15	1227.67	2.08	1238.20[28]	1237.63[40]
	318.15	1216.00	7.35	1227.40[28]	1226.94[40]
	323.15	1206.75	5.50	1216.90[28]	1216.22[40]
$[Hmim^+][Tf_2N^-]$	293.15	1235.75	2.98	1237.29[41]	1239[39]
	298.15	1221.75	1.50	1225.86[41]	1227[39]
	303.15	1214.50	2.08	1214.52[41]	1216[39]
	308.15	1203.75	0.50	1203.34[41]	1204[39]
	313.15	1193.25	2.63	1192.24[41]	1193[39]
	318.15	1184.25	1.26	1180.45[41]	1182[39]
	323.15	1174.25	1.50	--	1171[39]
$[N_{ip311}^+][Tf_2N^-]$	293.15	1292.32	3.75	--	--
	298.15	1278.16	2.01	--	--
	303.15	1267.96	2.38	--	--
	308.15	1252.28	2.28	--	--
	313.15	1244.43	1.40	--	--
	318.15	1232.60	2.70	--	--
	323.15	1219.44	2.02	--	--

Table E.2 Speed of sound in $[C_3mpy^+][Tf_2N^-]$ for two different water concentrations.

Temperature (K)	1073 ppm		142 ppm	
	Speed of sound (m/s)	Std. Dev. (m/s)	Speed of sound (m/s)	Std. Dev. (m/s)
293.15	1281.33	3.93	1273.66	4.73
298.15	1266.16	2.79	1258.00	3.46
303.15	1254.66	1.51	1251.66	2.31
308.15	1244.00	5.93	1238.00	2.65
313.15	1234.00	3.95	1227.66	2.08
318.15	1223.16	7.31	1216.00	7.35
323.15	1207.66	7.94	1206.75	5.50

Appendix F: Artifacts and Errors Associated with the Ubiquitous Presence of Fluorescent Impurities in Carbon Nanodots†

†This chapter is based on a published manuscript in Chem. Mater. The information contained herein is adapted with permission from Essner, J. B., **Kist, J. A.,** Polo-Parada, L., and Baker, G. A., Artifacts and Errors Associated with the Ubiquitous Presence of Fluorescent Impurities in Carbon Nanodots, Chem. Mater. **2018**, 30, 1878-1887. Copyright © 2018 American Chemical Society.

As second author of this publication, I assisted in various carbon nanodot syntheses and purification processes. I also performed cell toxicity studies, helped with quantum yield calculations, and assisted with the table.

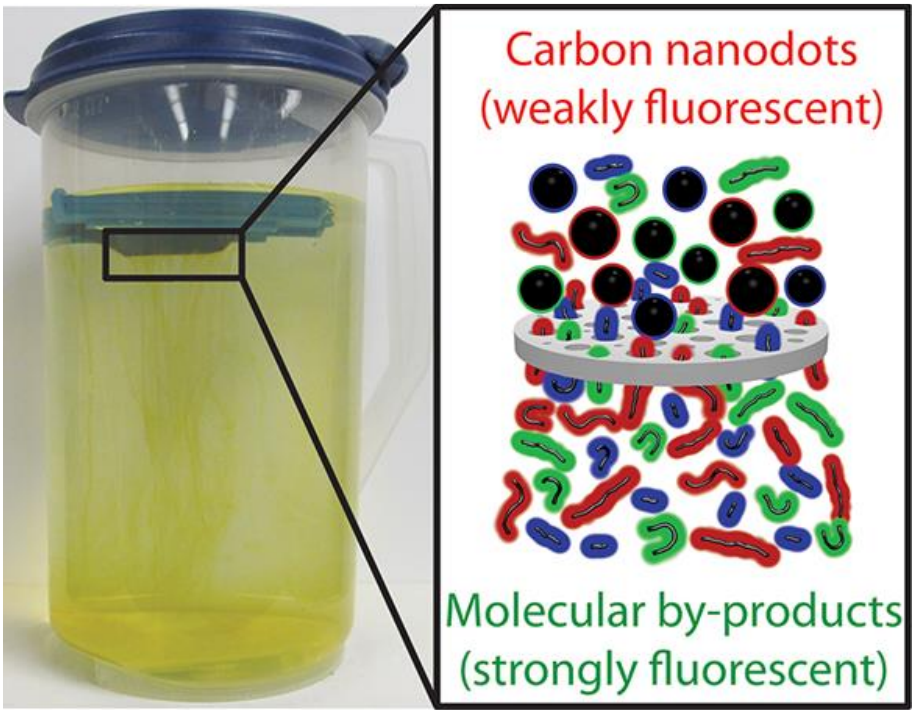

Scheme F.1 Graphical TOC alluding to the fact that the impurities in carbon nanodots contribute to fluorescence.

Abstract

Fluorescent carbon dots have attracted tremendous attention owing to their superlative optical properties which suggest opportunities for replacing conventional fluorescent materials in various application fields. Not surprisingly, the rapid pace of publication has been accompanied by a host of critical issues, errors, controversies, and misconceptions associated with these emergent materials, which present significant barriers to elucidating their true nature, substantially hindering the extensive exploitation of these nanomaterials. Of particular interest are expedient, bottom-up pathways to carbon dots starting from molecular precursors (*e.g.*, citric acid, amino acids, and alkylamines), although such routes are associated with generation of a ubiquity of small molecular weight or oligomeric fluorescent byproducts. A primary obstacle to progress is the inadequacy of purification in reported studies, an omission which gives rise to misconceptions about the nature and characteristics of the carbon dots.

In this work, we conducted a series of carbon dot syntheses using facile hydrothermal and microwave routes employing citric acid (paired with urea or ethylenediamine as a nitrogen source), followed by dialysis or ultrafiltration purification steps. Careful comparison and analysis of the optical properties of the resulting purification products (*i.e.*, dialysate/filtrate versus retentate fractions) affirms the formation of molecular fluorophores (potentially oligomeric or polymeric in nature) during the bottom-up chemical synthesis which contribute a majority of the emission from carbon dot samples. We provide clear evidence showing that the fluorescent impurities produced as byproducts of carbon dot synthesis must be rigorously removed to obtain reliable results. On the basis of our findings, the inadequate purification in many reports calls into question

published work, suggesting that many previous studies will need to be carefully revisited using more rigorous purification protocols. Of course, deficiencies in purification in prior studies only add to the ongoing debate on carbon dot structure and the origin of their emission. Moving forward, rigorous and consistent purification steps will need to be uniformly implemented, a tactical change that will help pave the way toward the development of carbon dots as next-generation agents for cellular imaging, solid-state and full-color lighting, photovoltaics, catalysis, and (bio)sensing.

Introduction

Nanoscale carbons are associated with a range of attractive properties, including electrical conductivity, biocompatibility, high thermal stability, and tunability (textural properties and doping), forming the subject of intensive research in recent years. The newest addition to the family of nanoscale carbons consists of fluorescent carbon dots (FCDs). Typically sized below 10 nm, FCDs display unique and useful optical features (*e.g.*, excitation wavelength-dependent fluorescence, tunable emission color, high photostability) not seen with their nanocarbon relatives (fullerenes, graphenes, carbon nanotubes, and nanodiamonds), while also offering biocompatibility, inertness, and low cytotoxicity, which make them preferable to conventional semiconductor-based quantum dots (*e.g.*, CdS).[1-8] Moreover, FCDs can be synthesized using a wide variety of top-down or bottom-up approaches. The literature suggests that FCDs can be produced as a result of appropriate thermal treatment of virtually any carbon-containing precursor, with examples including citrates,[9-15] saccharides (*e.g.*, glucose and chitosan),[16-22] food waste,[23-28] biomass,[29-32] human hair,[33-35] and even human urine[36] or animal feces.[37] Due to their facile preparation and promising characteristics, research on FCDs has exploded recently, with the majority

(> 3000) of the total publications (~3500 as of 2016) appearing within the past few years. The unbridled enthusiasm and extremely rapid pace of research has naturally led to a number of uncritical, unsubstantiated, and detrimental claims and misconceptions entering the publication record. In many instances, revisiting prior work with more scientific rigor is warranted, paying closer attention to consistency, purification, proper characterization, and sometimes nomenclature. Cayuela *et al.* recently published a highlight stressing the urgency for consistency in FCD research, proposing a unified nomenclature in the classification of fluorescent nanocarbons.[38] We agree with these authors, particularly given how frequently FCDs are haphazardly classified or given invented names or acronyms to give the false impression that a novel material is being introduced.

Currently, nearly a dozen names are (sometimes arbitrarily) used for fluorescent nanocarbons: graphene quantum dots (GQDs), carbon quantum dots (CQDs), carbon nanodots (CNDs), carbon dots, C-dots, carbogenic dots, carbon nanoclusters, polymer dots, nitrogen-rich quantum dots (Ndots), and graphitic carbon nitride dots, although several of these can be consolidated into a few subclasses. Indeed, Cayuela *et al.* proposed that only three categories (GQDs, CQDs, and CNDs) are sufficient to categorize all FCDs based on the chemical, physical, and photophysical properties specific to each subclass. Beyond troubling nomenclature inconsistencies, a very real barrier preventing maturation of the field is the fact that the purification of FCDs is frequently inadequate, unsubstantiated, or missing altogether. Several researchers have already alluded to the fact that, to elucidate the true origin of FCD fluorescence, efficient separation procedures to reduce sample complexity are urgently needed.[39-42] Worse, recent evidence suggests that the fluorescence associated with FCDs may originate significantly from organic (*e.g.*, oligomeric)

byproducts generated alongside FCDs.[43-46] Despite mounting evidence, the improper and insufficient purification of FCD samples remains common, making a unified purification approach all the more pressing. In response to this need, we report on the nanoscale features, photophysical properties, and cytotoxicities of representative FCDs made via top-down and bottom-up strategies. By evaluating the FCDs resulting from extensive purification using membrane dialysis, alongside unfractionated (as-synthesized) samples, we unequivocally demonstrate the importance of adequate purification to generate meaningful, error-free results, particularly in regard to luminescent characterizations. Indeed, our results suggest that inconsistencies and errors in published work are widespread and in need of re-evaluation. Moving forward, standardized purification procedures taking into account these findings will need to be implemented and remedial studies to gauge the veracity of previous claims will also be warranted in many instances.

Experimental

Materials and reagents

All experiments were carried out using Ultrapure Millipore water polished to a resistivity of 18.2 MΩ·cm unless otherwise stated. Anhydrous citric acid (791725, ≥ 99.5%), urea (U5378), ethylenediamine (E26266, ≥ 99%), sodium hydroxide (306576, 99.99% trace metals basis), sodium chloride (S7653, ≥ 99.5%), bis(3-aminopropyl) terminated polyethylene glycol (452572, Mn ~1,500 kDa), gold (III) chloride hydrate (520918, ≥ 99.9% trace metal basis), sodium borohydride (480886, 99.99% trace metal basis), sodium citrate tribasic dihydrate (C7254, ≥ 98%), quinine hemisulfate (quinine sulfate) salt monohydrate (22640, Z98.0%), coumarin 153 (01511, ≥ 99.0%), fluorescein sodium salt (F6377), sulforhodamine B (SRB), cell culture media, phosphate buffer solution (PBS),

trichloroacetic acid, acetic acid, the chloride salt of Hg^{2+} (ACS > 99.5%, and the sulfate salt of Cu^{2+} (≥ 98.0%) were all purchased from Sigma-Aldrich (St. Louis, MO). Rhodamine 610 (rhodamine B) chloride (06101) was acquired from Exciton, Inc (Dayton, OH). Branched polyethylenimine (bPEI) (06088, ≥ 99%, Mn ~1,200 kDa) was purchased from Polysciences, Inc (Warrington, PA). L-arginine (BP2505500, ≥ 99%, free base), Fisherbrand T_M syringe filters with 0.450 μm (09-719D) and 0.200 μm (09-719C) pore sizes, the 96 well plates and the chloride salt of Fe^{3+} (ACS > 98%) were obtained from Fisher Scientific (Pittsburg, PA). Ethanol (2716, 200 proof) and graphite rods (40766, 99.9995% metals basis) were procured from Decon Labs (King of Prussia, PA) and Alfa Aesar (Ward Hill, MA), respectively. Regenerated cellulose dialysis membranes with molecular weight cut-offs (MWCO) of 1, 3.5, 8, 15, and 50 kDa (Spectra/Por® 7, 132105, 132111, 132116, 132124, and 132130, respectively) were acquired from Spectrum Labs (Rancho Dominguez, CA). Ultrafiltration filter membranes with MWCOs of 1, 10, and 100 kDa (13312, 13612, and 14412, respectively) were purchased from Millipore (St. Charles, MO). Mice embryonic fibroblasts (MEF), homosapien mammary gland derived from metastatic site (pleural effusion; T47D ATCC H7B-133), and human cervical tumor cells (HeLa ATCC-CCL-2) were acquired from colleagues within the Dalton Cardiovascular Research Center. All chemicals were used as received.

Experimental procedures

Representative microwave,[13-14, 47-51] hydrothermal,[52-58] and electrochemical[59-64] synthetic routes were explored to elucidate possible shortcomings and misconceptions from previous literature reports.

Domestic microwave approach

Following a common and widely reported protocol,[13-14, 47-51] FCDs were synthesized from citric acid (CA) and urea (U) in a 1:3 CA: U molar ratio using a 900 W Frigidaire domestic microwave oven. More specifically, 6 g of CA and 6 g of U were dissolved in 20 mL of water in a round bottom flask stabilized in a beaker and were treated in the microwave on the default power setting (100% power) for 5 min, forming a charred, porous product. The resultant carbonaceous material was dissolved in 50 mL of water and the round bottom flask was rinsed with two additional 50 mL aliquots of water to ensure adequate removal of all the product. The three 50 mL fractions of the product were thoroughly homogenized resulting in 150 mL of final sample which was purified following the procedures outlined in the purification section below.

Hydrothermal approaches

Two hydrothermal approaches using different FDC precursors were explored: (1) L-arginine and (2) CA and ethylenediamine (EDA). For the L-arginine (Arg) derived FCDs, a 3 M aqueous solution of Arg was made by dissolving 26.13 g of Arg in 50 mL of water. Due to this concentration being beyond the solubility limit of Arg, the saturated solution was vigorously shaken and 10 mL was rapidly pipetted into a 23 mL Teflon-lined stainless steel autoclave. The solution was then hydrothermally treated at 180°C for 9 hours. For the CD-EDA derived FCDs, 0.42 g of CA and 536 μL of EDA were dissolved in 10 mL of water in a 23 mL Teflon-lined stainless-steel autoclave which was then hydrothermally treated at 200°C for 5 h. Both syntheses were repeated 5 additional times and the six samples of each type of FCD were thoroughly homogenized. The homogenized samples were cleaned up following the procedures outlined in the purification section below.

Electrochemical approach

FCDs were synthesized through an electrochemical route using graphite rods as both the cathode and anode submersed in 100 mL of an ethanol/water (95:5 v/v) mixture containing 0.4 g of NaOH similar to previously reported procedures.[59-64] The synthesis was conducted at constant voltage (60 V) for 4 h using an Agilent DC Power Supply E3612A. During the synthesis the solution changed from clear to yellow to orange and finally to dark brown and the current varied from 200-400 mA. The resultant samples were cleaned up following the procedures outlined in the purification section below.

FCD functionalization

The electrochemically-synthesized FCDs were functionalized with two commonly employed passivating agents; namely bis(3-aminopropyl) terminated polyethylene glycol (PEG-N; 1500 Da) and branched polyethylenimine (bPEI; 1200 Da).[65-68] To functionalize the FCDs, 5 mL of the as-synthesized material (after centrifugation; see purification section) was mixed with 5 mL of a 20 mM solution of either PEG-N or bPEI in a 23 mL Teflon-lined stainless steel autoclave and was hydrothermally treated at 180°C for 12 h. After the synthesis, the products were diluted with 10 mL of water. The synthesis using each passivating agent was repeated four additional times and the five samples of each type of passivated FCD were thoroughly homogenized prior to purification.

Purification

All as-synthesized FCD samples (excluding the functionalized FCDs) were centrifuged at 5,000 rpm for 30 min decanting the supernatant and discarding any sediment. The samples were then dialyzed using 1, 3.5, 8, 15, or 50 kDa MWCO cellulose membranes. Initially, the samples were dialyzed for 24 h against 0.5 or 1.0 L of exchange solvent in order to

obtain a more concentrated dialysate for further studies. After this, the samples were dialyzed for an additional 3-5 days against 1.5 L of solvent, changing the dialysate every 24 h. The duration of dialysis varied with the synthetic approach but all samples were dialyzed until the dialysates were visually clear to the eye and did not display any observable fluorescence using blue (405 nm) and green (532 nm) laser pointers. For the microwave- and hydrothermally-synthesized FCDs, the samples were dialyzed against ultrapure water while the electrochemically synthesized and functionalized FCDs were dialyzed against 100% and 50% (aq.) solutions of EtOH, respectively. It should be noted that for the Arg-derived FCDs, fractions of the retentates and dialysates were pulled off 6 h into the initial 24 h dialysis for further analysis. Additionally, more concentrated samples were used to acquire the pictures of the time-lapse dialysis to clearly illustrate the rapid mobilization of byproducts. Select as-synthesized samples were also subjected to (ultra)filtration using Fisherbrand T_M syringe filters (0.200 μm or 0.450 μm pore size) or a Millipore Amicon Ultrafiltration system (Model 8010 #5121) employing 1, 10, or 100 kDa MWCO filter membranes. The filtrates were retained for further analysis.

Gold nanoparticle (AuNP) syntheses

Benchmark dialysis and ultrafiltration experiments were conducted on AuNPs of two different size regimes (12-16 nm and 5-7 nm) to clarify nanoscale membrane permeability. To generate the larger AuNPs, the sodium citrate reduction known as the Turkevich Method[69-73] was employed. Specifically, 1 mL of 5 mM $HAuCl_4$ was diluted in 18 mL of water and the solution was brought to a boil in a round bottom flask placed in a water bath. Once boiling, 1 mL of a 0.5% sodium citrate solution was added under magnetic stirring (300 rpm) and the solution was heated until a color change was observed, after which the

round bottom flask was removed and allowed to cool to ambient temperature. During this cooling period, the solution color changed from dark purple to dark red. Water was added to the AuNP solution to bring the volume back to 20 mL, accounting for any solvent losses during boiling. To generate the smaller size regime of AuNPs, the sodium borohydride ($NaBH_4$) reduction of Au^{3+} that was recently reported by the Astruc group[74] was employed. Specifically, 1 mL of freshly prepared 50 mM $NaBH_4$ (aq.) was added to 19 mL of 0.25 mM $HAuCl_4$ (1 mL of 5 mM $HAuCl_4$ in 18 mL of water) at ambient temperature and under magnetic stirring. Upon $NaBH_4$ addition, the solution rapidly changed from a faint yellow to orange and over a few hours the solution color became a dark red-orange. The $NaBH_4$-generated AuNPs were allowed to ripen for 24 h prior to use. Both AuNP solutions were subjected to dialysis (against 0.5 L water) or ultrafiltration using 50 kDa or 100 kDa MWCO membranes, respectively.

Cell viability by Sulforhodamine B assay

The cell viabilities were evaluated based on the sulforhodamine B (SRB) colorimetric assay, as described in the literature. For the assay, solutions of freshly isolated mice embryonic fibroblasts (MEF), homosapien mammary gland derived from metastatic site (pleural effusion; T47D ATCC H7B-133), and human cervical tumor cells (HeLa ATCC CCL-2) were seeded into each well of a 96-well plate (5-8 x 10^3 cells in 100 μL of DMEM/NCS culture media) and allowed to adhere to the wells for 24 h at 37°C in a 10% CO_2 atmosphere. The cells were then treated with 100 μL of various FCD concentrations (0.002-2 mg/mL in saline solution, previously prepared by dissolving 9 g NaCl in 1 L water) for 24 h at 37°C in a 10% CO_2 atmosphere. After FCD treatment, the media was removed, the cells were washed twice with phosphate buffered saline (PBS), and the

surviving or adherent cells were fixed in situ by adding 100 μL of PBS and 100 μL of 50% cold trichloroacetic acid (TCA) followed by an incubation period at 4°C for 1 h. Lastly, the cells were washed with ice-cold water 5 times, dried, and then stained according to the SRB colorimetric assay protocol. The protocol involves staining the cells using 50 μL of 4% SRB (in 1 vol% acetic acid solution) for 8 min at room temperature. Any unbound dye was removed by washing the cells five times with cold 1% acetic acid and the stained cells were then dried. The absorbance of the dried stained cells was measured at 560 nm using a microplate reader. Each FCD concentration was tested in triplicate (at minimum).

Metal ion quenching studies

Stock solutions of the various metal salts with concentrations of at least 5 mM were generated, which were then diluted to 3.1 mM. The as-synthesized samples and their dialysate and retentate fractions were diluted to an absorbance of approximately 0.1 at 375 nm, where all absorbance values were 0.09 ± 0.03. For the metal screening tests, 100 μL of the 3.1 mM metal salt solutions was added to a cuvette containing 3 mL of the above diluted solutions. All data were blank subtracted and all fluorescence emissions were dilution corrected (when applicable). The fluorescence emission data were also corrected for inner filter effects through the approximate correction factor below:

$$F_{corr} = F_{obs}\left(10\ \frac{Aex + Aem}{2}\right)$$

where F_{corr} is the corrected fluorescence values, F_{obs} is the observed (blank subtracted and dilution corrected) fluorescence, A_{ex} is the absorbance of the sample at the excitation wavelength (375 nm), and A_{em} is the absorbance at each wavelength over the emission range collected (385-650 nm). For the quenching titrations, the emission of the

metal-free FCD solution (3 mL) was collected first then a 10 μL addition of a 31 μM aq. solution of Hg^{2+} was added to give a Hg^{2+} concentration of ~100 nM and the emission was re-collected. This process was repeated 9 additional times resulting in a final Hg^{2+} concentration of 1 μM. Next, nine separate 10.5 μL additions of a 310 μM aq. solution of Hg^{2+} were added to give Hg^{2+} concentrations of ~2,3,……9, 10 μM, after which, 9 separate 11 μL additions of a 3.1 mM aq. solution of Hg^{2+} were added to give Hg^{2+} concentrations of ~20, 30,…..90, 100 μM. Emission spectra were collected after each aliquot of Hg^{2+} was added. The fluorescence data for the titration quenching studies showed no measurable absorbance over 375-800 nm even at concentrations much higher (1 mM) than those used in the titrations (maximum concentration of 100 μM).

Approximate GQD molecular weight calculation

The approximate molecular weight of GQDs ranging in size from 1-20 nm (presented in Figure F.1C) were calculated from the equation below using the density of carbon atoms in graphene (*i.e.*, 3.21 x 10^{15} C atoms/cm^2). For simplicity, the calculation was based on completely spherical GQDs absent any heteroatom doping or functional groups.

$$MW_{Approx}(kDa) = GQD\ Area * \left(3.21\ x\ 10^{15}\ \frac{C\ atoms}{cm2}\right) * Carbon\ Molar\ Mass$$

$$MW_{Approx}(kDa) = \pi\left(\frac{10\ nm}{2}\right)2 * \left(\frac{1\ cm2}{1\ x\ 10\ 14\ nm2}\right) * \left(3.21\ x\ 10^{15}\frac{C\ atoms}{cm2}\right) * \left(\frac{12.01\ Da}{C\ atom}\right) * \left(\frac{1\ x\ 10^{-3}\ kDa}{1\ Da}\right)$$

$$MW_{Approx}(kDa) of\ a\ 10\ nm\ GQD = 35.03\ kDa$$

Characterization techniques

Absorbance and steady-state fluorescence data were collected on both a Hitachi U-3000 or Cary Bio 50 UV-Vis spectrophotometer and a HORIBA Jobin Yvon Fluorolog®-3 or Varian Cary Eclipse spectrofluorometer, respectively. All measurements were conducted at ambient temperature using 1 cm (1.4 mL or 4 mL) fluorescence quartz cuvettes and all samples were diluted to below 0.1 absorbance at 350 nm to minimize inner filter effects. Quantum yield values were calculated using the equation listed below with quinine sulfate, coumarine 153, fluorescein, and rhodamine B as reference fluorophores (fluorophore and fluorescence measurement information is provided below in Table G.1).

$$QY_S = QY_R \left[\frac{F_S}{F_R}\right]\left[\frac{OD_R}{OD_S}\right]\left[\frac{n_S^2}{n_R^2}\right]$$

where *R* and *S* stand for reference and sample respectively, *F* stands for integrated fluorescence intensity (calculated over the wavelength range of interest), *OD* stands for optical density (at the excitation wavelength used in the fluorescent measurements), and *n* stands for refractive index.

Transmission electron microscopy (TEM) studies were conducted on carbon coated copper grids (Ted Pella, Inc. 01814-F, support films, carbon type-B, 400 mesh copper grid) using a FEI Tecnai (F30 G2, Twin) microscope operated at a 300 keV accelerating electron voltage.

Results and Discussion

Literature survey of FCD purification methods

Since the serendipitous discovery of nanoscale fluorescent carbons by Xu *et al.* in 2004,[75] the number of articles published has grown exponentially (Figure F.1A), with the total

number of publications exceeding 3500 by the end of 2016. In accordance with the recommendations of Cayuela *et al.*, the publications have been broken into three FCD subclasses (*i.e.*, CQDs, GQDs, and CNDs) and are categorized according to their published classification, with the exception that the CND subclass encompasses the terms carbon nanodots, carbon dots, C-dots, and carbogenic dots. Figure F.1B shows a random sampling of more than 550 FCD papers (full citations can be found online in the Chem. Mater published manuscript), which are categorized according to the reported purification and further sorted by synthetic camp (top-down vs bottom-up). The experimental details for over 300 of these publications and any formulated abbreviations can also be found online in the Chem. Mater published manuscript. It should be noted that many of the reported dialysis or ultrafiltration purification protocols also include centrifugation and/or filtration steps prior to membrane separation. Figure F.1B illustrates a wide range of purification methods used in published FCD reports.

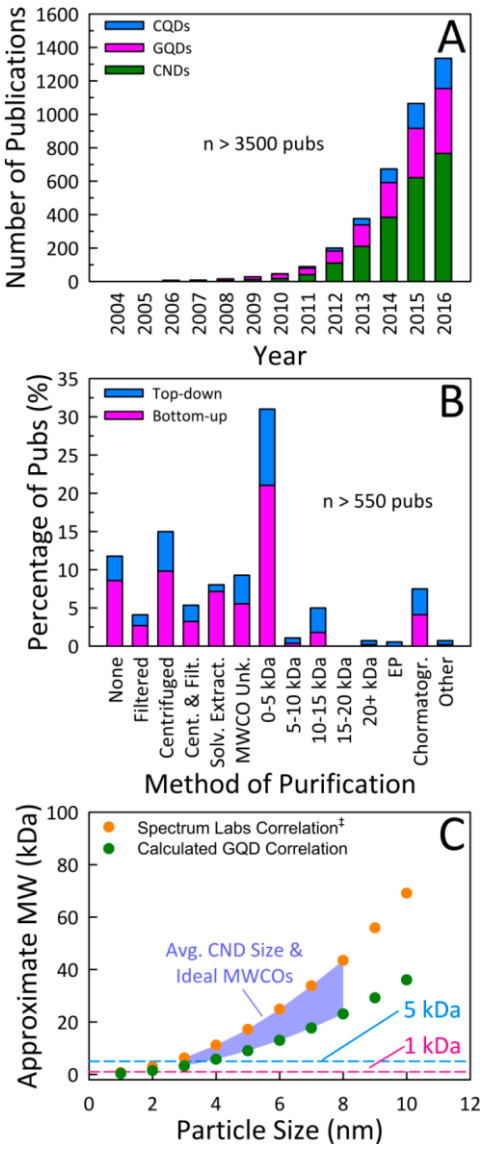

Figure F.1 (A) Trend showing the exponential rise in publications dealing with FCDs over the past decade. (B) A sampling of over 550 FCD publications categorized by their mode of purification. (C) An approximate molecular weight-to-size correlation suggesting that the use of < 5 kDa MWCO membranes is woefully inadequate for purifying these materials. The pink and blue lines demarcate 1 and 5 kDa MWCOs, respectively, while the purple shaded area represents the average FCD size and corresponding ideal MWCOs that should be employed for membrane-based FCD purification. ‡This is an approximation; there is no universally correct correlation between a 2D particle size and a 3D molecular weight. The abbreviations in Panel B are as follows: Cent. & Filt. = centrifugation and filtration (in no particular order); Solv. Extract. = solvent extraction; MWCO Unk. = MWCO for dialysis

not reported; EP = electrophoretic separation; and Chromatogr. = chromatographic separation. The bars labeled with specific MWCOs denote either dialysis or ultrafiltration as a means of purification.

As we will demonstrate, more than half of these reports employ purification procedures that are assuredly inadequate. In fact, ∼12% of these representative examples perform no purification whatsoever. To make matters worse, some go so far as to make the false claim that avoiding purification is an advantage in a clearly misguided belief that FCDs are the sole product generated. Considering that bottom-up approaches utilize molecular or ill-defined (*e.g.*, food waste) carbon sources, the chemical transformations taking place during synthesis may parallel those that transpire in the roasting of coffee,[76-78] malting of grain,[79-83] or the boiling of sugar−protein solutions (*e.g.*, wort) where nonenzymatic browning (*e.g.*, Maillard reaction, caramelization) occurs, for example. These carbonization reactions are exceedingly complex and can produce thousands of identifiable compounds, including melanoidins and other oligomeric or polymeric products, making side-product formation during FCD synthesis a certainty. Indeed, recent reports have shown that mild thermal treatment of common FCD precursors can yield highly fluorescent materials that are molecular in nature (*e.g.*, polymers, soft gels) and display fluorescence quantum yields > 60%.[84-88] These observations are in accord with recent reports that attribute observed fluorescence to organic fluorophore side-products,[43-46] making the notion of exclusive formation of FCDs by bottom-up approaches extremely improbable. In fact, earlier reports suggested the low temperature production of highly fluorescent polymeric products with significantly higher temperatures being required to

generate a carbogenic core, a feature associated with a substantially lower fluorescence quantum yield.[12, 43] We note that while top-down approaches might be deduced to result in more well-defined products and fewer impurities (most are derived from graphite, after all), this does not exempt them from the need for purification, which becomes even more critical when post-synthetic functionalization steps are involved. Given the above discussion, a full 20% of the surveyed literature (Figure F.1B) employs only centrifugation or bulk filtration (*i.e.*, excluding membrane ultrafiltration using a defined molecular weight cutoff, MWCO) yielding insufficiently purified FCDs.

To efficiently remove starting materials and putative molecular byproducts, a purification approach involving either chromatographic separation or dialysis with an appropriate MWCO membrane is required. Unfortunately, nearly 30% of the surveyed literature performed dialysis with a membrane MWCO of 5 kDa or below (Figure F.1B), with 1 and 3.5 kDa MWCOs being the most popular choices. In reality, larger MWCOs should be employed to ensure efficient removal of large oligomeric or polymeric byproducts. Figure F.1C presents a highly approximate correlation between molecular weight and colloid size for FCDs. The upper limit of the shaded region in Figure F.1C was adapted from a Spectrum Labs technical note,[89] and the lower limit is based on calculations for an unfunctionalized GQD using the density of carbon atoms found in graphene,[90] Given that the average FCD size culled from the references compiled in Figure F.1B falls in the 3−8 nm range, with recent estimates suggesting that the approximate molecular weight of 3−10 nm GQDs falls in the 15−30 kDa range[91-92] purification with larger MWCO membranes is desired to comprehensively remove organic molecular (especially, polymeric, supramolecular, or aggregated species) impurities and byproducts while

retaining the desired nanoscale FCD fraction. Indeed, notable examples exist in which 20 kDa^{+} MWCO membranes were employed for purification without losing the target FCDs.[93-94] At this point, it must be stated that nanoscale imaging (transmission electron microscopy, TEM, or atomic force microscopy, AFM analysis) of a colloidal dispersion coupled with a steady-state fluorescence study of the same sample is incapable of determining the origin of the emission (*i.e.*, molecular vs. nanoscale). Consider, for example, the following hypothetical scenario: Unbeknownst to an investigator, a colleague spikes a low concentration of an organic laser dye into their dispersion of well-defined but nonfluorescent nanoparticles. Absent any possible quenching or excessive scattering, the sample will emit brightly, as for a solution of the fluorescent dye itself. Meanwhile, TEM imaging will reveal the presence of well-defined nanoparticles. Being organic in nature (low Z-contrast), dilute, and small (typical laser dyes have molecular weights from 300 to 500 Da), the TEM will provide no indication that the laser dye is present at all.

Our hypothetical investigator can hardly be blamed for believing they have evidently generated fluorescent nanoparticles. Of course, we know she or he has been the unwitting victim of a laboratory prank. This contrived scenario, in fact, provides a surprisingly apt cautionary tale when interpreting the origin of luminescence from an FCD-containing sample. Thus, without adequate purification, one can neither confidently claim that FCDs are the primary product nor that the observed photoluminescence derives primarily from FCDs. In fact, to date, there is little direct evidence that the dots themselves fluoresce,[41] let alone proof they are the sole or even principal photoluminescent species present. Further complicating the matter, it was recently shown that, upon drying, small organic compounds can form nanocrystals whose properties are disconcertingly

reminiscent of FCDs,[95] calling into question many published results on FCDs.

Fluorescence and imaging analyses

To further elucidate possible shortcomings and misconceptions arising from previous literature reports on FCD synthesis, representative microwave,[13-14, 47-51] hydrothermal,[52-58] and electrochemical[59-64, 96] synthetic routes were evaluated, with particular emphasis on the microwave-generated samples. Detailed experimental procedures for these representative routes are provided in the aforementioned sections. The microwave generated samples, synthesized from citric acid (CA) and urea (U) in a 1:3 CA: U molar ratio (denoted as CA−U), were subjected to dialysis (1, 3.5, 8, 15, or 50 kDa MWCO membranes) or (ultra)filtration purification protocols (1, 10, or 100 kDa MWCO membranes; or 0.200 or 0.450 μm pore size syringe filters), after which the retentates, dialysates, and filtrates were characterized by their steady-state fluorescence (Figures G.1 and G.2) and wavelength-dependent quantum yields (Figure F.2). All of the microwave-generated CA−U samples (*i.e.*, retentates, dialysates, and filtrates) displayed the commonly reported excitation wavelength-dependent emission, with the dialysates (Figures G.2B, D, F, H, and J) and filtrates (Figures G.1B−F) displaying similar spectral features to the as synthesized (unpurified) samples (Figure G.1A). In general, samples universally showed diminishing fluorescence emission with increasing excitation wavelength.

To better elucidate this behavior, multi-excitation wavelength fluorescence quantum yield determinations were made using excitation wavelengths of 350, 421, 470, and 514 nm. The results, summarized in Figure F.2, are consistent with our previous observations that as the excitation wavelength increases, the calculated quantum yield generally decreases markedly.[9, 15, 36] Figure F.2A shows that regardless of the membrane

MWCO chosen for dialysis, the measured quantum yields of the retentates (closed symbols) were drastically lower than those of the as-synthesized samples as well as those of the dialysates (open symbols), which gave similar quantum yields.

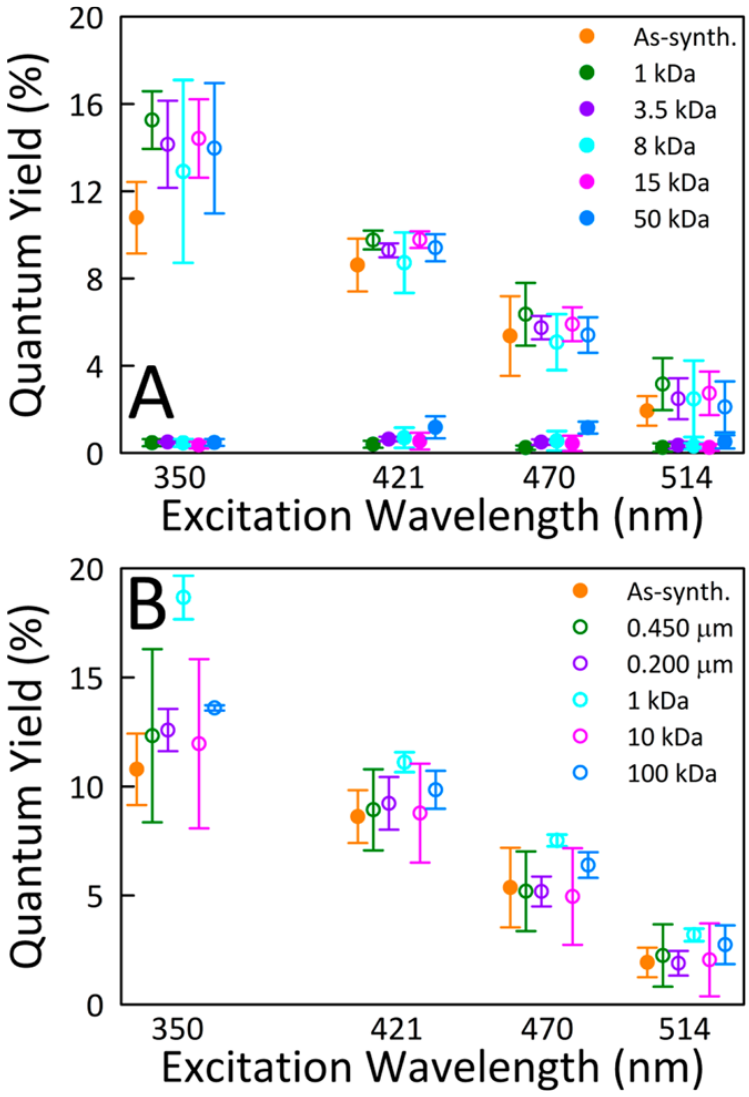

Figure F.2 Fluorescence quantum yields measured following (A) dialysis and (B) (ultra)filtration cleanup of CA−U derived FCDs. The retentate results are represented by closed symbols, and dialysate/filtrate quantum yields are denoted by open symbols. These sets of studies reveal that the smaller species permeating the membranes are associated with the majority of the fluorescence observed in the as-synthesized (as-synth.) samples, while the retentates show much weaker fluorescence.

From these results, we can infer that in popular microwave-generated FCD samples there exist at least two distinct populations of fluorophores: a population of molecular (< 1 kDa) species responsible for the majority of the observed fluorescence and a population of low quantum yield emitters much larger in size (≥ 50 kDa). We note that emission from aqueous dispersions of graphene oxide has been proposed to arise from quasi-molecular fluorophores, akin to polycyclic aromatic compounds coupled to the graphitic surface.[97-98] It is currently not possible to rule out a similar quasi-molecular involvement in FCD emission arising from organic fluorophore coupling at the carbon surface. The exact origin and nature of FCD emission remains elusive, although historically the observed FCD fluorescence has been variously attributed to a size-dependent quantum confinement effect and surface functionalities/defects.[1] However, there is mounting evidence that certain FCDs are not in fact quantum emitters and indeed not even "dots",[99] but are, instead, supramolecular clusters comprising an assembly of individual monomeric organic fluorophores contributing the bulk of the observed fluorescence.[40, 46, 99]

In this light, the two distinct populations of fluorophores each likely consist of a range of fluorophores that combine to produce the observed bulk fluorescence. Similar conclusions can be drawn from the (ultra)filtration studies of the microwave-produced CA−U samples, where the quantum yields measured for the filtrates (Figure F.2B) were comparable to or higher than those of as-synthesized material. This clearly demonstrates that the common practice of purifying with a syringe filter (*e.g.*, 0.200 μm) is wholly inadequate, offering essentially no purification whatsoever. Figures F.3 and G.3 further highlight the rapid mobilization of small molecular weight species through a 1 kDa membrane during dialysis of a microwave-produced CA−U (1:3) sample.

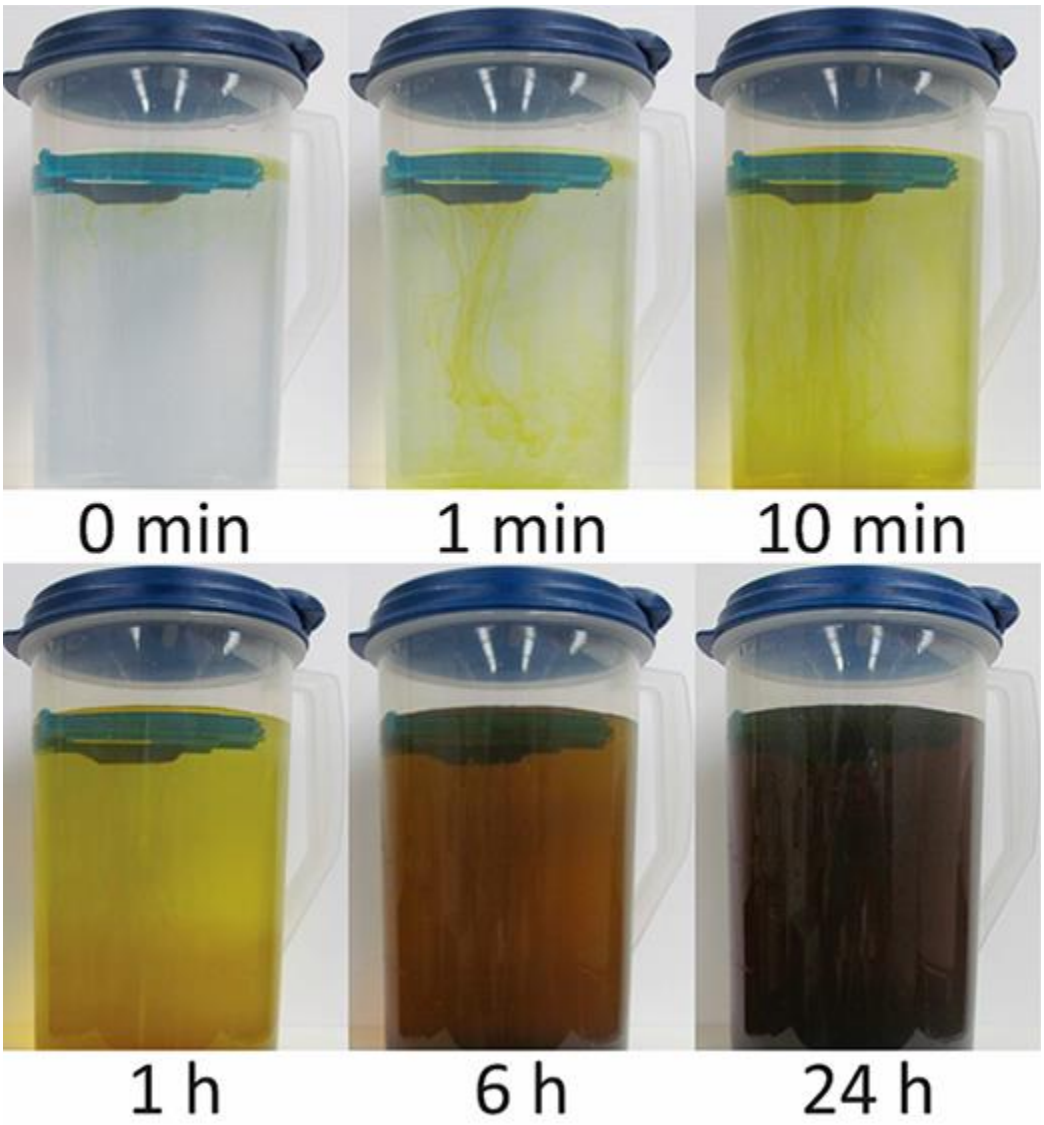

Figure F.3 Sequence of images showing the progress of dialysis for microwave-generated CA−U (1:3) samples using a 1 kDa MWCO membrane. The rapid passage of colored material through the membrane vividly illustrates the fact that large quantities of small molecular (non-nanoscale) byproducts result from bottom-up microwave routes to FCDs.

It is noteworthy that when the retentate from this 1 kDa dialysis was subjected to further dialysis with a 50 kDa MWCO membrane (Figure G.4), no colored species were observed to permeate the membrane after 24 h, further supporting the notion that two distinct, size-

disparate populations are generated for microwave treatment of molecular species such as CA−U.

To clarify nanoscale membrane permeability for a given MWCO, we performed benchmark experiments involving the dialysis (50 kDa MWCO) and ultrafiltration (100 kDa MWCO) of well-defined ∼14 nm citrate-stabilized[69-73] Au nanoparticles (AuNPs) compared with ∼6 nm borohydride stabilized AuNPs.[74] TEM images of these AuNPs are provided in Figure G.5. Conveniently, the localized surface plasmon resonance of the AuNPs allowed us to track permeation through the membrane. Comparison of UV−vis spectra collected on dialysate and filtrate samples (Figure G.6) with spectra for unfractionated AuNP samples reveals that neither 6 nor 14 nm AuNPs pass through the 50 kDa dialysis membrane, whereas small amounts of both AuNP sizes permeate the 100 kDa ultrafiltration membrane, with the larger citrate-stabilized AuNPs mobilizing to a lesser extent. This outcome suggests that nanoparticles in the 5−15 nm regime will not traverse a 50 kDa MWCO membrane but may begin to pass a 100 kDa MWCO membrane. Given a mean reported size of 3−8 nm for FCDs, dialyses with a membrane MWCO below 20 kDa is not recommended because there is potential for retention of molecular byproducts in addition to the FCD fraction. Figure F.4 presents representative TEM images of the retentate (A and C) and dialysate (B and D) fractions resulting from 1 and 50 kDa MWCO membrane dialysis of microwave generated CA−U material. Both retentate fractions appear to contain FCDs; however, the dots are often sequestered within amorphous deposits of undesired organic material, particularly for dialysis using a 1 kDa MWCO membrane (Figure F.4A), demonstrating that 1 kDa is completely insufficient for removing organic residues. Unfortunately, even when employing a 50 kDa MWCO membrane

(Figure F.4C), non-FCD impurities still appear on the TEM grid for the retentate sample, suggesting that even this high a MWCO membrane may not provide adequate purification. Both dialysate fractions appear to contain primarily organic byproducts that produced thin films on the grid, especially when dialyzing against a 1 kDa membrane (Figure F.4B).

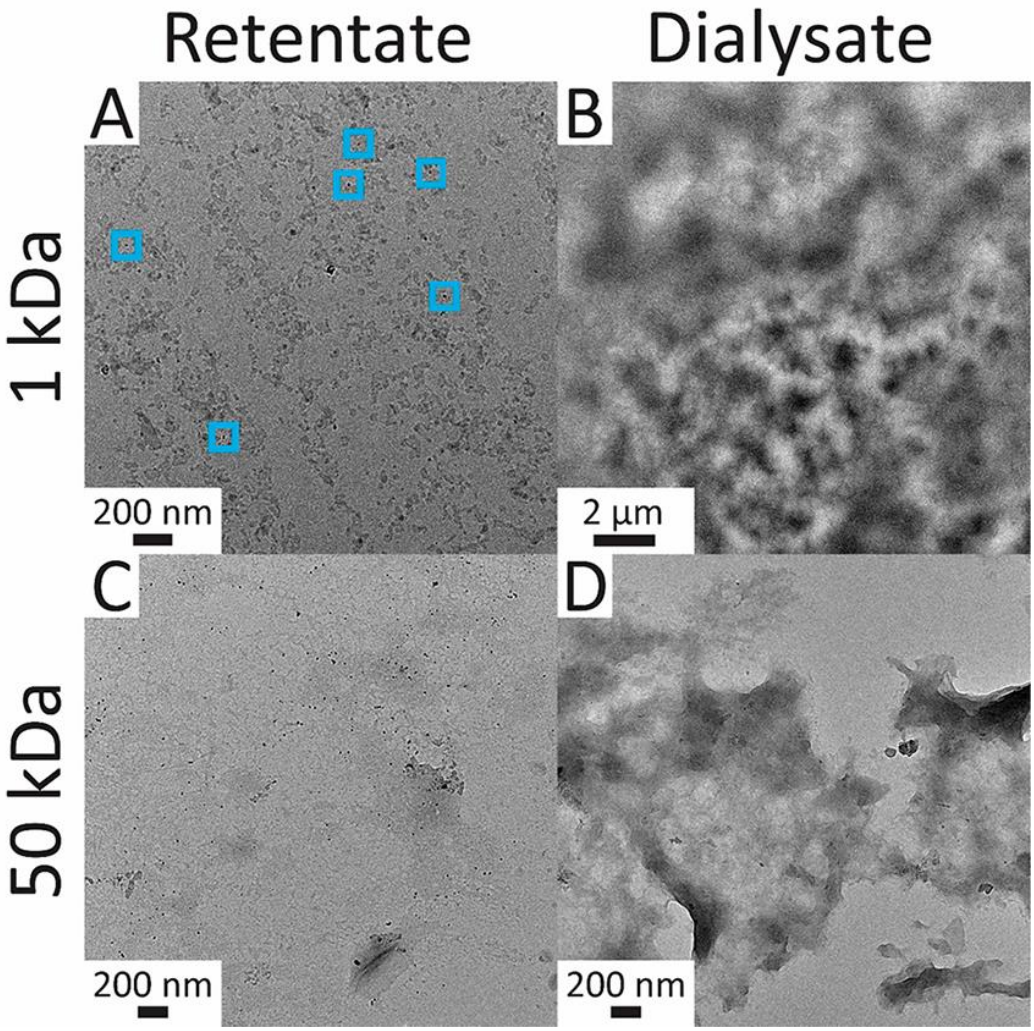

Figure F.4 Representative TEM images for the (A and C) retentate and (B and D) dialysate fractions resulting from (A and B) 1 kDa and (C and D) 50 kDa dialysis of samples produced by microwave treatment of CA−U (1:3). Some apparent FCDs are visible in the 1 kDa retentate (A; marked by the squares) but proved difficult to image due to the large quantity of byproduct residues. While the 50 kDa retentate proved easier to image and the FCDs were more visually prominent, a significant amount of non-FCD material remained

after purification. Some FCDs were visible in the 50 kDa dialysate samples, indicating that dialysis may not be capable of fully separating FCDs from organic molecular byproducts.

No FCDs were observed in the 1 kDa dialysate, although the polymer-like coating would surely obscure their observation, were they present. FCD-like structures were occasionally observed in the 50 kDa dialysate (Figure F.4D), although they were rare. Overall, these TEM studies demonstrate that dialysis against membranes having a MWCO < 50 kDa is most assuredly insufficient, although dialysis, in general, may be less than ideal due to the difficulty of separating the target FCDs from molecular (oligo- or polymeric) byproducts, a situation exacerbated by the possibility for supramolecular association of small, organic fluorophores.[40, 46, 99] Additional representative TEM images of the retentate and dialysate fractions resulting from 1 and 50 kDa MWCO membrane dialysis of the microwave-generated CA−U material are provided in Figure G.7.

To ascertain the prevalence of fluorescent organic impurities (byproducts) using other synthetic routes, the fluorescence properties of products resulting from a hydrothermal synthesis using L-arginine (Arg)[52-53] or citric acid and ethylenediamine (CA−EDA)[54-58] plus an electrochemical preparation from graphite[59-64, 96] were each explored next. The details for these synthetic routes can be found in the aforementioned sections. All samples were subjected to dialysis as per the microwave-synthesized FCDs, with the omission of the 3.5 and 8 kDa MWCO membranes earlier shown to be inadequate for FCD purification. In general, as was the case for the CA−U microwave FCDs, all samples displayed excitation wavelength dependent emission (Figures G.8 and G.14) and fluorescence quantum yields (Figures G.10 and G.17A), again indicating a distribution of

fluorophores, with the smaller species being the most photoluminescent. Contrastingly, the hydrothermally derived CA−EDA samples displayed an excitation wavelength-independent emission (Figure G.11), a known but rarer feature of FCD photoluminescence[1, 50, 100] thought to arise from a more homogeneous fluorophore composition. In spite of this key difference, the results for hydrothermal CA−EDA-derived products reinforce the conclusion that small organic molecular byproducts (and not nanoscale carbons) produce a majority of the observed fluorescence, a proposition further substantiated by fluorescence quantum yield measurements performed using 350 nm excitation (Figure G.12). Further evidence that two spectroscopically distinct species are generated is provided in Figure G.13, where the UV−vis spectra for the retentate fractions from 1 or 50 kDa MWCO membrane dialysis of CA−U and CA−EDA derived FCDs are markedly different from the parent samples and the dialysate. Specifically, for the CA−U retentate, the shoulders at 250 and 275 nm are no longer evident, whereas for the CA−EDA retentate, the peak wavelength blue-shifts by approximately 10 nm.

We note that in prior reports employing dialysis for FCD purification, the duration or conditions of dialysis are frequently inadequate. Although a number of factors influence the dialysis rate, standard protocols call for a 16−24 h period of dialysis with multiple dialysate changes throughout.[101] Many reports involving FCD dialysis fail to meet these standards, halting the dialysis prematurely, for example. To shed light on this questionable practice, fractions of the dialysates and retentates from Arg-derived hydrothermal samples were collected after dialysis for 6, 24, or 72 h (in the latter case, the exchange solvent was changed every 24 h), and fluorescence quantum yields were measured (Figure G.10). During the early stages of dialysis, the quantum yields of the retentate and dialysate

samples were relatively similar. Over time, however, the quantum yield associated with the retentate began to drop off, regardless of the chosen MWCO membrane. These results are further corroborated by time-lapse photos of the Arg derived FCDs undergoing dialysis with a 1 kDa MWCO membrane (Figure G.9). Clearly, these results demonstrate that 6 h of dialysis is inadequate, regardless of the membrane MWCO employed, urging researchers to not only employ an adequately large MWCO but also to allow dialysis to proceed for at least 24 h, preferably with frequent changes in the exchange water. Indeed, time-lapse photos of CA−U FCD dialysis (Figures F.3 and G.3) reinforce this notion as well. Graphitized CQDs/GQDs are often functionalized with an amine-containing passivating agent such as bis(3-aminopropyl) terminated polyethylene glycol (PEG-N)[65, 68] or branched polyethylenimine (bPEI)[66-67] to improve their fluorescence features.

Problematically, however, a majority of these reports perform no purification following functionalization, suggesting that the observed fluorescence enhancement may derive, at least in part, from organic fluorescent impurities generated in situ. In fact, to date, there is little irrefutable evidence that the observed fluorescence from FCD samples actually originates from the CQD/GQD core or surface functionality on the dot and not from side-reactions or degradation of the passivating agent used for surface functionalization. To highlight this uncertainty, electrochemically synthesized FCDs were hydrothermally treated with PEG-N (1500 Da) or bPEI (1200 Da) in an attempt to functionalize the nanodots, and the resulting samples were subjected to dialysis and ultrafiltration purification. The fluorescence emission spectra of the "functionalized" samples (Figures G.15 and G.16) showed a similar excitation-wavelength dependence as the parent material. However, in general, the dialysates and filtrates displayed fluorescence

quantum yields considerably higher (Figures G.17B and C and G.18) than those of the corresponding retentates (or unpurified functionalized samples), illustrating that highly fluorescent, molecular byproducts do indeed form during surface functionalization of FCDs with amine passivating agents. Thus, even top-down syntheses of FCDs require careful purification, particularly post-functionalization with molecular capping agents.

Effects on typical FCD applications

The lack of proven and widely adopted purification protocols to isolate FCDs free of fluorescent contaminants leads to misconceptions about their photophysical properties and will undoubtedly propagate errors and misinterpretations during their use in applications that rely on their fluorescent nature (*e.g.*, as sensory or bioimaging agents). As a first step toward examining such a possibility, the quenchability of as-prepared and dialyzed fractions (retentate vs dialysate) of CA−U (Figure F.5) and CA−EDA (Figure G.22) derived samples were evaluated using the transition-metal ions Cu^{2+}, Fe^{3+}, and Hg^{2+}. To provide a basis for direct head-to-head comparison, samples were diluted to an absorbance of 0.09 ± 0.03 at 375 nm, the excitation wavelength employed in the fluorescence quenching studies.

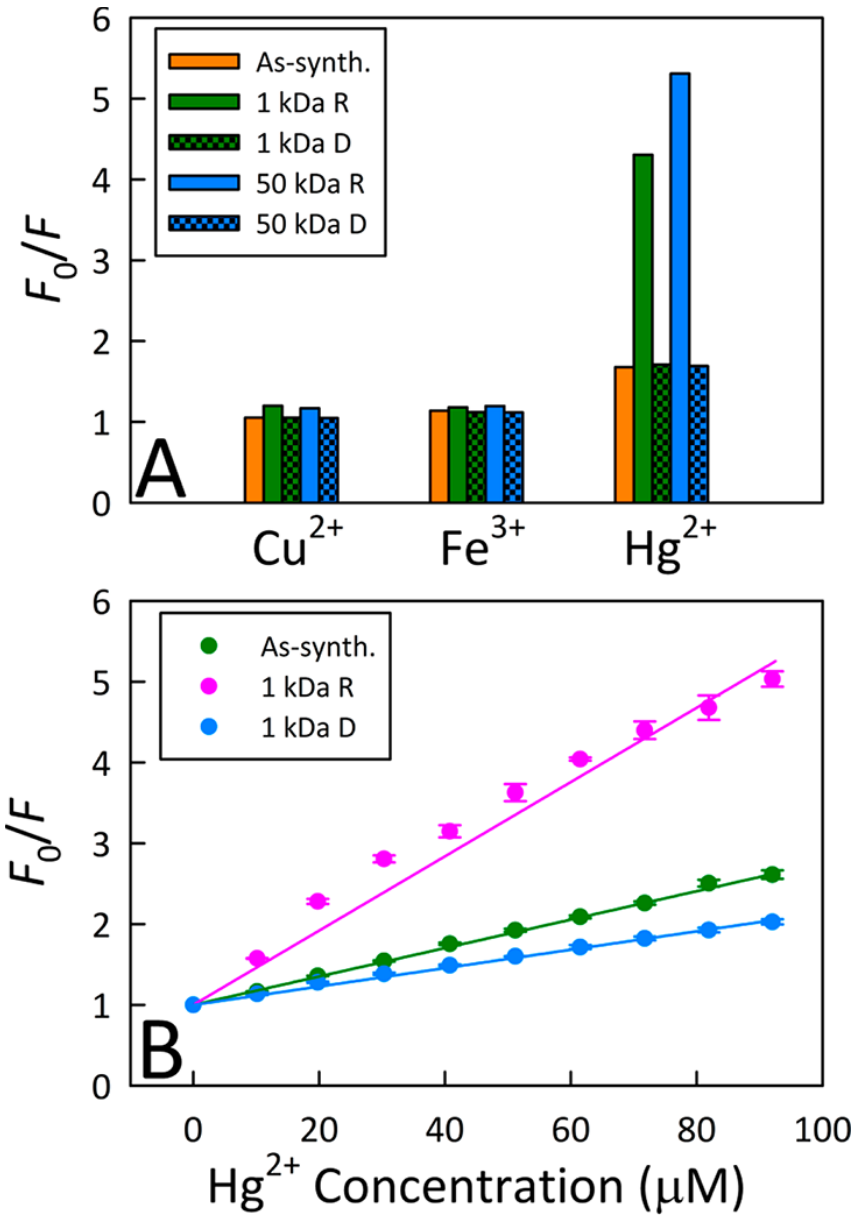

Figure F.5 (A) Metal ion quenching studies conducted on the retentate (R) and dialysate (D) fractions of the microwave-treated CA−U. For the metal ions tested (Cu^{2+}, Fe^{3+}, or Hg^{2+}), the retentates were quenched more strongly by 100 μM Hg^{2+} than the as-synthesized samples and the dialysates, while the quenching in the presence of 100 μM Cu^{2+} or 100 μM Fe^{3+} was essentially identical for all fractions. (B) Stern−Volmer plots of Hg^{2+} titrations of CA−U derived FCDs. These results reveal that improper purification can clearly impact the performance of the investigated material, in this case masking the analytical responsivity of the FCDs (the limit of detection for Hg^{2+} is actually 2−3 times better for

the retentate fraction compared with the dialysate). For all metal ion quenching studies, the concentration of the FCD fractions was "normalized" by adopting the same absorbance (~0.1) at the excitation wavelength (375 nm) employed in the fluorescence spectra acquisitions.

For the three metal ions tested, the retentates proved to be more strongly quenched than the unpurified samples or their dialysates, which were quenched to similar extents. Although the difference in quenching behavior between the retentate and dialysate was marginal for Cu^{2+} and Fe^{3+}, the retentate fraction was conspicuously more responsive to Hg^{2+} compared with the dialysate. To further explore this behavior, Hg^{2+} quenching titrations were conducted on an as-synthesized CA−U sample alongside the retentate and dialysate fractions resulting from dialysis using a 1 kDa MWCO membrane. Figure F.5B provides representative Stern−Volmer plots of Hg^{2+} quenching of the CA−U fluorescence where F_0 and F represent the fluorescence intensities in the absence and presence of Hg^{2+}, respectively. The limits of detection (LOD) were estimated from these data using the 3σ convention. For similar absorbances, the estimated LODs for as-synthesized, retentate, and dialysate CA−U samples were 607 nM, 229 nM, and 1.53 μM, respectively. This outcome demonstrates that the presence of molecular byproducts actually masks the true response of the FCDs, restricting their analytical potential. A larger implication of this result is that many previous works may need to be revisited with more meticulous purification to validate or refute the original findings.

Recently, Vinci *et al.* demonstrated than an unpurified FCD sample generated from the oxidation of graphite nanofibers was substantially more toxic than the individual fractions obtained from dialysis and HPLC fractionation,[102] an indication that sample

complexity can influence functional properties. In this light, the cytotoxicities of as-synthesized CA−U derived FCDs and their dialysis fractions (retentates and dialysates) were evaluated using three different cell lines: mice embryonic fibroblasts (MEFs; Figure G.19), human breast cancer (T47D) cells (Figure G.20), and HeLa cells (Figure G.21). Contrary to the results reported by Vinci *et al.*, regardless of the cell line studied or the membrane MWCO for dialysis, no clear trends emerged when comparing the toxicities for as-synthesized material with that of the retentate and dialysate fractions. At this point, the relative cytotoxicities of nanocarbons compared with those of the organic byproducts resulting from various synthetic routes remains an open question. In-depth cellular toxicity studies on chromatographically fractionated FCD samples are needed to truly understand the origin of any observed cytotoxicity and to show cellular compatibility.

Improperly-assigned fluorescence peaks

Another fallacy cultivated in the literature entails the improper collection and interpretation of FCD fluorescence emission. In some instances, FCDs have claimed to display red emission due to the appearance of the sample under illumination. In many of these cases, the red color is in fact a visual artifact arising from illumination of a concentrated solution already brick-red in color. This is illustrated in Figures G.23 and G.24 for CA−U derived and Arg-derived FCD samples. Comparing the emission spectra for the as-synthesized Arg-derived FCDs with results for 10- and 100-fold dilution samples (Figure G.24), the emission is more red-shifted for the undiluted dispersion. This phenomenon, which arises from the re-absorption of blue edge photons in highly absorbing solutions, is well-known. In this case, we note that although this secondary inner filter effect causes a red-shifted emission due to attenuation of the blue edge, the emission color remains in the blue under

UV excitation. Clearly, the ruddy appearance of the undiluted Arg derived FCD sample belies the true emission color. Figure G.24D provides a comparison of the emission maximum versus excitation wavelength for the various dilutions of Arg-derived FCDs, further highlighting this distortion, revealing the apparent insensitivity to excitation wavelength from 300 to 500 nm, an artifact of self-absorption. Although this distortion at high optical densities has been documented in the literature,[103] it has escaped the attention of many researchers.

Conclusions

The primary conclusion drawn from this study is that adequate purification of fluorescent carbon dots, while frequently neglected, is absolutely critical to acquiring meaningful results, especially for bottom-up chemical synthesis involving molecular precursors (*e.g.*, citric acid and food wastes). In fact, rigorous purification and fractionation is not needed solely to properly characterize the performance of carbon dots but also to answer questions on the hotly debated origin of their luminescence. Currently, purification practices have been frequently inadequate, with a majority of studies utilizing insufficient methods (*i.e.*, centrifugation and filtration), performing dialysis with inappropriate (*e.g.*, too low) molecular weight cut-offs, or performing no separation step of any kind. Consequently, numerous previous findings may be called into question and require careful revisitation. Certainly, fluorescence-based applications (*e.g.*, heavy metal detection and cellular imaging) will be heavily impacted by the unaccounted presence of organic molecular fluorophores. While some researchers have employed membrane-based fractionation as a means for successfully size separating carbon dots,[94, 104] a majority of these examples involve the fractionation of graphitic dots generated from a top-down approach (*e.g.*,

electrochemical etching of graphite electrodes). This is noteworthy because top-down formation of carbon dots appears to be associated with fewer molecular byproducts. In contrast, we provide clear and abundant evidence that in unpurified samples produced by bottom-up synthesis, carbon dot emission is dominated by fluorescence from small molecular weight organic fluorophores. Worse, even when performing dialysis with a membrane molecular weight cutoff of 50 kDa, the complete removal of fluorescent organic byproducts putatively formed alongside the carbon dots is not guaranteed.

As pointed out by Gong *et al.*,[105] as-synthesized carbon dots are complex, multicomponent systems, suggesting that dialysis, despite its convenience, may not be a satisfactory mode of purification in some instances. Chromatographic techniques likely represent the most analytically sound means for fractionating these complex mixtures,[40, 102, 105-116] illustrated by the extensive HPLC fractionation studies conducted by the Colón[102, 107-108] and Choi[105, 111-115] groups, although these currently constitute less than 10% of the reported purification protocols for carbon dots. One hallmark of such fractionation is, intuitively, a reduction in sample complexity. Indeed, individual fractions generally possess optical properties distinct from the starting mixture, such as an excitation wavelength independent emission.[102, 105] What is needed now is a scalable, analytically sound, and vetted separation method that can arrive at high-purity, single-component carbon dot samples in practical quantities (beyond laboratory scale). This remains an unmet challenge; however, if the field of carbon dot research is to continue unabated, it is a challenge that must be answered.

Acknowledgements

This work was supported by the Mizzou Advantage funding program at the University of Missouri.

References

1. Baker, S. N.; Baker, G. A., Luminescent Carbon Nanodots: Emergent Nanolights. *Angew. Chem. Int. Ed.* **2010,** *49* (38), 6726-6744.

2. Ding, C.; Zhu, A.; Tian, Y., Functional Surface Engineering of C-Dots for Fluorescent Biosensing and in Vivo Bioimaging. *Acc. Chem. Res.* **2014,** *47* (1), 20-30.

3. Li, H.; Kang, Z.; Liu, Y.; Lee, S.-T., Carbon Nanodots: Synthesis, Properties and Applications. *J. Mater. Chem.* **2012,** *22* (46), 24230-24253.

4. Li, L.; Wu, G.; Yang, G.; Peng, J.; Zhao, J.; Zhu, J.-J., Focusing on Luminescent Graphene Quantum Dots: Current Status and Future Perspectives. *Nanoscale* **2013,** *5* (10), 4015-4039.

5. Shen, J.; Zhu, Y.; Yang, X.; Li, C., Graphene Quantum Dots: Emergent Nanolights for Bioimaging, Sensors, Catalysis and Photovoltaic Devices. *Chem. Commun.* **2012,** *48* (31), 3686-3699.

6. Wang, J.; Xin, X.; Lin, Z., Cu2ZnSnS4 Nanocrystals and Graphene Quantum Dots for Photovoltaics. *Nanoscale* **2011,** *3* (8), 3040-3048.

7. Zhang, Z.; Zhang, J.; Chen, N.; Qu, L., Graphene Quantum Dots: An Emerging Material for Energy-Related Applications and Beyond. *Energ. Environ. Sci.* **2012,** *5* (10), 8869-8890.

8. Zheng, X. T.; Ananthanarayanan, A.; Luo, K. Q.; Chen, P., Glowing Graphene Quantum Dots and Carbon Dots: Properties, Syntheses, and Biological Applications. *Small* **2015,** *11* (14), 1620-1636.

9. Essner, J. B.; Laber, C. H.; Baker, G. A., Carbon Dot Reduced Bimetallic Nanoparticles: Size and Surface Plasmon Resonance Tunability for Enhanced Catalytic Applications. *J. Mater. Chem. A* **2015,** *3* (31), 16354-16360.

10. Bourlinos, A. B.; Stassinopoulos, A.; Anglos, D.; Zboril, R.; Karakassides, M.; Giannelis, E. P., Surface Functionalized Carbogenic Quantum Dots. *Small* **2008,** *4* (4), 455-458.

11. Bourlinos, A. B.; Stassinopoulos, A.; Anglos, D.; Zboril, R.; Georgakilas, V.; Giannelis, E. P., Photoluminescent Carbogenic Dots. *Chem. Mater.* **2008,** *20* (14), 4539-4541.

12. Krysmann, M. J.; Kelarakis, A.; Dallas, P.; Giannelis, E. P., Formation Mechanism of Carbogenic Nanoparticles with Dual Photoluminescence Emission. *J. Am. Chem. Soc.* **2012,** *134* (2), 747-750.

13. Qu, S.; Wang, X.; Lu, Q.; Liu, X.; Wang, L., A Biocompatible Fluorescent Ink Based on Water-Soluble Luminescent Carbon Nanodots. *Angew. Chem. Int. Ed.* **2012,** *51* (49), 12215-12218.

14. Wang, L.; Zhu, S.-J.; Wang, H.-Y.; Qu, S.-N.; Zhang, Y.-L.; Zhang, J.-H.; Chen, Q.-D.; Xu, H.-L.; Han, W.; Yang, B.; Sun, H.-B., Common Origin of Green Luminescence in Carbon Nanodots and Graphene Quantum Dots. *ACS Nano* **2014,** *8* (3), 2541-2547.

15. Laber, C. H. E., J. B.; Scott, T. A.; Polo-Parada, L.; Baker, G. A., Domestic Pressure Cooker as Inexpensive Hydrothermal Vessel: Demonstrated Utility for Eco-Friendly Synthesis of Non-Toxic Carbon Dots. *Nano-Structures & Nano-Objects* **2016,** *6*, 52-58.

16. Choi, Y.; Ryu, G. H.; Min, S. H.; Lee, B. R.; Song, M. H.; Lee, Z.; Kim, B.-S., Interface-Controlled Synthesis of Heterodimeric Silver–Carbon Nanoparticles Derived from Polysaccharides. *ACS Nano* **2014,** *8* (11), 11377-11385.

17. Yang, Y.; Cui, J.; Zheng, M.; Hu, C.; Tan, S.; Xiao, Y.; Yang, Q.; Liu, Y., One-Step Synthesis of Amino-Functionalized Fluorescent Carbon Nanoparticles by Hydrothermal Carbonization of Chitosan. *Chem. Commun.* **2012,** *48* (3), 380-382.

18. Chowdhury, D.; Gogoi, N.; Majumdar, G., Fluorescent Carbon Dots Obtained from Chitosan Gel. *RSC Adv.* **2012,** *2* (32), 12156-12159.

19. Shen, L.; Chen, M.; Hu, L.; Chen, X.; Wang, J., Growth and Stabilization of Silver Nanoparticles on Carbon Dots and Sensing Application. *Langmuir* **2013,** *29* (52), 16135-16140.

20. Shen, L.-M.; Chen, Q.; Sun, Z.-Y.; Chen, X.-W.; Wang, J.-H., Assay of Biothiols by Regulating the Growth of Silver Nanoparticles with C-Dots as Reducing Agent. *Anal. Chem.* **2014,** *86* (10), 5002-5008.

21. Yang, Z.-C.; Wang, M.; Yong, A. M.; Wong, S. Y.; Zhang, X.-H.; Tan, H.; Chang, A. Y.; Li, X.; Wang, J., Intrinsically Fluorescent Carbon Dots with Tunable Emission Derived from Hydrothermal Treatment of Glucose in the Presence of Monopotassium Phosphate. *Chem. Commun.* **2011,** *47* (42), 11615-11617.

22. Tang, L.; Ji, R.; Cao, X.; Lin, J.; Jiang, H.; Li, X.; Teng, K. S.; Luk, C. M.; Zeng, S.; Hao, J.; Lau, S. P., Deep Ultraviolet Photoluminescence of Water-Soluble Self-Passivated Graphene Quantum Dots. *ACS Nano* **2012,** *6* (6), 5102-5110.

23. Mewada, A.; Pandey, S.; Shinde, S.; Mishra, N.; Oza, G.; Thakur, M.; Sharon, M.; Sharon, M., Green Synthesis of Biocompatible Carbon Dots Using Aqueous Extract of Trapa Bispinosa Peel. *Materials Science and Engineering: C* **2013,** *33* (5), 2914-2917.

24. Lu, W.; Qin, X.; Liu, S.; Chang, G.; Zhang, Y.; Luo, Y.; Asiri, A. M.; Al-Youbi, A. O.; Sun, X., Economical, Green Synthesis of Fluorescent Carbon Nanoparticles and Their Use as Probes for Sensitive and Selective Detection of Mercury(Ii) Ions. *Anal. Chem.* **2012,** *84* (12), 5351-5357.

25. Prasannan, A.; Imae, T., One-Pot Synthesis of Fluorescent Carbon Dots from Orange Waste Peels. *Ind. Eng. Chem. Res.* **2013,** *52* (44), 15673-15678.

26. Vikneswaran, R.; Ramesh, S.; Yahya, R., Green Synthesized Carbon Nanodots as a Fluorescent Probe for Selective and Sensitive Detection of Iron(iii) Ions. *Mater. Lett.* **2014,** *136*, 179-182.

27. Zhou, J.; Sheng, Z.; Han, H.; Zou, M.; Li, C., Facile Synthesis of Fluorescent Carbon Dots Using Watermelon Peel as a Carbon Source. *Mater. Lett.* **2012,** *66* (1), 222-224.

28. Lu, W.; Qin, X.; Asiri, A. M.; Al-Youbi, A. O.; Sun, X., Green Synthesis of Carbon Nanodots as an Effective Fluorescent Probe for Sensitive and Selective Detection of Mercury(Ii) Ions. *J. Nanopart. Res.* **2012,** *15* (1), 1344.

29. Krysmann, M. J.; Kelarakis, A.; Giannelis, E. P., Photoluminescent Carbogenic Nanoparticles Directly Derived from Crude Biomass. *Green Chem.* **2012,** *14* (11), 3141-3145.

30. Briscoe, J.; Marinovic, A.; Sevilla, M.; Dunn, S.; Titirici, M., Biomass-Derived Carbon Quantum Dot Sensitizers for Solid-State Nanostructured Solar Cells. *Angew. Chem. Int. Ed.* **2015,** *54* (15), 4463-4468.

31. Liu, S.; Tian, J.; Wang, L.; Zhang, Y.; Qin, X.; Luo, Y.; Asiri, A. M.; Al-Youbi, A. O.; Sun, X., Hydrothermal Treatment of Grass: A Low-Cost, Green Route to Nitrogen-Doped, Carbon-Rich, Photoluminescent Polymer Nanodots as an Effective Fluorescent Sensing Platform for Label-Free Detection of Cu(Ii) Ions. *Adv. Mater.* **2012,** *24* (15), 2037-2041.

32. Qin, X.; Lu, W.; Asiri, A. M.; Al-Youbi, A. O.; Sun, X., Green, Low-Cost Synthesis of Photoluminescent Carbon Dots by Hydrothermal Treatment of Willow Bark and Their Application as an Effective Photocatalyst for Fabricating Au Nanoparticles–Reduced Graphene Oxide Nanocomposites for Glucose Detection. *Catal. Sci. Techol.* **2013,** *3* (4), 1027-1035.

33. Sun, D.; Ban, R.; Zhang, P.-H.; Wu, G.-H.; Zhang, J.-R.; Zhu, J.-J., Hair Fiber as a Precursor for Synthesizing of Sulfur- and Nitrogen-Co-Doped Carbon Dots with Tunable Luminescence Properties. *Carbon* **2013,** *64*, 424-434.

34. Wang, J.; Peng, F.; Lu, Y.; Zhong, Y.; Wang, S.; Xu, M.; Ji, X.; Su, Y.; Liao, L.; He, Y., Large-Scale Green Synthesis of Fluorescent Carbon Nanodots and Their Use in Optics Applications. *Adv. Optical Mater.* **2015,** *3* (1), 103-111.

35. Liu, S.-S.; Wang, C.-F.; Li, C.-X.; Wang, J.; Mao, L.-H.; Chen, S., Hair-Derived Carbon Dots toward Versatile Multidimensional Fluorescent Materials. *J. Mater. Chem. C* **2014,** *2* (32), 6477-6483.

36. Essner, J. B.; Laber, C. H.; Ravula, S.; Polo-Parada, L.; Baker, G. A., Pee-Dots: Biocompatible Fluorescent Carbon Dots Derived from the Upcycling of Urine. *Green Chem.* **2016,** *18* (1), 243-250.

37. D'Angelis do E. S. Barbosa, C.; Corrêa, J. R.; Medeiros, G. A.; Barreto, G.; Magalhães, K. G.; de Oliveira, A. L.; Spencer, J.; Rodrigues, M. O.; Neto, B. A. D., Carbon

Dots (C-Dots) from Cow Manure with Impressive Subcellular Selectivity Tuned by Simple Chemical Modification. *Chem.-Eur. J.* **2015,** *21* (13), 5055-5060.

38. Cayuela, A.; Soriano, M. L.; Carrillo-Carrión, C.; Valcárcel, M., Semiconductor and Carbon-Based Fluorescent Nanodots: The Need for Consistency. *Chem. Commun.* **2016,** *52* (7), 1311-1326.

39. Qi, B.-P.; Bao, L.; Zhang, Z.-L.; Pang, D.-W., Electrochemical Methods to Study Photoluminescent Carbon Nanodots: Preparation, Photoluminescence Mechanism and Sensing. *ACS Appl. Mater. Interfaces* **2016,** *8* (42), 28372-28382.

40. Hu, Q.; Meng, X.; Chan, W., An Investigation on the Chemical Structure of Nitrogen and Sulfur codoped Carbon Nanoparticles by Ultra-Performance Liquid Chromatography-Tandem Mass Spectrometry. *Anal. Bioanal. Chem.* **2016,** *408* (19), 5347-5357.

41. Demchenko, A. P.; Dekaliuk, M. O., The Origin of Emissive States of Carbon Nanoparticles Derived from Ensemble-Averaged and Single-Molecular Studies. *Nanoscale* **2016,** *8* (29), 14057-14069.

42. Sarswat, P. K.; Free, M. L., Light Emitting Diodes Based on Carbon Dots Derived from Food, Beverage, and Combustion Wastes. *Phys. Chem. Chem. Phys.* **2015,** *17* (41), 27642-27652.

43. Zhu, S.; Zhao, X.; Song, Y.; Lu, S.; Yang, B., Beyond Bottom-up Carbon Nanodots: Citric-Acid Derived Organic Molecules. *Nano Today* **2016,** *11* (2), 128-132.

44. Song, Y.; Zhu, S.; Zhang, S.; Fu, Y.; Wang, L.; Zhao, X.; Yang, B., Investigation from Chemical Structure to Photoluminescent Mechanism: A Type of Carbon Dots from the Pyrolysis of Citric Acid and an Amine. *J. Mater. Chem. C* **2015,** *3* (23), 5976-5984.

45. Schneider, J.; Reckmeier, C. J.; Xiong, Y.; von Seckendorff, M.; Susha, A. S.; Kasák, P.; Rogach, A. L., Molecular Fluorescence in Citric Acid-Based Carbon Dots. *J. Phys. Chem. C* **2017,** *121* (3), 2014-2022.

46. Shi, L.; Yang, J. H.; Zeng, H. B.; Chen, Y. M.; Yang, S. C.; Wu, C.; Zeng, H.; Yoshihito, O.; Zhang, Q., Carbon Dots with High Fluorescence Quantum Yield: The

Fluorescence Originates from Organic Fluorophores. *Nanoscale* **2016,** *8* (30), 14374-14378.

47. He, L.; Wang, T.; An, J.; Li, X.; Zhang, L.; Li, L.; Li, G.; Wu, X.; Su, Z.; Wang, C., Carbon Nanodots@Zeolitic Imidazolate Framework-8 Nanoparticles for Simultaneous Ph-Responsive Drug Delivery and Fluorescence Imaging. *CrystEngComm* **2014,** *16* (16), 3259-3263.

48. Karthik, S.; Saha, B.; Ghosh, S. K.; Pradeep Singh, N. D., Photoresponsive Quinoline Tethered Fluorescent Carbon Dots for Regulated Anticancer Drug Delivery. *Chem. Commun.* **2013,** *49* (89), 10471-10473.

49. Niu, Q.; Gao, K.; Lin, Z.; Wu, W., Amine-Capped Carbon Dots as a Nanosensor for Sensitive and Selective Detection of Picric Acid in Aqueous Solution Via Electrostatic Interaction. *Anal. Methods* **2013,** *5* (21), 6228-6233.

50. Strauss, V.; Margraf, J. T.; Dolle, C.; Butz, B.; Nacken, T. J.; Walter, J.; Bauer, W.; Peukert, W.; Spiecker, E.; Clark, T.; Guldi, D. M., Carbon Nanodots: Toward a Comprehensive Understanding of Their Photoluminescence. *J. Am. Chem. Soc.* **2014,** *136* (49), 17308-17316.

51. Qu, S.; Chen, H.; Zheng, X.; Cao, J.; Liu, X., Ratiometric Fluorescent Nanosensor Based on Water Soluble Carbon Nanodots with Multiple Sensing Capacities. *Nanoscale* **2013,** *5* (12), 5514-5518.

52. Chen, Y.-C.; Nien, C.-Y.; Albert, K.; Wen, C.-C.; Hsieh, Y.-Z.; Hsu, H.-Y., Pseudo-Multicolor Carbon Dots Emission and the Dilution-Induced Reversible Fluorescence Shift. *RSC Adv.* **2016,** *6* (50), 44024-44028.

53. Pei, S.; Zhang, J.; Gao, M.; Wu, D.; Yang, Y.; Liu, R., A Facile Hydrothermal Approach Towards Photoluminescent Carbon Dots from Amino Acids. *J. Colloid Interf. Sci.* **2015,** *439*, 129-133.

54. Zhu, S.; Meng, Q.; Wang, L.; Zhang, J.; Song, Y.; Jin, H.; Zhang, K.; Sun, H.; Wang, H.; Yang, B., Highly Photoluminescent Carbon Dots for Multicolor Patterning, Sensors, and Bioimaging. *Angew. Chem. Int. Ed.* **2013,** *52* (14), 3953-3957.

55. Bian, J.; Huang, C.; Wang, L.; Hung, T.; Daoud, W. A.; Zhang, R., Carbon Dot Loading and Tio2 Nanorod Length Dependence of Photoelectrochemical Properties in Carbon Dot/Tio2 Nanorod Array Nanocomposites. *ACS Appl. Mater. Interfaces* **2014,** *6* (7), 4883-4890.

56. Cui, X.; Zhu, L.; Wu, J.; Hou, Y.; Wang, P.; Wang, Z.; Yang, M., A Fluorescent Biosensor Based on Carbon Dots-Labeled Oligodeoxyribonucleotide and Graphene Oxide for Mercury (Ii) Detection. *Biosens. Bioelectron.* **2015,** *63*, 506-512.

57. Song, Y.; Zhu, S.; Xiang, S.; Zhao, X.; Zhang, J.; Zhang, H.; Fu, Y.; Yang, B., Investigation into the Fluorescence Quenching Behaviors and Applications of Carbon Dots. *Nanoscale* **2014,** *6* (9), 4676-4682.

58. Do, S.; Kwon, W.; Rhee, S.-W., Soft-Template Synthesis of Nitrogen-Doped Carbon Nanodots: Tunable Visible-Light Photoluminescence and Phosphor-Based Light-Emitting Diodes. *J. Mater. Chem. C* **2014,** *2* (21), 4221-4226.

59. Li, H.; He, X.; Kang, Z.; Huang, H.; Liu, Y.; Liu, J.; Lian, S.; Tsang, C. H. A.; Yang, X.; Lee, S.-T., Water-Soluble Fluorescent Carbon Quantum Dots and Photocatalyst Design. *Angew. Chem. Int. Ed.* **2010,** *49* (26), 4430-4434.

60. Zhang, H.; Huang, H.; Ming, H.; Li, H.; Zhang, L.; Liu, Y.; Kang, Z., Carbon Quantum Dots/Ag3PO4 Complex Photocatalysts with Enhanced Photocatalytic Activity and Stability under Visible Light. *J. Mater. Chem.* **2012,** *22* (21), 10501-10506.

61. Zhu, A.; Qu, Q.; Shao, X.; Kong, B.; Tian, Y., Carbon-Dot-Based Dual-Emission Nanohybrid Produces a Ratiometric Fluorescent Sensor for in Vivo Imaging of Cellular Copper Ions. *Angew. Chem. Int. Ed.* **2012,** *51* (29), 7185-7189.

62. Kong, B.; Zhu, A.; Ding, C.; Zhao, X.; Li, B.; Tian, Y., Carbon Dot-Based Inorganic–Organic Nanosystem for Two-Photon Imaging and Biosensing of Ph Variation in Living Cells and Tissues. *Adv. Mater.* **2012,** *24* (43), 5844-5848.

63. Tang, J.; Kong, B.; Wu, H.; Xu, M.; Wang, Y.; Wang, Y.; Zhao, D.; Zheng, G., Carbon Nanodots Featuring Efficient Fret for Real-Time Monitoring of Drug Delivery and Two-Photon Imaging. *Adv. Mater.* **2013,** *25* (45), 6569-6574.

64. Li, H.; Liu, R.; Lian, S.; Liu, Y.; Huang, H.; Kang, Z., Near-Infrared Light Controlled Photocatalytic Activity of Carbon Quantum Dots for Highly Selective Oxidation Reaction. *Nanoscale* **2013,** *5* (8), 3289-3297.

65. Sun, Y.-P.; Zhou, B.; Lin, Y.; Wang, W.; Fernando, K. A. S.; Pathak, P.; Meziani, M. J.; Harruff, B. A.; Wang, X.; Wang, H.; Luo, P. G.; Yang, H.; Kose, M. E.; Chen, B.; Veca, L. M.; Xie, S.-Y., Quantum-Sized Carbon Dots for Bright and Colorful Photoluminescence. *J. Am. Chem. Soc.* **2006,** *128* (24), 7756-7757.

66. Liu, X.; Liu, H.-J.; Cheng, F.; Chen, Y., Preparation and Characterization of Multi Stimuli-Responsive Photoluminescent Nanocomposites of Graphene Quantum Dots with Hyperbranched Polyethylenimine Derivatives. *Nanoscale* **2014,** *6* (13), 7453-7460.

67. Cao, L.; Wang, X.; Meziani, M. J.; Lu, F.; Wang, H.; Luo, P. G.; Lin, Y.; Harruff, B. A.; Veca, L. M.; Murray, D.; Xie, S.-Y.; Sun, Y.-P., Carbon Dots for Multiphoton Bioimaging. *J. Am. Chem. Soc.* **2007,** *129* (37), 11318-11319.

68. Zhang, Y.; Gonçalves, H.; Esteves da Silva, J. C. G.; Geddes, C. D., Metal-Enhanced Photoluminescence from Carbon Nanodots. *Chem. Commun.* **2011,** *47* (18), 5313-5315.

69. Turkevich, J.; Stevenson, P. C.; Hillier, J., A Study of the Nucleation and Growth Processes in the Synthesis of Colloidal Gold. *Discuss. Faraday Soc.* **1951,** *11* (0), 55-75.

70. Grasseschi, D.; Ando, R. A.; Toma, H. E.; Zamarion, V. M., Unraveling the Nature of Turkevich Gold Nanoparticles: The Unexpected Role of the Dicarboxyketone Species. *RSC Adv.* **2015,** *5* (8), 5716-5724.

71. Wuithschick, M.; Birnbaum, A.; Witte, S.; Sztucki, M.; Vainio, U.; Pinna, N.; Rademann, K.; Emmerling, F.; Kraehnert, R.; Polte, J., Turkevich in New Robes: Key Questions Answered for the Most Common Gold Nanoparticle Synthesis. *ACS Nano* **2015,** *9* (7), 7052-7071.

72. Kimling, J.; Maier, M.; Okenve, B.; Kotaidis, V.; Ballot, H.; Plech, A., Turkevich Method for Gold Nanoparticle Synthesis Revisited. *J. Phys. Chem. B* **2006,** *110* (32), 15700-15707.

73. Schulz, F.; Homolka, T.; Bastús, N. G.; Puntes, V.; Weller, H.; Vossmeyer, T., Little Adjustments Significantly Improve the Turkevich Synthesis of Gold Nanoparticles. *Langmuir* **2014,** *30* (35), 10779-10784.

74. Deraedt, C.; Salmon, L.; Gatard, S.; Ciganda, R.; Hernandez, R.; Ruiz, J.; Astruc, D., Sodium Borohydride Stabilizes Very Active Gold Nanoparticle Catalysts. *Chem. Commun.* **2014,** *50* (91), 14194-14196.

75. Xu, X.; Ray, R.; Gu, Y.; Ploehn, H. J.; Gearheart, L.; Raker, K.; Scrivens, W. A., Electrophoretic Analysis and Purification of Fluorescent Single-Walled Carbon Nanotube Fragments. *J. Am. Chem. Soc.* **2004,** *126* (40), 12736-12737.

76. Buffo, R. A.; Cardelli-Freire, C., Coffee Favour: An Overview. *Flavour Frag. J.* **2004,** *19* (2), 99-104.

77. Schenker, S.; Heinemann, C.; Huber, M.; Pompizzi, R.; Perren, R.; Escher, R., Impact of Roasting Conditions on the Formation of Aroma Compounds in Coffee Beans. *J. Food Sci.* **2002,** *67* (1), 60-66.

78. Esquivel, P.; Jiménez, V. M., Functional Properties of Coffee and Coffee by-Products. *Food Res. Int.* **2012,** *46* (2), 488-495.

79. Samaras, T. S.; Camburn, P. A.; Chandra, S. X.; Gordon, M. H.; Ames, J. M., Antioxidant Properties of Kilned and Roasted Malts. *J. Agr. Food Chem.* **2005,** *53* (20), 8068-8074.

80. Carvalho, D. O.; Correia, E.; Lopes, L.; Guido, L. F., Further Insights into the Role of Melanoidins on the Antioxidant Potential of Barley Malt. *Food Chem.* **2014,** *160*, 127-133.

81. Carvalho, D.; Øgendal, L.; Andersen, M.; Guido, L., High Molecular Weight Compounds Generated by Roasting Barley Malt Are Pro-Oxidants in Metal-Catalyzed Oxidations. *Eur. Food Res. Technol.* **2016,** *242* (9), 1545-1553.

82. Yahya, H.; Linforth, R. S. T.; Cook, D. J., Flavour Generation During Commercial Barley and Malt Roasting Operations: A Time Course Study. *Food Chem.* **2014,** *145*, 378-387.

83. Carvalho, D. O.; Gonçalves, L. M.; Guido, L. F., Overall Antioxidant Properties of Malt and How They Are Influenced by the Individual Constituents of Barley and the Malting Process. *Compr. Rev. Food Sci. Food Saf.* **2016,** *15* (5), 927-943.

84. Yang, J.; Zhang, Y.; Gautam, S.; Liu, L.; Dey, J.; Chen, W.; Mason, R. P.; Serrano, C. A.; Schug, K. A.; Tang, L., Development of Aliphatic Biodegradable Photoluminescent Polymers. *Proc. Natl. Acad. Sci. U.S.A* **2009,** *106* (25), 10086-10091.

85. Kim, J. P.; Xie, Z.; Creer, M.; Liu, Z.; Yang, J., Citrate-Based Fluorescent Materials for Low-Cost Chloride Sensing in the Diagnosis of Cystic Fibrosis. *Chem. Sci.* **2017,** *8* (1), 550-558.

86. Xie, Z.; Zhang, Y.; Liu, L.; Weng, H.; Mason, R. P.; Tang, L.; Nguyen, K. T.; Hsieh, J.-T.; Yang, J., Development of Intrinsically Photoluminescent and Photostable Polylactones. *Adv. Mater.* **2014,** *26* (26), 4491-4496.

87. Wang, H.-X.; Yang, Z.; Liu, Z.-G.; Wan, J.-Y.; Xiao, J.; Zhang, H.-L., Facile Preparation of Bright-Fluorescent Soft Materials from Small Organic Molecules. *Chem.-Eur. J.* **2016,** *22* (24), 8096-8104.

88. Kasprzyk, W.; Bednarz, S.; Żmudzki, P.; Galica, M.; Bogdał, D., Novel Efficient Fluorophores Synthesized from Citric Acid. *RSC Adv.* **2015,** *5* (44), 34795-34799.

89. Chart, S. L. I. P. S.

90. Pop, E.; Varshney, V.; Roy, A. K., Thermal Properties of Graphene: Fundamentals and Applications. *MRS Bull.* **2012,** *37* (12), 1273-1281.

91. Liu, Y.; Li, S.; Li, K.; Zheng, Y.; Zhang, M.; Cai, C.; Yu, C.; Zhou, Y.; Yan, D., A Srikaya-Like Light-Harvesting Antenna Based on Graphene Quantum Dots and Porphyrin Unimolecular Micelles. *Chem. Commun.* **2016,** *52* (60), 9394-9397.

92. Ryu, S.; Lee, K.; Hong, S. H.; Lee, H., Facile Method to Sort Graphene Quantum Dots by Size through Ammonium Sulfate Addition. *RSC Adv.* **2014,** *4* (100), 56848-56852.

93. Rajendran, R.; Sohila, S.; Muralidharan, R.; Muthamizhchelvan, C.; Ponnusamy, S., One-Pot Microwave Synthesis of Fluorescent Carbogenic Nanoparticles from Triton X-100 for Cell Imaging. *Eur. J. Inorg. Chem.* **2014,** *2014* (2), 392-396.

94. Kim, S.; Hwang, S. W.; Kim, M.-K.; Shin, D. Y.; Shin, D. H.; Kim, C. O.; Yang, S. B.; Park, J. H.; Hwang, E.; Choi, S.-H.; Ko, G.; Sim, S.; Sone, C.; Choi, H. J.; Bae, S.; Hong, B. H., Anomalous Behaviors of Visible Luminescence from Graphene Quantum Dots: Interplay between Size and Shape. *ACS Nano* **2012,** *6* (9), 8203-8208.

95. Khan, S.; Sharma, A.; Ghoshal, S.; Jain, S.; Hazra, M. K.; Nandi, C. K., Small Molecular Organic Nanocrystals Resemble Carbon Nanodots in Terms of Their Properties. *Chem. Sci.* **2018,** *9* (1), 175-180.

96. Yu, X.; Liu, R.; Zhang, G.; Cao, H., Carbon Quantum Dots as Novel Sensitizers for Photoelectrochemical Solar Hydrogen Generation and Their Size-Dependent Effect. *Nanotechnology* **2013,** *24* (33), 335401.

97. Kozawa, D.; Miyauchi, Y.; Mouri, S.; Matsuda, K., Exploring the Origin of Blue and Ultraviolet Fluorescence in Graphene Oxide. *J. Phys. Chem. Lett.* **2013,** *4* (12), 2035-2040.

98. Galande, C.; Mohite, A. D.; Naumov, A. V.; Gao, W.; Ci, L.; Ajayan, A.; Gao, H.; Srivastava, A.; Weisman, R. B.; Ajayan, P. M., Quasi-Molecular Fluorescence from Graphene Oxide. *Sci. Rep.* **2011,** *1* (1), 85.

99. Dekaliuk, M. O.; Viagin, O.; Malyukin, Y. V.; Demchenko, A. P., Fluorescent Carbon Nanomaterials: "Quantum Dots" or Nanoclusters? *Phys. Chem. Chem. Phys.* **2014,** *16* (30), 16075-16084.

100. Yang, C.; Zhu, S.; Li, Z.; Li, Z.; Chen, C.; Sun, L.; Tang, W.; Liu, R.; Sun, Y.; Yu, M., Nitrogen-Doped Carbon Dots with Excitation-Independent Long-Wavelength Emission Produced by a Room-Temperature Reaction. *Chem. Commun.* **2016,** *52* (80), 11912-11914.

101. Spectrum Labs Inc. Laboratory Dialysis Frequently Asked Questions. *http://spectrumlabs.com/dialysis/FAQ.html (accessed October 16, 2017)*.

102. Vinci, J. C.; Ferrer, I. M.; Seedhouse, S. J.; Bourdon, A. K.; Reynard, J. M.; Foster, B. A.; Bright, F. V.; Colón, L. A., Hidden Properties of Carbon Dots Revealed after Hplc Fractionation. *J. Phys. Chem. Lett.* **2013,** *4* (2), 239-243.

103. Khan, S.; Gupta, A.; Verma, N. C.; Nandi, C. K., Time-Resolved Emission Reveals Ensemble of Emissive States as the Origin of Multicolor Fluorescence in Carbon Dots. *Nano Lett.* **2015,** *15* (12), 8300-8305.

104. Zhao, Q.-L.; Zhang, Z.-L.; Huang, B.-H.; Peng, J.; Zhang, M.; Pang, D.-W., Facile Preparation of Low Cytotoxicity Fluorescent Carbon Nanocrystals by Electrooxidation of Graphite. *Chem. Commun.* **2008,** (41), 5116-5118.

105. Gong, X.; Chin Paau, M.; Hu, Q.; Shuang, S.; Dong, C.; Choi, M. M. F., Uhplc Combined with Mass Spectrometric Study of as-Synthesized Carbon Dots Samples. *Talanta* **2016,** *146*, 340-350.

106. Fuyuno, N.; Kozawa, D.; Miyauchi, Y.; Mouri, S.; Kitaura, R.; Shinohara, H.; Yasuda, T.; Komatsu, N.; Matsuda, K., Drastic Change in Photoluminescence Properties of Graphene Quantum Dots by Chromatographic Separation. *Adv. Optical Mater.* **2014,** *2* (10), 983-989.

107. Vinci, J. C.; Colon, L. A., Fractionation of Carbon-Based Nanomaterials by Anion-Exchange Hplc. *Anal. Chem.* **2012,** *84* (2), 1178-1183.

108. Baker, J. S.; Colón, L. A., Influence of Buffer Composition on the Capillary Electrophoretic Separation of Carbon Nanoparticles. *J. Chromatogr. A* **2009,** *1216* (52), 9048-9054.

109. Ding, H.; Yu, S.-B.; Wei, J.-S.; Xiong, H.-M., Full-Color Light-Emitting Carbon Dots with a Surface-State-Controlled Luminescence Mechanism. *ACS Nano* **2016,** *10* (1), 484-491.

110. Liu, H.; Ye, T.; Mao, C., Fluorescent Carbon Nanoparticles Derived from Candle Soot. *Angew. Chem. Int. Ed.* **2007,** *46* (34), 6473-6475.

111. Gong, X.; Hu, Q.; Chin Paau, M.; Zhang, Y.; Zhang, L.; Shuang, S.; Dong, C.; Choi, M. M. F., High-Performance Liquid Chromatographic and Mass Spectrometric Analysis of Fluorescent Carbon Nanodots. *Talanta* **2014,** *129*, 529-538.

112. Hu, Q.; Paau, M. C.; Choi, M. M. F.; Zhang, Y.; Gong, X.; Zhang, L.; Liu, Y.; Yao, J., Better Understanding of Carbon Nanoparticles Via High-Performance Liquid Chromatography-Fluorescence Detection and Mass Spectrometry. *Electrophoresis* **2014,** *35* (17), 2454-2462.

113. Gong, X.; Hu, Q.; Paau, M. C.; Zhang, Y.; Shuang, S.; Dong, C.; Choi, M. M. F., Red-Green-Blue Fluorescent Hollow Carbon Nanoparticles Isolated from Chromatographic Fractions for Cellular Imaging. *Nanoscale* **2014,** *6* (14), 8162-8170.

114. Hu, Q.; Paau, M. C.; Zhang, Y.; Gong, X.; Zhang, L.; Lu, D.; Liu, Y.; Liu, Q.; Yao, J.; Choi, M. M. F., Green Synthesis of Fluorescent Nitrogen/Sulfur-Doped Carbon Dots and Investigation of Their Properties by Hplc Coupled with Mass Spectrometry. *RSC Adv.* **2014,** *4* (35), 18065-18073.

115. Hu, Q.; Paau, M. C.; Zhang, Y.; Chan, W.; Gong, X.; Zhang, L.; Choi, M. M. F., Capillary Electrophoretic Study of Amine/Carboxylic Acid-Functionalized Carbon Nanodots. *J. Chromatogr. A* **2013,** *1304*, 234-240.

116. Wei, J.; Qiu, J., Unveil the Fluorescence of Carbon Quantum Dots. *Adv. Eng. Mater.* **2015,** *17* (2), 138-142.

Appendix G: Supporting Information for Appendix F: Artifacts and Errors Associated with the Ubiquitous Presence of Fluorescent Impurities in Carbon Nanodots

Jeremy B. Essner, **Jennifer A. Kist**, Luis Polo-Parada, and Gary A. Baker

Table G.1: Reference fluorophores used to determine quantum yield (QY) values.

Fluorophore	**Excitation Wavelength (nm)**	**Solvent**	**n[a]**	**QY (%)**	**Ref.**
Quinine sulfate	350	0.1 M H_2SO_4	1.343	58	35
Coumarin 153	421	EtOH	1.366	38	36
Fluorescein	470	0.1 M NaOH	1.336	91	37
Rhodamine B	514	Water	1.334	31	38

[a] refractive index.

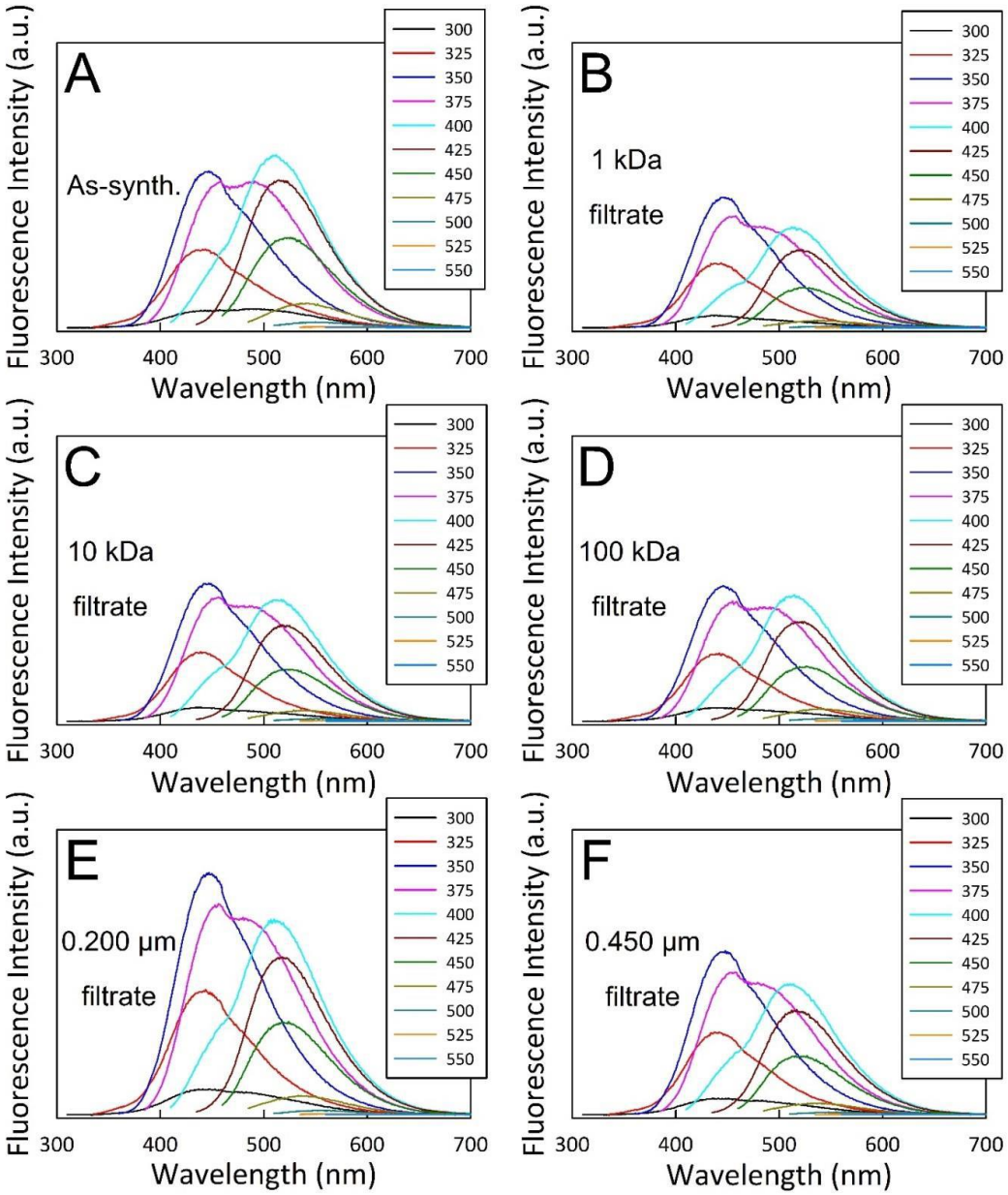

Figure G.1 Excitation wavelength-dependent emission of the as-synthesized (as-synth.) CA-U microwave sample (A) and its filtrate fractions after ultrafiltration with 1 kDa (B), 10 kDa (C), or 100 kDa (D) MWCO membranes or bulk filtration with 0.200 µm (E) or 0.450 µm (F) pore size syringe filters. The emission profiles of the filtrates were all essentially identical to those of the as-synthesized sample indicating that the small organic material (< 1 kDa) that traverses the membrane is associated with a majority of the observed fluorescence. Further, these results highlight that the common practice of purifying solely with a syringe filter is entirely inadequate.

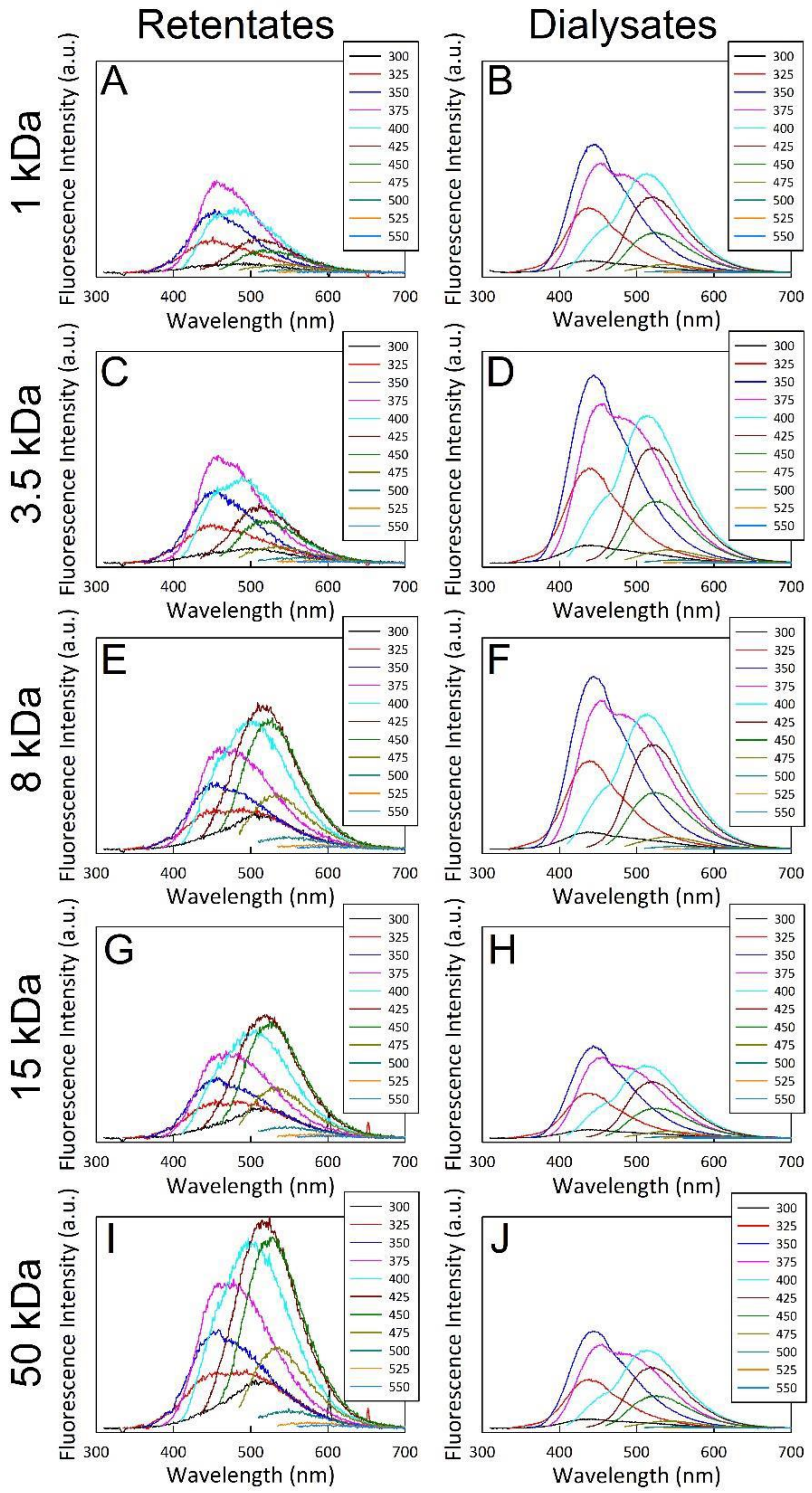

Figure G.2 Excitation wavelength-dependent emission of the retentate (A, C, E, G, and I) and dialysate (B, D, F, H, and J) fractions from dialysis of the CA-U derived microwave-generated FCDs. Within each respective category (*i.e.*, retentate or dialysate), the fractions displayed similar spectral characteristics to one another regardless of the membrane

MWCO, however, the emission profiles in cross-category comparisons were markedly different, alluding to the existence of at least two distinct populations of fluorophores. Even further, when the emission was collected on fraction "normalized" to similar absorbance values in the near-UV region, the retentate fractions presented drastically lower emission intensities compared to the dialysate fractions. Note that the y-axis maxima for the retentate fraction is an order of magnitude lower than that for the dialysate fractions to better show the spectral features. These results indicate that the retentates, which should contain the desired FCDs (if present), are not nearly as fluorescent as once thought and that a majority of the fluorescence arises from small molecular species (< 1 kDa) that permeate the membrane.

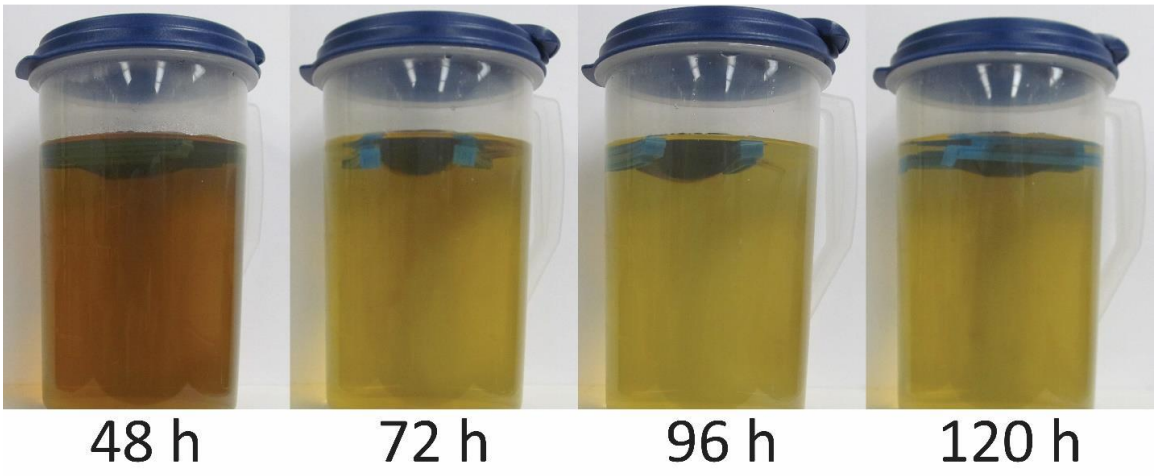

Figure G.3 Sequence of images showing the progress of dialysis for microwave-generated CA-U derived FCDs after 48, 72, 96, and 120 h of dialysis, where the images were collected immediately before replenishing the exchange solvent (*i.e.*, ultrapure water). These results highlight the sheer quantity of small molecular material (< 1 kDa) that continues to permeate the membrane even after four additional 24 h dialysis periods against fresh exchange solvent.

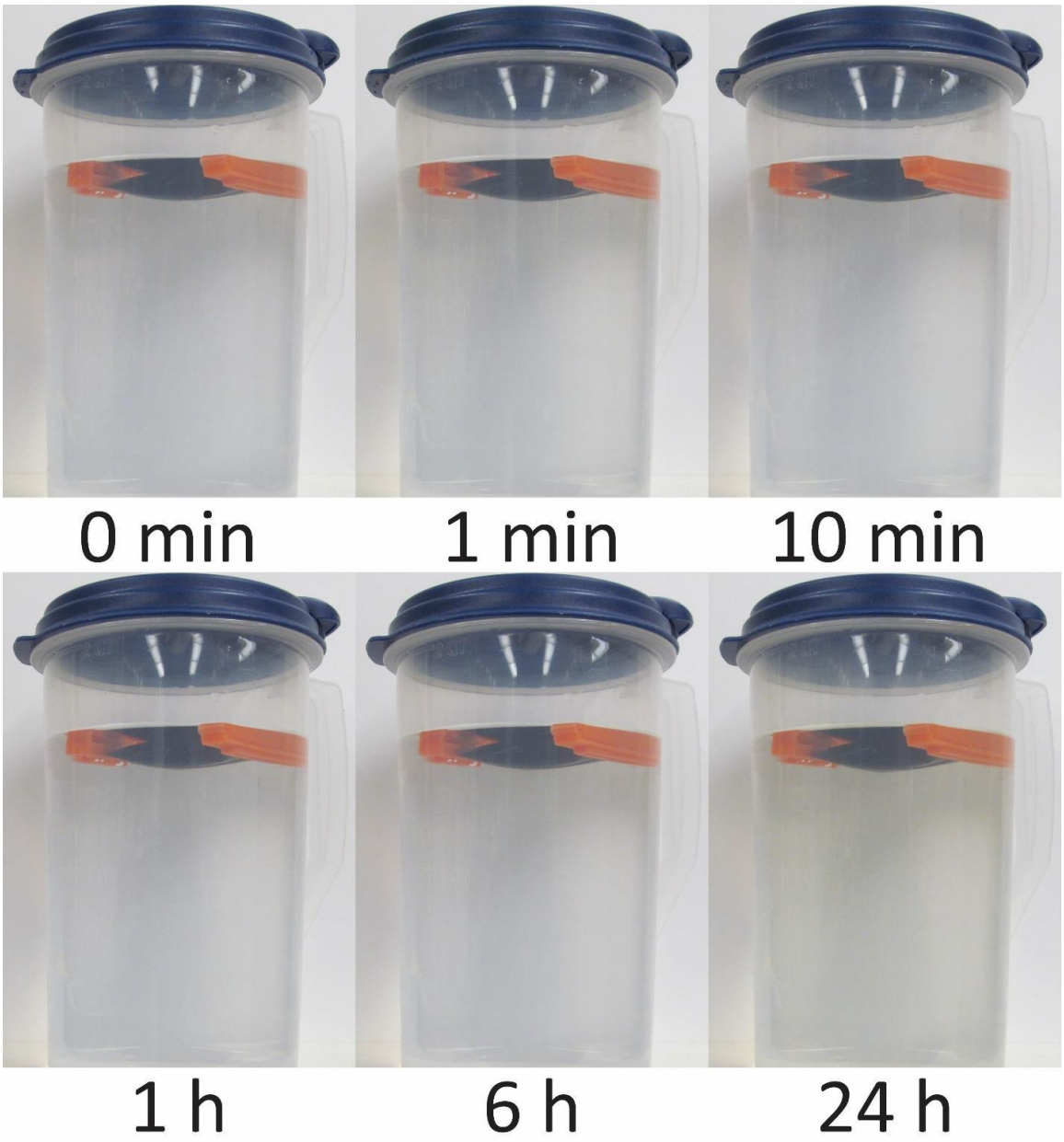

Figure G.4 Sequence of images showing the progress of dialysis of a microwave-generated CA-U derived sample against a 50 kDa MWCO membrane. The sample employed in this study was the retentate fraction that was obtained after extensive dialysis against a 1 kDa MWCO membrane. These images further highlight that the resulting product consists of two size-disparate species: one < 1 kDa (molecular/polymeric material) and the other ≥ 50 kDa (FCDs).

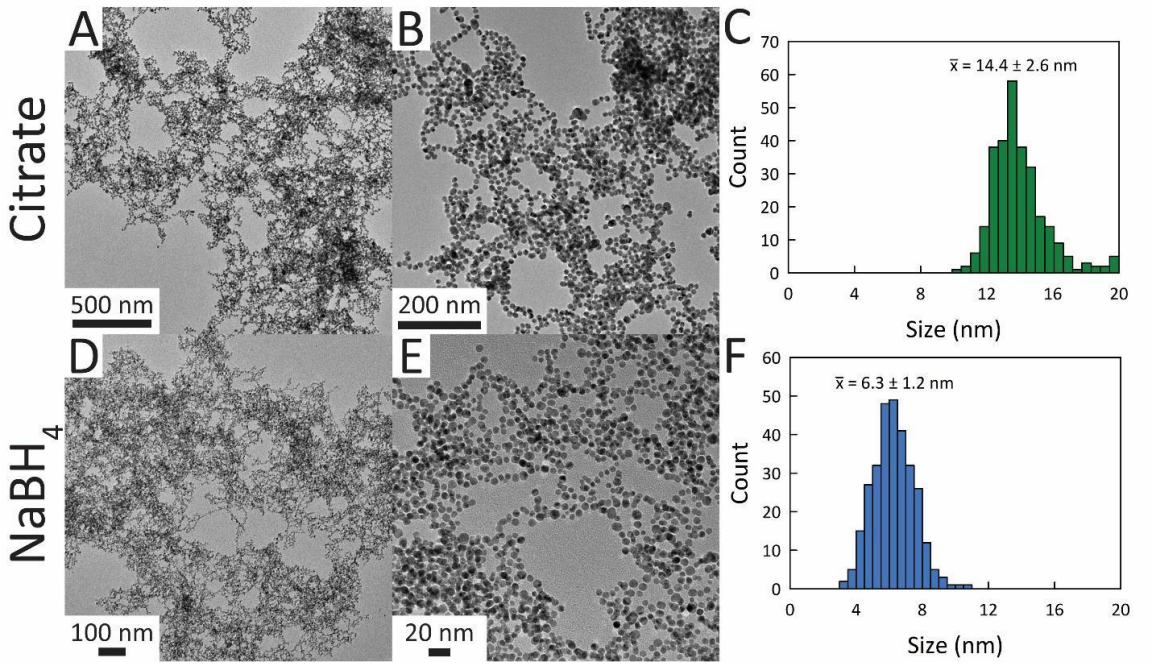

Figure G.5 Representative TEM images of the citrate- (A and B) and $NaBH_4$-stabilized (D and E) AuNPs along with their corresponding histograms (C and F). The AuNPs were used as a convenient means to clarify nanoscale membrane permeability for a given MWCO.

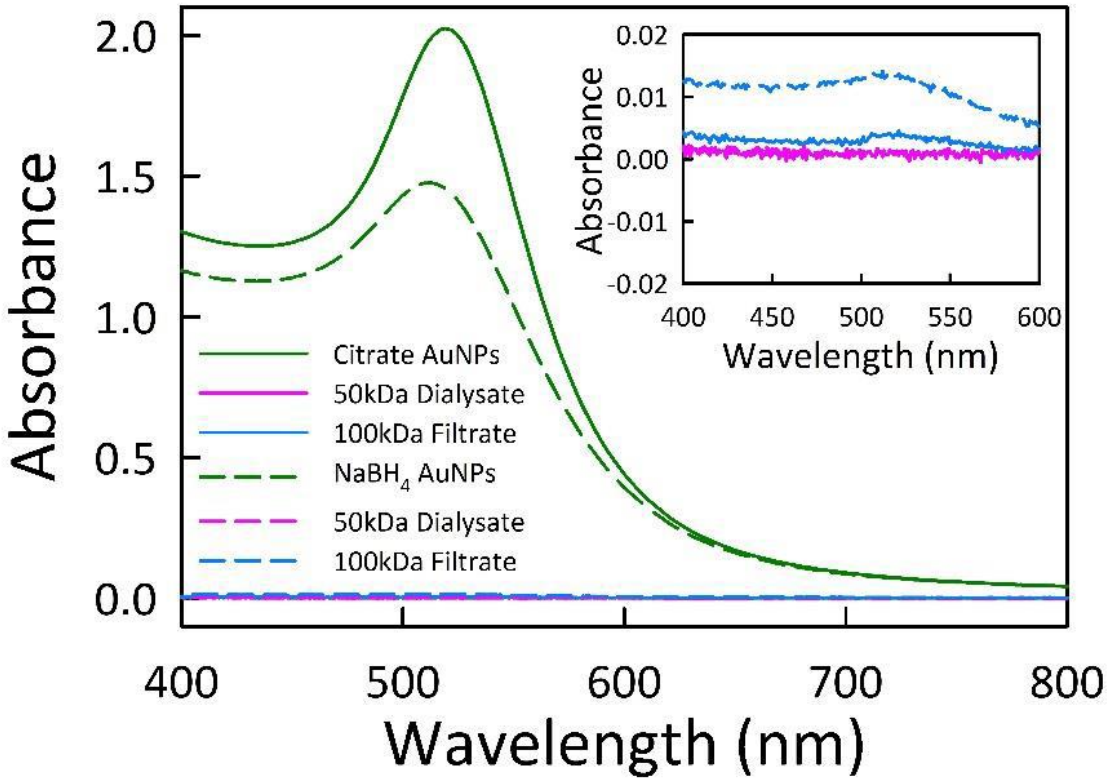

Figure G.6 UV-vis spectra of the dialysate and ultrafiltration fractions of the 14 nm citrate-stabilized and 6 nm $NaBH_4$-stabilized AuNPs compared to their parent (unpurified) solutions. These benchmark experiments reveal that neither AuNP samples permeate the 50 kDa dialysis membrane, whereas minute quantities of both AuNP sizes pass through the 100 kDa ultrafiltration membrane, with the larger citrate-stabilized AuNPs mobilizing to a lesser extent. The inset Panel is a magnified plot of the spectra for the dialysate and filtrate fractions to better highlight these revelations.

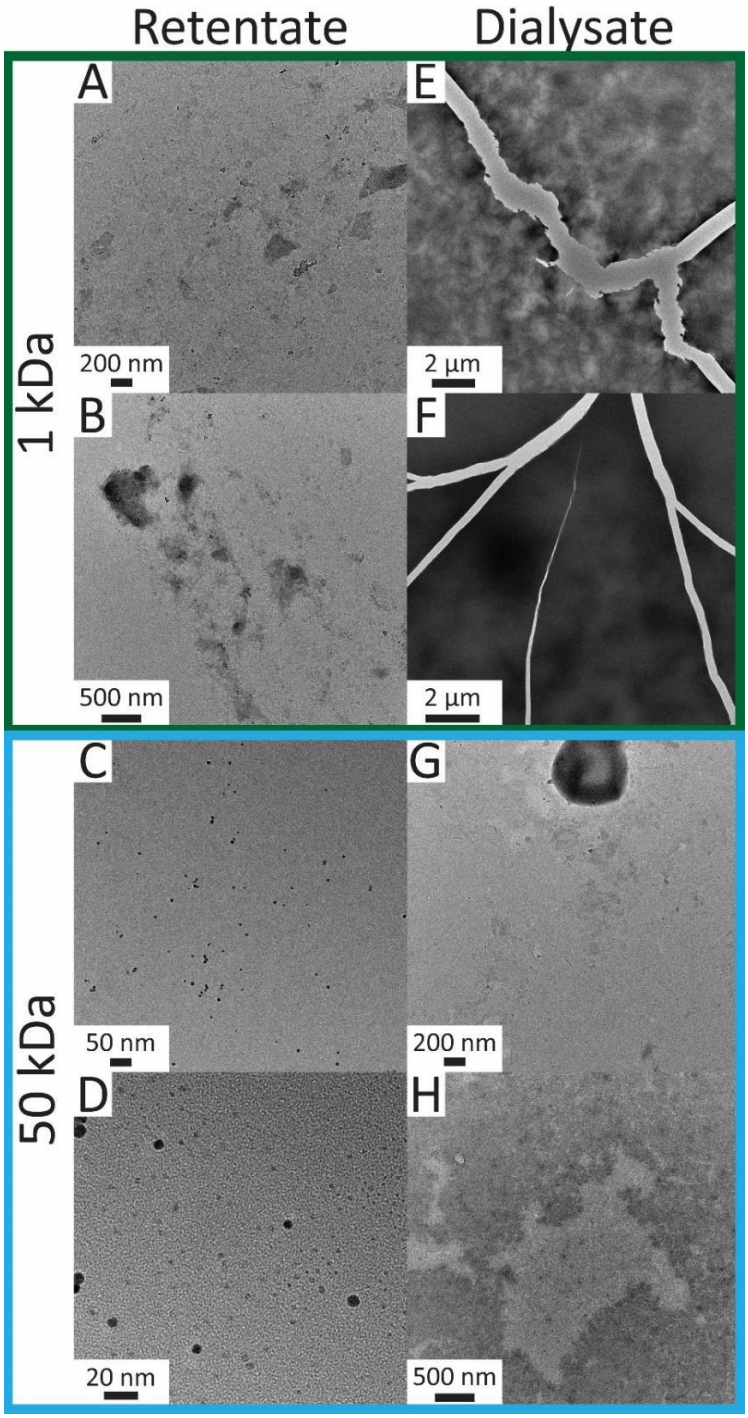

Figure G.7 Representative TEM images of the 1 kDa (A, B, E, and F) and 50 kDa (C, D, G, and H) MWCO retentate (A-D) and dialysate (E-H) fractions from dialysis of the microwave-generated CA-U material. Some of the FCDs were visible in the 1 kDa MWCO retentate fraction but proved difficult to image due to the large quantity of film-forming molecular byproducts still present. Contrarily, FCDs were more prominent in the 50 kDa

retentate fraction and were more easily imaged due to fewer (or no) byproduct impurities still contaminating the fraction. However, some apparent FCDs were visible in the 50 kDa MWCO dialysate fraction indicating that, in general, dialysis may be less than ideal due to the difficulty in segregating the target FCDs from molecular (oligo- or polymeric) byproducts, a scenario worsened by the potential for small, organic fluorophores to form supramolecular aggregates that resemble FCDs under TEM imaging.

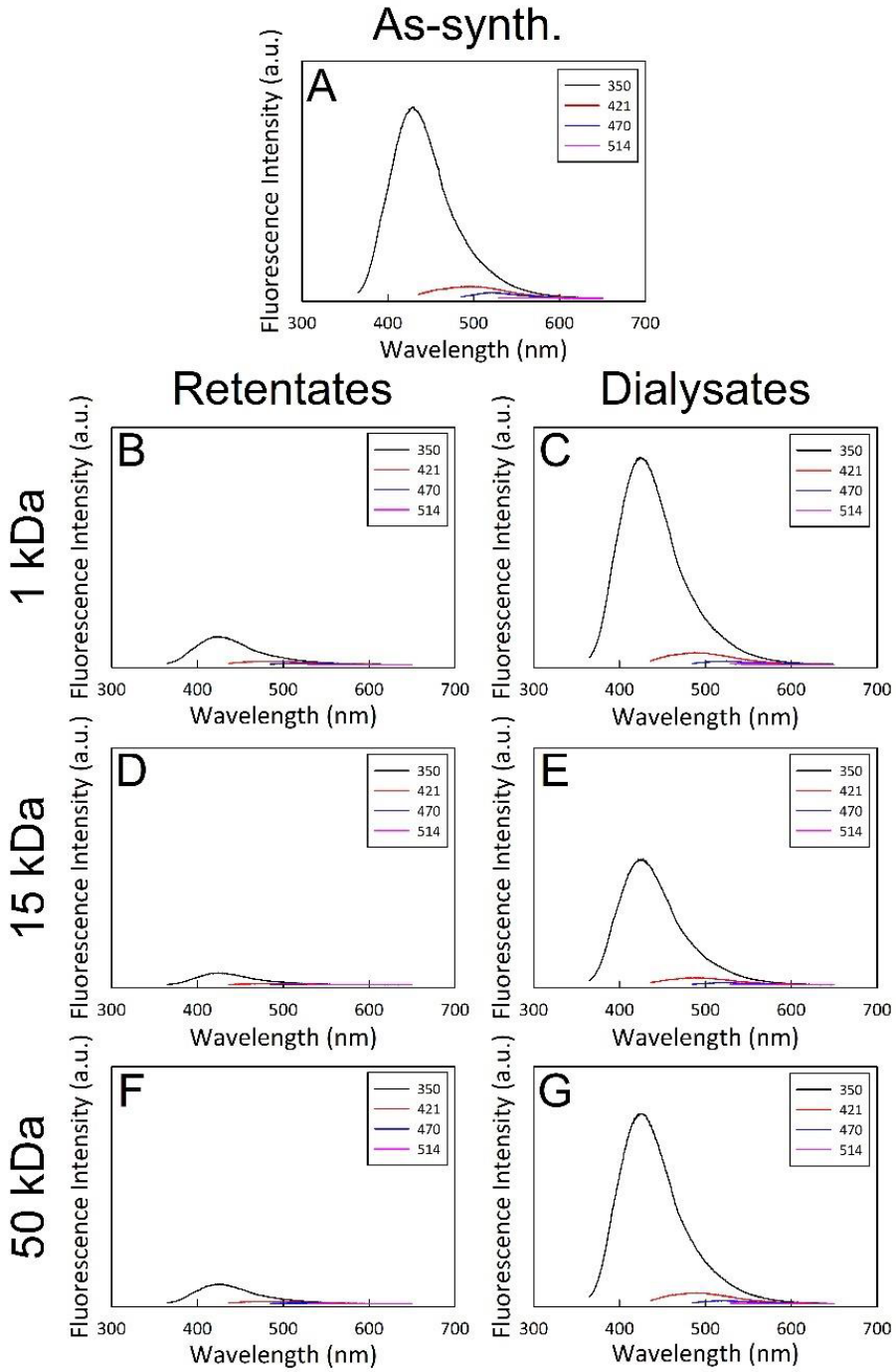

Figure G.8 Excitation wavelength-dependent emission of the as-synthesized (as-synth.) hydrothermal Arg-derived sample (A) and the retentate (B, D, and F) and dialysate (C, E, and G) from the membrane MWCO-dependent dialysis study. All of the samples had similar spectral characteristics to one another although the emission of the retentate fractions was drastically lower despite all fractions possessing similar absorbance values in the near-UV region. This, in combination with the fluorescence quantum yield data

(Figure F.10), further iterate that a majority of the photoluminescence arises from all molecular species (< 1 kDa) and not FCDs.

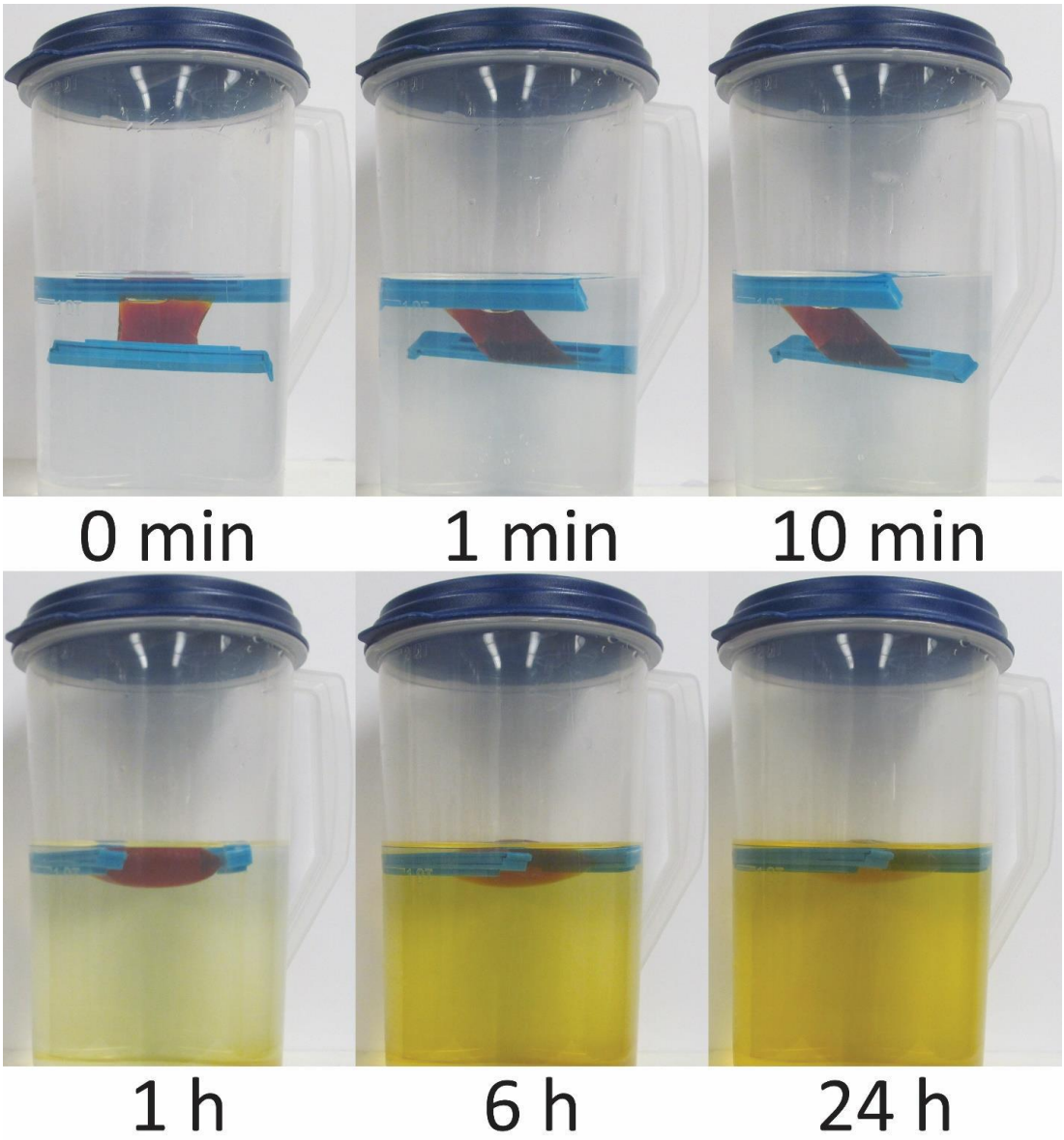

Figure G.9 Sequence of images showing the progress of dialysis against a 1 kDa MWCO membrane for the hydrothermal Arg-derived FCD samples further highlighting that a single dialysis treatment of < 24 h is wholly insufficient to fully fractionate the target FCDs from small molecular byproducts.

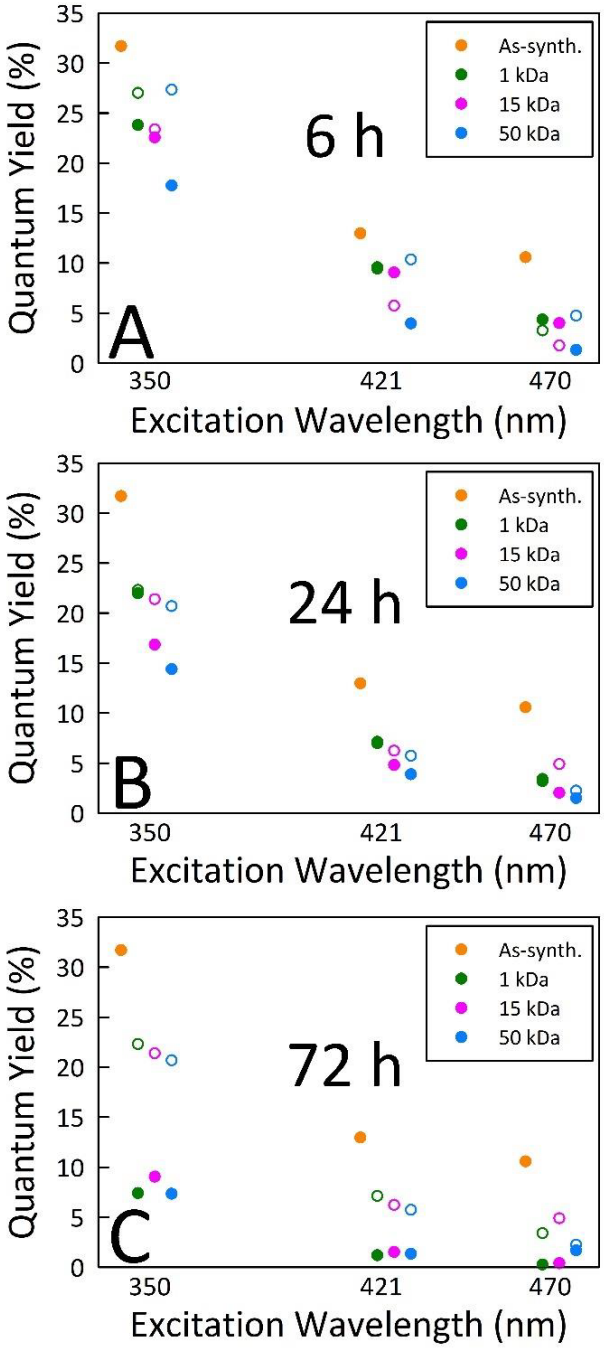

Figure G.10 Fluorescence quantum yields measured for the hydrothermally-synthesized Arg-derived FCDs and the corresponding retentate (closed symbols) and dialysate (open symbols) fractions after dialysis for 6 h (A) and 24 h (B). Panel C compares the measured fluorescence quantum yield of the 24 h dialysate fractions to those determined for the retentate fractions after an additional 48 h of dialysis (72 h in total, where the exchange solvent was replenished every 24 h). The results clearly show that 6 h of dialysis is

insufficient and that after an extended dialysis period, the quantum yields of the retentate fractions further decrease, supporting the notion that a majority of the observed fluorescence of the as-synthesized sample originates from the material constituting the dialysis fraction (*i.e.*, byproducts).

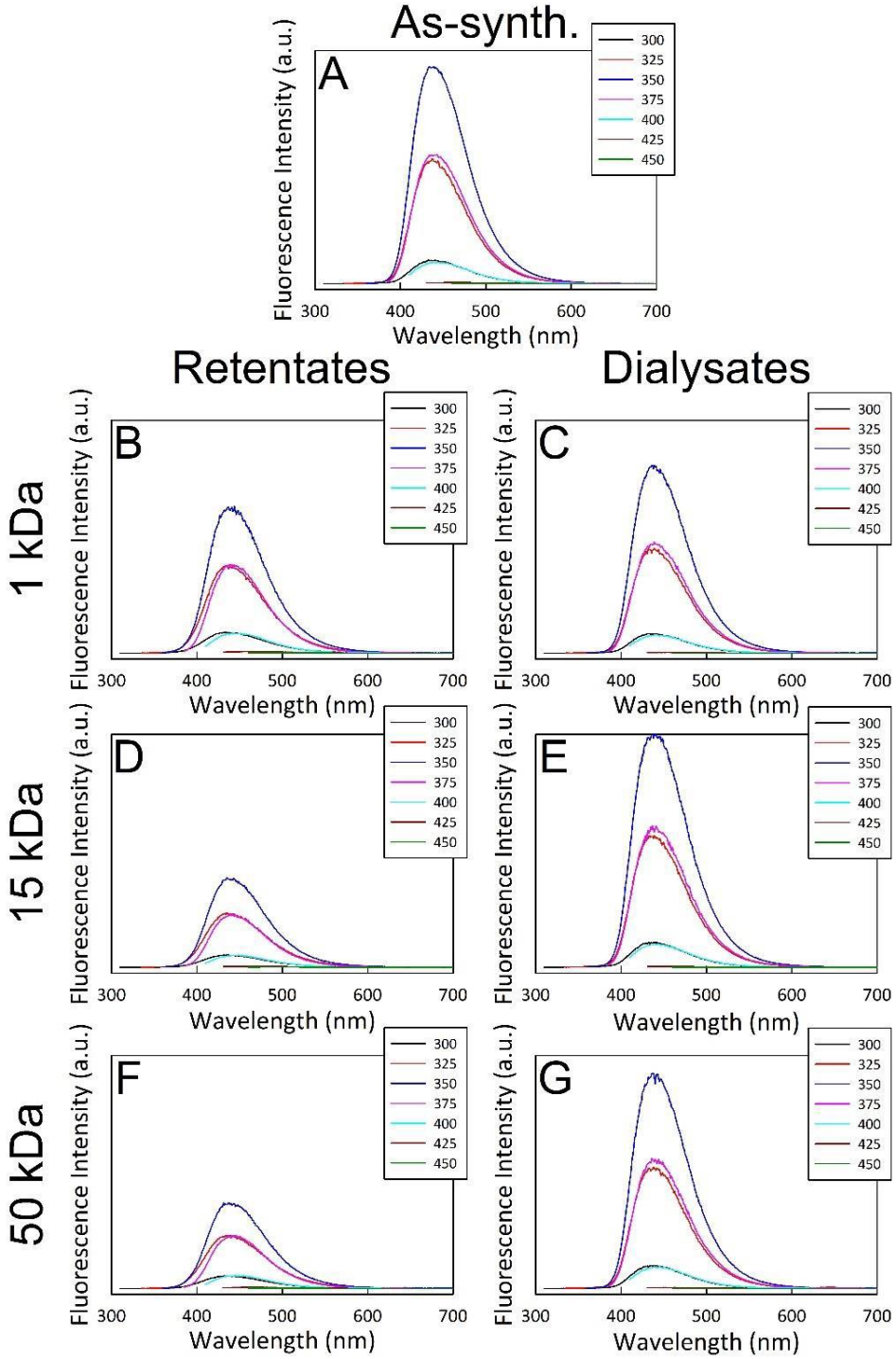

Figure G.11 Excitation wavelength-independent emission of the as-synthesized (as-synth.) hydrothermal CA-EDA derived FCD sample (A) and the corresponding retentate (B, D, and F) and dialysate (C, E, and G) fractions from the membrane MWCO-dependent dialysis study. All fractions had similar spectral characteristics to one another although the emission of the retentates was drastically lower for samples with similar absorbance values,

consistent to the previous systems studied, again alluding to the majority of the fluorescence originating from small molecular species (< 1 kDa).

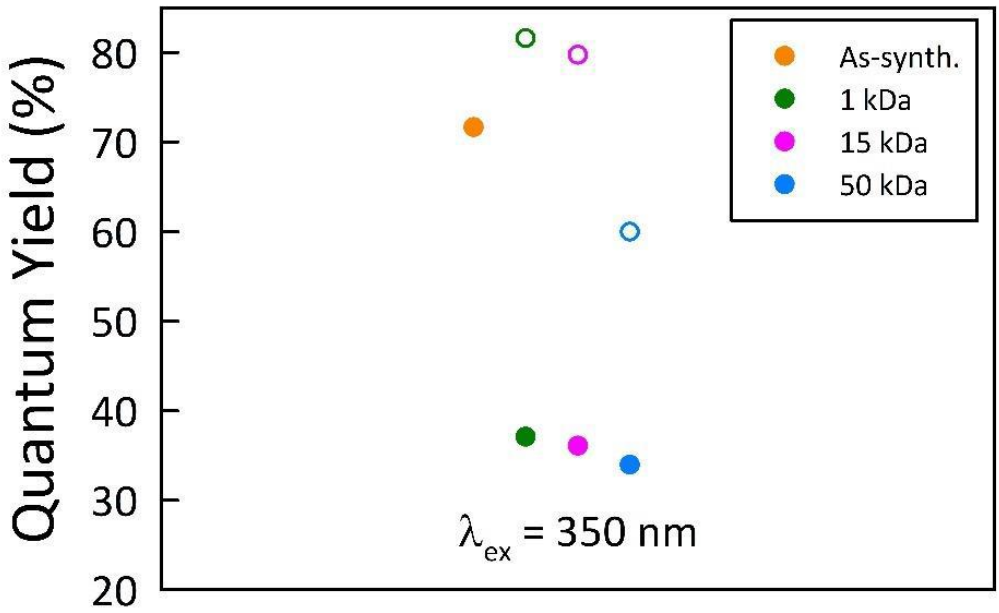

Figure G.12 Fluorescence quantum yields of the hydrothermally synthesized CA-EDA derived sample (as-synth.) and its corresponding 72 h retentate (closed symbols) and 24 h dialysate fractions (open symbols). The results are consistent with all other dialysis studies and clearly show that the retentate fractions consist of less photoluminescent species, whereas the majority of the fluorescence of the as-synthesized sample originates from the species in the dialysate fractions. The excitation wavelength (λ_{ex}) was 350 nm for all fractions.

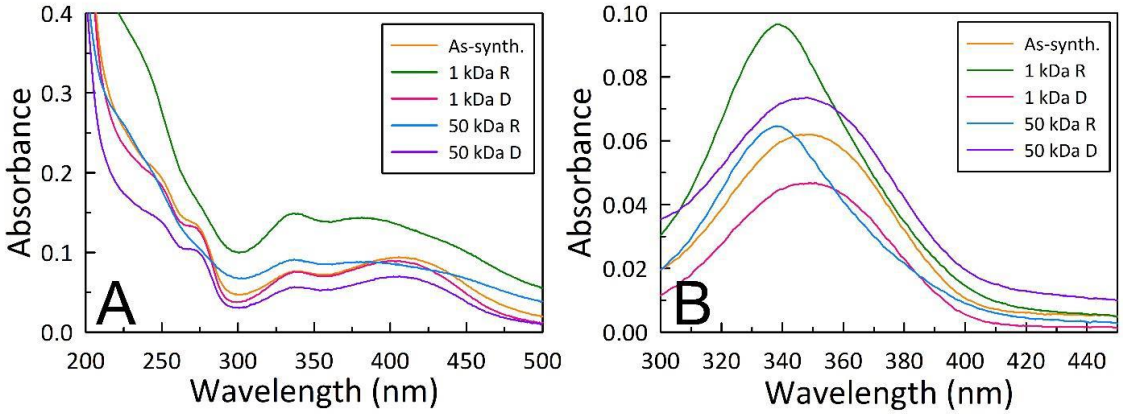

Figure G.13 UV-vis spectra of the as-synthesized (as-synth.), retentate (R), and dialysate (D) fractions from CA-U (A) and CA-EDA (B) samples highlighting the spectral differences between the retentate and dialysate fractions, the latter of which displays features identical to the as-synthesized sample.

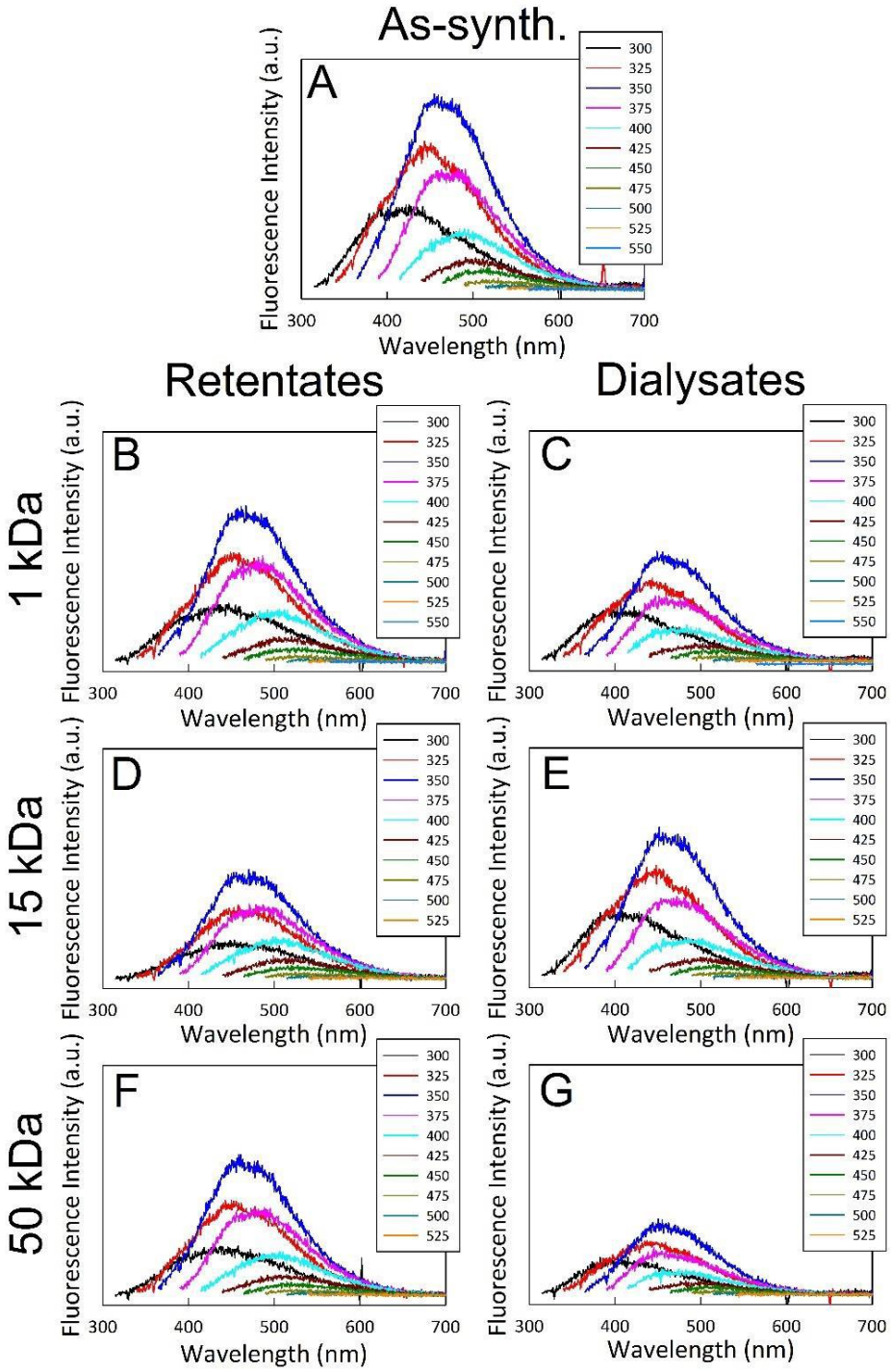

Figure G.14 Excitation wavelength-dependent emission of an electrochemically-synthesized graphite-derived FCD sample (A) and the corresponding retentate (B, D, and F) and dialysate (C, E, and G) fractions from a membrane MWCO-dependent dialysis study. While all fractions had similar spectral characteristics to one another, the results

highlight that top-down approaches are not exempt from purification due to small photoluminescent byproducts generated in situ during FCD synthesis.

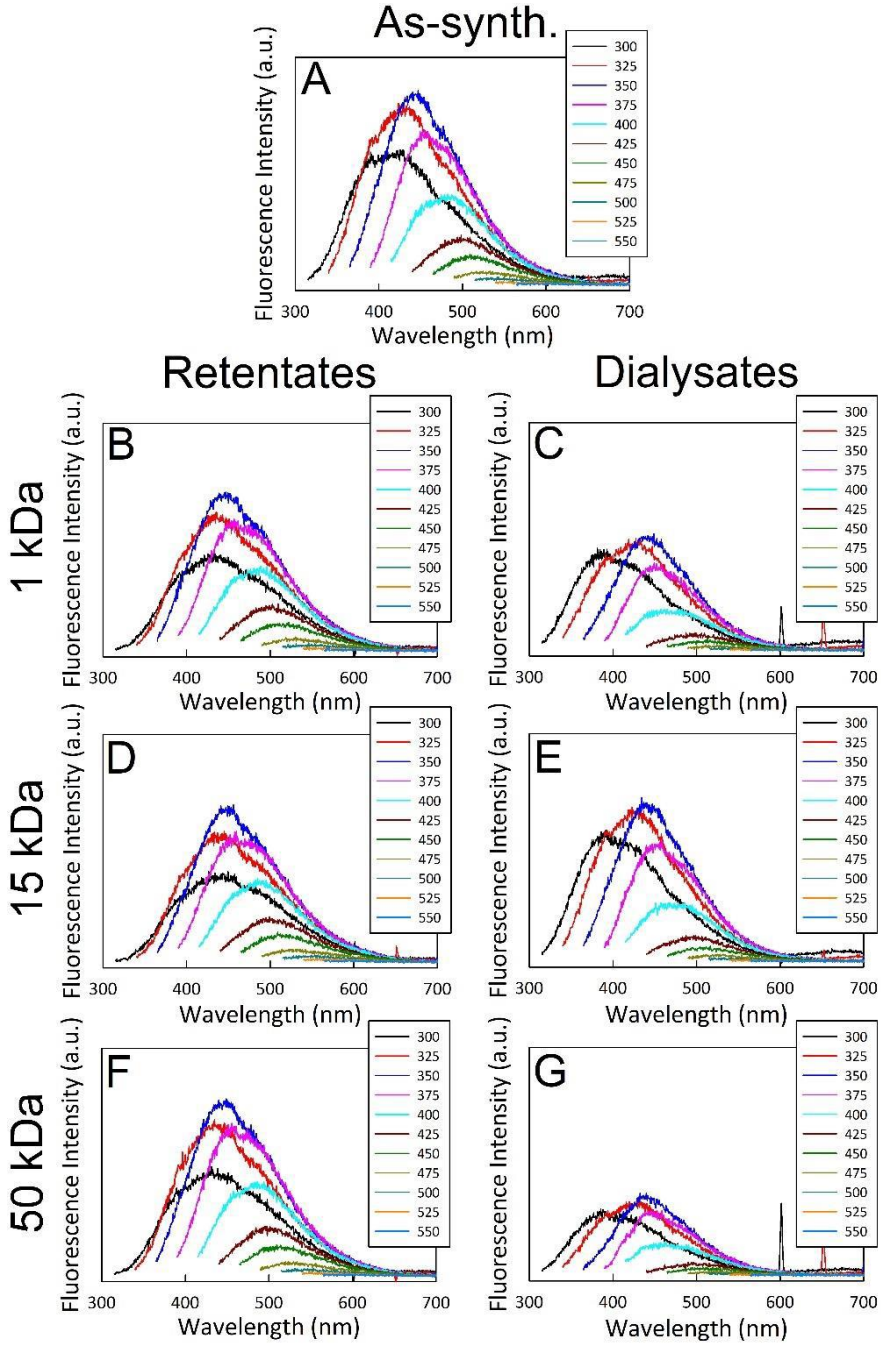

Figure G.15 Excitation wavelength-dependent emission of the hydrothermally-PEG-N-functionalized (1500 Da) FCDs (A) and the corresponding retentate (B, D, and F) and dialysate (C, E, and G) fractions from a membrane MWCO-dependent dialysis study. These results highlight that the products from FCD functionalization reactions are not

solely comprised of passivated FCDs but also contain small fluorescent molecular species (< 1 kDa), thus indicating that post-functionalization purification is an absolute necessity. The parent FCDs were electrochemically-synthesized from graphite.

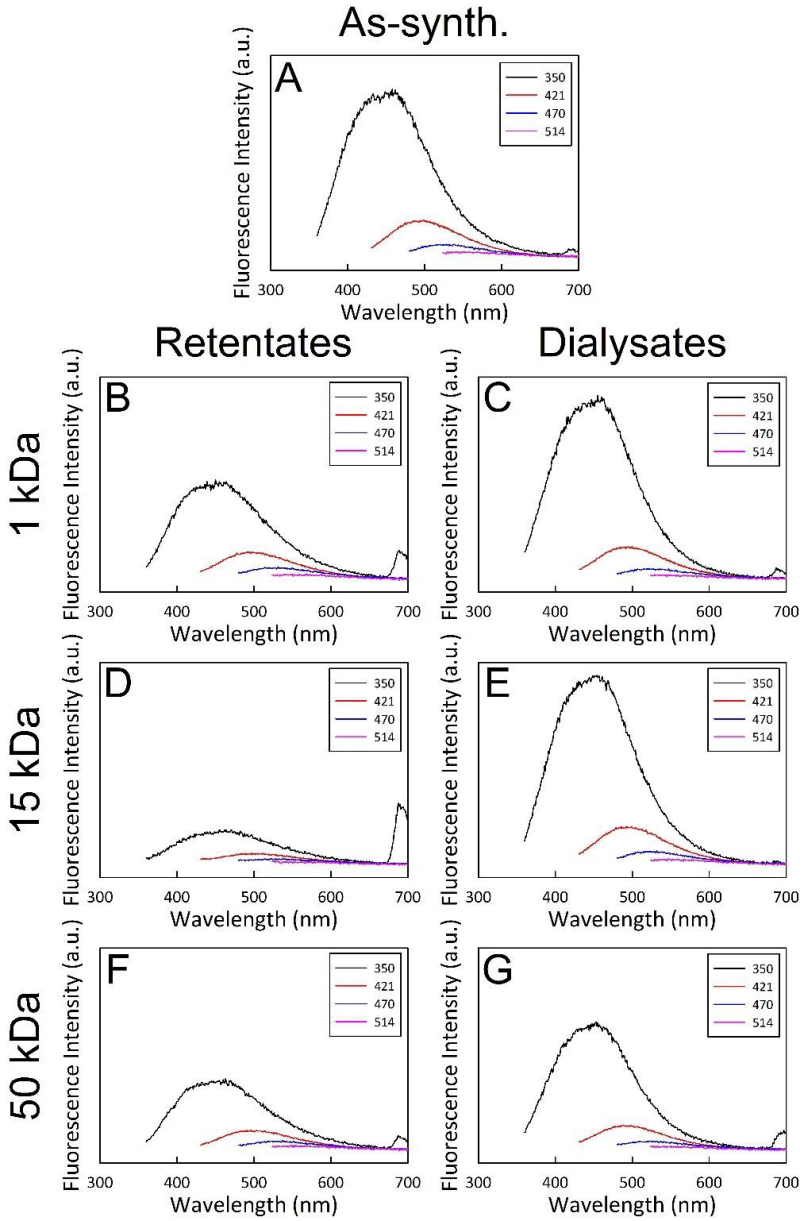

Figure G.16 Excitation wavelength-dependent emission of the hydrothermally-PEI-functionalized (1200 Da) FCDs (A) and the corresponding retentate (B, D, and F) and dialysate (C, E, and G) fractions from a membrane MWCO-dependent dialysis study. Consistent with the results for dialysis of PEG-functionalized FCDs, these results show that post-functionalization purification is essential to adequately separate the putatively

functionalized FCDs from molecular (oligo- or polymeric) byproducts. The parent FCDs were electrochemically-synthesized from graphite.

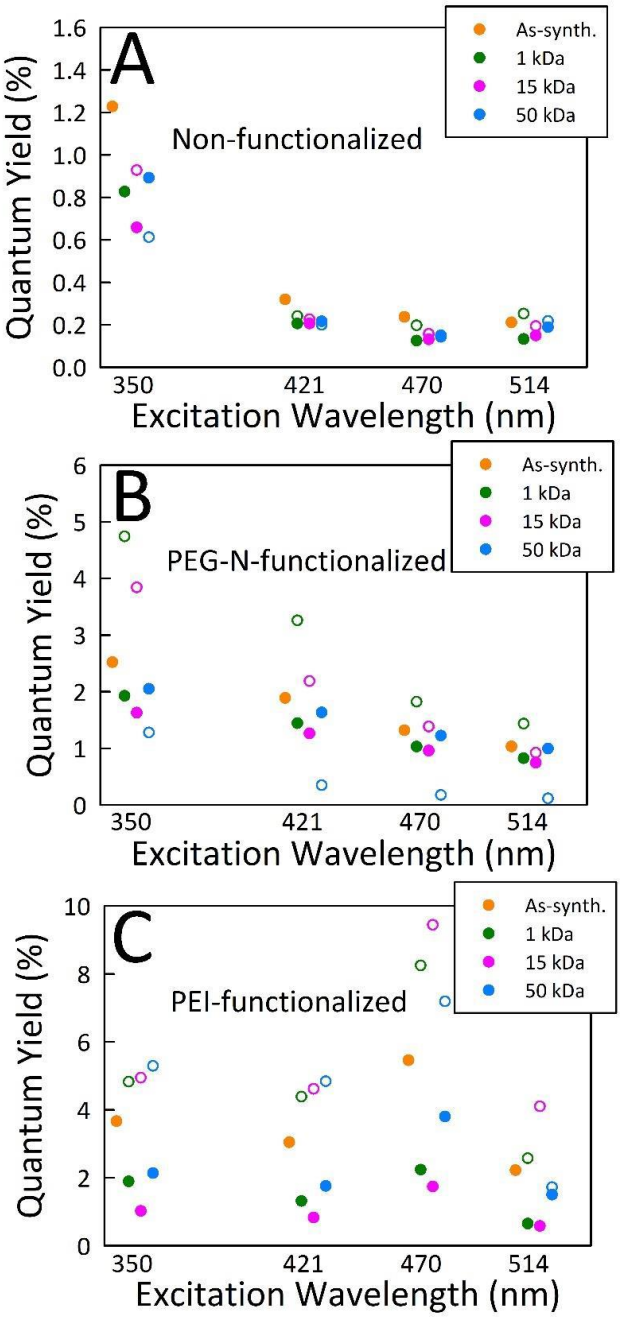

Figure G.17 Fluorescence quantum yields measured for the electrochemically-synthesized FCDs (A), PEG-N-functionalized (1500 Da) FCDs (B), PEI-functionalized (1200 Da) FCDs (C), and their respective retentate (closed symbols) and dialysate (open symbols) fractions. The resultant values highlight that even for top-down syntheses and their

subsequent functionalization, adequate purification is a necessity after the initial synthesis as well as post-functionalization.

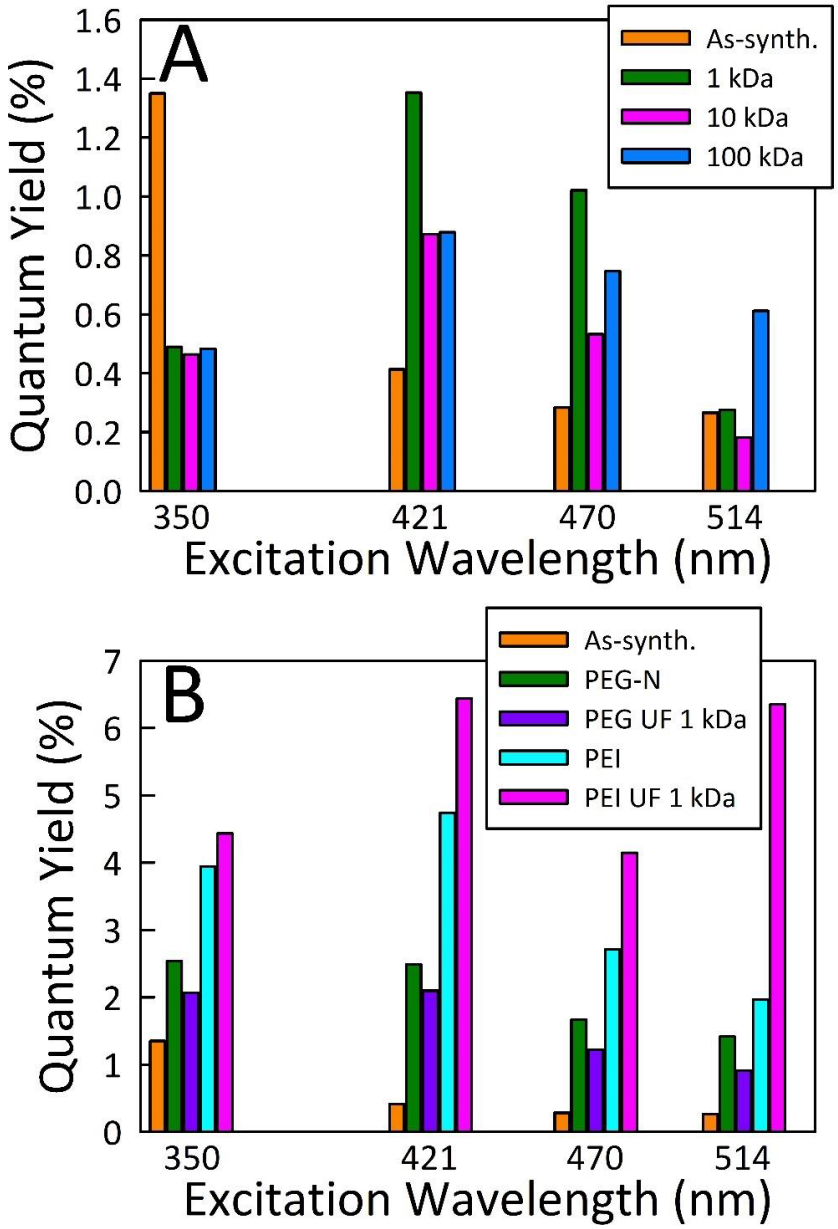

Figure G.18 (A) Fluorescence quantum yields determined for the electrochemically-synthesized (as-synth.) FCDs and the filtrate fractions after ultrafiltration with 1 kDa, 10 kDa, or 100 kDa MWCO membranes further highlighting the need for adequate purification. (B) Fluorescence quantum yields of the as-prepared PEG-N-functionalized (1500 Da) and PEI-functionalized (1200 Da) FCDs and the corresponding filtrate fractions

after ultrafiltration (UF) with a 1 kDa MWCO membrane showing that highly fluorescent non-functionalized byproducts are indeed generated, necessitating fractionation from the target FCD. The quantum yield of electrochemically-synthesized (as-synth.) FCDs is included in Panel B for comparison.

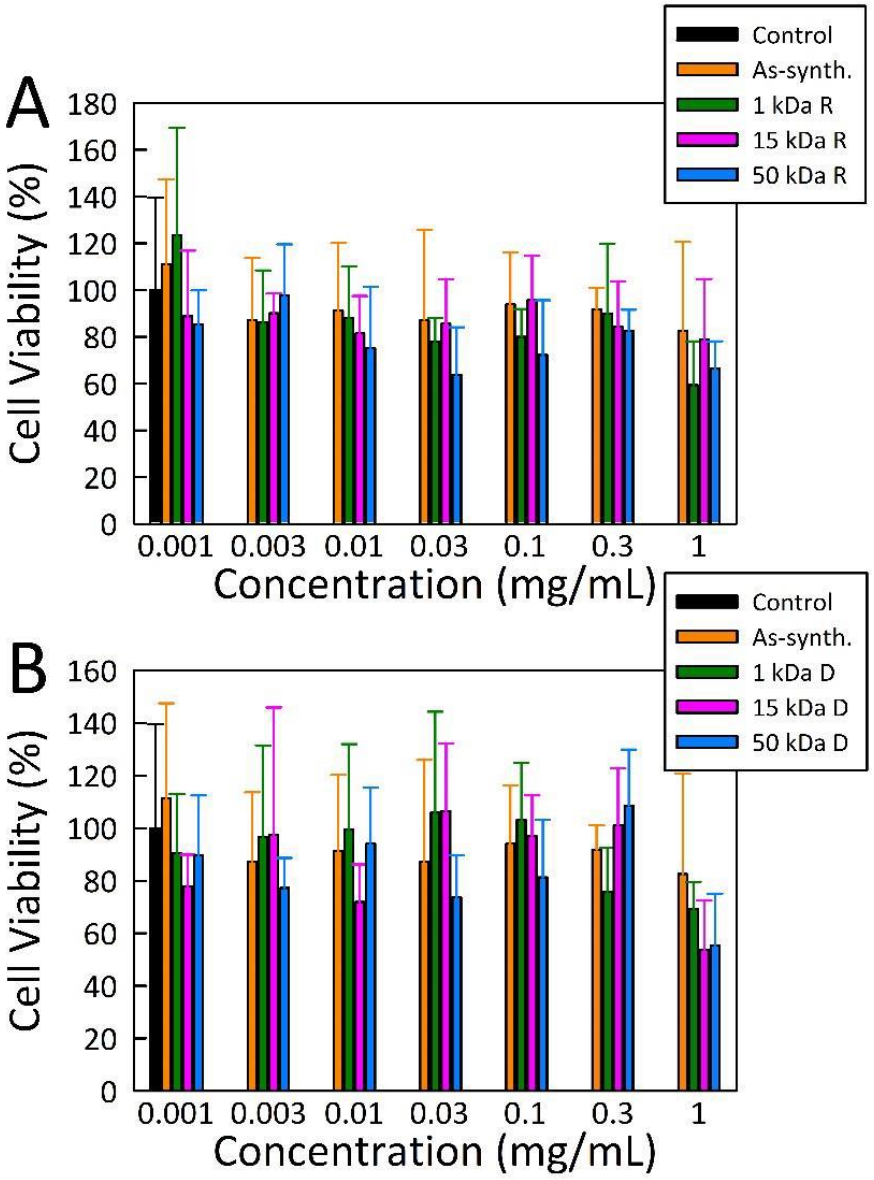

Figure G.19 Toxicity of microwave-generated CA-U derived FCD (A) retentate (R) and (B) dialysate (D) fractions toward mice embryonic fibroblasts. Minimal toxicity was observed for concentrations at or below 0.3 mg/mL while slight toxicities arose for concentrations of 1 mg/mL. No clear difference was apparent between the retentates and

dialysates. The toxicity of the as-synthesized (as-synth.) samples is provided in both panels for comparison.

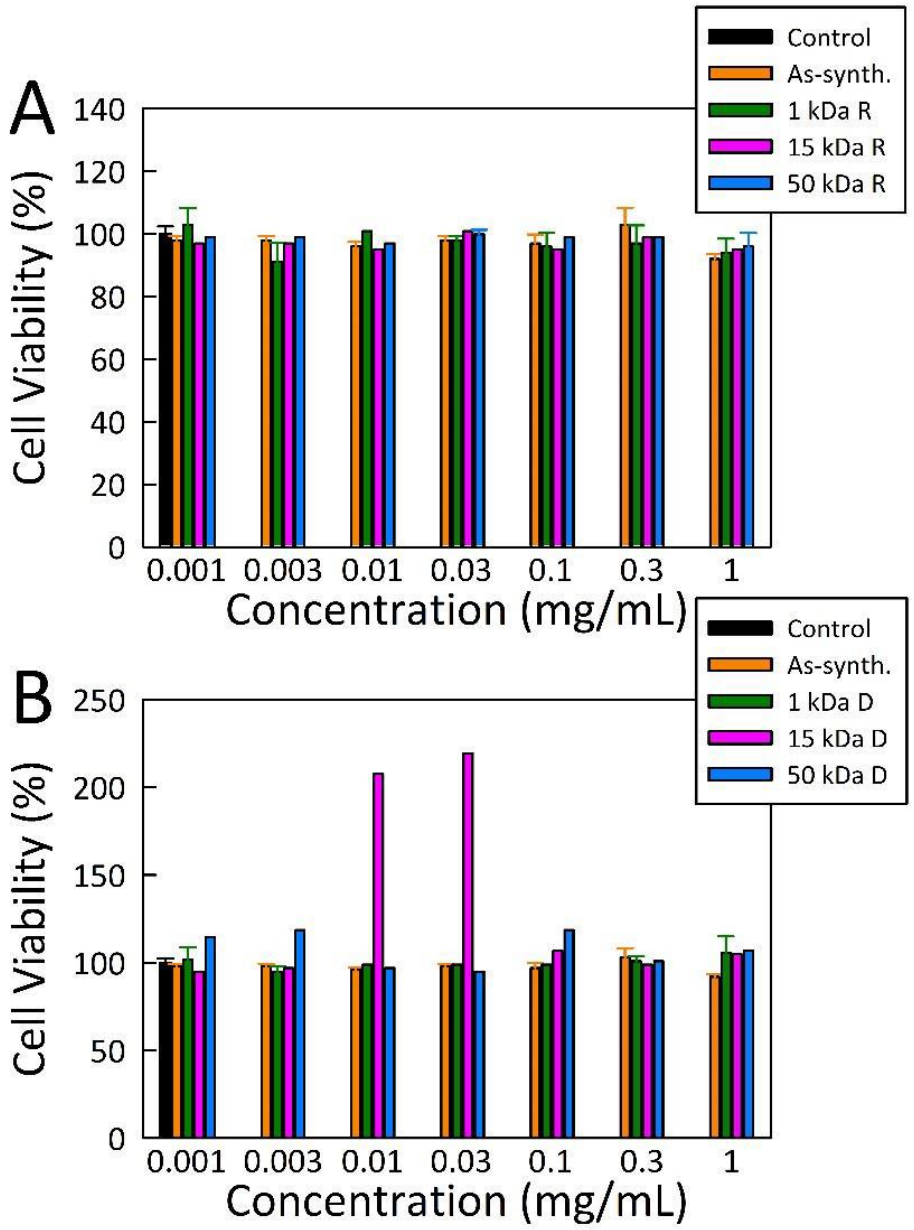

Figure G.20 Toxicity of microwave-generated CA-U derived FCD (A) retentate (R) and (B) dialysate (D) fractions toward human breast cancer cells (T47D). Both the retentate and dialysate fractions for all membrane MWCOs studied had no toxic effects on this specific cell line. The toxicity of the as-synthesized (as-synth.) sample is provided in both panels for comparison.

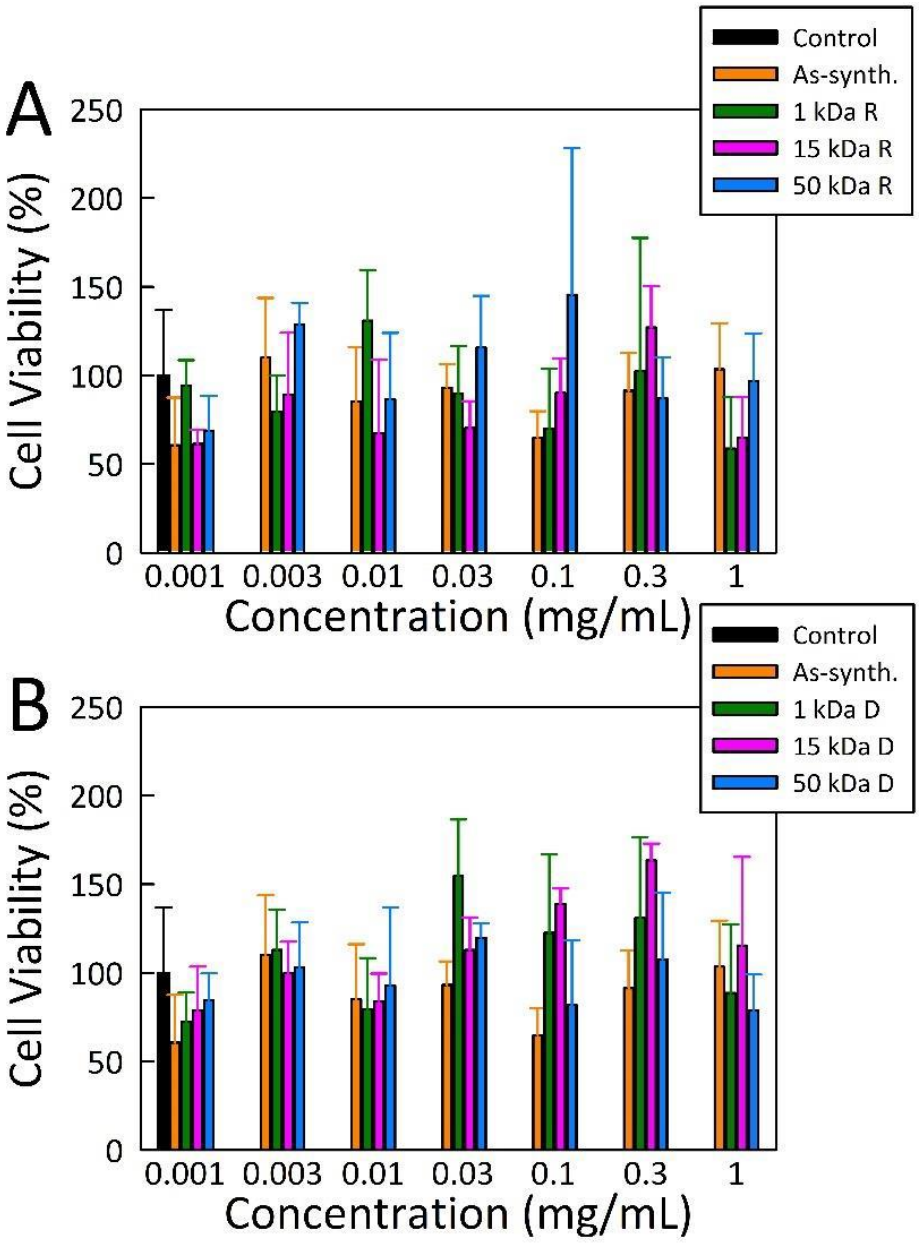

Figure G.21 Toxicity of microwave-generated CA-U derived FCD (A) retentate (R) and (B) dialysate (D) fractions toward HeLa cells. For the most part, the fractions were essentially non-toxic but no clear trends arose within each sample set and no difference was apparent between the retentate and dialysate fractions. The toxicity of the as-synthesized (as-synth.) sample is provided in both panels for comparison.

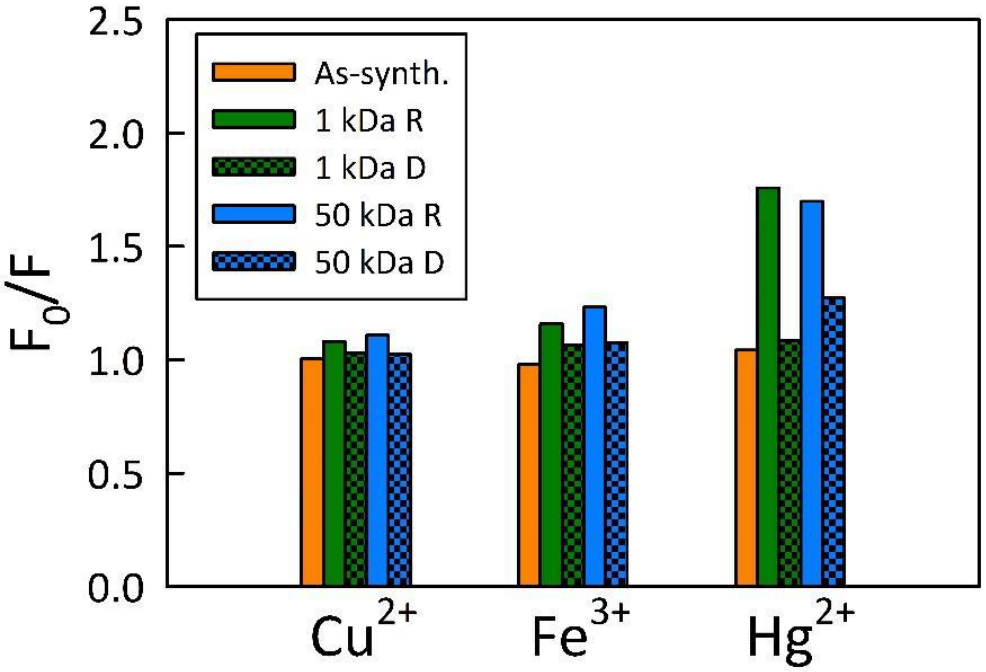

Figure G.22 Metal ion quenching studies of hydrothermally synthesized CA-EDA derived FCDs (as-synth.) and the corresponding retentate (R) and dialysate (D) fractions. In general, Cu^{2+} and Fe^{3+} induced little to no quenching for all fractions, however, in the presence of Hg^{2+} the retentate fractions were quenched more strongly than the as-synthesized samples and the dialysates. These results are consistent with the microwave-generated CA-U derived FCD quenching studies.

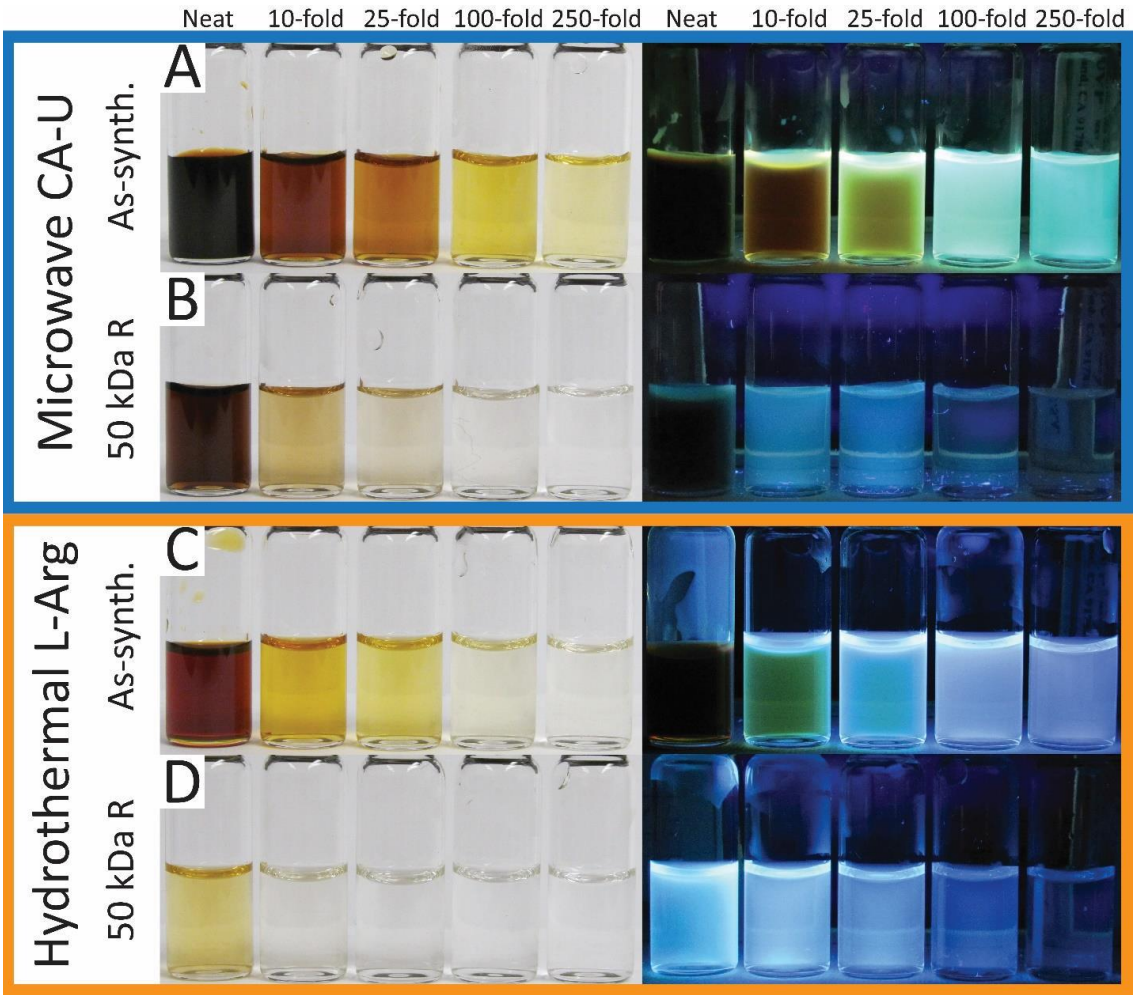

Figure G.23 Composite image of the (A and C) as-synthesized (as-synth.) and (B and D) 50 kDa retentate (R) fractions for the CA-U and Arg-derived FCD samples, respectively, under white light (left Panels) and 354-nm UV light (right Panels). The image illustrates the misleading fluorescence results that arise when the samples are not properly diluted to a similar concentration (or absorbance value). At higher concentrations, the samples will appear to fluoresce at more red-shifted wavelengths due to the illumination of the already orange or red colored solutions.

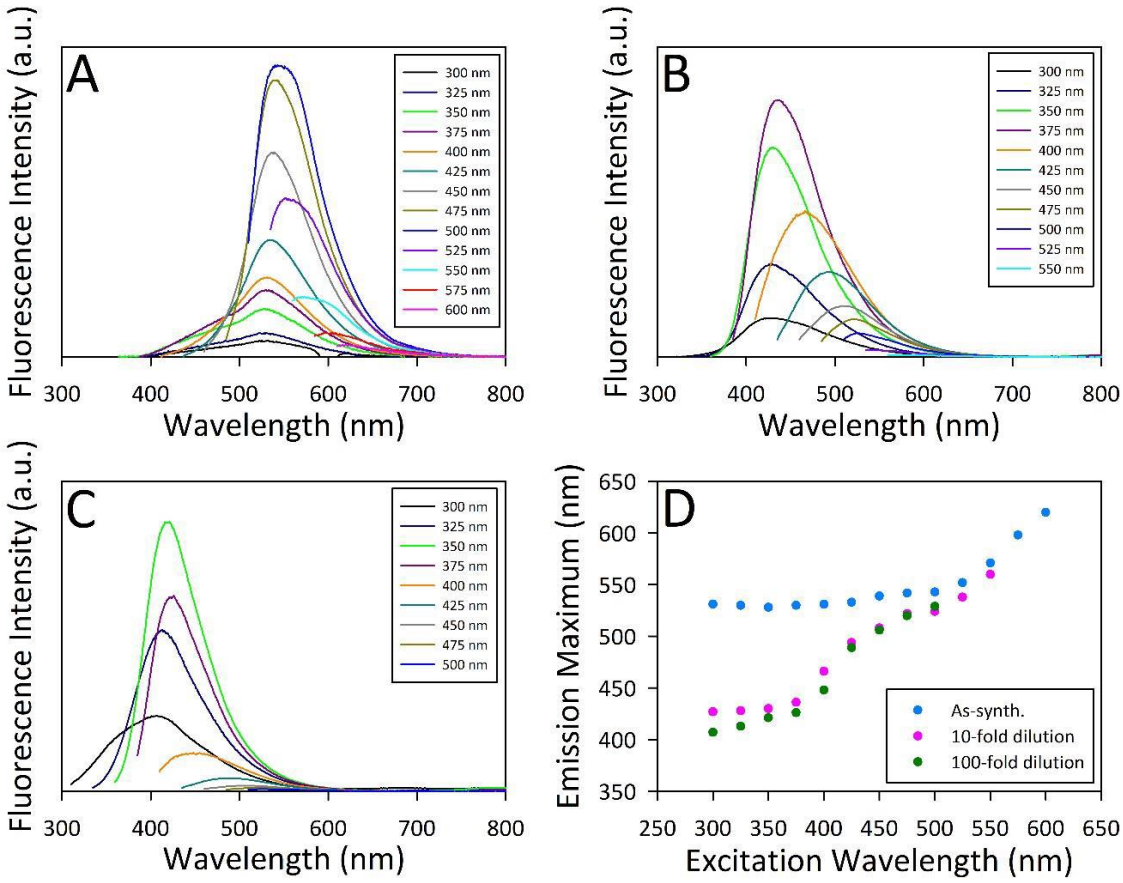

Figure G.24 Excitation wavelength-dependent emission spectra of the (A) as-synthesized (as-synth.), (B) 10-fold diluted, and (C) 100-fold diluted hydrothermally-generated Arg-derived samples which show that as the sample is diluted, the fluorescence blue-shifts which might lead one to believe that at higher concentrations the samples emit redder wavelengths. However, the apparent bathochromic shift simply arises from inner filter effects that lead to attenuation of the blue edge. The emission maxima were extracted from Panels A-C and plotted as a function of the excitation wavelength (D) which further highlights the observed emission shift.

VITA

Jennifer Ann Kist was born in 1988 in Naples, Italy to Joseph and Mary Kist. Her parents were in the Navy and her and her brother, Matthew, were born on the Naval Base in Italy. Jennifer grew up in Vincennes, Indiana and attended Lincoln High School, where she was actively involved in show choir, musicals, and colorguard/marching band. After she graduated high school in 2006 with high Honors, Jennifer attended Vincennes University, the local community college, where she received her bachelor's degree in Secondary Education with an emphasis in Chemistry in 2010. She also received her teaching license in the state of Indiana and taught for one year at Dugger Middle/High School.

After some time off from teaching, Jen decided to go to graduate school. She attended the University of Missouri-Columbia in the Fall of 2014 and worked for Dr. Gary Baker in his analytical research lab. During graduate school, Jen worked on nanoparticle syntheses with various reducing agents and protein thermostability in deep eutectic solvents and ionic liquids. She successfully defended her thesis in December of 2022.

For her future, Jennifer has accepted a post-doctoral position at the University of Cincinnati under the leadership of Dr. Patrick A. Limbach working on RNA modifications using LC/MS. Her goal is to become a professor and instill the knowledge and passion for learning that her teachers and mentors have instilled in her. Specifically, Jen would like to thank her elementary and high school teachers, Paula Hendrix, Karen Livers, Betsy Couchenour, and Kreg Battles, as well as her undergraduate chemistry professor, Jay Bardole. These teachers inspired her to become a teacher and her hope is to encourage, uplift, and inspire future generations of scientists in the years to come.